DEVELOPMENT OF EMC ANTENNAS AND THEIR APPLICATION IN ON-LINE SE MEASUREMENT OF CONDUCTIVE COMPOSITE PLASTIC MATERIALS

A thesis for the degree of Ph.D.
presented to
DUBLIN CITY UNIVERSITY

by

HAFIZUR RAHMAN, B.Sc. Engg., M.Sc. Engg.

SCHOOL OF ELECTRONIC ENGINEERING
DUBLIN CITY UNIVERSITY

RESEARCH SUPERVISOR
MR. JIM DOWLING
and
DR. THOMAS CURRAN

March 1994

DECLARATION

I hereby certify that this material which I now submit for assessment on the programme of study leading to the award of Ph.D. is entirely my own work and has not been taken from the work of others save and to the extent that such work has been cited and acknowledged within the text of my work.

Signed:  .

Hafizur Rahman

Date: 25 February 1994.

ACKNOWLEDGEMENTS

I would like to express my profound gratitude to my supervisor, Jim Dowling, a man of good reasoning and forbearance for his guidance and tuition in the course of this work. I found his constant help, support and encouragement enormously fulfilling throughout the long road to this dissertation. Without his brilliant touch at every paragraph of this dissertation, it would have been impossible for me to organize it in the present form.

To Dr. Tommy Curran, a special word of appreciation and sincerest gratitude for affording me the opportunity to pursue this work.

I am grateful to Reshma, for her ceaseless efforts in preparing this thesis from scratch. Moreover for all her love, supports, patience and understanding especially over the last three years, I remain in her debt.

I must also acknowledge my dearest friend, Dr. Ziaul Karim, for his continuous support from the very beginning of this work. He made me acquainted with the research facilities of this University and boosted me up with encouragements at every crucial stage of this research work.

This project has been funded by EOLAS and TELTEC, Ireland and I am thankful to those organizations for their support. Especially I thank Mr. John McAuley for his kind help while I was performing the experiments in the EMC laboratory of EOLAS.

My colleague, Mr. P. K. Saha, was a co-worker in this EMC laboratory and the useful discussions which I had with him played a vital role towards the technical fulfilment of this work, I would therefore, like to thank him for all his co-operations. I would also thank Dr. Jeevakumar Kanagaratnam from the Speech laboratory for his invaluable suggestions in developing the computer programs for this work.

For most of the mechanical design parts of this research work, I had discussions with Mr. Maksud Hilali and it is a pleasure for me to acknowledge his useful suggestions. All other Bangladeshi friends, here in DCU, also helped me a lot on different occasions regarding this research work and I also thank them all.

I would like to express my gratitude to Dr. Zakia Rahman, Dr. Abdur Rahman and Mr. Paraic Brannic of University of Limerick for their great help during the most important experiments of this research at the EMC laboratory of PEI, UL.

I am grateful to Prof. Charles McCorkell, Dr. Ronan Scaife and Dr. Aungus Murray of this school and Prof. M. S. J. Hashmi of the school of Mechanical and Manufacturing Engineering for inspirational discussions and timely assistance towards fulfilling this work. I would like to thank John Whelan, Conor Maguire, Paul Wogan, Liam Meany, David Condell, Peter McGorman of Electronic Engineering department for their help and co-operation and Ian Hooper of Mechanical Workshop for building the experimental rigs.

DEDICATION

To Mum and Dad,

who have dedicated life for the sake of their children's education.

DEVELOPMENT OF EMC ANTENNAS AND THEIR APPLICATION IN ON-LINE SE MEASUREMENT OF CONDUCTIVE COMPOSITE PLASTIC MATERIALS

Hafizur Rahman

ABSTRACT

The development of three new EMC antennas, namely the V-conical-lens antenna (VCLA), half of a Transverse Electromagnetic-T (TEM-T) cell (acting as an antenna) and the Q-loop antenna (a quarter of a loop antenna in front of 90^{o} corner reflector) is described. These antennas, when calibrated, are designed with a view to employing them in the measurement of on-line Shielding Effectiveness (SE) of conductive composite materials. Test devices incorporating those newly developed antennas for measuring SE against high impedance and low impedance wave are introduced.

The theoretical model of the VCLA is developed and design features are presented as a state-of-the-art project with a view to developing this technique in the near future for measuring the plane wave SE of conductive plastics during their production process.

A modified TEM-T cell designed to simulate a high impedance field on the material under test (MUT) in its (TEM-T cell's) near field region is presented. The field simulated by this device in the test location is studied theoretically. The device measures the high impedance field SE of planar sheet-like conductive plastic materials in a situation that attempts to reconstruct the on-line environment likely to prevail in the manufacture of such plastics. This test device is calibrated by taking into account the background noise, indirect path signal infringement and radiation losses.

The newly developed Q-loop antenna is designed to be used to measure the low impedance field SE of conductive plastic materials. An analytical model of the Q-loop antenna is developed using image theory and the theory of pattern multiplication. This model is verified experimentally. Calibration experiments are performed to facilitate applying the antenna in an on-line SE measurement technique.

A new class of filled composite material with a two dimensional regular array of conductive flakes (like a Frequency Sensitive Surface (FSS)) in plastic resin is proposed. A theoretical model of the suggested configuration is formulated and used to predict SE values. The SE of such material is also determined experimentally and compared with the theoretical predictions. This SE is compared with the SE of an available filled composite in which the flakes are randomly distributed. The improvement in the shielding capability of the new class of material is highlighted.

Relative radiation patterns of the developed antennas are measured and compared with predictions. Apart from the anomalies which can be attributed to (simplifying) assumptions made in the development of the theoretical analysis, the measured radiation patterns and other antenna parameters are in good agreement with predictions.

CONTENTS

LIST OF SYMBOLS

c	Speed of light (= 3×10^8 m/s)
f	Frequency, Hz
ω	Angular frequency, rad/s
λ	Wavelength, m
λ_0	Wavelength in free space, m
β	Phase constant (=$2\pi/\lambda$), rad/m
η	Intrinsic impedance
η_0	Intrinsic impedance of free space (=377 Ω)
ρ_v	Volume resistivity , Ω-m
σ	Conductivity, S/m
μ	Permeability, H/m
μ_0	Permeability of free space (= $4\pi\times10^{-7}$ H/m)
ε	Permittivity, F/m
ε_0	Permittivity of free space (= 8.852×10^{-12} F/m)
δ	Skin depth (= $1/\sqrt{(\pi f\mu\sigma)}$)
ρ	Reflection coefficient
τ	Transmission coefficient
n	Refractive index (=λ_0/λ)
Ψ, Φ	Hertz scalar functions
$\vec{A}$	Vector magnetic potential
$\vec{F}$	Vector electric potential
σ	Standard deviation
SE	Shielding effectiveness, dB
SE_E	Shielding effectiveness against E-field, dB
SE_H	Shielding effectiveness against H-field, dB
A	Absorption loss
R	Reflection loss
B	Successive re-reflection loss or correction factor
P_r	Received power
P_t	Transmitted power
VSWR	Voltage standing wave ratio

LIST OF ACRONYMS

BCA	Bi-conical antenna
CSM	Clamped stationary measurement
EMC	Electromagnetic compatibility
EMI	Electromagnetic interference
EUT	Equipment under test
IL	Insertion loss
LPA	Log periodic antenna
MUT	Material under test
NCSM	Non contacting stationary measurement
OLM	On-line measurement
PET	Polyethylene Terephthalate
Q-loop	Quarter of a loop antenna in front of 90^{o} reflector
RFCP	Regularly filled conductive plastic
TEM	Transverse electromagnetic
TEM-T	Transverse electromagnetic-T
VCA	V-conical antenna
VCLA	V-conical lens antenna

Chapter 1

EMC AND SHIELDING

EMC AND EMI
DESIGN OF SHIELDED ENCLOSURE
CONDUCTIVE COMPOSITE PLASTIC MATERIALS
IMPORTANCE OF ON-LINE SE MEASUREMENT
OBJECTIVE AND LAYOUT OF THE THESIS

1.1 INTRODUCTION

Electronic appliances and instruments are part of every aspect of our day to day life starting from kitchen tools to satellite communication. Because of their widespread proliferation, the electromagnetic environment has become polluted. Electromagnetic interference (EMI) both inter- and intra- device is the well-known "pollutant". Electromagnetic Compatibility (EMC) studies both reflect and promote the awareness among the designers and manufacturers of electronic equipment of the need to combat EMI.

Enclosing electrical and electronic equipment with conducting materials is the simplest way of reducing ingress or emission of EMI. Conductive composites are potential candidates for such applications. On-line SE determination of these materials is particularly important for waste reduction, quality control and possible improvement of SE at a minimum cost.

This introductory chapter thus presents some general discussion on the growing interest in EMC in the next section. The sources and victims of EMI are described in section 1.3. In Section 1.4, the implication of the new EMC regulations prounegated by the lyistable oyanistans are discussed.

EM compliance is achieved very often through a shielded enclosure and its efficacy can be determined through SE measurements. The design of shielded enclosures and the role of shielded material in such design are discussed in section 1.5.

Conductive composites are promising materials in designing shielded enclosures and various techniques of imparting shielding capability to plastics are described in section 1.6. The importance of on-line SE measurements of such plastics is indicated in section 1.7. The objective of this research, in this context, is described in section 1.8. At the end of this chapter, in section 1.9, the layout of the thesis is specified.

1.2 GROWING INTEREST IN EMC

The definition of EMC is given by the *IEEE Dictionary* [1] as "The capability of electronic equipment or systems to be operated in the intended operational electromagnetic environment at designed levels of efficiency" and EMI is defined as "Impairment of a wanted electromagnetic signal by an electromagnetic disturbance".

There are a variety of problems associated with EMI which range from minor disturbances such as static on car radios, to catastrophic equipment failure which can even result in the destruction of life. Computer malfunction and memory erasure, "ghosting" on a television set, navigational errors in marine and aircraft equipment, failure of medical equipment and unauthorised information access are only a few of the common interference effects.

Concern about EMC dates back to 1934, which was the year of the formulation of the international Special Committee on Radio Interference (CISPR) [2]. Although authorities in Europe were concerned with limiting radio frequency interferences (RFI) since then, no international consensus was formulated until the end of second world war. The first EMC military standard was published in June, 1945 [3]. However, until very recently the awareness was confined mostly among the military users of electronic communications.

Although several terms have been used over the years by the community involved in the electronic industries to represent the EM disturbances such as RFI, radio noise, EMI, electromagnetic pollution, immunity and susceptibility, no concerted effort towards developing a discipline to cover these topics was evident until the end of the 1950s. However, with the increasing use of semiconductors and solid-state circuits, which are inherently prone to interference from electrical disturbances, the problems became more pressing and the need for integrating the various aspects of such problems into a unique subject was obvious. EMC then came into prominence to encompass this complete area of research.

In the last two decades, with the emergence of microprocessors, micro controllers, and the miniaturization of computers along with the development of satellite communication, EMC has gained paramount importance. Then in the current decade, this has been enhanced as networking of computer hardware became widely affordable and even smaller companies with personal computers were drawn to this economical means of sharing peripherals and productivity increasing software [4].

EMC is now a topic relevant to the safe and reliable operation of medical instrumentation, military communications, marine and air traffic navigation, automobile and all other sophisticated automated industries, broadcasting and telecommunications, networking and as such most of our day to day life.

Scientists and engineers in the field of EMC are always interested in designing electronic systems which are invulnerable to hostile or interfering EM environments and at the same time electromagnetically harmless to their neighbouring devices. Like other branches of electronic engineering EMC also covers a very broad spectrum of research areas.

However, achieving desired levels of shielding capability in component, equipment and system level against EMI, either conducted or radiated, is the pivotal element of the research interests on EMC. Source recognition, system design, introducing EMC at the design stage, enclosing the equipment with an efficient shield and measuring the shielding performance and EM compatibility are the major areas of research in EMC.

1.3 SOURCES AND VICTIMS OF EMI

It is difficult to differentiate the sources of EMI from its victims. Perhaps most of the sources (except the natural sources of EMI) are also victims of EMI generated by other sources. Thus in the following discussion in some cases the same system is mentioned both as a source and as a victim.

1.3.1 SOURCES OF EMI

They may be classified as natural sources and man-made sources. Natural sources include lightning and solar and cosmic sources. Man-made sources cover Electrostatic Discharges (ESD), Electromagnetic Pulse (EMP), emissions from electrical and electronic devices, variations in the mains supply voltage and radio transmitters.

Lightning usually appears in the form of very short duration pulses of heavy current in the range of several kA to several hundred kA. It thus emits a very wide band of RF up to 50-100 MHz [15, pp. 9].

The changes that occur in the ionosphere because of the sun, cause problems for radio transmission due to varying ionosphere reflection (in the 2-30 MHz bands) and affect satellite communications by varying ionospheric transmission (150-500 MHz).

ESD results from the accumulation of static charge on objects due to contact with any other object moving relative to it. Such charging can build up voltage as high as

10-25 kV with stored energies of 20-30 millijoules [28]. The discharging of this energy produces fast rising current pulses which can damage electrical equipment.

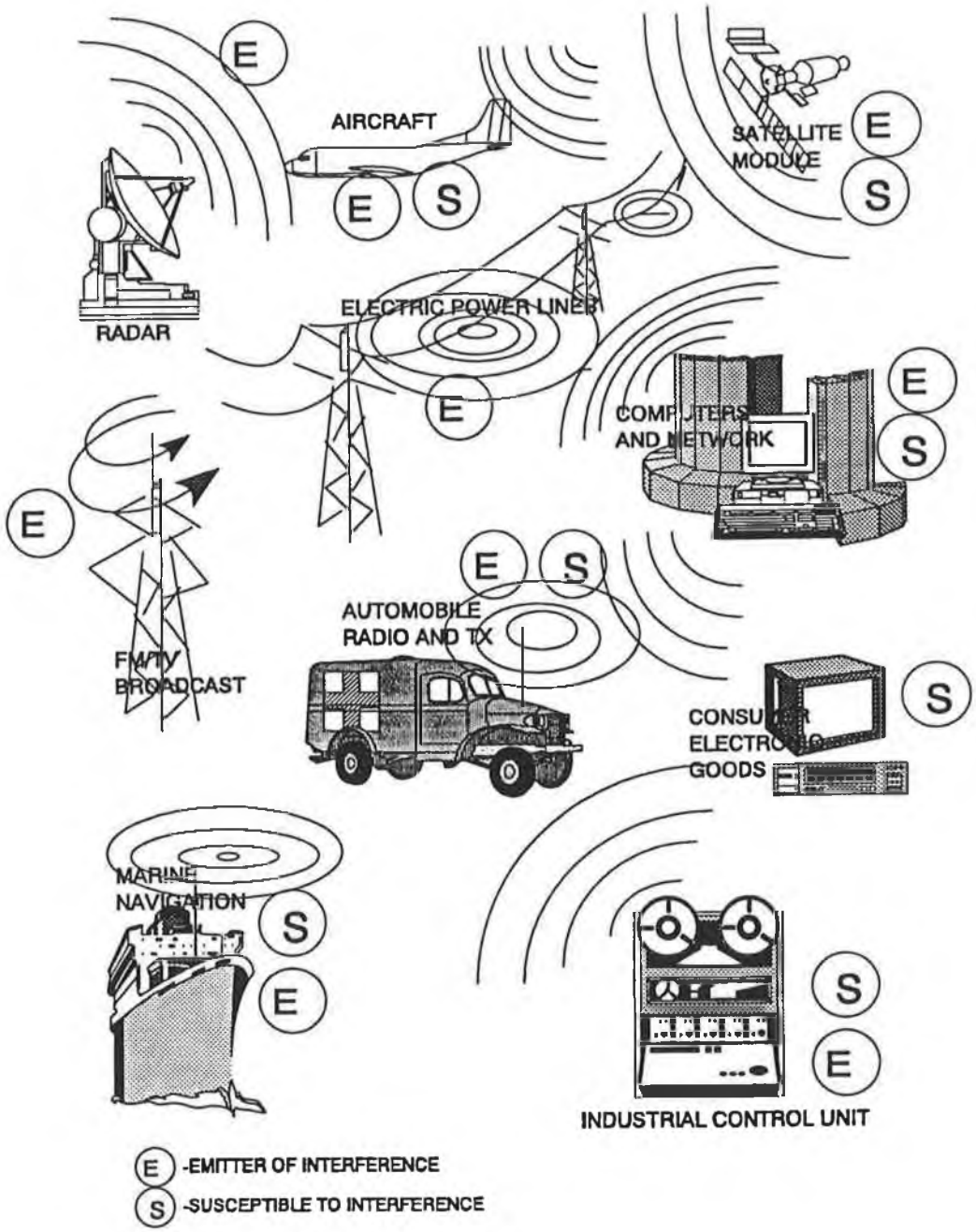

Fig. 1.1 Areas involved with EMC problems. Sources and victims of EMI are indicated as E and S respectively. Adapted from [130].

EMP is the electromagnetic pulse resulting from nuclear explosion [29]. Although obviously very important for military system EMC designers, it has serious implication for civilian applications as well. However, it is only in the case of exoatmospheric or high-altitude nuclear explosions that the interference effect of the EMP is spread over vast areas [180]. In a high-altitude nuclear explosion, gamma rays and x-rays are produced which travel until they collide with electrons in the air molecules of the upper atmosphere. The compton electrons, those scattered by the gamma rays, are accelerated in circular or spiral paths by the geomagnetic field [181] and produce intense electric current. This current, in turn, sets up the EMPs, which radiate downward toward the earth. Depending on the altitude of the burst, the source area may be extremely large and the area exposed to the high fields may encircle several hundreds of km in diameter and the intensity of the electric field at earth's surface may rise up to 50 kV/m. It may cause very strong EMI problems for the power [31] and communication networks [30].

Automotive noise sources (such as ignition system, alternators, electric motors), aircraft emitter sources (such as electrified jet-engine exhaust systems as well as conventional ignition systems); power distribution systems, power lines, ac and dc substations, generating stations; industrial equipment such as welding machines, induction heaters, circuit breakers, microwave heaters, cranes, variable speed drives using pulse width modulated inverters, local oscillators, digital equipment including computers, are all potential sources of EMI polluting the EM environment. The frequency range of emissions may cover a wide spectrum from audio to microwave frequencies.

AM/FM/TV broadcast transmitters, land-mobile and portable/personal communication transmitters may cause significant amount of interference in the EM environment. They can effect power cords to electronic equipment, telephone systems and other broadcast or receiving stations. The frequency of interference may cover a wide spectrum of several hundred kHz to a few GHz.

The increasing use of high powered microwave (HPM) appears as another menacing agent in the EM environment. One such application lies in broadcasting HPM radiation in the form of pencil beams resulting in an EM environment potentially damaging to electronic systems [32]. HPM radiation may not penetrate through metallic portions of a system but if it can enter circuits (through apertures provided in electronic enclosures for ventilation) it may lead to upset, damage or burn-out of components.

1.3.2 VICTIMS OF EMI

As stated earlier, every aspect of electrical and electronic engineering is somehow or other involved with EMC problems. Fig. 1.1 illustrates the different sources and the victims of EMI, and thus demonstrates the extent of the problems.

Process-control instruments are very sensitive to undesired emissions. One distinguishing feature of these instruments is the huge industrial environment in which it must operate, and the attendant undesired RF environment. The susceptibility of Industrial/Scientific/Medical (ISM) equipment to EMI is also of great concern.

Computers may be exposed to extremely strong undesired RF emission, but are generally immune to all but the most powerful emissions[1], the extent of immunity being dependent upon details of manufacture [11]. However, the use of inexpensive unshielded cables in local area networks (LANs) intended to support digital data transmission at a frequency of multimegabit/s, often causes severe EMC problems. One effect is system lockup or freezup, where the users equipment fails to communicate with other system components, because it cannot transfer data without errors.

AM/FM/TV Broadcasting receivers, land-mobile and portable/personal communication receivers and safety systems' (such as medical, fire, police) receivers are all susceptible to EMI.

Receptor susceptibilities exist in a multitude of electronic control systems used in modern aircraft, in addition to navigation and communications systems. Automotive electronics are used mainly for the control of fuel-air mixtures, for anti-skid braking, for electronic ignition and for diagnostics. Such systems are, for the most part, potentially susceptible to external EM fields such as powerful radar and broadcast transmitters. The susceptibility of these vehicular electronic systems are of great concern because their failure might cause severe accidents.

Not only is the electronic equipment affected by EMI but biological elements may also be affected by such emissions. It has been observed that the low frequency and RF

[1]It has been shown in a study carried out by Interference Control technology [130, Fig. 3-5] that the digital circuits lie in the rarely susceptible or relatively unsusceptible region for most of the RF frequency band; their susceptibility index (A measure of receptor in-band susceptibility expressed in terms of noise sensitivity, bandwidth, input impedance and absolute temperature viz. Eqns. (3-1) and (3-2) of [130]) remain $\leq$ 130 dB which is very low compared to that (above 200 dB) of most of the video and audio amplifiers and receivers.

spectrum of the EM waves may cause considerable hazardous effects on biological cells. Recent researches suggest that excessive amounts of EM exposure bears the risk of cancer [5,6,7].

Fig. 1.2 illustrates IEEE standard C95.1-1991, which sets the safety limits for human exposure to RF electromagnetic fields [12]. At frequencies higher than 100 MHz, limits are described in terms of the power density of the electromagnetic field emitted by various products, such as the antenna or door of a microwave oven. At frequencies below 100 MHz, E- and H- fields interact with the body in distinctly different ways, and hence are given their own thresholds. In the transition zone, either can be used, depending on the type of the equipment involved. Note that the minimum values for the limits occur within the frequency range between 30 MHz and 300 MHz, which corresponds to the frequency where whole body resonance is likely to occur [130].

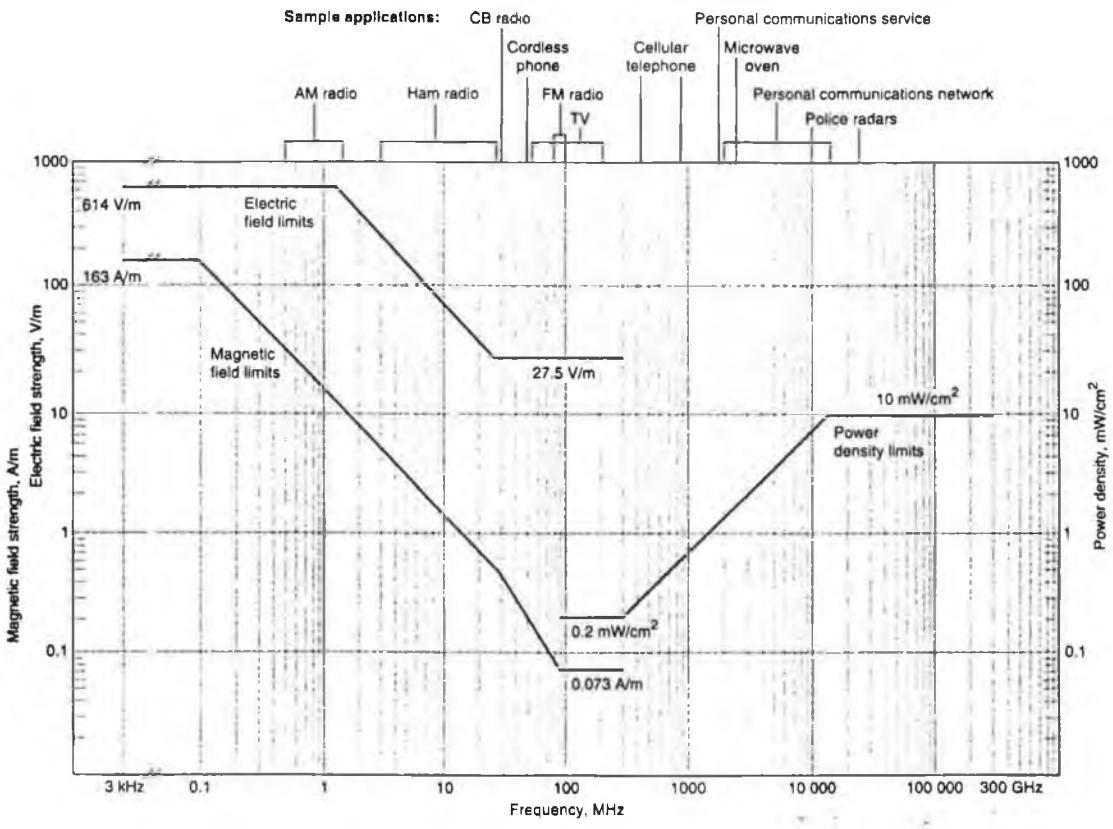

Fig. 1.2 The IEEE standard C95.1-1991 which sets safety limit for human exposure to RF electromagnetic fields. Adapted from IEEE spectrum, June 1993.

The intense RF radiation which exists near powerful radar and broadcast stations, can affect volatile systems, such as explosives and fuel which are exposed to it. Although

basic explosives (and ammunition) are not known to be directly susceptible to RF energy, electro-explosive devices (EED's) used as detonators can be activated prematurely. Fuel systems are also susceptible to ignition or explosion as a result of RF energy. Under certain circumstances it can result in spark formation in the presence of an ignitable fuel-air mixture [11].

1.4 IMPLICATIONS OF THE EMC REGULATIONS

Faced with the increasing amount of EMC problems, government agencies have responded with stringent regulations. Regulations regarding the susceptibility and emission levels of the different classes of electronic equipment as well as detailed guidelines for measurement systems to demonstrate conformance with the standards.

In the United States the Federal Communications Commissions (FCC), the Department of Defence (DoD), the Interdepartmental Special Committee on Radio Interference (IRAC) and the National Centre for Devices and Radiological Health (NCDRH) are the different government organizations issuing regulations regarding the susceptibility and emission standards which cover all sorts of electronic appliances. The Department of Trade and Industries (DTI), the British Standards Institute (BSI) are issuing the standards applicable for all the electronic industry in Britain. In Germany, the Verboard Deutscher Elektrotechniker (VDE) is the regulatory organization for the electronic industry to comply with EMC requirements. In Europe an EMC directive is due to be enforced from 1 January 1996 [13] and it states that all the electrical and electronic product to be sold in the member countries, affixing a ***CE*** mark on them, must meet minimum requirements regarding the emissions of and immunity to EMI.

Most of the standardizing institutes of the individual countries who are concerned about EMC are internationally affiliated with CISPR, the section of the International Electrotechnical Commission, which deals with radio interference and control. CISPR is responsible for recommendations on RFI which can only become law if the individual member countries take the appropriate actions themselves.

Since October 1983, all computing devices produced in the USA or equipment produced for export to the USA must conform to the FCC legislation (FCC docket no. 20780 Part 15J) which covers two classes of equipment, (Class A) commercial, business and industrial equipment and (class B) home and residential equipment.

Moreover, in May 1989 a European directive (89/336/EEC) was issued by the European Committee for Electrotechnical Standards (CENELEC) based on the recommendations of CISPR, to which all member states would have to comply. The requirements of the directive are as follows:

(1) Apparatus must be manufactured in such a manner that any disturbance it generates allow radio, telecommunications equipment and other apparatus to operate as intended.
(2) Apparatus must be constructed to provide adequate level of intrinsic immunity from EMI, even when near sources of EM disturbances.

Infringement of the EMC regulations and other directives in respect of safety and the safeguarding of health represent a violation of the law and are punishable. The standards are valid in all the EC member states, and it must be possible to sell products approved in one EC country in all the other countries of the community.

It is well recognized that the imposition of stringent EMC regulations could form a trade barrier so that international agreement is essential. However, as discussed earlier FCC, VDE and European standards are all equivalent to that of CISPR recommendations [15, Table 1.3].

It is equally apparent that agreement on limits of emission and immunity requirements would be dependent on prior agreement on measuring techniques and instrumentation. It is thus necessary to establish unified test standards and test methods selection as well as the development and standardization of test instruments.

1.4.1 EM COMPLIANCE TESTING

Investigation of EMC problems involves the measurement of complex waveforms varying considerably, and often erratically, in amplitude and time. Methods of measurement have been devised to give consistent, repeatable results which where possible, bear some relation to the interference caused to reception. There are numerous measurement techniques available for making EMC/EMI tests depending on the following considerations [16]:

1) size of the test equipment,
2) frequency range,

3) test limits,
4) types of field to be measured,
5) polarization of the field,
6) electrical characteristics of the test signals

Conformance testing of electrical and electronic equipment is usually performed in two different aspects. The first step is to make measurements to determine if any undesired signals being radiated from the equipment (radiated EMI) and/or appearing on the power lines, control lines, or data lines of the equipment (conducted EMI) exceed limits set forth by the standardizing institutes. Measurements of radiated EMI from electronic equipment are referred to as emission measurements.

The second step is to expose the electronic equipment to selected levels of EM fields at various frequencies to determine if the equipment can perform satisfactorily in its intended operational environment. Exposing the equipment to EM fields of various strengths is referred to as susceptibility or immunity testing.

In the USA, Britain, Europe and Japan recommendations on standard test methods and instruments are made by the regulatory organizations such as American Society for Testing and Measurements (ASTM), MIL-STD 462 (Defence Logistic Agency, National Electrical Manufacturers (NEMA), Ministry of Defence, Directorate of Standardization (DEF STAN 59.41), National Measurement Accreditation Service (NAMAS), DTI Radiocommunications Agency, CENELEC and European Telecommunications Standards Institute (ETSI) and Japanese Standards Organization.

1.4.2 ACHIEVING CONFORMITY

Once standards covering the emission and susceptibility limits of most of the electrical and electronic equipment are available, along with clear indication of acceptable standards of measurements and measuring instruments, the obvious implication for the manufacturers is then to achieve sufficient level of EM compliance of their product with the minimum possible cost to survive in the market. A recent case study [27] suggests that it is worth even investing a handsome capital for considering EMC early at the design stage or prior to large scale manufacturing.

Manufacturers can achieve compliance by considering the EMC behaviour of their products at the design stage while they have at their disposal for example the

techniques, such as suppression of emission at the source level from printed circuit board by proper designing of the signal flow paths, decoupling power supplies and oscillators, proper positioning of the clock lines, reduction of cross-talk, suitable grounding, application of multilayer PCBs and even possible suppression of EMI at the design stage of ICs. Moreover power line filtering could attenuate conducted EMI on ac mains cables and dc power cords. This form of suppression deals with both "Common mode" and "Differential mode" interference and prevent interaction both between internal circuits and external sources of conducted EMI. Grounding and screening of interconnected systems, and relative positioning of the system components also improves the overall EMC of a system. However, in many or most cases it will still be necessary to provide a shielded enclosure for the whole system or sub-systems.

1.5 SHIELDING, BASIC ELEMENT IN ACHIEVING EMC

It is obvious that electronic equipment which operates at RF or microwave frequencies cannot be free from spurious emission. Even electrical or electronic appliances which work at audio or power frequency may emit a considerable amount of EMI to disturb neighbouring devices. Thus it is essential to make shielded enclosures for electronic equipment, not only for preventing it from radiating unwanted emissions of noise but also for protecting it from ambient noise or interference. How effective the enclosure is in preventing the spurious emission or ingress of EMI is usually determined through SE measurements. The term "Shielding Effectiveness (SE)", usually expressed in dB, relates to the ability of a material[2] to reduce the transmission of propagating fields in order to electromagnetically isolate one region from the other [36]. The larger the SE value the better the enclosure.

1.5.1 SHIELDED ENCLOSURE DESIGN

Ideal enclosures should be made of materials having good conductivity and magnetic permeability as well as sufficient thickness to prevent EMI through reflection and

[2]SE of planar sheet like materials mainly depends on the thickness and constitutive properties of the material but when an enclosure is made of that material, shielding efficiency of the enclosure does not depend on the material only but also on the dimensions and the shape of the enclosure, even it can be made continuous and perfectly closed. It has been demonstrated analytically by Field [182], that the SE of enclosures of different regular geometric shape depends on their dimensions. It has also been shown [182] that for a given material, with the same thickness and equivalent dimensions, the SE of a cylinder is better than that of a sphere. However, in the present analysis, a simplified approach has been taken, assuming that the shape and size of the enclosure would be the same, and thus the shielding characteristics of the enclosure can be graded largely on the basis of the SE of the material used for its construction.

absorption. Even if an enclosure is constructed with such a material, there may be leakage of EM wave through apertures, seams and joints, and due to poor grounding.

Apertures have to be provided in the enclosure for ventilation, power lines, connectors, antennas, front panel seams, control shafts, and for various other reasons [43]. Away from the direct coupling of EM wave through the aperture to the system levels, the overall shielding performance of the enclosure may be reduced due to the apertures which may be explained as follows: shielding mechanisms are related to the induction of current in the shield material, but the current must be allowed to flow freely. If it has to detour around slots and holes, the shield loses much of its effectiveness.

Aperture planning i.e. manipulating the size, shape and relative position of the aperture to reduce EMI improves the overall shielding performance of an enclosure. The radiation from and coupling through apertures of regular geometric shape has been widely investigated by many authors [44-46], by considering the aperture as an isolated source or sink of EM radiation. Moreover recent publications [47-51] treating the radiation from apertures in shielded enclosures both experimentally and numerically illustrate the importance of the subject. Numerical simulations are helpful during the design stage and the experimental investigations are useful during the prototype development stage of electronic equipment shielded by a box of conducting material.

Another important factor which improves the overall shielding capability of an enclosure is "grounding". Proper grounding of an enclosure provides shielding against ESD, transients and mains-borne interferences as well. Current seeks the path of lowest resistance. If several paths are characterized by similar impedances, the current flow may randomly switch paths. This switching may appear as oscillations and cause interference ("noise") with electronic equipment. Grounding provides a known, fixed, lowest impedance path for the incident EM wave to be diverted into the ground [52].

Electrically imperfect seams and joints can dramatically reduce the shielding performance of an enclosure. Such joints result in discontinuity of the electrical path along the length of the joint and appears in the form of high resistivity and thereby shielding through absorption is lowered. Penetration via bolted joints can produce strong resonant behaviour due to the lack of re-radiation [53]. However, Dikvall [54] reported somewhat better performance of lap joints in a shielded enclosure even in a sophisticated application against EMP penetration.

Fig. 1.3 illustrates just two possible ways of constructing a shielded enclosure on the basis of SE measurement to check its conformity with the EMC standards. It is evident that the route described in Fig. 1.3(b) is more efficient than that described in Fig. 1.3(a) since it attempts to incorporate shielding performance in the design process. Thus there is a requirement for focussing on the materials used in enclosure construction, their design, their production and their properties.

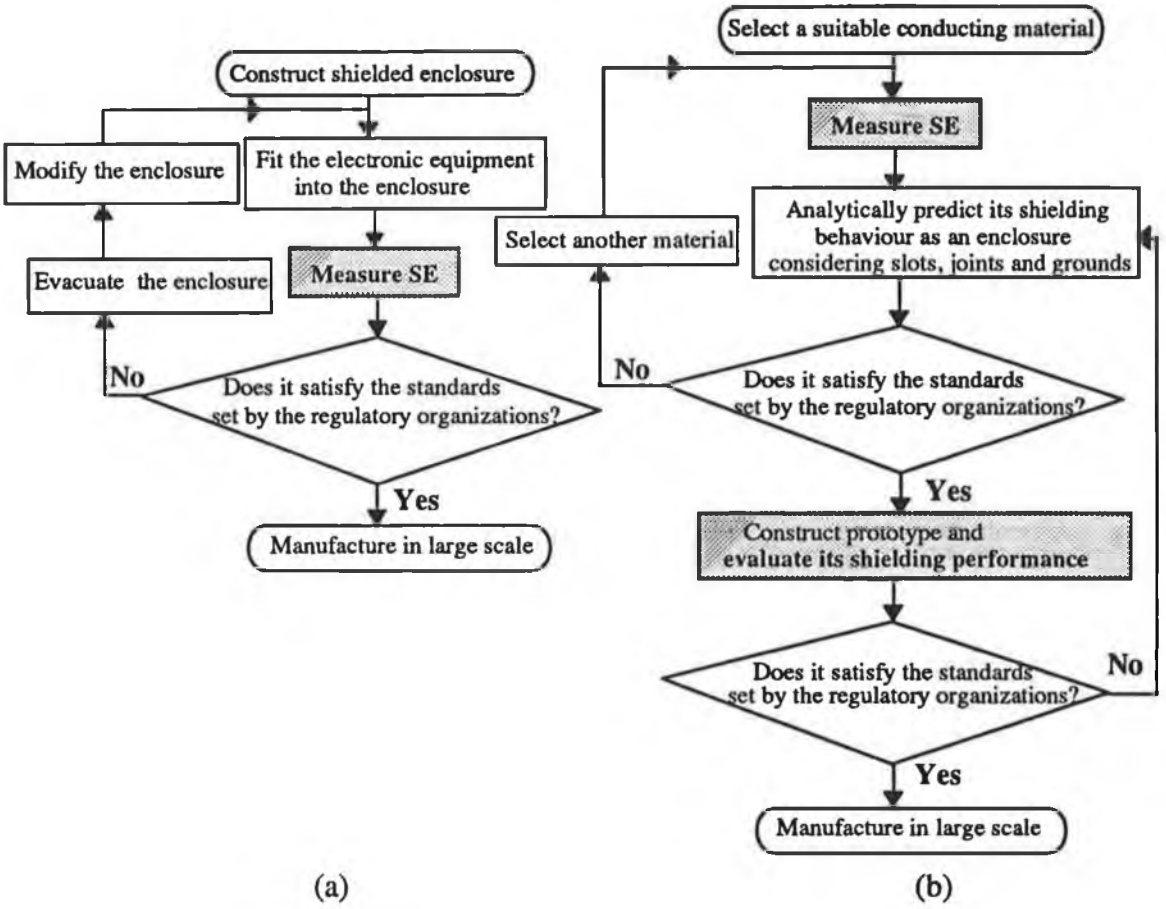

Fig. 1.3 Two different possible ways (simplified) of manufacturing shielded enclosure for electronic equipment, (a) Measurement of SE after constructing a shielded enclosure and (b) Measurement of SE of the sheet material which construct the enclosure.

1.5.2 SELECTION OF MATERIAL IN ENCLOSURE DESIGN

The design and development of a suitable shielded enclosure is a target to be achieved by the electrical and electronic equipment manufacturers, and the process begins with the selection of the shielded material that would be used for fabricating the enclosure as illustrated in Fig. 1.3 (b). Although aperture planning, grounding and proper joints play a

vital role in enclosure design, it is obvious that a good quality shielding material is a prime important factor.

Traditionally the use of a metallic "Faraday Cage" was an integral part of achieving proper shielding for electronic equipment. However, mainly cost and weight considerations compelled the designers to look for an alternative. The emerging technology of imparting conductivity into thermoplastic materials is an outcome of that. It is well-known that metal sheets possess very good SE (even a thin sheet of 0.1 mm aluminium or copper can offer SE as high as 200 dB at 100 MHz) compared to that of a very high quality conductive plastics (ranges between 40-100 dB). Very high SE values, however, are not always mandatory. Table 1.1 grades the level of SE according to the requirement.

Since conductive plastics can provide good or even excellent shielding capability as well as other important features, such as lower cost, ease of formability, improved aesthetics and light weight, they have become attractive for constructing shielded enclosures for electronic equipment.

Table 1.1[3] Levels of Shielding Effectiveness

0 to 30 dB	poor
30 to 60 dB	average
60 to 90 dB	good
90 to 120 dB	excellent

A review of the existing as well as the emerging techniques of imparting shielding behaviour to plastic materials is discussed in the next section. In particular, reference to their methods of production is important so that the possible frame of inclusion of the intended SE measurement technique can be identified. Reference is also made in this context to the newly proposed regularly filled conductive plastic (RFCP), which is a developed form of available filled conductive plastics.

[3]This table has been adapted and modified from M. Morita and H. Inamoto," Composite materials for electronic engineering," p. 155, in standards published by the Institute of Electronics, Information and Communication Engineers of Japan, 1986. Poor, average and good indicate no expectation or simple shielding, normal shielding and sufficient shielding for most applications, respectively. However, similar levels have been indicated by P. Rowberry of University of Warwick, Advanced Technology Centre in a lecture given at the IEE colloquium on screening of connectors, cables and enclosures held at Savoy Place, London on 17 January 1992.

1.6 CONDUCTIVE COMPOSITE PLASTIC MATERIALS

Conductive composites usually refer to the materials that are mixtures of conducting particles mixed into, or laminations (or layers) of a conducting material suspended between an insulating matrix usually of, plastic or polymeric resins. The most common plastic materials that are used as the polymeric resins such as polycarbonate, ABS (Acrylonitrile Butadiene Styrene), polystyrene, nylon, polyphenylene oxide, polyethylene, polypropylene and maleated polystyrene (SMA) co-polymer.

Unlike metals, plastics or polymers are inherently non-conductive. In order to meet the SE requirement, however, there is a wide variety of techniques available to impart EM shielding in plastics. Metallizing plastic is the most common among these various techniques. In the late 1970s and early 1980s, when the conversion to plastic began, plastic processors and electronic manufacturers naturally turned to the then existing metallizing processes as a quick fix for shielding [55]. Vacuum metallization, electroplating and zinc arc spraying are thus the techniques which initiated this industry.

However, the growth of the plastics EMI shielding market inevitably led to new technologies such as conductive paints, filled composites and electroless plating. Flexible laminates, conductive fabrics and conductive tapes are also gaining importance for special purpose uses. The wide variety of available conductive composites are classified in the following subsections and the newly proposed RFCP material is also discussed as a separate class.

1.6.1 SURFACE METALLIZED PLASTIC

The surface (usually the inner surface, when it is used for enclosure) is coated with a metallic coating. A wide variety of techniques ranging from the expedient to exotic are available for manufacturing metal coated plastics. Expedient methods include conductive painting, arc spraying, electroless plating and vacuum metallization.

1.6.1.1 Conductive paints

Conductive paints have a solids' content which is composed of binders(e.g. acrylic, urethane) and electroconductive fillers (e.g. copper, silver, graphite, nickel) in the form of powder. In this technique conventional paint spraying equipment can be used for

painting a plastic substrate. A simplified diagram of the continuous process flow of a typical robotic controlled conductive spraying system is shown in Fig. 1.4.

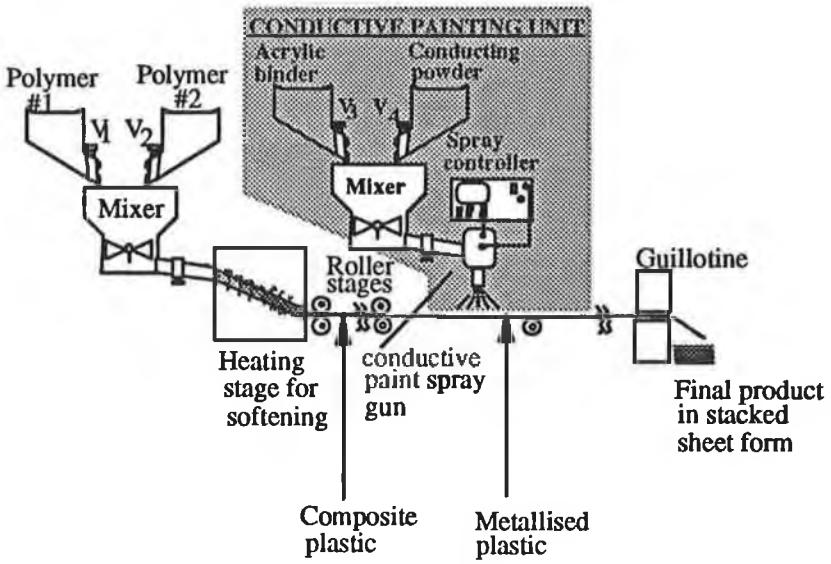

Fig. 1.4 Schematic diagram of the manufacturing process of conductive painted plastic. An automated painting process has been shown.

The carrier system needs to be carefully selected to avoid chemical attack of the plastic which can reduce impact strength and may compromise the adhesion properties. Nickel based systems are the most popular [55]. SE values depend on the type of conductive filler and paint thickness.

1.6.1.2 Electroless plating

Electroless plating deposits a film of pure homogeneous metal whose thickness can be varied from 0.25-1.0 μm on a plastic substrate. It depends on the immersion of the substrate in a series of chemical solutions to produce metal plating by auto catalytic means instead of dc current [56]. Copper and nickel are generally used as metals for plating. Depending on the metal used and the thickness of the plating, excellent SE (above 100 dB) values can be achieved by this technique.

1.6.1.3 Vacuum metallization

Vacuum metallization involves deposition of an extremely thin metallic film (generally aluminium) on a plastic substrate by evaporation in a high vacuum chamber. The vaporisation is achieved by energising tungsten filaments with high current, where,

because excessive heat is generated, pellets of metals (usually aluminium) are converted into gaseous form. The aluminium gas particles have sufficient kinetic energy to generate high velocities, which when applied to the plastic substrate produce both a chemical and a mechanical bond. A simplified model of the vacuum coating process is shown in Fig. 1.5.

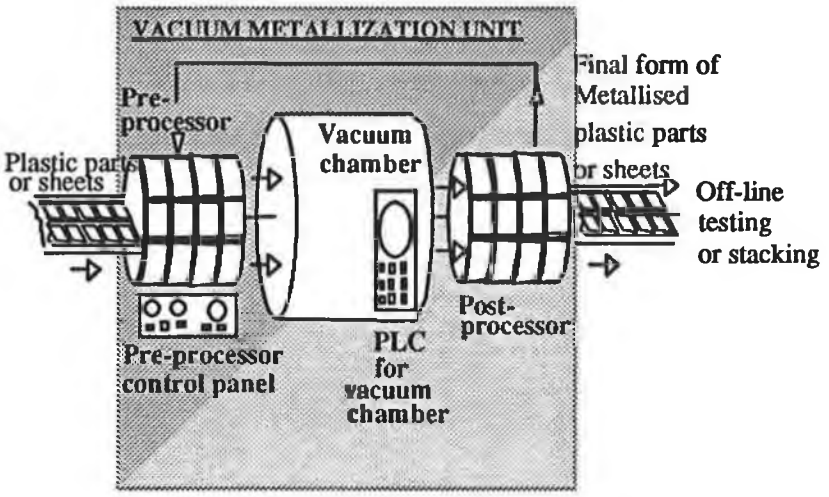

Fig. 1.5 Process flow diagram of vacuum metallization technique.

Aluminium layer thicknesses range from 0.5-25 μm. Adhesion of the aluminium to the plastic is promoted using a plasma discharge process during the vacuum cycle. This is achieved by the generation of gas ions which strike the plastic at high velocity and provide a clean surface prior to the application for the aluminium.

1.6.1.4 Arc spraying

In Arc spraying the pure metal (generally zinc) is melted by electric arc and propelled by compressed air, spraying droplets of molten metal onto the part to be coated [57], [58]. Thickness of coating varies from .05- .075 mm.

More exotic methods include ion plating, cathode sputtering, silver reduction and other thin metal film deposition technologies. Although conductive painting is claimed to be the most popular low cost surface metallizing technique, the specific product application dictates which technique would be cost effective. Particularly for screening a plastic enclosure with numerous mounting holes and "secret until lit" windows vacuum coating is the preferred solution [59].

1.6.2 FLEXIBLE LAMINATES

Laminates of metal foil (usually aluminium and copper) bonded to a reinforcing substrate (e.g. polyester, PVC, polyamide etc.) are now being designed in as an integral part of the EMC of a unit or a building [60]. This class of materials are termed as flexible laminates. Their applications in EMI control are increasing in recent years. It is obvious that the SE of such materials would depend essentially on the thickness and conductivity of the metal foil used.

1.6.3 FILLED COMPOSITES

Filled composite plastic is a homogeneous mixture of plastic resin and conductive filler, usually metal or carbon. The most widely used conductive fillers in the form of flake or fibre are graphite, copper, aluminium, stainless steel, nickel and nickel coated carbon. Shielding capability varies with the type and amount of conductive filler added to the plastic. The continuous process flow diagram of a typical filled composite is shown in Fig. 1.6.

High loading (volume percentage of filler material in the resin) of aluminium flakes is required to achieve even moderate level of shielding (40 % loading for 40 dB SE [3]), which in turn adversely affects the mechanical properties of the plastic. Moreover at such high loading a risk of flake conglomeration at the extrusion or moulding stage leads to resin rich sections with minimal conductivity.

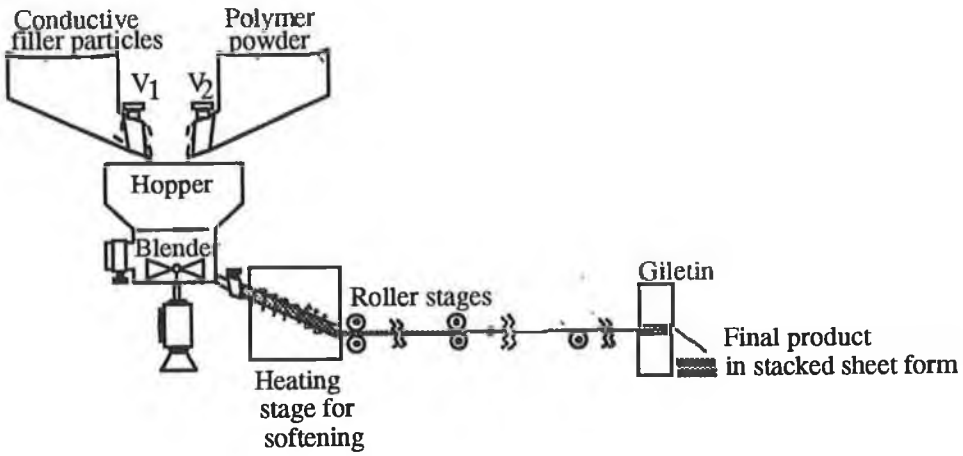

Fig. 1.6 Schematic diagram of the continuous production process of a typical filled conductive composite material.

On the other hand significant reduction in fibre/flake concentration is possible with stainless steel to achieve the same level of shielding (only 5% loading for 40 dB attenuation [3]). The resulting rigidity of the plastic because of the reinforcement is an additional advantage with stainless steel fibres. However the expense of, and serious wear to the moulding equipment (e.g., screws and moulds) due to the abrasive nature of these fibres are the main constraints.

In graphite filled polymers, thousands of tiny strands of graphite fibre are individually coated with nickel solution and encapsulated in a polymeric sheathing that is diced into pellets and dissolves during processing to disperse the fibres [115]. Although the loading level is almost double that of stainless steel, it is much lower than that of aluminium flakes and the processing costs are similar to stainless steel fibres.

Filled composites are widely used in the electronic industry as electrostatic discharge (ESD) protection in silicon chip storage bins, anti static floor mats, handling gloves and wrist straps which ground any build up of static electricity.

1.6.4 REGULARLY FILLED CONDUCTIVE COMPOSITES (RFCP)

A new class of filled composite material has been proposed with a two dimensional regular array of conductive flakes (like a Frequency Sensitive Surface (FSS)) in plastic resin. Fig. 1.7 shows a probable configuration of an RFCP together with a conventional filled conductive plastic sample.

A FSS (Frequency Sensitive Surface) is a surface which exhibits different reflection or transmission coefficients as a function of frequency. Usually a FSS consists of identical antenna elements such as dipoles. When the elements resonate and the resistive part of the load connected to each of the array elements is zero then the array can provide complete reflection. This unique feature of the FSS is exploited in the present work to construct a new class of filled composite materials with improved shielding effectiveness (SE) against electromagnetic waves.

Although this type of material would be frequency sensitive like FSS, its bandwidth of high reflectivity to EM waves can be widened by manipulating the dipole size and separation. This design flexibility would be an added advantage of these new composites over the conventional filled composites.

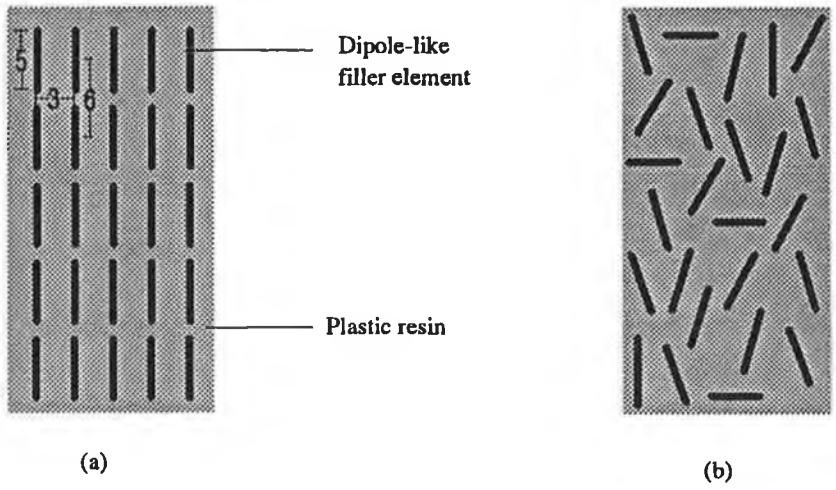

Fig. 1.7 Filled conductive plastic samples (a) FSS-like regularly filled sample with filler size and separations expressed in cm and (b) Randomly distributed conductive fillers in plastic resin to show a typical conventional filled composite.

The effect of reflection loss due to the scattering from the filler particles in case of conventional filled composites discussed in the previous section has not been considered so far. In the analysis of RFCP this effect is highlighted and a possible improvement of this scattering behaviour has been proposed by arranging the conductive flakes as a regular array as opposed to distributing them at random. Obviously the suggested arrangement widely differs from the actual filled composites in a sense that there exists no probable closed loop or network to provide conduction. Nevertheless, this could be achieved by using closed loop fillers, such as square loop, circular loop and square aperture which are also being used as typical FSS patches [123]. However, the scope of this work is to study the improvement in reflection loss achievable by regular distribution over irregular distribution of flakes. Hence only thin strip-like FSS patches are included for analysis.

1.6.5 INTRINSICALLY CONDUCTIVE POLYMERS (ICP)

This is a relatively new material class being developed by Westinghouse R&D laboratory and others [61]. In 1987, Germany's B.A.S.F.A.G. corporation produced a conductive polymer that was measured to have conductivity in the region of 1.47×10^7 S/m [62]. ICPs are usually available in the form of thermoplastic blends. The blends are composed of a matrix polymer, either polyvinyl chloride (PVC) or nylon, compounded with an ICP (e.g. polyaniline). Such ICPs, depending on the particular choice of polymer, can have conductivities in the range from 1 to 10^7 S/m [59]. Previous tests on ICPs have

shown promise, but prospects for applications were limited by problems with environmental stability and by the fact that the conductive polymers were not melt-processible in their conductive form [63]. Williams *et al.* [64] of Penstate University produced and tested the shielding behaviour of an ICP, which is a mixture of a silicone polymer and a non-silicone polymer; the non-silicone polymer is a carbon-based material. At microwave frequencies the polymer showed excellent performance against EMI. Colaneri *et al.* [65] reported the manufacturing of melt-processible thermoplastic blends of PVC and polyaniline which have conductivities as high as $2x10^3$ S/m.

1.6.6 OTHERS

Conductive fabrics are fine wires of solid metals (e.g. nickel, copper, silver and gold) woven, knitted or formed into sheets to be glued with fabrics (e.g. polyester, polyamide, rayon). Conductive fabrics can be used for imparting shielding capability to plastics in lieu of conductive paints or other metallic coating [66]. Another class of conductive elastomeric composites, used specially for EMI gasket manufacturing uses carbon blacks [67], carbon fibre and particulate carbon black [68], [69] in rubber materials. Some investigators reported the improved magnetic as well as electrical conductivity of these materials using ferrites as fillers [70]-[73], while Jana *et al.* [74] showed better performance of barium-ferrite-vulcanized polychloroprene filled with short carbon fibre.

A comparative table of the conductive plastics showing their SE values, production cost, applicability and important other properties is given in Appendix A1. RFCP is not included in the table as it is just proposed and not yet commercially manufactured.

From the above discussion it is evident that conductive composites offer some exciting possibilities:

- Continuous production methods such as extrusion or injection moulding
- Possibility of on-line control of SE
- Wide range of forming possibilities
- Direct substitution for existing non-conductive plastic materials
- Existing production machinery or techniques can be employed

The shielding characteristics of metals are well understood from their known electrical properties and it is possible to predict theoretically [41], the SE of metallic sheet using Schelkunoff's [42] plane wave theory. SE of conductive plastics, on the other

hand, are often unpredictable as their electrical properties are not always evident. It is this important aspect which necessitates the development of reliable measurement techniques for the SE of this class of materials. Particularly if an on-line SE measurement technique could be developed for use during the production process, it could also contribute to the improvement of their SE at reduced cost.

1.7 NEED FOR ON-LINE SE MEASUREMENT

Computer assisted on-line product characterization plays a leading role in the framework of automatic manufacturing. It effectively performs features such as quality control of manufactured goods and in- and post-process surveillance [100], [101].

Like other on-line product characterization, SE measurements of conductive composites during the production-cycle may also play a very important role in the complete manufacturing process. Quality control of the final product can be optimized by on-line characterization. By comparing the SE values of the MUT with the desired level of shielding continuously within the production cycle, the mechanism of imparting shielding capability to the material may be regulated accordingly. This would in turn ensure waste reduction. Off-line SE measurement incurs costly spoilage of materials, thereby increase the overall production cost.

Another important feature of on-line measurement is the significant reduction in time, time of the manufacturing process and personnel. Quality control by off-line measurement sometimes render the whole process and involved personnel out of the production line, causing unnecessary delay of the mechanism. This is another factor which increases the production cost. Thus on-line SE measurement ensures quality control of conductive composites by the optimization of the material and time resulting in good quality product at reduced cost.

Conductive spraying is a widely used technique in the EM shielding industry, where on-line SE measurement may be introduced effectively. In the process of automated spraying on plastic, on-line SE measurement may be employed as a check for uniformity of the metal coating or more specifically the required shielding capability. In Fig. 1.8, the possible stage of inclusion of on-line SE measurement is shown. SE of the final product could be controlled by changing the contents of the paint, flow rate and spray velocity following the feedback instruction after SE measurement and the quality control of the final products can thus be ensured.

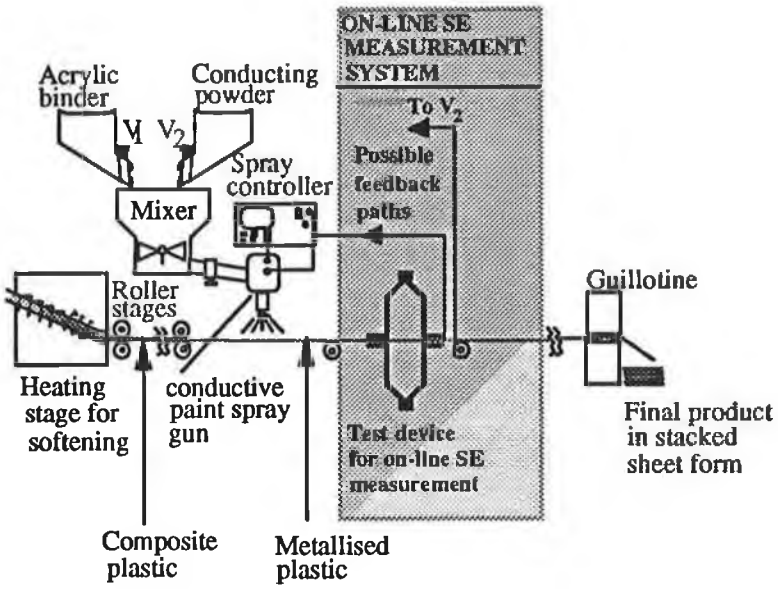

Fig. 1.8 Schematic diagram of the manufacturing process of conductive painted plastic with the possible application of on-line SE measurement and probable feedback paths.

In the vacuum metallization process, on-line SE measurements could offer the interesting possibility of a feedback control mechanism. Fig. 1.9 shows the probable feedback control paths. SE of the final form of the metallised plastic parts or sheets could be varied by controlling the pre-processing parameters or by changing the parameters of the vacuum chambers which can easily be accomplished through feed back signals to the pre-processor controller or the programmable logic controller (PLC) of the vacuum chamber.

In the manufacturing of filled composites, uniformity of the filler concentration throughout the resin is very important and an efficient control mechanism can be established with the aid of on-line SE measurement. SE of the final product could be varied by changing the flow-rate of the ingredients prior to mixing stage as shown in Fig. 1.10. There may be several other parameters, such as the quality of blending or mixing, softening temperature, duration of extrusion stage, which could be regulated to improve the shielding capability. These parameters can thus be controlled through some feedback signals determined on the basis of the SE data obtained at some stage within the production process. Particularly with the high loading of filler materials the necessity of such a mechanism is evident [102].

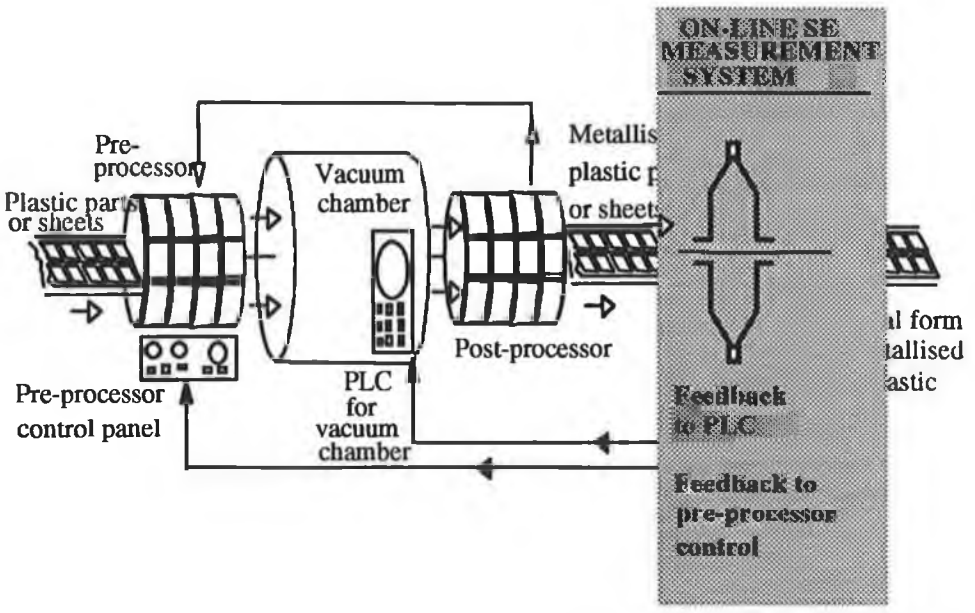

Fig. 1.9 Process flow diagram of vacuum metallisation technique with the possible inclusion of on-line SE measurement technique and the feedback paths.

On-line SE measurement may be a very efficient inclusion in the production cycle of the newly proposed RFCP type of filled composites. Reflectivity, a measure of the shielding capability of such materials, is a variable of filler size and separation, which could optimally be maintained by the application of on-line shielding characterization.

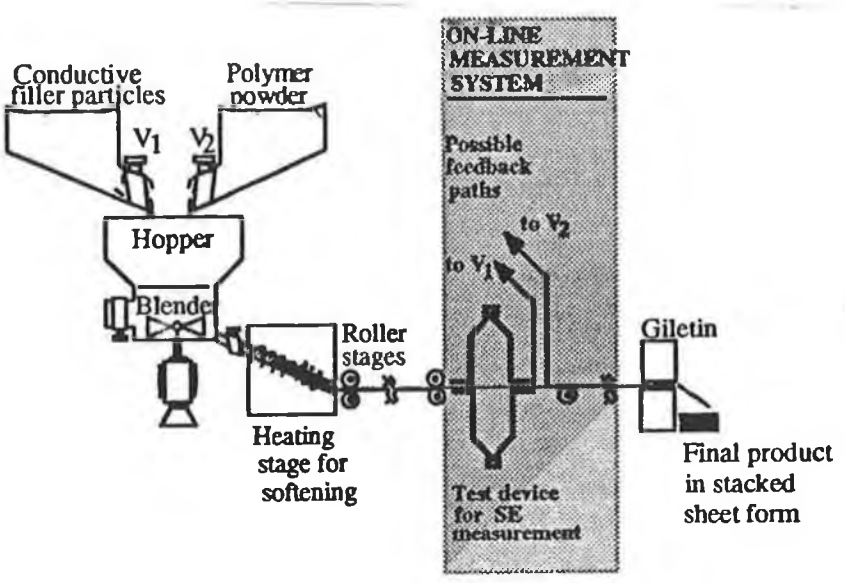

Fig. 1.10 Schematic diagram of the continuous production process of a typical filled conductive composite material with the possible application of the on-line SE measurement technique and the feedback paths.

1.8 OBJECTIVE OF THIS RESEARCH

There are of course a wide variety of techniques available for assessing the shielding capability of conductive plastics but are mostly for laboratory measurements and thus unsuitable for on-line SE measurement purposes. The obvious disadvantages associated with such off-line measurements have been stated in the previous section. Moreover they require stringent sample preparation which means the material is to be manufactured first and then a piece of that bulk material is to be taken as a sample which is to be treated prior to measurement and then the measurements are to be taken in a laboratory. If it fails to satisfy the requirement the materials produced before is a total wastage. Above all, it is a lengthy and inefficient process. On the other hand if the measurement of SE can be done during the production process the aforementioned benefits of on-line measurement can be achieved.

This work was, therefore, aimed at developing on-line SE measurement technique for planar sheet-like conductive composite materials during a continuous production process. Three new EMC antennas, namely the V-conical-lens antenna (VCLA), the Transverse Electromagnetic-T (TEM-T) cell half (acting as antenna) and the quarter loop antenna in front of 90^{o} reflector (henceforth referred to as Q-loop antenna) were designed for this purpose. TEM-T cell and Q-loop antenna was calibrated and employed in the measurement of on-line SE of the aforementioned materials.

1.9 ORGANIZATION OF THE THESIS

This thesis is divided into seven chapters. The layout of the chapters is depicted in Fig. 1.11. The background to the work has been given in this introductory chapter.

Chapter 2 identifies the problem at hand and proposes a solution to that problem. The wide variety of the available SE measurement techniques is reviewed in this chapter which gives an understanding of the basic principles of such measurements and the type of test devices necessary. Probable on-line test configurations for sheet-like materials are described and compared with the production process of conductive plastics. The criteria of on-line SE measurement techniques are determined on the basis of these discussions. Three new EMC antennas are proposed for the construction of non-contacting, free-space SE measurement techniques as solutions to the problem of on-line SE measurement.

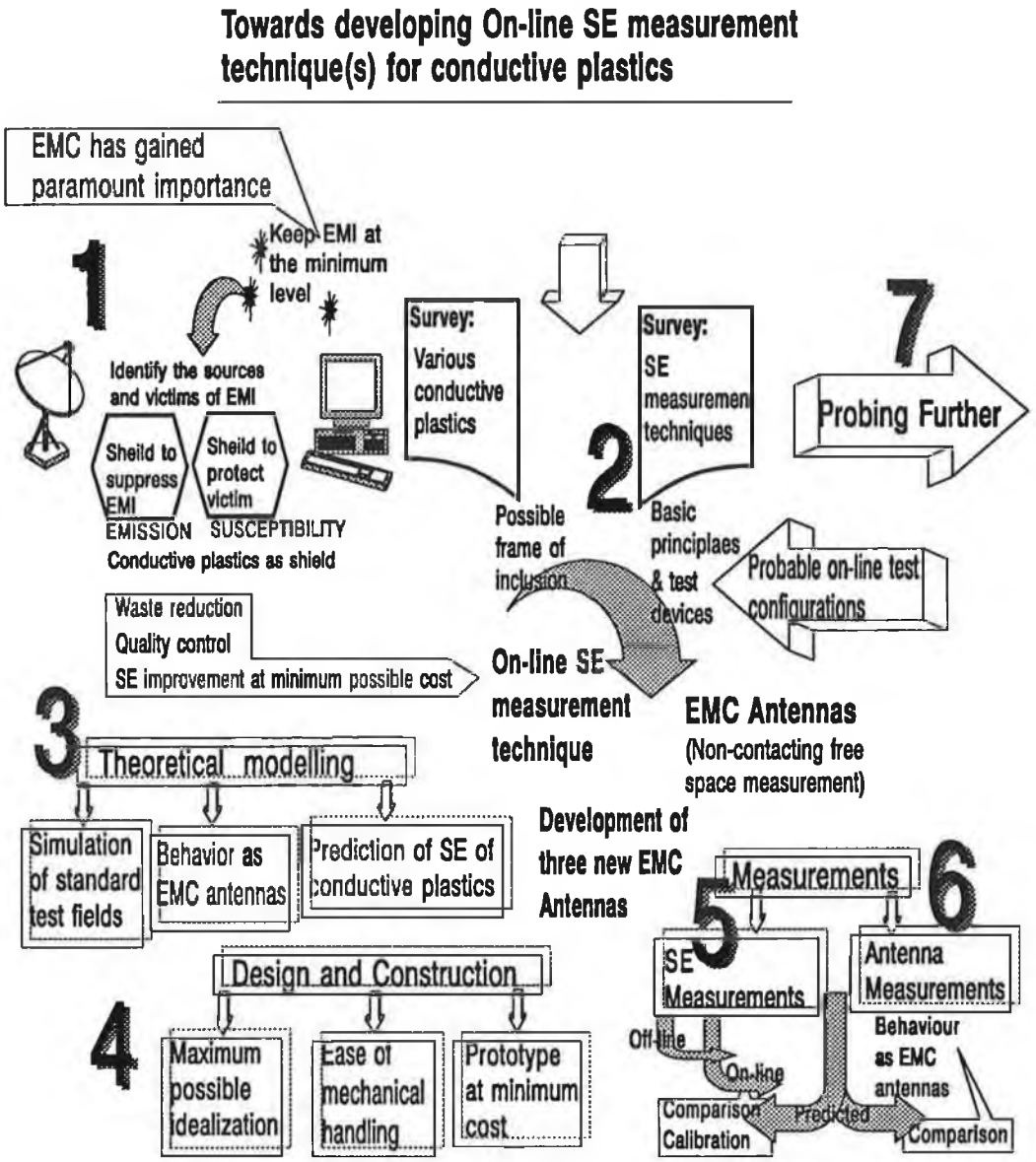

Fig. 1.11 The scope of this work and the layout of the thesis.

Chapter 3 contains the theoretical background of the overall study. There are three different aspects of analytical modelling: (i) theoretical predictions of SE of conductive plastics (if possible) can be an useful tool of comparing the test results; (ii) meaningful SE measurements require simulation of standard test fields at the test location, so analytical verifications of the fields produced by the antennas on the material under test (MUT) are thus essential; (iii) finally the desired characteristics of the developed EMC antennas, such as directional property, improved directivity and gain should be studied theoretically. Analytical models of these three important aspects are categorically presented in chapter 3.

While it was not possible to construct and test VCLA, the other two test devices were manufactured as prototypes. Design and constructional details of these devices are given in chapter 4. Although the VCLA could not be constructed its design features are mentioned and constructional procedures are proposed in this chapter. The measurement fixtures and the instrumentation involved in the measurement are also discussed.

SE measurements were performed with four different samples. It was necessary to calibrate the test devices and as such measurements were also taken for calibrations. All those measurement procedures and test results are presented in chapter 5. Comparison of the test results with the predicted SE values are also included in this chapter.

Chapter 6 presents the results of antenna measurements performed with two of the newly developed antennas. Each half of the TEM-T cell acts as an aperture antenna and the Q-loop acts as a magnetic dipole, thus their radiation patterns and other important antenna parameters (such as directivity, gain, VSWR) were measured. The experimental results are then compared with the theoretical results obtained in chapter 3.

Chapter 7 is the overall conclusion of the thesis. The other possible applications of the newly developed antennas are also mentioned and a few other research topics related to the test devices are pointed out.

Chapter 2

IN QUEST OF ON-LINE SE MEASUREMENT

EMC MEASUREMENTS
REVIEW OF EXISTING SE MEASUREMENT TECHNIQUES
CRITERIA OF ON-LINE SE MEASUREMENT TECHNIQUE
ROLE OF NEWLY DEVELOPED EMC ANTENNAS

2.1 INTRODUCTION

SE measurement is crucial in determining the EMC of an item of equipment. The main goal of this work was to design and develop SE measurement techniques to monitor the shielding capability of conductive composite materials during their production process where the material under test (MUT) would most often be in sheet form. A simple, non-contacting, free space technique for measuring SE of a planar sheet-like sample would appear to be the best choice for such an on-line measurement system. Unfortunately such techniques are not readily available among the wide variety of existing SE measurement systems. Thus modifications of the existing techniques or developing some new techniques were deemed to be essential.

This chapter sets out to define the problem and describes the paths taken to produce solutions to that problem. EMC measurements very often involve similar sets of instruments, test sites and test procedure. An understanding of the instrumentation, test site and tests necessary for EMC measurements, thus forms the background to the desired SE measurement system. A brief discussion of EMC measurements is given in the next section which is then followed by the discussion on the variables of interest of the present SE measurement systems in section 2.3.

Prior to designing the on-line SE measurement system it is essential to be familiar with the existing SE measurement techniques. Therefore, a comprehensive review of the available techniques with particular reference to thermoplastic materials in sheet form as the MUT was undertaken and the findings are presented in section 2.4. In section 2.5, the probable configurations of on-line characterisation of sheet-like materials are discussed. Salient features of a SE measurement system that can be employed in such characterisation are given in section 2.6. The role of the EMC antennas employed in the present measurement system in satisfying the requirements is noted in sections 2.7 and 2.8.

2.2 EMC MEASUREMENTS

EMC measurements play a pivotal role in the complete process of "retrofitting" EMC into electronic equipment. Measurement techniques with special attention to the type and source of EMI (in which environment the equipment under test (EUT) is intended to be operated) and measuring instruments (specially designed antennas and probes for simulating and detecting the test fields) are particularly important for this purpose.

2.2.1 INSTRUMENTATION FOR EMC MEASUREMENTS

Measuring instruments for the frequency domain are based on radio receiver designs and the detecting and measuring circuits most commonly employ peak and quasi-peak detectors. The former is used in the determination of compliance with military specifications while the latter is extensively used in the determination of compliance with legal regulations and national and international standards.

Spectrum analyzers and EMI receivers are extensively used for examination of spectra over a very wide frequency range, for example the harmonics generated by local oscillators, RF heating equipment and digital signals. EMI measurement distortion can be caused due to the spectrum analyzer being driven into compression by high energy signals [17], which can be reduced by connecting a preselector before the spectrum analyzer. The preselectors usually have tracking filters to reject out-of-band interference significantly thus enable low level signals to be monitored in the presence of high level ambients. On the other hand a family of preamplifiers may be used together with the EMI receivers and spectrum analyzers to strengthen the poor received signal for better recognition.

Specially designed (according to the standard specifications) synthesized and tracking signal generators, are available which can generate RF and microwave frequency signals of reasonable strength to simulate the test fields suitable for EMC measurements. A wide variety of RF power amplifiers usable in conjunction with these signal generators is also available to successfully amplify the test signals prior to inputting where simulation of high power noise is involved.

Standard antennas are available for EMC measurements. They act as suitable transducers for converting guided waves into free space waves of known form and polarization as well as free space waves into guided waves, and thus play a very important role in simulating and detecting test fields in a specified region. Bandwidth limitations of antennas and non-linear phase response with frequency made their application limited to frequency domain measurements [16]. There are other problems associated with antennas that far field simulation requires sufficiently large test area and near field measurements introduce nonuniformity of the field over the test volume occupied by the equipment under test (EUT) and interaction effects.

Possible alternatives to EMC antennas are Transverse Electromagnetic (TEM) cells, GTEM (Gigahertz TEM) cells and reverberating chambers. These are capable of producing standard test field over a wide range of frequencies within a comparatively small area as well as in large volumes if needed [18]-[20]. They simulate desired test fields within a shielded environment and as such successfully eliminate the difficulties associated with the use of antennas.

Moreover, with the automation of most types of sophisticated measuring instrument, for example, using the IEEE-488 general purpose interface bus, the time consuming and often tedious EMC measurements have assumed a new dimension [35]. The cost of a test system is reduced considerably [36]. Implementing this rapid and regulated data transfer facility between various interconnecting system instruments very fast and reliable emission [37] and susceptibility [38] measurement systems can be developed. A typical automated EMC test facility experienced an overall reduction of 70% in test execution time compared to a previous test conducted manually [39]. Speed and accuracy with repeatability of test results are the major benefits achievable with automated test systems and these are extremely desirable for EMC measurements.

2.2.2 TEST SITE

It is essential for a valid measurement that it has to be carried out in a known EM environment. It could be an open area test site (OATS) as recommended by IETC [21] and FCC [22] and other international organizations [23]. Although OATS is convenient to perform both radiated susceptibility (RS) tests for large systems over a wide frequency range, there are some disadvantages associated with this method of measurement such as requiring a sizeable measurement site and that the surrounding area be free of metallic objects. Also there is a lack of isolation between the experimental set-up and the external environment. This results in interference to others and susceptibility of the test site to ambient noise and unfavourable weather conditions. Hence the repeatability of the test results become poor.

The only possible alternative is to use indoor measurements. More normally an electromagnetically anechoic chamber or a screened room is used. Such enclosures are made reflection and resonance free by mounting pyramidal absorbers on nearly all the surfaces [24] thereby producing a known invariable EM environment at the test locations. The limitations are the huge expense involved and the difficulties for frequencies below 200 MHz. Standard specifications are available for them [25], [26] .

2.2.3 TESTS AND MEASUREMENTS

The evolution of techniques for the measurement of noise and unwanted signals generated by electrical equipment has been influenced by propagation conditions and the way in which interference is caused in households and industrial installations. Investigation of the interference problems showed that the domestic and industrial mains wiring provides a propagation medium where transmission in the frequency range up to about 10 MHz is accompanied by relatively little attenuation. At higher frequencies the mains wiring becomes less efficient as a propagation medium as attenuation increases rapidly above 30 MHz. The dominant propagation mode at these higher frequencies then becomes direct radiation from the device or circuit itself or from the wiring in the immediate vicinity of the source of disturbance. Thus in order to achieve compliance according to the specifications, all or some of the following tests are to be done:

Table 2.1 Classification of Emission and Susceptibility Tests

Conducted Emission (CE) Test
Conducted Susceptibility (CS) Test
Radiated Emission (RE) Test
Radiated Susceptibility (RS) Test

Radiated test can refer to both reactive and radiation fields. It measures the fields emitted by the EUT which is RE tests or the effect of the incident fields on the correct operation of the EUT referred to as RS tests. While CE tests measure the currents generated by the EUT on cables connected to the equipment such as mains, signal and control cables, CS tests are performed to observe the consequences of the these injected currents on the normal operation of the EUT [15, pp. 18].

It is to be noted here that among the four different types of EMC measurements (refer to table 2.1), SE measurements of planar sheet-like materials require only RE and RS types of tests not the conducted ones (CE and CS measurements). Thus susceptibility and emission, henceforth, refer to RS and RE respectively.

2.3 VARIABLES OF SE MEASUREMENTS

Usually a shielded enclosure is designed to make the electronic equipment immune from outside interference as well as to prevent unwanted radiation from the equipment into the surroundings. SE determination for the materials that are intended to be used for constructing shielded enclosures thus requires both susceptibility and emission measurements.

2.3.1 TYPE OF INCIDENT FIELD

Susceptibility determines the vulnerability of a test object to EMI originating from other sources. It thus refers to sources both man made and natural, such as communication links, radio transmitters and lightning and the interference seems to reach the victim from far away. Hence the incident fields are essentially plane wave in nature. Conversely, emission measures unwanted radiation from internal sources which are close to the shield thus requiring near field SE data.

It is well-known that the field in front of any type of source of EM radiation viz., dipole, loop, travelling wave antennas, slot or aperture antennas, reflector antennas changes from being more reactive to being more radiative (real power) as it moves further from the source. According to Poynting's theorem the radiative field (containing real power only) cannot have a component in the direction of propagation, so the electric and magnetic field components lie completely in a plane normal to the direction of propagation [128] and it can be shown from Maxwell's curl equations that these field vectors become perpendicular to each other [129] when they are radiative. Thus the far field of any source constitutes the so called Transverse Electromagnetic (TEM) wave. Moreover this propagating wave, although spherical, has negligible curvature at large distances from the source and is well represented by a plane wave.

Near field, on the contrary, is the field in a region very close to the source. Close to the source, most of the energy is contained in the reactive field. The energy that constitutes a net flow away from the source is contained in the radiation field (described previously as far field), whereas the energy in the reactive field is stored for one quarter of a cycle and returned to the source in the next quarter cycle.

The type of the field is categorised by "wave impedance", which is the ratio of the total electric field to the total magnetic field of an electromagnetic wave. In the far

field region of any radiator it can be shown that this ratio is

$$\frac{E_t}{H_t} = \sqrt{\frac{\mu}{\varepsilon}} \qquad (2.3.1)$$

where E_t and H_t represent the transverse components i.e. the total electric and magnetic fields, since in the far field the electric and magnetic fields lie in plane transverse to the direction of propagation. $\sqrt{(\mu/\varepsilon)}$ is equal to 377 Ω in free space and is known as the intrinsic impedance of free space. The wave impedances (normalized to 377 Ω and expressed in logarithms) of the fields in front of a short dipole and a loop antenna are shown in Fig. 2.1, as a function of distance from the source (normalized to phase constant, $\beta=\lambda/2\pi$, where λ is the wavelength). The wave impedances are higher or lower than 377 Ω until a distance of six times $\lambda/2\pi$ is reached.

The transition between near and far field usually depends on the type of the radiator. Some of the EMC handbooks [130], however, often use a crude dividing line based on the value of $\lambda/2\pi$, as

$$r_{near} \leq \lambda/2\pi \qquad (2.3.2)$$
$$r_{far} \geq \lambda/2\pi$$

which is not obviously true for all types of radiators. Some authors [107, pp. 461] define the transition in terms of type of energy content; if the parameter r_{far} is defined to be the distance from the source to where 99% of the total energy is contained in the radiation field, then for all practical purposes it can be shown that

$$r_{far} > 16\lambda \qquad (2.3.3a)$$

and similarly the parameter r_{near}, if defined as the distance from the source at which 99% of the total energy is contained in the reactive field, then it can be shown that

$$r_{near} \leq 0.0016\lambda \qquad (2.3.3b)$$

Thus to be in the safe side some researchers [15] define the working distance as

$$r_{near} \leq 0.1(\lambda/2\pi) \qquad (2.3.4)$$
$$r_{far} \geq 10(\lambda/2\pi)$$

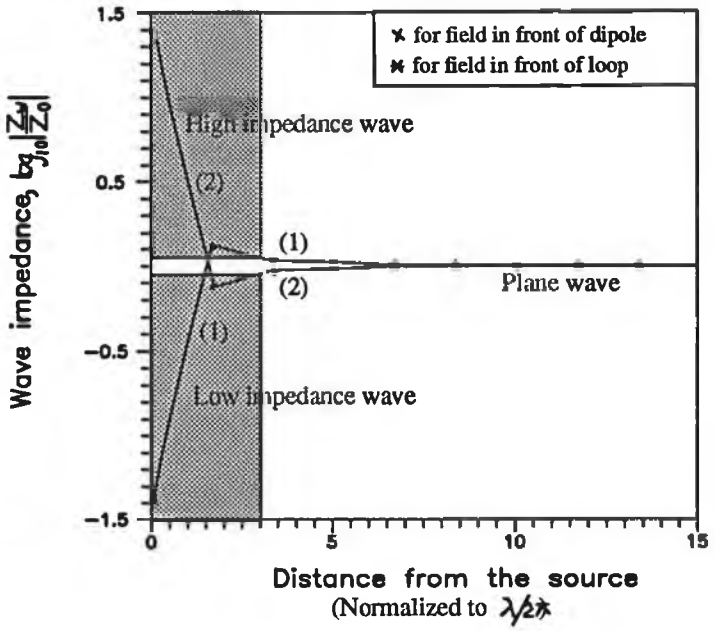

Fig. 2.1 Classification of EM waves on the basis of wave impedances. Curve (1) indicates radiated field in front of a loop antenna and curve (2) indicates that in front of a short dipole.

Thus there may be two different types of near field situations, high impedance (i.e. impedance > 377 Ω), frequently referred to as predominantly E-field, and low impedance (i.e. impedance < 377 Ω) or predominantly H-field. Usually dipoles or line type sources produce high impedance fields and loop type sources produce low impedance fields in the near region (see Fig. 2.1).

The shielding behaviour of a material varies significantly depending on the type of field. Materials which can offer very good shielding against E-field (such as thin aluminium or copper foil) may be useless in a predominantly magnetic field environment. In the present work, both far field and near field SE determinations are discussed while in near field measurements high impedance and low impedance cases are considered separately.

2.3.2 FREQUENCY RANGE

Much of the present interest is in SE data covering 0.1 to 1000 MHz. This range includes domestic FCC rules, the German VDE 0871/6.78 standard which is essentially that proposed by CISPR [76], affecting commercial equipment sold to EEC communities and Japan, and mostly military requirements such as MIL-STD-461.

2.3.3 MATERIAL UNDER TEST (MUT)

The shape of the object is an important criteria in selecting or developing an SE measurement system. Techniques applicable for measuring sheet form objects may not be usable for enclosure SE measurements. Similarly test devices that measure SE of enclosures are not suitable for SE measurements of sheet materials. A TEM cell is used for susceptibility and emission measurements of enclosures and a coaxial test fixture for sheet materials, while neither of them could be used for both types of MUT. The MUT in the present problem is the conductive polymer during its production process, assumed to be in planar sheet form.

2.3.4 DYNAMIC RANGE OF THE TEST SYSTEM

Dynamic range of a test system may be defined as the ratio of maximum and minimum signal levels which can be handled by the system within a specified accuracy. In case of SE measurements usually it limits the maximum value of SE that can be measured with a particular test system. It is well known that the instruments used in the measurements and the inherent limitations of the test device (probable leakage and susceptibility to ambient noise) are the factors influencing the dynamic range of a test system. As mentioned above a major element of this work is to measure the SE of various conductive polymers that are currently available. The shielding capability of this class of materials are known to vary from 30 dB to 80 dB. Thus for practical purposes a dynamic range of 50 to 80 dB would be required.

2.4 SE MEASUREMENT TECHNIQUES, A REVIEW

The usual practice followed for experimental SE measurement techniques is to measure the insertion loss (IL) that results from introducing the test sample. *IL* is measured by comparing the received signal strength with (P_r') and without the MUT (P_r) in the test device (the transmitted power being held constant) and is given by

$$IL = 10\log_{10}\frac{P_r}{P_r'} \qquad (2.4.1)$$

A short review of several SE measurement techniques which are currently being used by reputed EMC compliance testing organizations for testing the shielding capability of conductive plastic materials in sheet form is given below. The discussion is summarized in tabular form in Appendix B1 where the techniques are graded on the basis of some basic variables of interest.

2.4.1 MIL-STD 285 TEST METHOD

A simple, widely used and comparatively old [77] method is the MIL-STD 285 type test. The MUT sheet is mounted over an aperture in the wall of a shielded room, and the transmission loss between the two antennas, one inside the shielded room and the other outside, is compared to the transmission loss between the same two antennas at the same separation in free space. The power of the transmitting antenna is kept constant for both configurations. IL or SE can then be found by using Eqn. (2.4.1). An EMI gasket is used for mounting the MUT on the aperture in an RF tight condition. The test set-up is illustrated in Fig. 2.2.

A modified MIL-STD 285 method has been described by Ma *et al.* [78], where the aperture is in the common wall of a shielded room having two compartments, one antenna is housed in each compartment. The reference measurement is made inside the room rather than in free space, without covering the aperture with the sample.

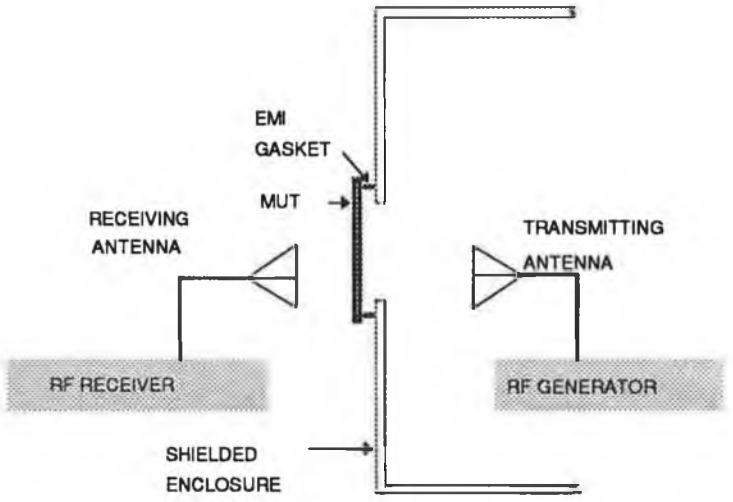

Fig. 2.2 MIL-STD 285 type test set-up. A section of the shielded room has been shown.

The major limitations of this system are that the receiving antenna is susceptible to picking up ambient noise and higher order mode resonance might occur inside the shielded room which in turn reduces the upper frequency limit of the test system.

2.4.2 ASTM ES7-83 DUAL CHAMBER TEST FIXTURE

This fixture was introduced by ASTM ES7[1] in 1983 [79]. The test arrangement is almost like the modified MIL-STD 285, except that the chambers are small boxes pivoted at one end and the other end is clamped so that the boxes are in piggy-back style before getting SE data. Each chamber has a small antenna mounted inside to emit (or receive) the radiated power and the sample is sandwiched between the piggy-back walls of the two chambers. Spring finger stock gasketing is provided as a seal between the sample and the input chamber. Fig. 2.3 shows the test fixture.

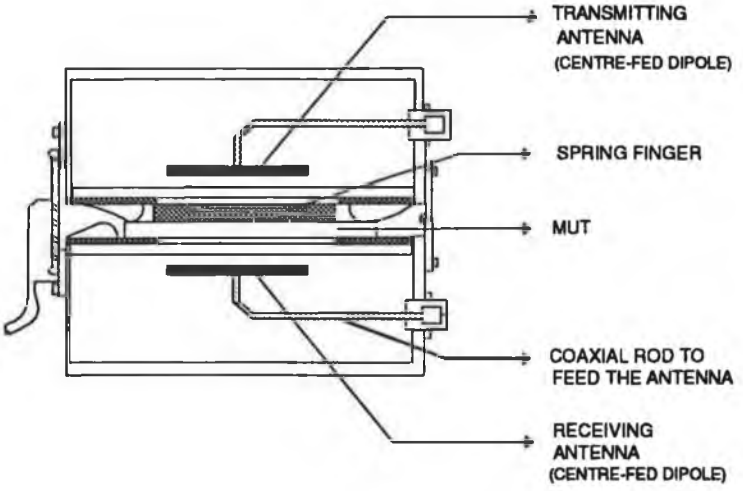

Fig. 2.3 ASTM ES7-83 dual chamber test fixture. A sectional view is presented. Adapted from [79].

Sample preparation may sometimes be necessary depending on the type of material to be tested [80].

2.4.3 CIRCULAR COAXIAL TRANSMISSION LINE HOLDERS.

There may be two versions namely, the continuous conductor (CC) version and the split conductor (SC) version. This technique is basically an insertion loss (IL) measurement using a substitution method. In case of CC, the test device is a section of expanded 50-Ω co-axial transmission line which tapers at each end to mate with ordinary 50-Ω co-axial line. The holder may be disassembled to allow the insertion of an annular washer shaped test sample. When assembled both the inner and outer conductors ideally form continuous connections.

[1] American Society of Testing and Materials. Electrical Standards(ES), Committee 7

In case of the split conductor version the inner conductor is not continuous, it is also segmented in two parts. Flanges are used as outer conductors to secure the sample and capacitively couple the conductors. Three pieces of material are needed for the sample. Measurement for the loaded case require a disk shaped sample with diameter equal to that of the outer flange dimension. The unloaded reference measurement is done with an annular piece of material matching the outer flange dimensions and a disk matching the diameter of the inner conductor. This arrangement repeats the capacitive coupling of the loaded case, when establishing the reference level, while leaving the space between the two conductors free (unloaded). Nylon screws are used to fasten the flanges together. It is essential for these test systems that the MUT should be an isotropic material.

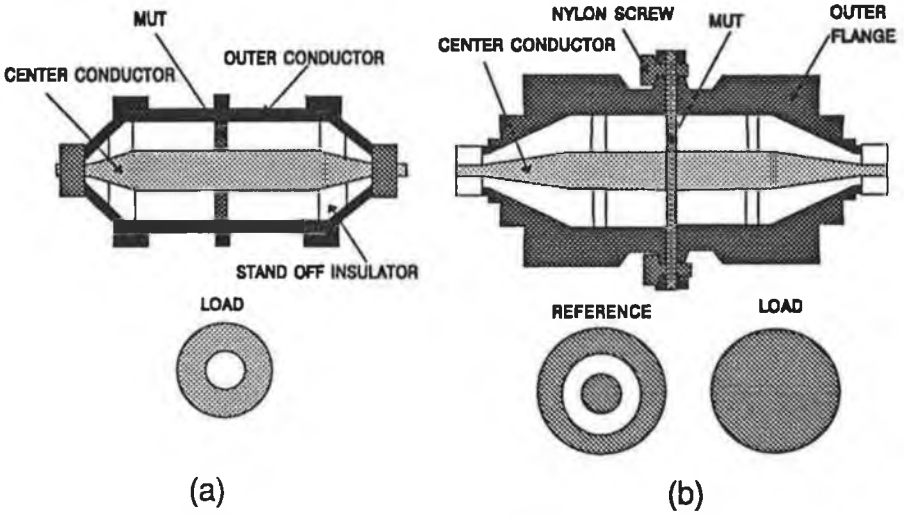

Fig. 2.4 Sectional view of coaxial holder test fixture. (a) continuous conductor CC holder. (b) Split conductor CC holder. Adapted from [36].

2.4.4 TIME DOMAIN APPROACH

Instead of continuous wave sources, pulsed or time domain (TD) signals are directed through the test sample. Use of a TD source makes it possible to differentiate between the direct path (through the test sample) and indirect path (diffracted), signal at the receiving end [83]. It facilitates the time windowing out the indirect path signal to the receiver. An impulse generator is used to generate an impulse of a few hundreds of pico-second width [84] to be radiated through a TEM horn antenna (because TEM

horns have linear amplitude and phase response for a wide frequency range [85]). At the receiving end the pulse is detected by a similar antenna connected to a waveform recorder (sampling oscilloscope). The transmitting antenna is spaced sufficiently from the test material so that it is in the far field region of the sample (the direct path fields would then be approximately plane wave).

Ideally a large sample sheet is required with this method in order to get longer "clean time" (clean time is defined [36] as the interval between the arrival of the desired direct path signal and the first unwanted indirect path signal). Longer clean time results in data covering a wider frequency range. If small samples are to be tested one must resort to an aperture measurement. In that case, the MUT sheet is mounted on a small aperture in a large metal screen [86]. Shielding Effectiveness measurements can be made with the same TD system, but transmitting the signal through an aperture in the wall of a shielded room, keeping the impulse transmitting system inside the shielded room and the TD receive system outside the room [87].

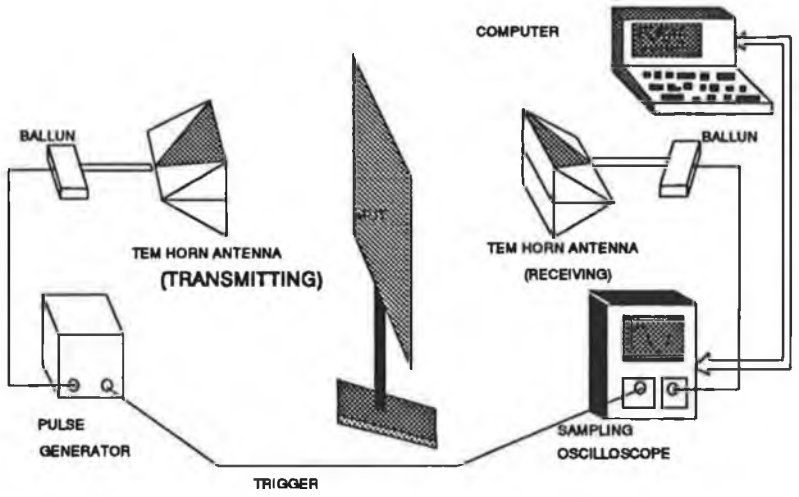

Fig. 2.5 Schematic diagram of the time domain SE measurement system. Modified and adapted from [36].

2.4.5 COMPLEX PERMITTIVITY APPROACH

By applying the theoretical approach suggested by Schulz [41] and expressing the losses in terms of complex permittivity the SE of a planar sheet can be represented by the well-known equation

$$SE = A + R + B \qquad (2.4.2)$$

where the three different loss terms are given by

Absorption loss

$$A = 0.1285\sqrt{\mu_r(|\varepsilon_r| - \varepsilon_r')}l \quad \text{dB} \qquad (2.4.3)$$

Reflection loss

$$R = 20\log\frac{|\varepsilon_r|}{4} \quad \text{dB} \qquad |\varepsilon_r| >> 1 \qquad (2.4.4)$$

Correction term

$$B = 20\log|e^{-2\gamma t}| \quad \text{dB} \qquad \text{where} \gamma = j0.02f\sqrt{\varepsilon_r} \qquad (2.4.5)$$

If the complex permittivity of a material could be determined with sufficient accuracy then it is easy to get the SE values from the above set of equations.

The open-ended coaxial probe is a common test device for measuring the complex permittivity for dielectric materials in solid and liquid form [88], [89]. The Hewlett-Packard company has recently begun marketing a model HP8507A flanged open-ended coaxial probe (as shown in Fig. 2.6(a)) for determining complex permittivity of solids and liquids for use with network analyzers [90].

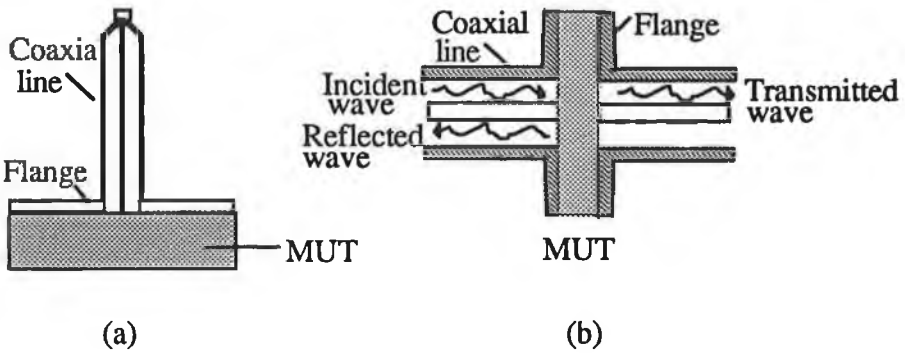

Fig. 2.6 Sectional view of the coaxial probes for complex permittivity measurement. (a) open-ended coaxial probe (HP8507A type probe) (b) new test fixture proposed by Scott [143].

A new simple technique for measuring the complex permittivity of planar sheet like materials has been proposed by Scott [143]. The MUT is sandwiched between a pair of open-ended flanged coaxial probes as shown in Fig. 2.6(b). No sample preparation is necessary which is an obvious advantage of this technique in the context of on-line SE determination (described later in section 2.7). The transmission coefficient of the fixture can be expressed in terms of the capacitive coupling between the centre conductors and the admittance of the radial transmission line formed by the flanges; both of them are functions of the complex permittivity of the test sample. The transmission coefficient can be measured using a Hewlett-Packard HP8510 network analyzer. Substituting the measured value of this coefficient in the expression, one can calculate complex permittivity of the MUT.

The analysis presented by Fan *et al.* [164] for the application of an open-ended coaxial probe in determining the complex permittivity of layered dielectric material may also be useful in the determination of SE for flexible laminates. Similar analysis has been presented by Xu *et al.* [144] for the determination of complex permittivity of dielectric substrates coated with thin conducting films using similar probes and that may also be useful for determining SE of coated conductive plastics.

2.4.6 DUAL TEM CELL FOR NEAR FIELD SE MEASUREMENT

A TEM cell is an expanded section of rectangular co-axial transmission line. In dual TEM cell (DTC) measurement, two identical TEM cells are connected in piggy-back [91], [92] style. The common aperture coupling is the basis of the dual TEM cell test fixture. If an aperture is cut in the top wall of the cell's outer conductor, the known and uniform field [93] generated in the cell would couple through the aperture. If a second cell is placed on top of the first one in piggy-back style, the field radiated in the first cell can be measured in the second cell. When the MUT is placed over the aperture, the coupling from the source cell to the sensor cell is reduced. The amount of this reduction is a direct measure of the materials IL.

The DTC is unique in that it has two output signal ports for a given input signal, and the aperture couples energy to the two output ports asymmetrically. The coupling through the aperture in the forward direction of the receiving cell is proportional to the difference of the normal electric and tangential magnetic polarizabilities of the aperture while that in the backward direction is proportional to the sum of the polarizabilities

[94]. Thus by hybridizing the two output ports for summing and subtracting, one can get the polarizabilities individually. Ratio of the electric polarizabilities with and without the MUT indicates IL offered by the MUT against high impedance field while the ratio of magnetic polarizabilities denotes IL against low impedance field [94].

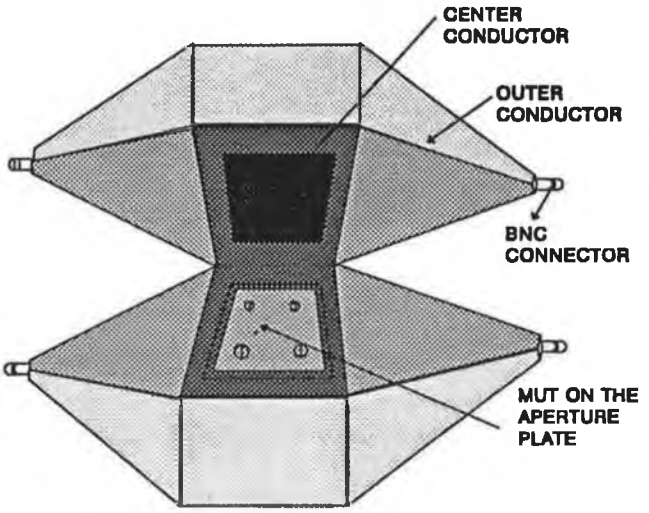

Fig. 2.7 Dual TEM cell test fixture for near field SE measurement. Adapted from [97].

2.4.7 APERTURED TEM CELL IN A REVERBERATING CHAMBER

An alternative to the DTC is to use a reverberating chamber to excite an apertured TEM cell. A reverberating chamber [95] is a simple shielded room with a paddle wheel in the ceiling or in the wall inside the room. The paddle may be turned continuously (stir mode) or in small discrete steps (tune) [96].

In any given paddle position we simply have a shielded room with an added boundary condition. As the paddle positioning is varied, the field generated inside the test zone of the chamber is statistically a plane wave [16]. A test field has, of course, to be generated first by supplying power to the transmitting antenna.

The analysis of an apertured TEM cell in a reverberating chamber is similar to that for the DTC except that the source field is distinctly different [97].

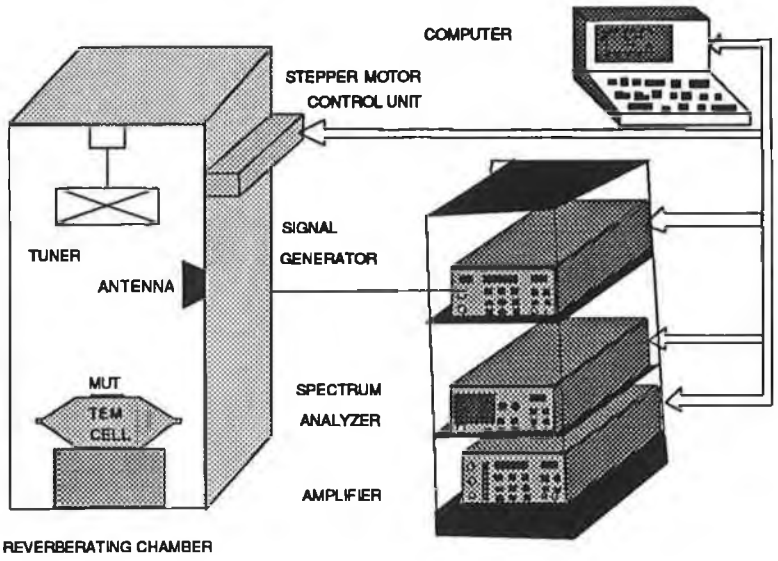

Fig. 2.8 Near field SE measurement using an apertured TEM cell in a reverberating chamber. Modified and adapted from [97].

2.4.8 TEM-T CELL

A comparatively new SE measurement technique has been reported by Hariya [81] and Catrysse [82]. The test cell almost resembles a flanged co-axial holder except that the cross-section is rectangular like a TEM cell. Two different test devices are used to determine electric field SE and magnetic field SE individually. It is obvious that samples must cover completely the outer flanges but the center conductor should not touch the sample because the coupling between this conductor and the sample is capacitive in nature (non-contacting). Fig. 2.9 illustrates the test device.

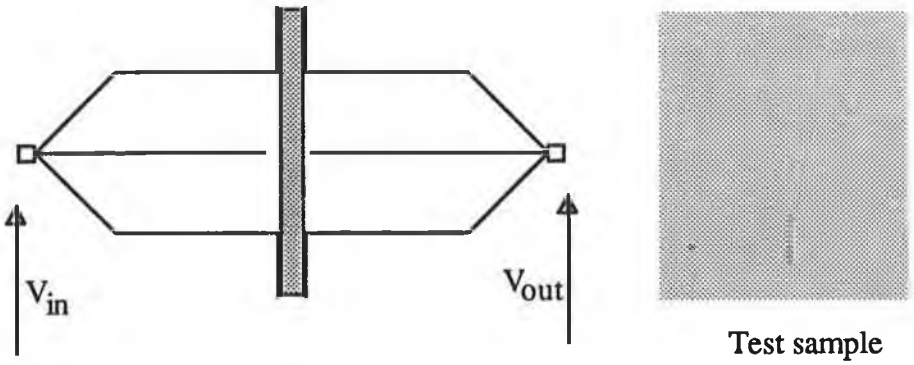

Fig. 2.9 TEM-T cell test device. The sample is sandwiched between the two halves of the cell but the centre conductor is not in contact with the sample. The sample size and shape is also shown in the diagram. Adapted from [14].

The magnetic field SE data can be obtained by modifying the cell halves [81]. Three quarters of a loop antenna are placed inside a copper box made of 3 mm thick copper sheet, while the remaining one quarter is protruded through a 90° reflector, set at the flanged face of the box. The test sample is to be inserted between the flanges to get magnetic field SE data.

2.4.9 TRANSFER IMPEDANCE APPROACH

The concept of surface transfer impedance [43], defined as the ratio of the current induced at one face of a planar material due to the field incident at the opposite face, constitutes a basis for calculating SE of samples having specific geometric shape. For a locally planar shield, the approximate expression for the SE is given by [98]

$$SE = 20log\left|\frac{Z}{Z_{st}}\right| \qquad (2.4.6)$$

where,

Z_{st} = The surface transfer impedance.

Z = An impedance term which is a function of the incident field type and the shield geometry. Expressions are available in [98] for different geometries and incident field types.

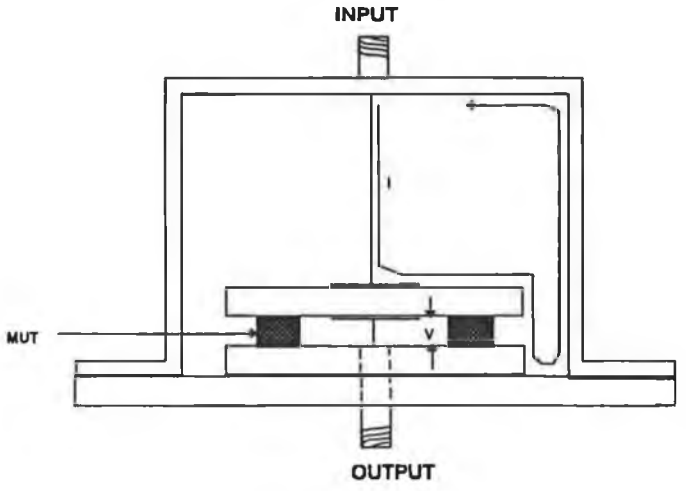

Fig. 2.10 Transfer impedance approach of measuring the near field SE. Adapted from [97].

One standard method [99] of measuring the transfer impedance uses a coaxial test fixture. The fixture allows pressurized air to be injected into the top chamber, enabling accurate, uniform control of the pressure exerted on the test sample. Very

good electrical contact can thus be ensured. The surface transfer impedance may be measured by comparing the voltage V (as shown in Fig. 2.10) across the MUT to the driving current I [97]. The coaxial structure makes it easy to determine the frequency dependence of the transfer impedance.

2.5 PROPOSED ON-LINE TEST CONFIGURATIONS

Introduction of a particular SE measurement technique into the continuous composite material production process requires knowledge of the probable configurations which could be incorporated in the sheet material manufacturing industries for on-line monitoring of the product characteristics. Investigating the continuous manufacturing processes of different sheet-like materials, some probable on-line test configurations can be described as follows:

2.5.1 CONTINUOUS DATA ACQUISITION

The sheet would move continuously and the variable of interest (VI i.e. SE) would be measured without stopping it. The test device may remain stationary or may move continuously along the sheet if the test fixture permits. Data acquisition should be fast enough to get VI values at all points of the sheet (not only at few sampling points).

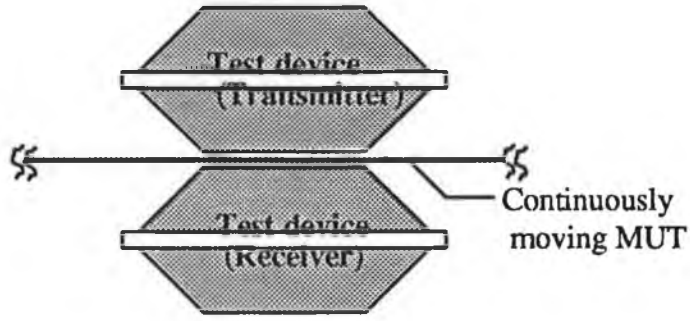

Fig. 2.11 Continuous data acquisition process. The test device is stationary and the MUT sheet is moving continuously at a moderate speed.

2.5.2 CLAMP AND MOVE SAMPLING DATA ACQUISITION

This is essentially a sampling process. At different sampling points, the test device would clamp on to the continuously moving sheet and continue to move along with it for the duration of measurement. As one set of data acquisition is over it would disengage, return to the original position and be ready for next set of data. The test

device should not place any obstacle to the movement of the sheet. The steps involved in such data acquisition are shown in Fig. 1.

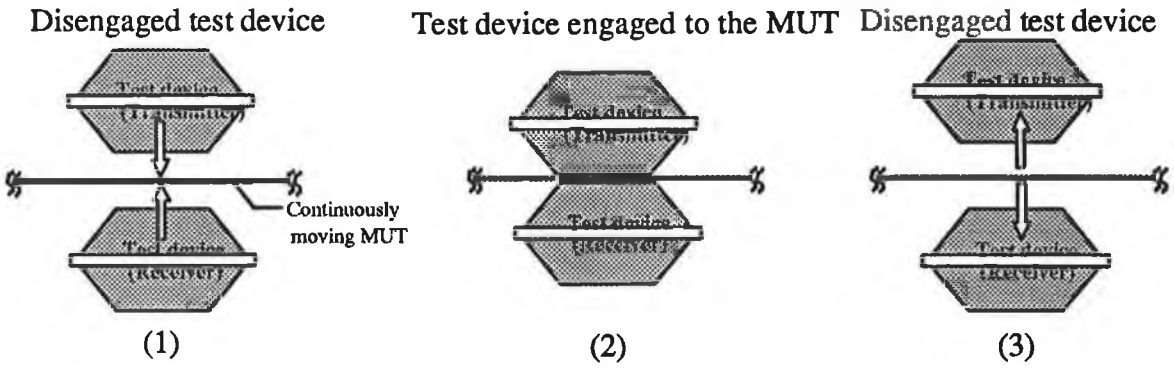

Fig. 2.12 Steps involved in clamp and move data acquisition; (1) The two halves of the test device are about to be engaged with the continuously moving MUT (2) The two halves of the test device engaged with the MUT and (3) After the data acquisition has been completed the two halves are disengaged again.

2.5.3 SCANNING DATA ACQUISITION AT SAMPLE LENGTHS

The test device would scan along the sheet in a direction transverse to its motion. The scanning would start at different sampling positions and until one set of measurements is done, the test device would move forward with the sheet (scanning path is shown in Fig. 2.13). As one set of measurements is completed it would return to its original position and prepare for the next set of measurements.

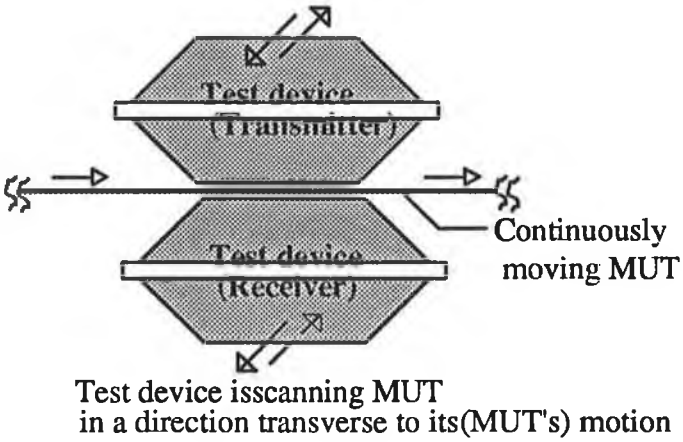

Fig. 2.13 Sampling scan data acquisition.

2.5.4 ACCUMULATOR ROLLS: SAMPLING DATA ACQUISITION

In manufacturing processes involving continuous sheet of fabric production (for example, paper, cloth, carpet and plastics) the process can be temporarily "paused" using a set of accumulator rolls. Accumulator rolls act as buffer storage area taking up material stack thus allowing the material downstream to remain stationary for a short period of time. Positioning a test device at this downstream location would permit appropriate data acquisition while the process is paused. The process can be repeated for any number of sample lengths.

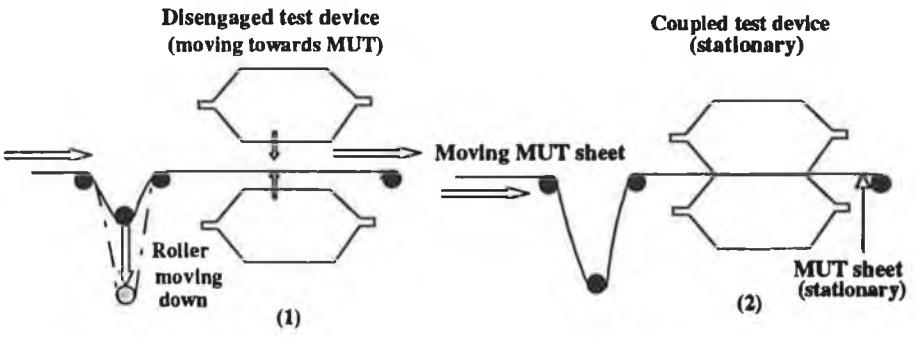

Fig. 2.14 Accumulator rolls data acquisition. During data acquisition process the test device gets engaged to the MUT and the specific region of the MUT (where the test device is engaged) remains stationary.

2.5.5 CUT LENGTHS DATA ACQUISITION

In some plastic processes sheet is cut into fixed-length pieces and stacked rather than rolled on a drum, it is possible to measure the VI of the cut length pieces of the sheets before being stacked. In that case the test system would no longer be strictly on-line.

2.6 CRITERIA FOR ON-LINE SE MEASUREMENT TECHNIQUES

The manufacturing process flow diagrams of conductive painting, vacuum metallization and filled composite are shown in Figs. 1.4 through 1.6. Probable locations of the proposed on-line SE measurement system are shown in Figs. 1.8 through 1.10.

Bearing in mind the probable on-line data acquisition techniques described in section 2.5 and the location of the proposed on-line SE measurement system, it is evident that apart from reasonable cost and the test device simplicity, an appropriate SE measurement system would have to meet the following specifications:

(1) No pre-processing or sample preparation as accommodation of pre-processing complicate the system and cause a distortion of the product.

(2) Clamping the test device tightly with the material under test (MUT) would involve the control of high quality sensors and precision movement mechanisms [103] and hence should be avoided. Moreover the MUT may not have fully cooled at that point in the process where the measurement is being made and may therefore be still soft. Clamping a test device to it at this point could easily damage the material's surfaces.

(3) The facility for fast data acquisition and manipulation to ensure real-time observations of SE values. It should at least be fast enough to yield real-time data.

(4) It should be possible to handle material thickness within defined limits.

(5) It should not place constraints on the mechanical properties of the material (viz., constraints like a definite amount of rigidity, hardness or elasticity) which are sometimes difficult to fulfil in a practical situation.

The temperature of the MUT may be higher than the ambient at this stage. So the conductivity of the metallic fillers or layer would be lower which might result in recording lower SE values than the actual. However, this effect can be taken into account through calibration, because the test device would be fitted permanently at a section of the manufacturing process where the temperature of the product would always remain the same (there would be little or negligible fluctuations of temperature at a particular section of the manufacturing process).

2.7 TECHNIQUES OF THE PRESENT RESEARCH

The purpose of any SE measurement system is to study the EM shielding behaviour of the MUT in the presence of a specific simulated source of EMI. As stated earlier in section 2.2, for radiated susceptibility and emission measurements, it is necessary to simulate both uniform plane wave (far-field) sources and near-field (high and low impedance) sources.

A thorough review of the existing SE measurement techniques, as mentioned in section 2.4, reveals that there are two different ways of simulating standard test fields on the MUT. In free space, antennas can be used to produce the desired field on the MUT or in a closed test fixture, waveguides may be employed to deliver standard test field to the MUT. It is also evident from the review that both far field and near field SE data acquisition is not possible through a single technique. Moreover, it is difficult to accommodate the simulation of both types of near field sources in a single technique. The situations become even severe when the stringent conditions of on-line measurement as described in section 2.6, are to be satisfied. Thus in the present analysis, three different test devices are proposed in order to simulate the three desired types of sources.

2.7.1 FAR FIELD SE MEASUREMENT

If conventional antennas are used in free space techniques, from the discussion of section 2.3.1 and from the Figs. 3.11(b) and 3.19(b), it is evident that to simulate a far field situation, the minimum distance at which the test object is to be placed from the loop or dipole radiator is $6\times(\lambda/2\pi)$, which is approximately 3 m for a 100 MHz incident wave.

The major problem is thus the large test area necessary to perform the measurements. It is difficult to maintain such a large test area immune from ambient noise and to prevent the possible indirect path signal from reaching the receiver. Measurements done in a fully anechoic room may provide useful data but are very expensive and impractical to use with an on-line SE measurement system. Moreover, bandwidth limitations of such antennas (dipole or loop) and the non-linear phase response with frequency are other factors that are to be considered with due importance, especially when on-line measurement is desired.

A possible alternative is the time domain technique which has the facility of time windowing out the indirect path signal to the receiver. However, it also requires a large test site and involves using a very expensive (state-of-the-art) high frequency pulse generator (to generate pico-second width pulses), which limit the application of this technique for the on-line SE measurement.

Closed test fixtures (laboratory techniques) such as the CC and SC coaxial holders can simulate far field in a very small volume but are inappropriate for on-line

SE measurement techniques because very stringent sample preparation is necessary and tight mounting (ensuring good electrical contact) of the sample into the test device is also very important.

Hence it is desirable to develop some antenna or device which would produce a uniform plane wave in a very confined region and would not require clamping of the test device with the MUT sheet. The proposed VCLA assembly could satisfy both the requirements.

Although both the V-conical and the lens antennas are well-known among the antenna researchers the combined assembly of the two as a VCLA has only been proposed in the present work.

The VCLA assembly, chosen for far field source simulation, is intended to provide parallel beams of uniform plane wave (as will be described in the next chapter) at the test location and thus there is no possibility of indirect path signal reaching the receiver. This is a non-contacting free space technique and no sample preparation is necessary. Therefore it satisfies all the requirements of an on-line measurement technique together with the special feature of producing a uniform plane wave in a confined region which can be exploited in many other EMC measurements (noted in chapter 7).

In a simple test configuration two VCLA assemblies would be placed (stationary) face-to-face and the MUT would pass through them. If the reference measurement (reception level without the MUT in between) were recorded before and the receiving instrument compared the on-line received signal strength (while MUT is passing through the test device) with this reference, continuous real-time SE data acquisition would be possible with this test device.

2.7.2 NEAR FIELD SE MEASUREMENT

Ideally, near-field SE could be measured by placing the test material (preferably an infinite sheet) between closely spaced antennas, such as dipoles. If a finite sample must be used, there will necessarily be signal components arriving at the receiving antenna that do not go through the material. These signals that arrive by indirect paths may be eliminated by placing the transmitting antenna in a shielded box but at the expense of perturbing the desired field distribution. Anechoic materials may be used to suppress

reflections from the shielded box but the huge cost, the complexity of the fixture and above all the extreme frequency dependence of these materials make them unsuitable for the present applications.

Waveguides are extensively used for near field measurements instead of using radiating antennas in free space or in shielded boxes. The Dual TEM cell (DTC) test fixture developed by Wilson *et al.* [94] is a very good example of such a waveguide technique, as has been described in section 2.4. The complementary test device of apertured TEM cell in a reverberating chamber and another approach, namely the transfer impedance technique are also discussed in the same section. Nevertheless all of them have the improper features of stringent sample preparation and the requirement of good electrical contact between the test sample and the test device. Hence contact-less free space measurement is preferred to wave guide approaches.

Again, it is very difficult to develop a single technique which can give both high impedance and low impedance types of near field data in a contact-less measurement. Nevertheless the aperture coupling techniques provide both types of shielding data but are inappropriate for the present purpose of on-line measurement since good electrical contact is essential for those (aperture coupling) techniques. Therefore, in the present application instead of selecting a single aperture coupling technique two different contact-less free space techniques have been adapted for simulating two different types of near field sources. A modified TEM-T cell is the preferred technique employed in the present analysis for near E-field simulation while a newly developed Q-loop antenna is employed for near H-field source simulation.

2.7.2.1 Near E-field SE measurement

The TEM-T cell test device, described in section 2.4 has the advantage that no sample preparation is required and the sample is not to be clamped tightly with the test device, hence the test fixture is not a closed one. However, a good electrical contact between the flanges and the sample is to be maintained [82].

If this technique is to be introduced for on-line SE data acquisition, among the five different configurations, discussed earlier in section 2.6, perhaps the most suitable one is the "Clamp and Move" configuration. However, even for a moderate size test device, clamping the two halves of the TEM-T cell with the continuously moving test sheet would cause damage to the sheet which has just been processed. Moreover

sophisticated control of the precise movement of the heavy test device would make the system very expensive. These two drawbacks may be overcome by providing a gap between the flanges and the sample. This configuration is referred to as the modified TEM-T cell in the present analysis. In such modified form, the TEM-T cell provides a simple non-contacting free space means of producing predominant electric field on the MUT sheet and can constitute a "continuous data acquisition" process for near E-field (High impedance field) SE data. Thus it can be a complementary test device to the VCLA as mentioned above.

With the above mentioned modification of the TEM-T cell test device, both "continuous data acquisition" and "scanning: sample data acquisition" on-line configurations could be employed. The latter configuration involves continuous to-and-fro movement of the test device which might have implications for the associated wiring also [103]. That is to say, there is a strong possibility that the signals to and from the test device will be disturbed due to cable movement. "Cut lengths data acquisition", although applicable with the modified TEM-T cell test fixture, is not being considered here because of its off-line nature. "Accumulator rolls: sampling data acquisition" seemed to be inappropriate in case of conductive thermoplastic industry as the sheet is to be bent at large angles at least at the section where it would be slacked for a while, which may not be technically feasible with this type of sheet (because of its rigidity).

The modification of providing gaps between the TEM-T halves and the MUT sheet would introduce error in the test results. The simulated field type would still remain Transverse Magnetic (TM) (as discussed in chapter 3), the errors would be caused by the radiation loss and the possibility of indirect path signal reaching the receiver. The effect of radiation loss partially cancels out when comparing the test results with the empty cell reference measurements. The infringement of indirect path signal to the receiving half could be minimized by placing the two halves very close to the sheet. Moreover, making the test device considerably narrower than the MUT sheet, the possibility of such indirect path signals could be significantly reduced. Anyway if the test device is calibrated against background noise, indirect path signal infringement and leakage due to radiation and increased transmission loss, it could give reasonably accurate SE data in real-time measurements.

2.7.2.2 Near H-field SE measurement

The Q-loop antenna is one of the major outcomes of the present research where one

quarter of a loop is mounted on a Krauss reflector (90^{o} corner reflector) to produce the effect of a magnetic dipole in a confined region. This newly developed antenna has been employed to constitute a complementary test device to the TEM-T cell to monitor the near H-field SE of the MUT.

The imaging effect of the reflector transforms the quarter loop virtually into a complete loop which means the Q-loop acts as a magnetic dipole in front of the reflector with negligible radiation behind. Thus it produces typical low impedance field in a quasi-shielded test environment which is particularly important in the measurement of SE against EMI.

Two such Q-loop antennas can be placed in face-to-face position in a similar test fixture to that proposed for the VCLA, where the MUT is allowed to pass through them. "Continuous data acquisition" of low impedance field SE of the MUT would thus be possible with a simple test configuration. Calibrations (similar to those made with the modified TEM-T cell) would also be necessary for this test device in order to get reasonably accurate SE data through such on-line measurements.

2.8 FURTHER BENEFITS OF THE NEW EMC ANTENNAS

Antennas that are presently available for contact-less free space EMC measurements are not free from the limitations, such as the radiation loss, the possibility of the contamination of the test fields by indirect path signals and background noise and the edge diffractions as noted earlier in sections 2.2.1 and 2.7. The three new antennas proposed in this thesis are, therefore, specifically designed to overcome those limitations.

The VCLA could be used to simulate a uniform plane wave in a very small volume. In a typical on-line measurement of conductive composites, however, the diffractions can occur only along its (MUT's) width since the continuously moving test sheet is deemed to be infinite longitudinally. Hence in order to reduce this effect considerably, the dimensions of the newly developed antennas are made small compared to the width of the test sheet and the antennas are placed very close to the MUT in the measurement systems. This topic is described in detail in chapters 4 and 5.

Attempts should also be made to lessen the distortion of the test field caused by the probable scattering from nearby objects and the possibility of background interference. In this work the application of a lens antenna in the VCLA assembly, the

addition of large flanges at the open mouth of the TEM-T halves and mounting the Q-loop element on a corner reflector in the Q-loop antennas are suggested mainly to satisfy these requirements.

In the following subsection, some additional desirable features of EMC antennas, particularly suitable for contact-less free space techniques, are noted.

2.8.1 IMPORTANT FEATURES OF EMC ANTENNAS

The desired characteristics of EMC antennas are the frequency range of operation, directional property, improved directivity and impedance matching. A brief discussion on these features are in order.

2.8.1.1 Frequency of operation (EMC range of frequency)

It is desirable that a single antenna can cover the whole range of frequency that is necessary in a standard EMC measurement. The recently developed Bi-Log antenna [175] is an outcome of this requirement. Special attention is to be paid to the RF range of 20 MHz to 1 GHz [176].

2.8.1.2 Directional property

This is one of the most important features of EMC antennas. Directional behaviour of the test antenna can reduce the cost of a test system significantly because if such an antenna is used in a screened room for EMC measurements only a small portion of the walls of the room may be needed to cover by absorbing materials (which are expensive). Moreover, it may be possible to target the test object precisely if the antenna radiates in directional patterns.

2.8.1.3 Improved directivity and gain

Improved directivity is an obvious outcome of the directional behaviour of an antenna and as such a desirable feature for EMC antennas. An antenna with improved directivity can produce a stronger test field on a specific test location in comparison with an antenna which may be a more efficient radiator but has lower directivity. Gain, being directly proportional to the directivity, improves with improved directivity if efficiency remains the same.

2.8.1.4 Standard field simulation

As described earlier in section 2.3 susceptibility measurements require the simulation of uniform plane wave at the test location whereas emission measurements require the simulation of either high impedance field or low impedance field. One of the basic requirements for EMC antennas are, therefore, the capability of producing such standard fields at the test site.

2.8.1.5 Shielding performance against ambient noise

Another very important feature of an EMC antenna is that it itself is immune from background noise. The standard test field simulated by the test antenna, indeed, can only be ensured if the antenna can be made free from such noise.

2.8.1.6 Impedance matching

In most of the EMC applications it is essential to develop test fields of significant strength at the test location and at the same time since the received signal strengths are usually very poor, impedance matching is also necessary at the detection level. Thus for efficient operation of the antennas and measurement systems, impedance matching is vitally important.

Attempts have been made to accommodate most of the aforementioned features in the three newly developed antennas which will be analyzed both theoretically and experimentally in the subsequent chapters. They, therefore, constitute a useful class of antennas particularly for EMC applications. One such application is the development of on-line SE measurement systems that have been the subject matter of this dissertation.

2.9 SUMMARY

A general description of EMC measurements has been given and the variables of interest of the SE measurement systems are noted. Existing SE measurement techniques have been reviewed and the probable on-line test configurations are described and combining these discussions with that of section 1.6, the criteria of on-line SE measurement techniques have been resolved. Finally the three different test devices developed as part of the present research to meet those requirements have been

introduced. Features of the newly developed antennas useful for EMC applications have been noted.

Among the four different probable configurations of on-line data acquisition, a single configuration (continuous data acquisition) is chosen for all three test devices to make the measurement systems consistent.

Chapter 3

ANALYTICAL BACKGROUND

THEORETICAL MODELS OF SE OF CONDUCTIVE PLASTICS
ANALYSIS OF THE FIELD SIMULATED BY THE ANTENNAS
THEORETICAL MODELS OF ANTENNA PARAMETERS

3.1 INTRODUCTION

Three different antennas have been proposed in this project to construct simple test devices for on-line SE measurement of conductive plastic materials. Thus the features deserving analytical studies are the SE of conductive plastics, the fields produced by the antennas and the properties of the developed antennas useful for on-line SE measurement and other EMC applications.

If the intrinsic shielding capability of the MUT can be assessed theoretically, the test results can then be compared with these theoretical models to verify the efficacy of the measurement techniques. Secondly, simulation of standard test fields on the MUT is an essential precondition of a meaningful SE measurement system. Thus it is necessary to verify analytically the test fields simulated by the newly developed antennas at the test location. Moreover, as mentioned in section 2.8, the proposed antennas provide features that are particularly suitable for a contactless free space measurement of SE. They might also be useful for other EMC measurement purposes. It is therefore, necessary to establish analytical models to study such behaviours of these antennas.

The theoretical determination of SE of conductive composite materials is often tedious. In some recent literature, however, attempts have been reported by Liao [106], [107, pp. 47-59] and others [108], [109] to analytically model the shielding capability of some of the variety of conductive plastics mentioned earlier in section 1.6. Some reliable models among them are illustrated in the next section and the shielding capability of the newly proposed RFCP type of filled composite is theoretically developed in this context.

The proposed VCLA assembly, mentioned earlier in section 2.7, could produce plane wave in a confined region thus simulating the test field required for far field (susceptibility) SE measurement. The field produced by VCLA is analyzed in Section 3.3.

The TEM-T cell, as noted in section 2.7, produces a planar TM wave which approximately simulates the near field pattern of an ideal dipole source. This produces predominantly electric field behaviour in its near field region. The Q-loop antenna, on the other hand, acts as a complementary source to develop a predominantly magnetic field at the test location.

In section 3.4, the analytical model of the typical high impedance field produced by the modified TEM-T cell on the MUT is established. A detailed analysis of the radiated field of the flanged open ended rectangular coaxial transmission line (RCTL), which is the transmitting half of the TEM-T cell, is presented there along with the theoretical models of its other antenna parameters useful for EMC applications. It is established analytically in section 3.5 that the Q-loop antenna produces a low impedance field in its near region like a loop antenna. The features of directional behaviour, improved directivity and gain of this antenna are demonstrated analytically in this section.

3.2 SE OF CONDUCTIVE COMPOSITES

A brief treatise on general aspects of conductive composites has been presented in section 1.6 where it has been shown that a wide variety of such materials are being used to serve EM shielding purposes. Metals have well understood EM properties, as have plastics, but when a composite is made of these two constituents, the end product often exhibits less predictable EM behaviour.

It is evident from the analysis of various techniques of imparting shielding capability to plastics that no single standard formulation for the SE of such a broad class of materials is possible. Separate models are necessary to describe the shielding behaviour of surface metallized plastics, flexible laminates, and filled conductive composites (ICPs can be included in this category) as far as theoretical SE determination is concerned. Regularly filled conductive plastic (RFCP), although a special type of filled conductive composite, should be dealt separately as its analysis resembles mostly that of a FSS, embedded in a dielectric.

3.2.1 SE OF SURFACE METALLIZED PLASTIC

SE of surface metallized plastics may well be treated by the formula of Klein [108] which he suggested for electroconductive (EC) coated dielectric slabs. The formula is presented in Appendix C1. The assumptions, employed in the derivation of this formula are (a) that the coating is electrically thin ($t/\delta << 1$, t is the thickness of the metal coating and δ is its skin depth which is given by $\delta = 1/\sqrt{(\pi f \mu \sigma)}$, f is the frequency, μ the permeability and σ is the conductivity of the metal) and (b) that it has a low intrinsic impedance compared with the impedance of free space ($|\eta_t| << \eta_0$). Theoretical SE calculation of surface metallized plastic materials using formula (C1-1) thus, requires

knowledge of exact thickness of the metallic coating, the EM properties of the metal specimen and the electrical specifications of the plastic substrate.

The thickness of the metal (usually copper or aluminium) film or coat deposited on different types of surface metallized plastics as mentioned in section 1.6.1 are of the order of a fraction of one micron to few microns. Referring to the discussion of that section and noting that the skin depths of copper and aluminium are given by $0.0660/\sqrt{f}$ and $0.0826/\sqrt{f}$ respectively [85, pp.153], where f represents the frequency in Hz, one can determine the applicability of the above mentioned formula. Thus at 100 MHz the skin depths of copper and aluminium are 6.6 μm and 8.2 μm, and as a result formula (C1-1) does give an accurate estimate of the SE value of conductive painted and electroless plated materials (metal coat thickness, 0.05-1μm is much smaller than the skin depths), and is only approximate for vacuum metallized objects (metal coat thickness is of the order of a few microns).

3.2.2 SE OF FLEXIBLE LAMINATES

It is obvious that the SE of flexible laminates would depend essentially on the thickness and conductivity of the metal foil used. If it is electrically very thin ($t/\delta << 1$) and if its impedance is very low then formula (C1-1) would be equally applicable for SE determination. More accurate analysis requires consideration of reflections and transmission through each layer of the laminated sheet including the polymer layers as depicted in Fig. 3.1

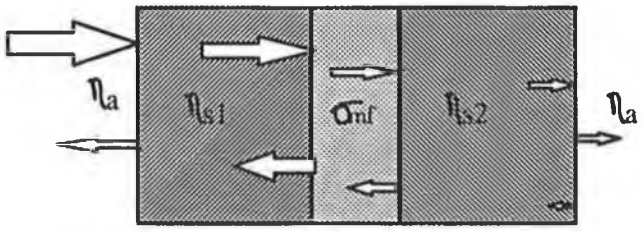

Fig. 3.1 Flexible laminate composed of two layers of backing polymer and single layer of metal foil. The incident, reflected and transmitted waves are shown by the arrow-heads. The length and width of these arrow-heads qualitatively indicate the intensities of the EM waves.

3.2.2.1 Far-field SE of laminates

Electromagnetic shielding offered by any material to a uniform plane wave (far-field)

consists of three different contributions, namely the absorption loss, reflection loss and the correction term and is indicated by Eqn. (2.4.2), where the absorption loss A, is due mainly to the metallic foil in case of laminates and is given by Eqn. (D6-2). Thus it depends on the thickness, permeability and conductivity of the metal foil.

The reflection loss *R* due to the multiple boundaries of the reinforcing substrates and the metallic foil can be analysed by means of the energy-transmission theory and it can be expressed as [107, pp.48]

$$R = 20\log\frac{|\eta_a + \eta_{s1}||\eta_{s1} + \eta_{mf}||\eta_{mf} + \eta_{s2}||\eta_{s2} + \eta_a|}{16|\eta_a||\eta_{s1}||\eta_{mf}||\eta_{s2}|} \qquad (3.2.1)$$

where η_a, η_{s1}, η_{s2} and η_{mf} are the intrinsic impedances of air, two backing substrate material layers and metal foil respectively of the two backing substrates.

Again the correction factor for the flexible laminates in Eqn. (D6-1) is chiefly due to the successive re-reflections that would occur inside the metal foil and for electrically very thin foil, the value of the absorption loss *A* is much less than 10 dB and the correction term is given by Eqn. (D6-4) of Appendix D6.

However, this type of formulation is meaningful only in the far field. In the near field, the EMI could be 90% E-field, in which case reflection loss is dominant or it may be 90% H-field where absorption loss would be dominant.

3.2.2.2 Near -field SE of laminates

In the near field region, the EM wave is either predominantly electric or predominately magnetic depending on the type of the source. While prevented by a shield, predominent E-field (henceforth referred to as E-field) suffers attenuation due mainly to reflection whereas predominent H-field (henceforth referred to as H-field) is attenuated chiefly by absorption [52, pp. 8], a phenomenon which is obvious from the view point of wave impedance. An E-field when incident on a metallic barrier is reflected back to the original medium largely because of the huge impedance mismatch at the interface. A H-field suffers a minimum amount of reflection loss as it is incident on a metallic barrier; and the attenuation mainly results from the absorption into the shield material.

Thus SE of single layered planar sheet material against an E-field may be formulated as the reflection loss, R suffered by the wave at the air-shield interface, which is given by Eqn. (D6-3) of Appendix D6. where k is the ratio of the wave impedance's in the two different media, i.e.,

$$k = \frac{Z_w}{\eta} \tag{3.2.2}$$

Z_W = wave impedance in free space or air.

η = intrinsic impedance of the shield material.

An ideal example of E-field is the near field region of an electric dipole source, where the wave impedance in the radial direction in free space is defined as [110, pp. 652]

$$Z_w = \eta_0 \frac{1 + j\beta r - (\beta r)^2}{j\beta r - (\beta r)^2} \tag{3.2.3}$$

where η_0 = intrinsic impedance of free space.

β = wave number in free space = $\frac{2\pi}{\lambda}$

In the near field region $r<<1/\beta$, thus $Z_W = 1/j\omega\varepsilon_0 r$. Substituting for Z_W and η defined in Eqns.(3.2.3) and (E5-4), as η_c into Eqn. (D6-3), gives the expression of SE against E-field as

$$SE_E = 186.4 + 10\log\left|\frac{\sigma}{f^3 r^2 \mu}\right| \text{ dB} \tag{3.2.4}$$

For a laminated shield of layered materials the analysis can be extended by calculating the impedance ratio at each interface and thereby adding the reflection losses of all the interfaces. However, since the wave impedance in the dielectric layers and that in the free space is not significantly different the main contribution to SE will result from the reflections at the metal foil interfaces.

A loop antenna or magnetic dipole produces a H-field in the near zone. SE of a planar single layered shield against such a low impedance field may be formulated as the sum of reflection loss, albeit minimal, and the absorption loss into the shield. Reflection loss can be computed following the previous analysis, bearing in mind that the wave impedance in the radial direction in free space in front of a magnetic dipole is [110, pp. 654]

$$Z_w = \eta_0 \frac{j\beta r - (\beta r)^2}{1 + j\beta r - (\beta r)^2} \tag{3.2.5}$$

Thus $$R = 20 \log \left(\frac{0.460}{\sqrt{\frac{f\sigma}{\mu}} r} + 0.135 \sqrt{\frac{f\sigma}{\mu}} r + 0.354 \right) \quad \text{dB} \tag{3.2.6}$$

and $$SE_H = 8.686 t \sqrt{\pi f \mu \sigma} + R \quad \text{dB} \tag{3.2.7}$$

in most cases R given by Eqn.(3.2.6) being negligible, SE_H is mainly the absorption loss given by the first term of the right hand side of Eqn.(3.2.7)

Laminated shields would not provide much better performance over the single layered shield against H-field, since no absorption loss of the penetrating EM wave occurs in the extra layers which are dielectrics in most cases.

3.2.3 SE OF FILLED COMPOSITES

Being highly anisotropic in their electrical properties analytical determination of the shielding characteristics of conventional filled composites is complex. The statistical approach adopted by Hendricks [111] to theoretically model the antenna properties of randomly distributed arrays may prove to be useful in tackling this problem, but it is beyond the scope of this analysis.

It is accepted that the major constituent of the shielding capability of a filled composite is the conduction resulting from the conductivity, albeit low, of the filler materials. There are two possible electron paths in a filled plastic. The simplest path being formed by the probable closed network of the touching filler particles. This is the case for relatively highly loaded (filler concentration is high) samples and obviously the conductivity of such a composite is proportional to the number of conduction paths [112]. The existence of a continuous path is not always evident from photographic studies of such materials [113]. Moreover in some cases filler particles are encapsulated into a thin film of polymer, effectively insulating them from each other. Such a composite can still exhibit conductivity with the mechanism called tunnelling. Tunnelling means the penetration of an electron through a potential barrier instead of climbing over it, the phenomenon being well described in quantum mechanical terms [114]. It is observed that the conductivity of such materials is a function of the average width of the gap between the filler particles [115].

The conductivity, rather than being a linear function of loading (volume percentage of filler material in the resin) typically shows the behaviour depicted in Fig. 3.2. (data obtained from [40]). Initially the conductivity is insensitive to loading, and as a specific level (depends on the type of the filler material) of loading (referred to as "percolation threshold") is reached, conductivity rises dramatically.

Shielding capability varies with the type and amount of conductive filler added to the plastic. In addition to the flake conductivity and loading, its shape and size also play a vital role in determining the SE of filled composites. Fibrous fillers yield a percolation threshold at lower loading than flakes of irregular shape [116].

ICPs, although described as a separate class of materials in chapter 2, may be treated as a special type of filled conductive composite where the conductivity of the filler materials (i.e., the ICPs) are small compared to that of metals and as such their concentration must be very high in order to achieve desired levels of SE. However, Colaneri *et al.* [65] has given a comprehensive treatise on the analytical determination of both far field and near field SE values of such polymers. The analysis has been presented in Appendix C2 with little modification with a view to applying it in the theoretical determination of the SE of such a class of materials.

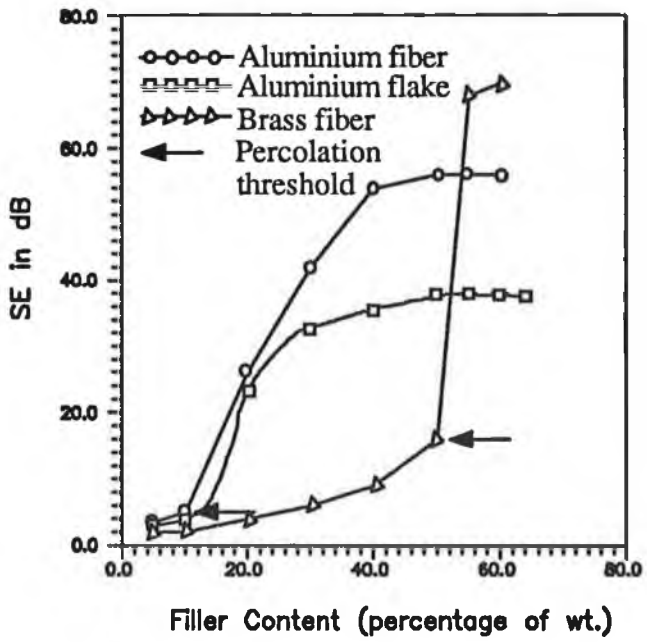

Fig. 3.2 SE of filled composites of different filler materials as a function of filler concentration.

3.2.4 SE OF REGULARLY FILLED CONDUCTIVE COMPOSITES (RFCP)

In determining the SE offered to a normally incident plane wave by a FSS, it is essential to determine the transmission and reflection coefficients of the FSS for such an incident field. It is obvious therefore that, with reference to Eqn. (D6-1), the attenuation of an incident EM wave is principally due to the reflectivity of FSS. Hence determination of the reflection coefficient is sufficient to get an estimate of the shielding capability of such materials.

Basically five different approaches have been employed to analyze periodic scattering arrays, namely (a) variational; (b) point matching; (c) mutual impedance; (d) modal matching and (e) spectral analysis.

Variational methods introduced by Kieburtz [117] considered a complementary problem of conducting thin screen perforated with square holes. A theoretical curve of the transmission coefficient for normal incidence of plane waves was developed.

Ott *et al.* [118] applied a point matching technique to derive the reflection and transmission coefficient of a periodic planar array of dipoles for normal incidence. Munk *et al.* [119] later simplified the analysis by assuming the elements of the array as antennas and determined the reflection coefficient in terms of the driving point impedance of individual elements. Non-normal incidence was covered in this analysis. Since in calculating the driving point impedance, the mutual effect of all the elements of the array are considered, it is known as the mutual impedance method.

The modal matching technique has been discussed in detail by a number of authors [120], [121]. In the modal matching technique starting from the Floquet mode vectors for TE and TM modes the mode vectors are computed for E- and H-fields, from which then the modal impedance is computed. The analysis for a thick slot (or the complementary problem of thick conducting strips embedded in dielectric) can then be carried out by expressing the incident and specularly reflected waves in terms of the unknown modal coefficients; applying the boundary condition of zero tangential E-field in the conducting portion of FSS, these coefficients can then be evaluated. An assumption of symmetric and antisymmetric excitation would make the analysis simpler and the free space reflection coefficient can be expressed in terms of symmetric and antisymmetric reflection coefficients.

The spectral domain analysis is more involved since it deals with the fields scattered from the FSS in terms of the unknown induced current on the conducting part of it. The periodicity of the geometry of FSS is exploited by writing the scattered field equations in the Fourier integral form. These integral equations are then solved for the unknown induced current by using the method of moments. Hence it is obvious that knowledge of the scattered field will allow one to determine the above mentioned coefficients easily through a set of simple algebraic relations. A detailed analysis can be found in many recent publications on this topic [122]-[124].

3.2.4.1 Formulation of SE of RFCP

To understand the frequency dependence of the reflection behaviour of such an array it is desirable to utilize the relatively simple but adequately accurate mutual impedance analysis, without treating the difficult and often non-converging scattering problem. Hence, in the present analysis, the reflection coefficient is determined on the basis of the driving point impedance of the array elements. The formulation follows that of Munk *et al.* [119] with some modification in the derivation of driving point impedance.

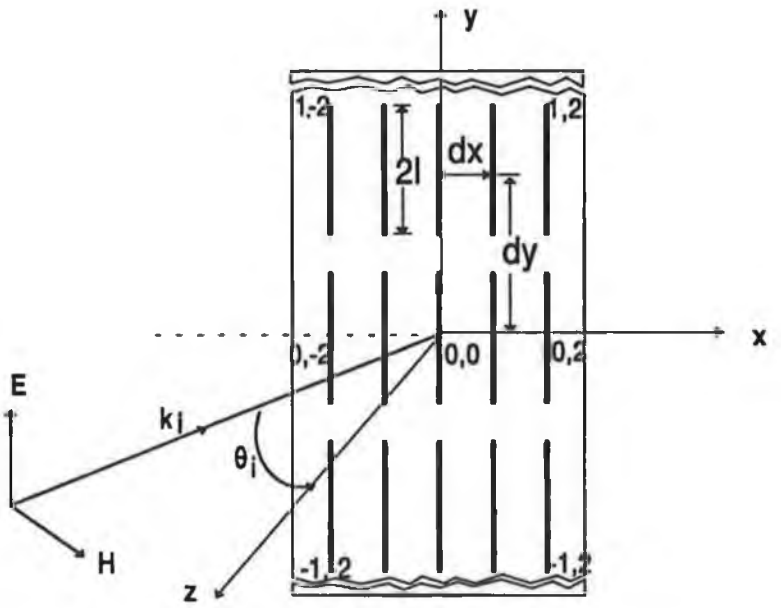

Fig. 3.3 Geometry of the RFCP. 25 metallic filler elements are embedded in the form of a regular array. The incident EM wave is assumed to be vertically polarized.

A doubly periodic array of thin conducting strips acting as dipoles, as shown in Fig. 3.3, is considered for analysis. The planar array is located in the XY plane and the

length of each of the strips is $2l$, all of which are y-directed. For ease of analysis it is assumed that a linearly polarized (y-directed E-field) plane wave is incident at an angle θ_i with the YZ plane. The specular reflection coefficient for such an array can be expressed as

$$R = \frac{K(l_\lambda , l_e , Z_L , Z_D)\, l^4 \sec^2\theta_i}{[d_x d_y (Z_D + Z_L)]^2} \tag{3.2.8}$$

where

$$K(l_\lambda , l_e , Z_L , Z_D) = 3600\frac{\left|F_{e1}-\left(\frac{Z_L}{Z_D}\right)F_{e2}\right|^2 F_{e3}^{\,2}}{\pi^2 l \lambda^4} \tag{3.2.9}$$

$$F_{e1} = \frac{\sin\beta l - \beta l \cos\beta l_e}{1-\cos\beta l_e} \tag{3.2.10}$$

$$F_{e2} = \frac{1}{\sin\beta l_e}[1-\cos\beta l_e - F_{e1}\sin\beta l_e] \tag{3.2.11}$$

and

$$F_{e3} = \frac{\cos\beta\Delta l - \cos\beta l_e}{\sin\beta l_e} \tag{3.2.12}$$

In the above equations, $l_\lambda = l/\lambda$, where λ is the wavelength of the incident wave; l_e is half the effective length of each dipole; $\Delta l = l_e - l$; $\beta = 2\pi/\lambda$ is the phase constant, Z_L and Z_D are the load impedance and the driving point impedance of each element respectively. The driving point impedance of the array is given by [119]

$$Z_D = \sum_{p=-m}^{m} \sum_{q=-n}^{n} e_q Z_{0,pq} \cos(\beta d_x q \sin\theta_i) \tag{3.2.13}$$

where ε_q is the Neumann factor defined by

$$\varepsilon_q = \left.\begin{array}{l} 1, \text{ for } q = 0 \\ 2, \text{ for } q \neq 0 \end{array}\right\} \tag{3.2.14}$$

p and q denote the row and column number respectively, where p varies from $-m$ to m and q varies from $-n$ to n, as are indicated in Fig. 3.3. For $p = 0$ and $q = 0$, the self impedance $Z_{0,00}$ is computed using the expression given by Jordan *et al.* [125, pp. 540-

547] with a modification for rectangular strips as suggested by Elliot [44, pp. 325] i.e. substituting radius by 0.25 (width + thickness) of the strip.

The mutual impedance $Z_{0,pq}$ is derived by following the procedure mentioned in *Antennas* by Krauss [126, pp. 422-430],

$$Z_{0,pq} = j\frac{\beta}{8\pi\omega\varepsilon_0 \sin^2\beta l_e}\int_{pd_y+l}^{pd_y-l}\left[\sin(\beta l_e - |y|)\int_{l}^{-l}\left\{\frac{\partial}{\partial y}\left(\frac{e^{-j\beta(\Delta y'+r)} + e^{j\beta(\Delta y'-r)}}{r}\right)\right\}dy'\right]dy$$

$$- j\frac{\omega\mu_0}{8\pi \sin^2\beta l_e}\int_{pd_y+l}^{pd_y-l}\left[\sin(\beta l_e - |y|)\int_{l}^{-l}\left\{\frac{\partial}{\partial y}\left(\frac{e^{-j\beta(\Delta y'+r)} - e^{j\beta(\Delta y'-r)}}{r}\right)\right\}dy'\right]dy \qquad (3.2.15)$$

where

$$r = [(pd_x)^2 + (y - y')^2],$$
$$\Delta y' = l_e - y' ,$$

and y' is the y co-ordinate on the dipole. The integrations in Eqn. (3.2.15) have been performed numerically.

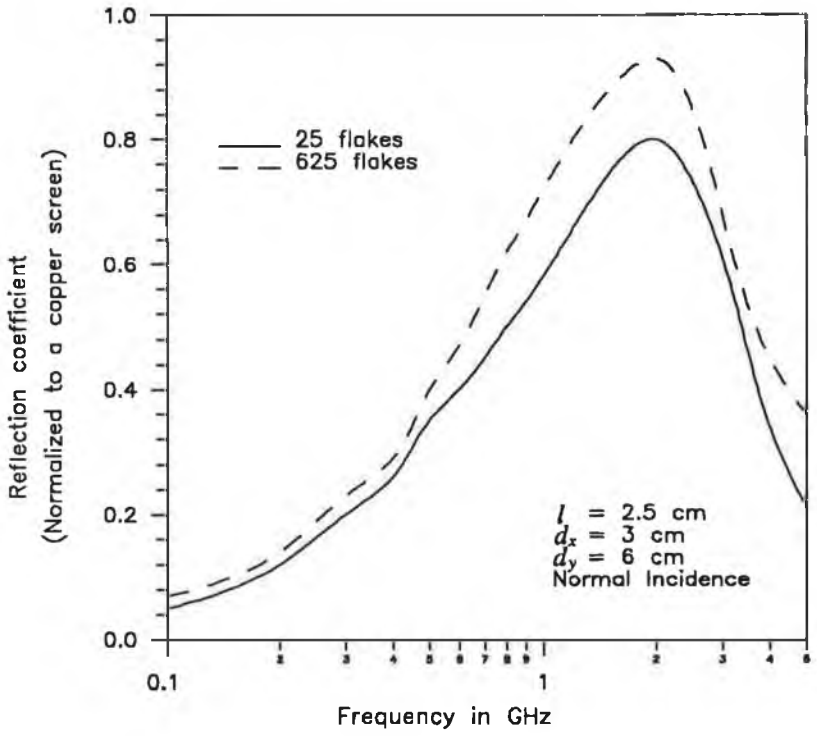

Fig. 3.4 Theoretically predicted reflection coefficient (a measure of the SE) of two different RFCP samples. The reflection coefficient of a continuous copper screen of the thickness of the strips is assumed to be unity.

3.2.4.2 Numerical results

A computer program was developed (see Appendix C12) to compute the reflection coefficient of a periodic array. The analysis of a typical array of 625 elements for 10 different frequencies takes about two hours to run on a PROTURBO 386 computer. Two examples of the reflection coefficients for 625 and 25 elements with the similar seperation and the flake size are shown in Fig. 3.4. No loading was assumed in both the cases (i.e., $Z_L = 0$).

The 25 element array gives lower reflectivity. One probable reason is that in the analysis of driving point impedance it was assumed that the array is very large and as such the driving point impedance of the central element ($Z_{D,00}$) can be repeated for all the elements in the array. This is not true in the case of a truncated array such as the 25 element one. Again the current on all the elements was assumed to be identical except for a variation in phase (doubly infinite phased array), which is also not accurate for a small array. Accurate analysis of a truncated array would require the more involved analysis as mentioned by Ko *et al.* [127] and Preston *et al.* [124]. However a rough estimate can be made that the highest reflectivity occurs at a frequency for which $2l \approx \lambda /4$. The arrays offer high refelectivity only for a narrow band of frequency which, however, can be widened by manipulating the seperation of the elements.

The SE of the wide variety of available conductive plastic materials can be predicted following the theoretical models presented above. An approximate theoretical model of the SE offered by the newly proposed RFCP type material is also established. Predictions of SE based on these models would subsequently be used in chapter 5 for verifying the test results. The remainder of this chapter is devoted to study of the field pattern, and the important parameters of the newly developed antennas.

3.3 FAR FIELD SIMULATION BY VCLA

The V-conical antenna (VCA) is a high fidelity (hi-fi) antenna (developed recently in the Gordon McKay Laboratory of the Harvard University) which has the significant feature of producing frequency independent pure spherical TEM waves even in the near region [105]. A properly designed plano-convex lens, if fitted to its (V-cone's) open mouth, transforms this spherical wave into a uniform plane wave and the combination (referred to as VCLA) thus simulates a standard far field situation. The analytical model of the field distribution in front of such an assembly is presented below.

3.3.1 V-CONICAL ANTENNA

Generally any infinitely long angular antenna is frequency independent when the point source is located at the origin of the co-ordinates [42, chap. 11]. Angular antennas have metal surfaces that are functions of angular co-ordinates rather than the radial co-ordinate *r*. When the driving voltage is applied at the origin O, the currents and charges on the surfaces and the electromagnetic fields in space are all spherical waves of the form $f(\theta,\phi)\frac{e^{-jkr}}{r}$, where $f(\theta,\phi)$ is the directional distribution determined by the angular structure of the antenna [35]; it is frequency independent.

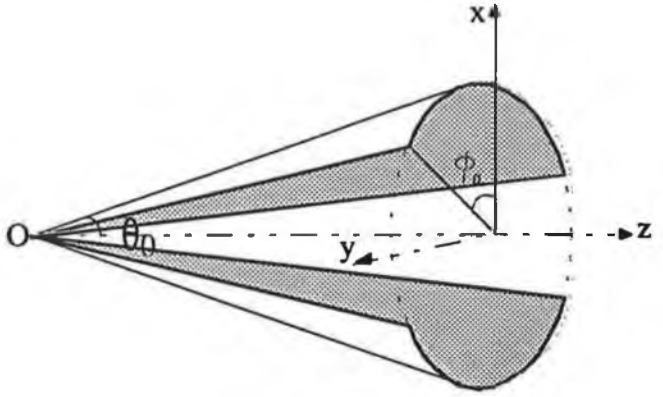

Fig. 3.5 V-conical antenna. The two identifying angles, azimuthal structural angle ϕ_0 and the semi-vertical angle θ_0 are shown.

The VCA, as shown in Fig. 3.5, is a pair of long arc shaped metal plates, each of them bent around a cone at an angle $2\phi_0$. The whole structure is identified by only two angles: the semi-vertical angle θ_0 and the azimuth angle ϕ_0 . This is an angular antenna. When the source is located at the origin O, and the boundaries are related to angular dimensions, it can be proved that the excited EM wave is in the TEM-mode only [131] and can be expressed in terms of the Hertz scalar function Π_{er}. Field expressions are given in Appendix C3 following the analysis of [105].

The VCA which is designed for the present application is specified by the azimuthal structural angle $\phi_0 = 89^o$ (The reason of selecting this angle is described in section 4.2.1.2) and the semi-vertical angle $\theta_0 = 30^o$, the reasons behind selecting those angular measures are given in the following chapter. Substituting these specifications in the field expressions presented in Appendix C3, the field patterns are computed and the plot of the patterns are given in Fig. 3.6. One notable feature of this pattern is that the

EM field in the region $\theta<\theta_0$, although not uniform, more predominent than that outside the cone ($\theta<\theta_0$). This property may prove to be very useful in the present application.

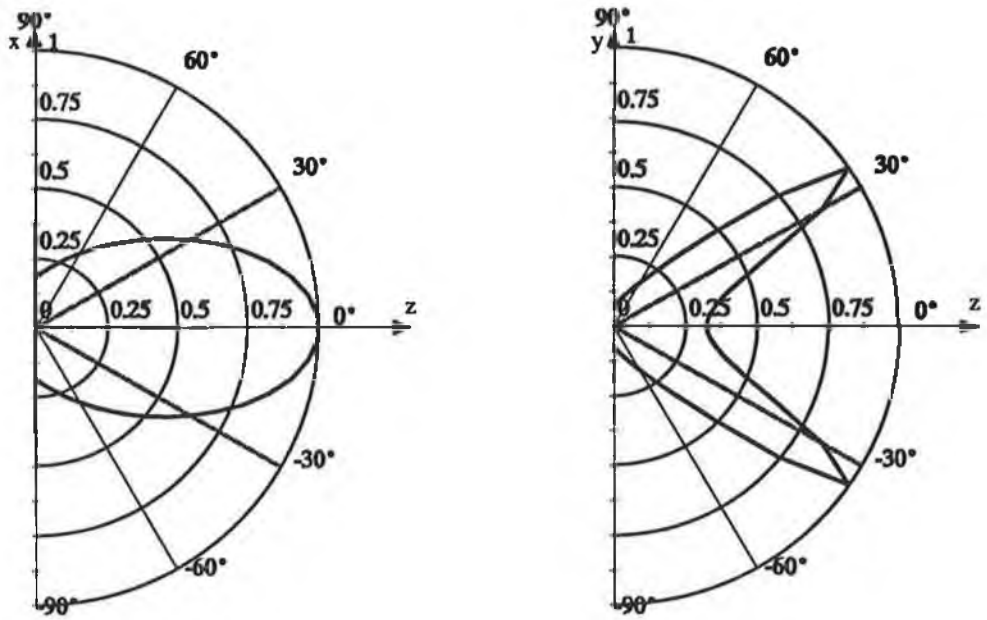

Fig. 3.6 Normalized field patterns of $E_\theta(\theta,0)$ and $E_\phi(\theta,\pi/2)$; Normalized to the maximum field intensity, (a) $E_\theta(\theta,0)$ pattern in plane $\phi=0$ (i.e. x-z plane) where $E\phi(\theta,0)=0$ and (b) $E_\phi(\theta,\pi/2)$ pattern in plane $\phi=\pi/2$ (i.e. y-z plane) where $E_\theta(\theta,\pi/2)=0$.

3.3.2 LENS ANTENNA

The inaccuracies in RF and microwave measurements using free space methods are mainly due to the diffraction effects at the edges of the sample and distortion of the test field caused by the probable scattering from nearby objects. The possibility of background interference is also an important factor to be considered in such measurements. However, in some recent publications [132]-[138], applications of horn-lens combinations have been reported for electrical characterization (dielectric constant measurement) of composite materials in free-space measurements at microwave frequencies from 5.85-40 GHz. In those applications, the above mentioned limitations of free-space measurements have been successfully overcome.

In the measurement system of Fig. 3.7, A VCA is applied for simulating the spherical wave front of a TEM wave which is then transformed into a plane wave front by the use of a lens antenna fitted at the face of the VCA. An EM lens antenna can be used to perform the function for EM waves as optical lenses do for light. Thus EM

lenses can be used to transform the spherical wave front from an isotropic point source or primary antenna into plane wave front or vice versa as shown in Fig. 3.8. However, ideally a lens of infinite width could produce a plane wave even at a distance very far from the lens but in practice a narrow beam of plane wave can only be obtained at a distance very close to the lens (if we neglect the diffraction at the edges) and after that the radiated EM wave would diverge and would no longer be a plane wave.

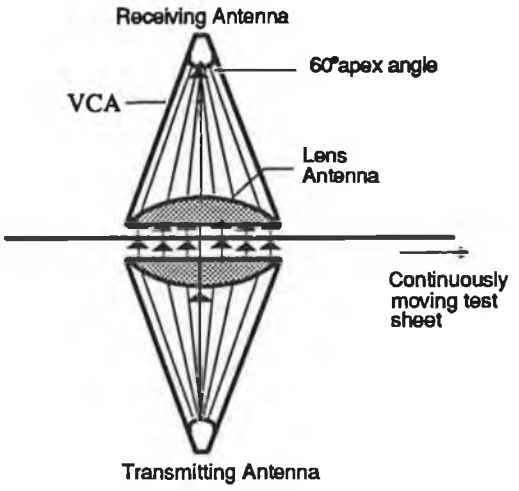

Fig. 3.7 Schematic diagram of the SE measurement system using VCLA assembly.

Certainly the use of a lens antenna would substantially reduce the size of the test system compared to that required if conventional test methods were used for the same frequency band. Moreover it would provide plane wave in a confined area so that the possibility of indirect path signal reaching the receiving antenna can be reduced significantly.

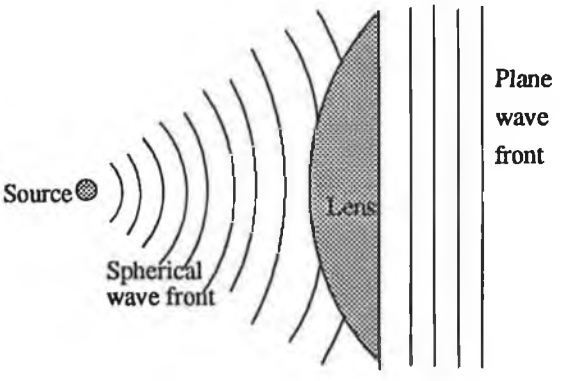

Fig. 3.8 Transformation of EM wave (from spherical to plane wave) while passing through the lens antenna. Adapted from [126, pp. 662]

The design and constructional details of the lens antenna which is particularly suitable for the present application will be described in the next chapter, a brief analysis of the major limitations of the presently available lens antennas and probable solutions to those problems are referred to in the following subsection.

3.3.2.1 Limitations of the lens antenna and means to overcome them

The main limitations of the so-called dielectric lens or the metallic lens are the reflection from the curved face and the non-uniformity of the wave emanating from its plane surface. Reflection occurs due to the impedance mismatch between the lens material and the medium in which it is embedded (usually air). The effect of reflection is shown in Fig. 3.9. Since the incidence of the radial EM rays on the curved surface of lens are at different angles (other than normal incidence), reflected rays, after suffering successive reflections from the inner surface of the VCA, would perturb the spherical TEM wave originating from the source. Again the reflected wave from the air-lens interface at its plane face would follow the original path, thereby changes the incident wave impedance.

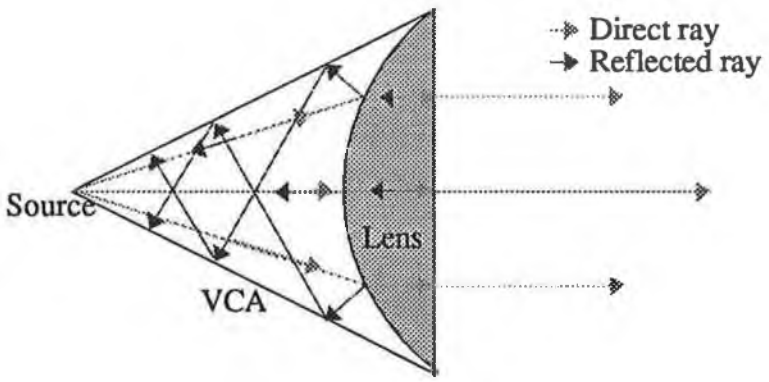

Fig. 3.9 Effect of reflections from the air-lens interfaces. Reflected rays from the curved and flat faces of the lens and the direct rays are indicated as dark and light lines respectively.

In order to reduce reflection the air-lens impedance mismatch is to be minimised. Although the incidence of an EM wave does not occur perpendicularly on the curved surface of the lens in practice, in order to get an understanding how the reflections can be minimized, for the time being, let us assume normal incidence of TEM wave on the air-lens interface, so the reflection coefficient is

$$\rho = \frac{n-1}{n+1} \qquad (3.3.1)$$

where n = the refractive index of the material of the lens = $\sqrt{\frac{\varepsilon_r}{\mu_r}}$; ε_r and μ_r are the relative permittivity and permeability of the lens material respectively.

Hence, for small reflection low refractive index is desirable, which is possible if dielectric materials of small ε_r is used (such as polyethylene) or if magneto-dielectric materials whose permittivity and permeability are very close to each other, are used for constructing the lens.

Non-uniformity of the field emerging from the flat face of the lens is due to the difference in physical path length travelled by EM rays at different height of the lens. Points near the edges are furthest from the source while those near the axis are nearest. Fig. 3.10 illustrates the tapered illumination of the plane wave in front of a nylon lens (calculations are performed by Mathcad®).

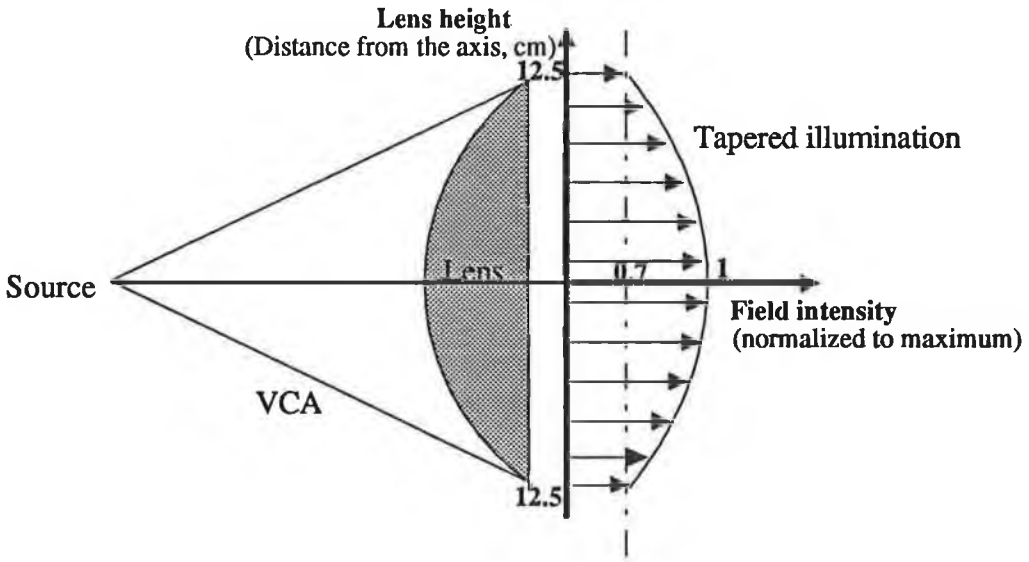

Fig. 3.10 Tapered illumination available in front of a nylon lens. Normalized field intensity profile is shown by the locus of the arrow heads (refer to Appendix C4 for calculations).

This non-uniformity can be avoided by letting the waves suffer a definite amount of penetration loss, while passing through the lens. It essentially demands a specific EM absorption property (definite amount of conductivity and permeability) of the lens material. Selection of a magneto-dielectric material could thus contribute to the elimination of this problem as well.

3.4 NEAR E-FIELD SIMULATION BY MODIFIED TEM-T CELL

As discussed earlier in section 2.7, a modified TEM-T cell is the preferred technique employed in the present analysis for near E-field simulation. In the following subsections, the characteristics of the near E-field source, how TEM-T cell offer those characteristics and some other relevant antenna parameters of the TEM-T half are described.

3.4.1 CHARACTERISTICS OF NEAR E-FIELD SOURCE

The ideal example of a near electric field is the field available in the near region of a dipole. The radiated field of a small and thin dipole of length L carrying a hypothetically uniform current $I_0 e^{j\omega t}$ can be expressed as [15]:

$$
\begin{aligned}
E_r &= \frac{I_0 L e^{j(\omega t-\beta r)}\cos\theta}{j4\omega\varepsilon_0\pi r}\left[\frac{2j\beta}{r}+\frac{2}{r^2}\right] \\
E_\theta &= -\frac{I_0 L e^{j(\omega t-\beta r)}\sin\theta}{j4\omega\varepsilon_0\pi r}\left[\beta^2-\frac{j\beta}{r}-\frac{1}{r^2}\right] \\
H_\phi &= -\frac{j\omega\mu_0 I_0 L e^{j(\omega t-\beta r)}\sin\theta}{4\pi r}\left[j\beta+\frac{1}{r}\right]
\end{aligned}
\qquad (3.4.1)
$$

It is evident from the above equations that at a large distance, where $r>>\lambda$, terms containing $1/r^2$ and $1/r^3$ may be neglected compared to the terms containing $1/r$. Thus in the far field region, the radiated field of a dipole antenna is TEM containing only E_θ and H_ϕ components. On the other hand, the region close to the dipole radiator, where the terms in $1/r^2$ and $1/r^3$ dominate over the $1/r$ terms, is known as its near field region. In this region the electric field has a radial component as well as the polar component (E_θ) but the magnetic field has only the azimuthal (H_ϕ) component.

The direction of propagation of the spherical wave in front of the dipole is obviously along the radius (of the spherical volume taking the dipole as the axis). Thus in the near region the field may be characterized as transverse magnetic (TM) since the magnetic field always lies in a plane normal to the direction of propagation. Fig. 3.11(a) illustrates the situation. Another important characteristic of this wave (very close to the dipole) is that its impedance is greater than the plane wave impedance as shown in Fig. 3.11(b). Z_0 indicates the plane wave impedance.

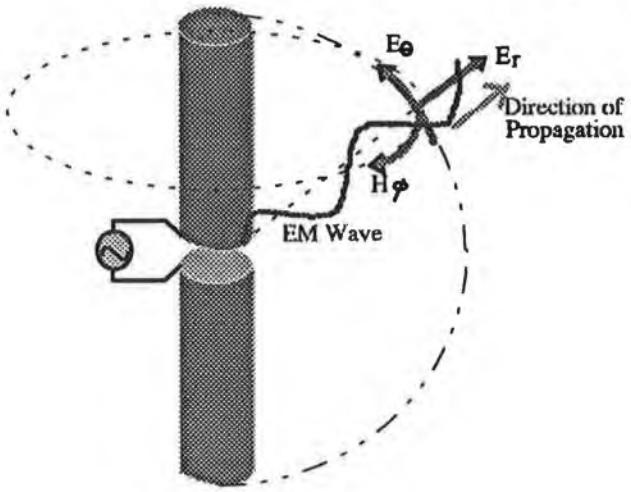

(a)

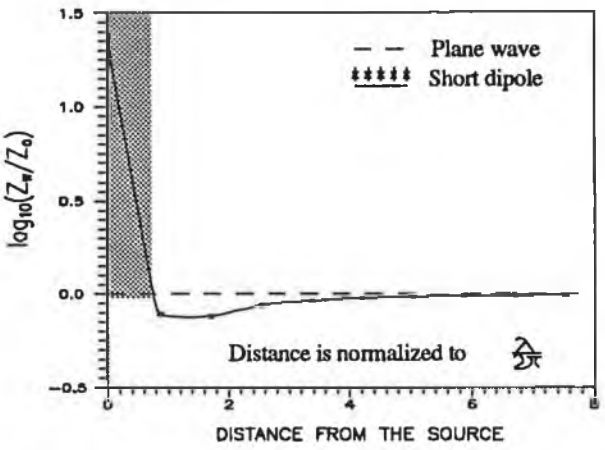

(b)

Fig. 3.11 Characteristics of the EM wave in front of short dipole (a) Spherical TM wave in the near field region of a dipole (b) wave impedance in front of a dipole.

3.4.2 TEM-T CELL AS A SOURCE OF NEAR E-FIELD

The field simulated by the modified TEM-T cell would be Transverse Magnetic (TM) and exhibits high impedance in the near region which are the requirements of near E-field SE measurement. Analysis of the field simulated by the TEM-T cell test device in the new configuration requires an understanding of the radiated field from an open-ended coaxial line. The incident field on the test sheet, in front of such an open ended coaxial structure, can be analysed by a method described by numerous authors, who investigated the application of open ended coaxial lines or two port coaxial cells for the determination

of constitutive parameters of different materials (mostly dielectric) [139]-[143]. The open end of a TEM-T cell half may be treated as an aperture antenna. The rectangular aperture which caps the open end of this half is the main source of radiation. Although not ideal, the flange at the open mouth of the outer conductor acts as a ground screen (an ideal ground screen should be infinite in extent).

The analysis begins with the exact expression of the aperture field of the TEM-T cell and by the application of Huygens' principle this is then expressed in terms of equivalent magnetic and/or electric current sheets. These sources constitute the vector electric and magnetic potentials ($\bar{F}$ and $\bar{A}$). The radiated field may then be determined from the vector potentials.

3.4.2.1 Aperture Field

The geometry of the transmitting half of a TEM-T cell is shown in Fig. 3.12. The x-y plane of the co-ordinate system is at its open face and the origin is at the middle of the center conductor. Because of the symmetry, knowledge of the aperture field in the first quadrant is enough to determine the total aperture field.

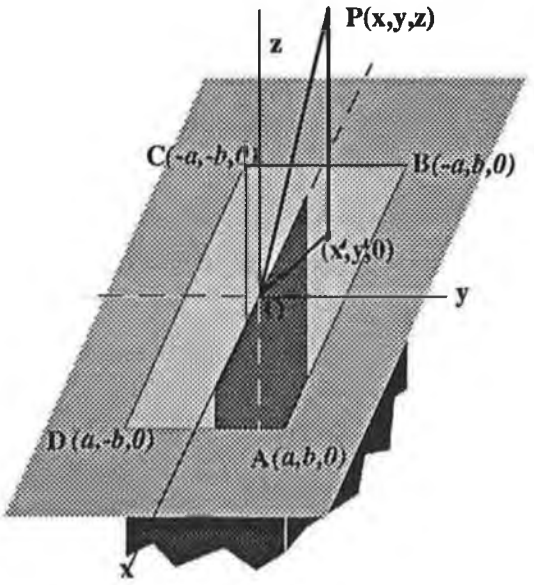

Fig. 3.12 Geometry of the aperture of the transmitting half of a TEM-T cell as source of radiation.

Due to the abrupt transition from 50 Ω (the characteristic impedance of the coaxial line) to open circuit, there would be reflections at the open mouth. Close to the

open end, the field structure becomes very complicated due to the presence of the evanescent higher order modes, but to the first approximation the effect of these higher order-modes may be neglected as long as the transverse dimensions of the coaxial line are smaller than the wavelength [144]. Hence even up to 1 GHz (λ = 30 cm) this assumption is valid in our analysis (the transverse dimension of the TEM-T cell is 30×15 cm). Thus only the principal propagating mode is assumed at the aperture ABCD of the open end.

An exact expression of the electric field of the principal TEM mode inside a TEM cell with very thin inner conductor has been developed by Tippet *et al.* [145],

$$E_t = \frac{Vm}{K'(\alpha)} \frac{jdn(mz,k)}{[P_0(z)]^{1/2}} \tag{3.4.2}$$

where V = the total voltage at the septum (incident plus reflected) and

α = sn(mw,k), the Jacobian elliptic function of modulus k,

$$K'(\alpha) = \int_0^1 \frac{dt}{\sqrt{(1-t^2)\left(1-(1-\alpha^2)t^2\right)}}$$

$$m = \frac{K(k)}{a} = \frac{K'(k)}{b} \tag{3.4.3}$$

$$P_0(z) = sn^2(mw,k) - sn^2(mz,k)$$

dn(mz,k) is the Jacobian elliptic function of another form defined as $\sqrt{1-k^2 sn^2(mz,k)}$

j = $\sqrt{-1}$ and here indicates the phasor rotation of 90° to represent the y component.

The field is denoted by E_t, since it is tangential to the aperture. The definitions of the necessary Jacobian elliptic functions for complex arguments are given in Appendix C5 and the modulus k is determined from the requirement,

$$\frac{K(k)}{K(k')} = \frac{a}{b} \tag{3.4.4}$$

where *K(k)* is the complete elliptic integral of the first kind. The approximation of the existence of only the principal propagating mode (i.e. TEM mode) is valid inside a TEM cell up to the cut-off frequency of the first higher order mode (i.e., TE_{10} mode). This cut-off frequency can be computed from [146] as:

$$f_c = \frac{c}{2\pi}\left[\left(\frac{\pi}{2a}\right)^2 + \delta_{10}{}^2\right]^{1/2} \tag{3.4.5}$$

where δ_{10} is to be calculated from the equation

$$\cot(b\delta_{10}) = \frac{a\delta_{10}}{\pi}\left[\ln\left(\frac{8a}{\pi g}\right) - 2\right] \tag{3.4.6}$$

This equation was solved using Mathcad® [147] for the specific cell and δ_{10} was found to be $\delta_{10} \cong 20.5$. Hence the cut-off frequency was found to be approximately 1.0 GHz. Thus for $f<f_C$, we can reasonably assume that,

$$\bar{H}_t = \hat{x}H_x + \hat{y}H_y \tag{3.4.7}$$

with

$$H_x = -\frac{E_y}{\eta_0}$$

$$H_y = \frac{E_x}{\eta_0}$$

η_0 is the free space intrinsic impedance.

The electric and magnetic field configurations at the open mouth of the specific TEM-T cell have been computed from Eqns. (3.4.2) and (3.4.7) and are shown as vector plots in Fig. 3.13.

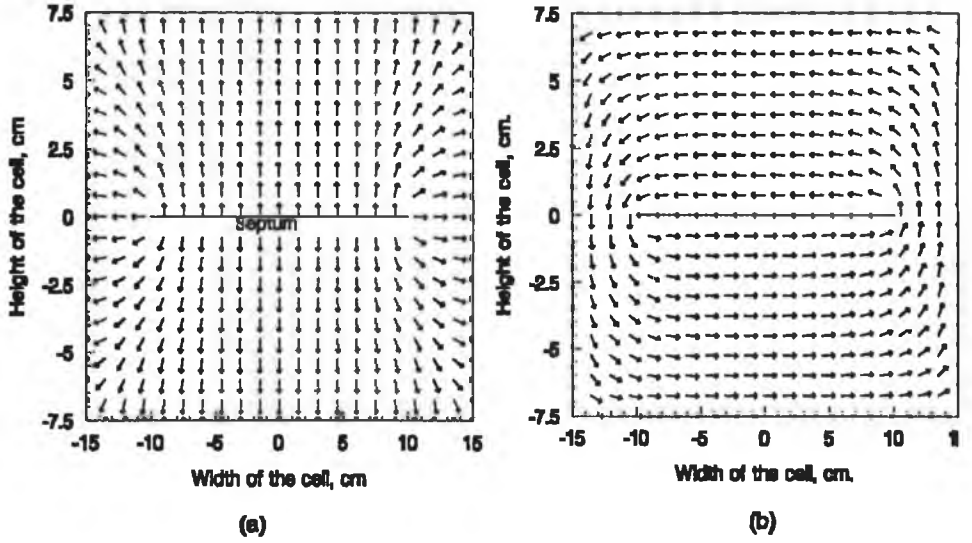

Fig. 3.13 Field configurations at the open mouth of a TEM-T half; (a) Electric field (b) Magnetic field.

3.4.2.2 Fields as Source of Radiation

According to Huygen's principle (Field Equivalence Principle), any wave front can be considered as the source of secondary waves that add to produce distant wave fronts. Thus knowing the field distribution over an aperture should yield the radiated field in front of the aperture.

Consider the rectangular aperture ABCD of the open mouth of the TEM-T cell lying in the x-y plane as shown in Fig. 3.12. The tangential components of the aperture fields E_t and H_t given by Eqns. (3.4.2) and (3.4.7) may be replaced by their equivalent magnetic and electric current sheets respectively over the aperture ($-a \le x' \le a$, $-b \le y' \le b$ and $z = 0$) as follows

$$\begin{aligned} \vec{M}_s(x',y') &= -\hat{z} \times \vec{E}_t(x',y') \\ \vec{J}_s(x',y') &= \hat{z} \times \vec{H}_t(x',y') \end{aligned} \tag{3.4.8}$$

The resulting electric and magnetic vector potentials at the observation point P(x,y,z), can then be found from these current densities

$$\begin{aligned} \vec{F}(x,y,z) &= \frac{\varepsilon}{4\pi} \int_{x'=-a}^{a} \int_{y'=-b}^{b} \frac{\vec{M}_s(x',y') e^{-j\beta\sqrt{[(x-x')^2+(y-y')^2+z^2]}}}{\sqrt{[(x-x')^2+(y-y')^2+z^2]}} dx'dy' \\ \vec{A}(x,y,z) &= \frac{\mu}{4\pi} \int_{x'=-a}^{a} \int_{y'=-b}^{b} \frac{\vec{J}_s(x',y') e^{-j\beta\sqrt{[(x-x')^2+(y-y')^2+z^2]}}}{\sqrt{[(x-x')^2+(y-y')^2+z^2]}} dx'dy' \end{aligned} \tag{3.4.9}$$

The radiated fields at point P(x,y,z) into the free space may be evaluated from these vector potentials as [148]

$$\begin{aligned} \vec{E}(x,y,z) &= \vec{E}_A + \vec{E}_F = \left[-j\omega\vec{A} - j\frac{1}{\omega\mu\varepsilon}\nabla(\nabla.\vec{A}) \right] + \left[-\frac{1}{\varepsilon}\nabla\times\vec{F} \right] \\ \vec{H}(x,y,z) &= \vec{H}_A + \vec{H}_F = \left[\frac{1}{\mu}\nabla\times\vec{A} \right] + \left[-j\omega\vec{F} - j\frac{1}{\omega\mu\varepsilon}\nabla(\nabla.\vec{F}) \right] \end{aligned} \tag{3.4.10}$$

But as the open end of the TEM-T cell has a large conducting screen (flange), the radiated field would exist only in the positive z-direction and only the electric vector potential would contribute to the radiation. The electric current sheet and its image

would cancel out while the magnetic current density is to be doubled to account for the image effect [125]. Thus the radiated field in front of the open end of the cell will be given by

$$\vec{E}(x,y,z)=\left[-\frac{1}{\varepsilon}\nabla\times 2\vec{F}\right]$$
$$\vec{H}(x,y,z)=2\left[-j\omega\vec{F}-j\frac{1}{\omega\mu\varepsilon}\nabla(\nabla.\vec{F})\right] \qquad (3.4.11)$$

The radiated electromagnetic field in the near field region is calculated (see Appendix C11 for computer program) from Eqns. (3.4.2), (3.4.7), (3.4.9) and (3.4.11) and the vector plot is shown in Fig. 3.14(a), from which it is evident that the field very close to the open end of a TEM-T half is essentially TM (transverse magnetic) in nature.

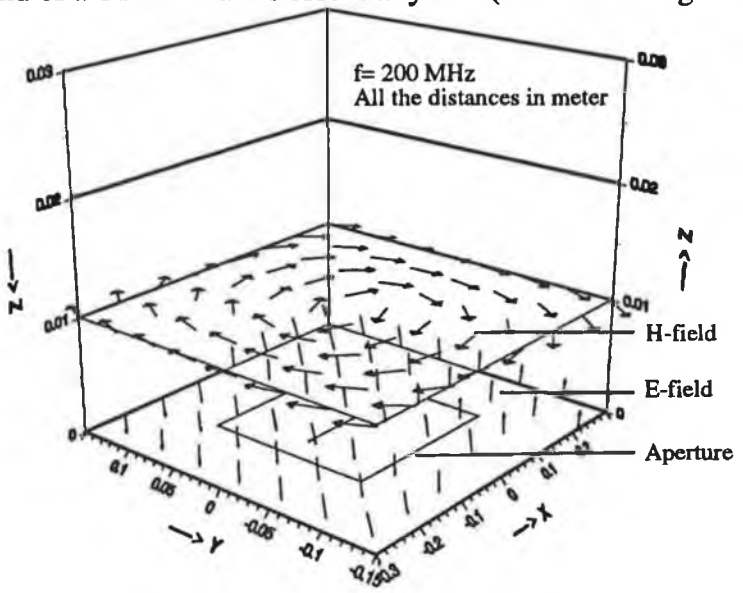

(a)

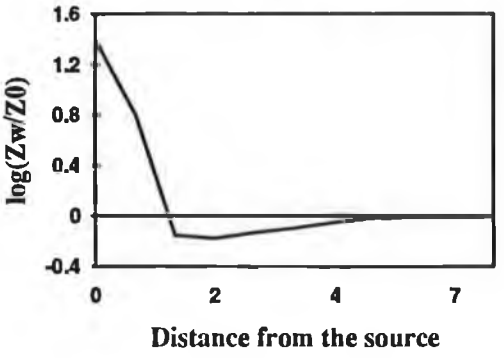

(b)

Fig. 3.14 Properties of the EM wave in front of the TEM-T half (a) TM wave in the near field region of a TEM-T cell (b) Wave impedance axially in front of a TEM-T cell half acting as a transmitter (distance is normalized to $\lambda/2\pi$, where λ is the wavelength).

The plot of the wave impedance in front of a TEM-T half is also shown in Fig. 3.14(b), where it is found that the wave resembles the high impedance field of a dipole radiator (near field). For a better understanding, this field distribution and the wave impedance profile may be compared with those of the short dipole radiator, shown in Fig. 3.11.

3.4.3 RADIATION PATTERN OF TEM-T CELL HALF

The transmitting half of the TEM-T cell as described earlier in section 2.7, may be treated as an antenna which resembles the family of the stub antennas over a ground plane [126, Sec.16-5] or sleeve antennas [126, Sec.16-6]. This has similarity with open ended rectangular waveguide (OEG) antennas [149], except that the aperture field at the open end is TEM instead of TE. The radiation pattern of this antenna is of directional type and thus it may be very useful in EMC measurements. The radiation pattern and other important antenna parameters of this radiator can be determined analytically by the application of Huygen's principle, described earlier.

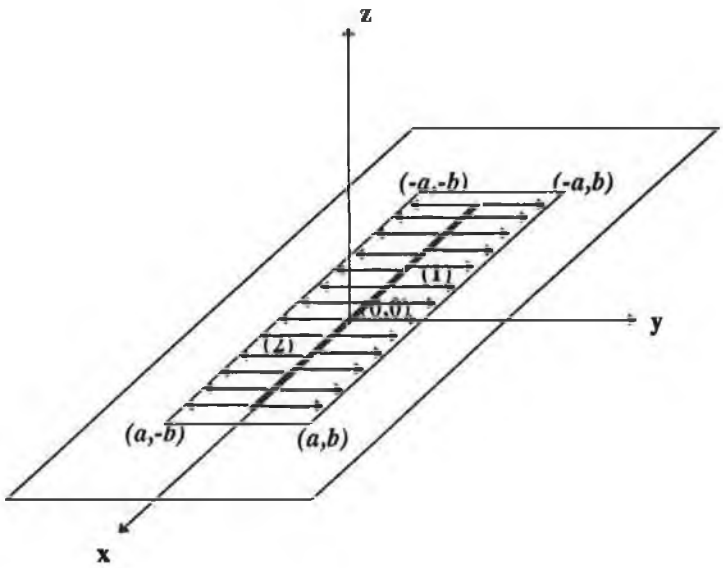

Fig. 3.15 Electric field lines for simplified model of TEM-T transmitting half radiation pattern.

The radiation pattern of the TEM-T cell half which is acting as a transmitting antenna can be analyzed by assuming a simplified model of the aperture field at the open mouth. The analysis begins with the approximation that the electric field lines originate from the septum and terminate at the outer conductor as mutually parallel straight lines.

As shown in Fig. 3.15, in the upper half of the aperture these lines are directed along the positive $\hat{y}$ axis while in the lower half of the aperture along the negative $\hat{y}$ axis.

Then as a second approximation the electric field at the aperture will be expressed as that appearing between two parallel plates having potential difference of V and separated by a distance d. Thus in the upper half of the aperture the electric field may be considered as,

$$E = \hat{y}E_o \cong \hat{y}\frac{V}{b} \tag{3.4.12}$$

Then with TEM wave approximation for the aperture field the magnetic field is given by

$$\bar{H} = -\hat{x}H_o \cong -\hat{x}\frac{E_0}{\eta_0} = -\hat{x}\frac{V}{b\eta_0} \tag{3.4.13}$$

Now from the field equivalence principle, the equivalent current sheets are

$$\begin{aligned} \bar{J} &= \hat{n}\times\bar{H} = -\hat{z}\times\hat{x}\frac{V}{b\eta} = -\hat{y}\frac{V}{b\eta} \\ \bar{M} &= \hat{n}\times\bar{E} = \hat{z}\times\hat{y}\frac{V}{b} = -\hat{x}\frac{V}{b} \end{aligned} \tag{3.4.14}$$

and with paraxial approximation, the far-zone field (where far-zone is defined by $z \geq \frac{2D^2}{\lambda}$, D is the largest dimension of the aperture, here D = 2a and λ is the operating wavelength) is given by [85, section 12.13],

$$\bar{E}(x,y,z) = \frac{je^{-jkr}}{\lambda r}\iint_{s'}\bar{E}(x',y')e^{jk(xx'+yy')/r}dx'dy' \tag{3.4.15}$$

where $\bar{E}(x',y')$ represents the electric field at an arbitrary point (x',y') in the aperture and $j=\sqrt{-1}$. Now the differential field due to an elementary aperture in the upper half of the TEM-T open face,

$$d\bar{E}_u = \hat{y}\frac{j}{\lambda}\frac{E(x',y')e^{-jkr_u''}}{r_u''}dx'dy' \tag{3.4.16}$$

where,

$$r_u'' = \left[(x-x')^2+(y-y')^2+z^2\right]^{1/2}$$

$$\cong r\left[1-2(xx'+yy')/r^2\right]^{1/2}$$
$$\cong r-(xx'+yy')/r \quad (\text{for phase consideration})$$
$$\cong r \quad (\text{for amplitude consideration})$$

Similarly, the radiated field due to an elementary aperture in the bottom half of the TEM-T open face is

$$d\bar{E}_l = -\hat{y}.\frac{j}{\lambda}\frac{E(x'-y')e^{-jkr_l''}}{r_l''}dx'dy' \qquad (3.4.17)$$

where,

$$r_l''=\left[(x-x')^2+(y+y')^2+z^2\right]^{1/2}$$
$$\cong r\left[1-2(xx'-yy')/r^2\right]^{1/2}$$
$$\cong r-(xx'-yy')/r \quad (\text{for phase consideration})$$
$$\cong r \quad (\text{for amplitude consideration})$$

The above assumptions for distance considerations are accepted in most of the texts on antennas [126], [151] and electromagnetism [85].

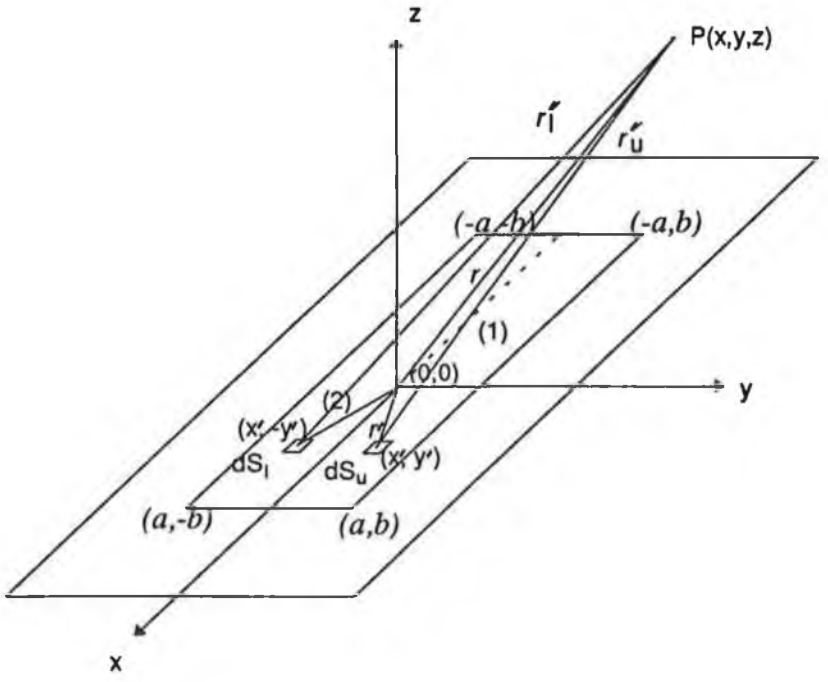

Fig. 3.16 Geometry of the aperture of TEM-T half radiating in free space.

Thus the differential field due to a pair of elementary apertures, one in the upper half and the other in the bottom half of the TEM-T open face is

$$
\begin{aligned}
d\vec{E} &= d\vec{E}_u + d\vec{E}_l \\
&= \hat{y}.\frac{j}{\lambda}E_0\frac{e^{-jkr}}{r}\left[e^{jk(xx'+yy')/r} - e^{jk(xx'-yy')/r}\right]dx'dy' \\
&= \hat{y}.\frac{j}{\lambda}E_0\frac{e^{-jkr}}{r}e^{jkxx'/r}.2j\sin(kyy'/r)dx'dy'
\end{aligned}
\tag{3.4.18}
$$

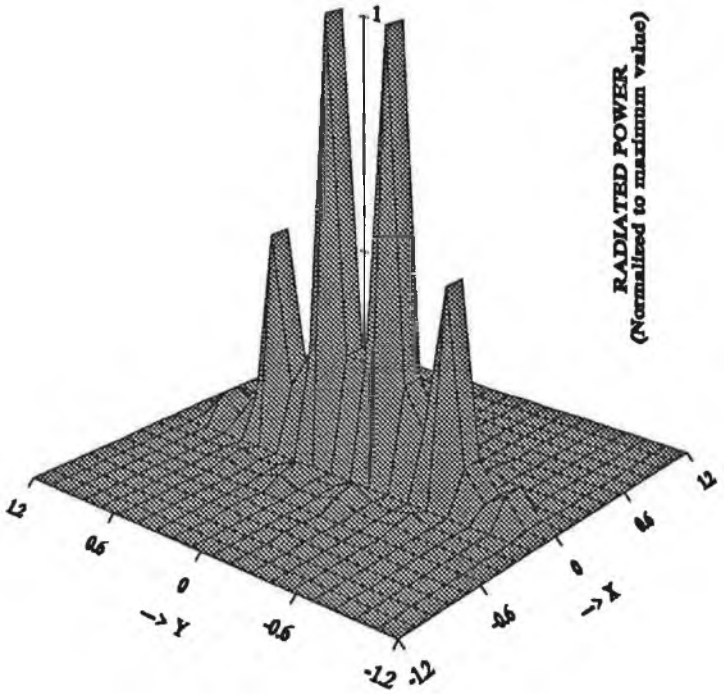

Fig. 3.17 Radiation pattern of the TEM-T half (relative power pattern). In order to show the over all beam width, x and y axes have been expanded away from the flange dimensions. The pattern has been plotted at z = 1 m, at a frequency of 1 GHz.

because of the symmetry,

$$
\begin{aligned}
E(x,y,z) &= -\frac{2}{\lambda}E_0\frac{e^{-jkr}}{r}\int_{-a}^{a}e^{jkxx'/r}dx'\int_{o}^{b}\sin\left(\frac{kyy'}{r}\right)dy' \\
&= -\frac{2E_0e^{-jkr}}{\lambda r}2a\,\mathrm{sinc}\left(\frac{kax}{r}\right)\left[1-\cos\left(\frac{kby}{r}\right)\right]\frac{r}{ky} \\
&= -\frac{4abE_0e^{-jkr}}{\lambda r}\mathrm{sinc}\left(\frac{kax}{r}\right)\mathrm{sinc}\left(\frac{kby}{r}\right)\sin\left(\frac{kby}{2r}\right)
\end{aligned}
\tag{3.4.19}
$$

and this field will be y-directed. In the far field region the magnetic field will be given by

$$H(x,y,z) = \frac{4abE_0 e^{-jkr}}{\lambda r \eta} sinc\left(\frac{kax}{r}\right) sinc\left(\frac{kby}{r}\right) sin\left(\frac{kby}{2r}\right) \qquad (3.4.20)$$

and this field will be x directed. Thus the average radiated power can be computed from the complex Poynting vector $\vec{S} = \frac{1}{2}\left(\vec{E} \times \vec{H}^*\right)$ as

$$P_{av} = \frac{8}{\eta}\left(\frac{abE_0}{\lambda r}\right)^2 sinc^2\left(\frac{kax}{r}\right) sinc^2\left(\frac{kby}{r}\right) sin^2\left(\frac{kby}{2r}\right) \qquad (3.4.21)$$

Fig. 3.17 illustrates the approximate radiation pattern. Relative power pattern (normalized to the maximum) has been plotted. The radiated field pattern is also plotted in Fig. 3.18 and this will later be compared with the measured pattern in chapter 6.

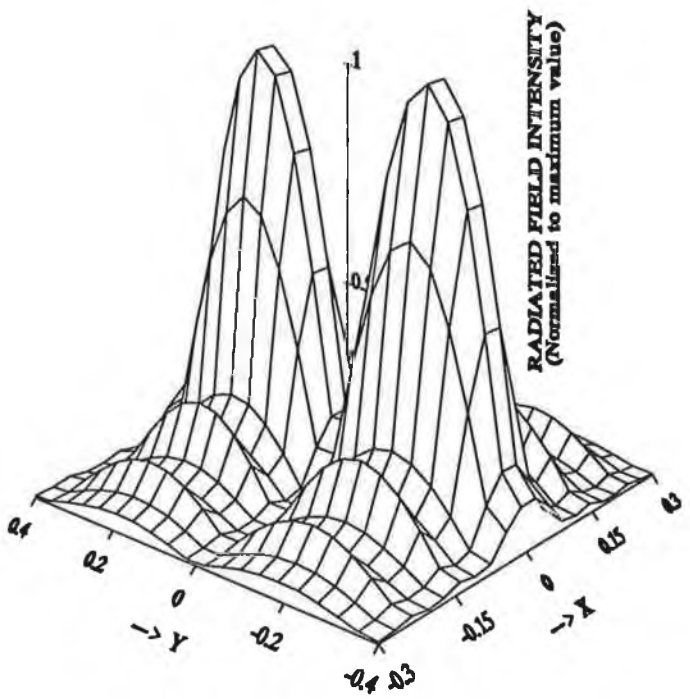

Fig. 3.18 Radiation pattern of the TEM-T half (relative field intensity pattern). Radiation along y-direction is significant even away from the perimeter (-0.15 to +0.15 m) of the flange, so the axis limit is extended in that direction. The pattern has been plotted at z = 1 m, at a frequency of 1 GHz. All the dimensions along the x- and y- axes indicated in the diagram are in meters.

From Fig. 3.18, it is evident that the radiation level is significantly reduced just beyond the perimeters of the flange (The flange lies between -0.3 to 0.3 meter along x-axis and between -0.15 to 0.15 meter along y-axis). This interesting feature proved to be very useful in a contact-less SE measurement system which will be discussed later in chapter 5. A pair of large shoots centred around the two segments of the aperture are evident as the septum divides the rectangular aperture into two identical sections.

3.4.4 ANTENNA PARAMETERS OF THE TEM-T CELL HALF

Only a few important antenna parameters are deduced analytically for the TEM-T half. Directivity, gain and input impedance of the TEM-T half are determined. These parameters of the TEM-T half are determined on the basis of the simplifying assumptions presented in the analysis of the previous section.

3.4.4.1 Directivity

The directivity is an indicator of the relative directional properties of the antenna. Usually the directional properties of the antenna are determined by comparing with an isotropic radiator. It is defined as the ratio of the radiation intensity in a given direction from the antenna to the radiation intensity averaged over all directions (or in other words the radiation intensity if it were an isotropic radiator). If P_r is the total radiated power then the average radiation intensity in all directions is given by

$$U_{av} = U_{iso} = \frac{P_r}{4\pi} \quad \ldots \quad \ldots \quad (3.4.22)$$

where 4π sr is the solid angle subtended by a sphere. Thus the directivity in any direction θ,ϕ is

$$D = \frac{U(\theta,\phi)}{U_{av}} = \frac{4\pi U(\theta,\phi)}{P_r} \quad \ldots \quad \ldots \quad (3.4.23)$$

where $U(\theta, \phi)$ is the radiation intensity in the direction (θ, ϕ). Usually it refers to the direction of maximum intensity which is specified as $U_m(\theta, \phi)$.

The determination of directivity begins with the calculation of the total power radiated by the antenna, which requires knowledge of the average Poynting vector, S_r at a distant point from the antenna. The expression for S_r is

$$S_r = \frac{1}{2}\Re e\left(\vec{E} \times \vec{H}^*\right) \tag{3.4.24}$$

In order to get the radial Poynting vector it is essential to determine the E_θ and H_ϕ components of the electric and magnetic fields. They can be obtained from the E_y and H_x components expressed by the Eqns. (3.4.19) and (3.4.20) where,

$$\begin{aligned} E_\theta &= E_y \sin\theta \sin\phi \quad \text{and} \\ H_\phi &= -H_x \sin\phi \end{aligned} \tag{3.4.25}$$

Determining E_θ and H_ϕ and substituting them in Eqn. (3.4.26), and then performing the following integration

$$P_r = \int_{\theta=0}^{\pi} \int_{\phi=0}^{2\pi} S_r r^2 \sin\theta d\theta d\phi \tag{3.4.26}$$

one can obtain the total power radiated by the TEM-T half. Since it is assumed in the analysis that the radiation occurs only in the semi-infinite region in front of the TEM-T half, in order to calculate the total radiated power, integration is to be performed only on the hemisphere where θ varyies from 0 to π and ϕ varyies from 0 to 2π. Now substituting P_r from Eqn. (3.4.26) and the maximum radiation intensity, which can be obtained from Eqn (3.4.21) as

$$U(\theta,\phi) = \frac{8}{\eta}\left(\frac{abE_0}{\lambda r}\right)^2 \tag{3.4.27}$$

in Eqn. (3.4.23), the directivity of the TEM-T half radiator can readily be found .

3.4.4.2 Input impedance

The input impedance of the TEM-T half shown in Fig. 3.12, can be determined after expressing the field in the semi infinite free space region in front of the half in terms of the aperture fields at z = 0. For the purposes of impedance calculations it may be assumed that only the principal waveguide mode is present at the aperture [150].

The principal propagating mode in the TEM-T cell half is TEM which propagates in the positive z direction. As described earlier in section 3.4.2.1, in fact there are also reflected waves near the open mouth of this half because of the abrupt transition of impedance which would generate higher order modes in the half as well. Obviously,

these higher order modes will be of evanescent nature and would die out travelling only a small distance into the cell half. The fields, very close to the open mouth into the cell half would be a superposition of principal TEM and TE and TM higher order modes. TE and TM modes can be derived from the Hertz scalar functions Ψ and Φ respectively.

The scalar functions are derived for the rectangular coaxial waveguide structure of the TEM-T half (the derivations are given in Appendix C7) by expressing them as a superposition of a complete set of basis functions Ψ_{mn} and Φ_{mn} (m and n are integers and vary up to infinity). They are from Eqns. (C7-5) and (C7-7) and with assumed $e^{-j\omega t+\gamma z}$ (time and space) variations

$$\Psi = \sum_{m,n} A_{mn} \cos\left(\frac{m\pi}{2a}(x+a)\right)\cos\left(\frac{n\pi}{b}y\right)e^{-j\omega t-\gamma_{mn}z} \tag{3.4.28}$$

and,

$$\Phi = \sum_{m,n} B_{mn} \sin\left(\frac{m\pi}{2a}(x+a)\right)\sin\left(\frac{n\pi}{b}y\right)e^{-j\omega t-\gamma_{mn}z} \tag{3.4.29}$$

where A_{mn} and B_{mn} are the unknown amplitudes. The reflected waves would move backward into the cell half and as such $e^{-\gamma_{mn}z}$ is considered in the above equations. γ_{mn} are the propagation constants of higher order modes.

The radiated field components in the free space are related to these scalar functions by the set of Eqns. (C6-3) and (C6-4) presented in Appendix C6. After multiplying (C6-3a) with $\cos\left(\frac{m\pi}{2a}(x+a)\right)\sin\left(\frac{n\pi y}{b}\right)$ and (C6-3b) with $\sin\left(\frac{m\pi}{2a}(x+a)\right)\cos\left(\frac{n\pi y}{b}\right)$ and then integrating over the aperture at z = 0, it follows that

$$A_{mn} = \frac{2\varepsilon_{m}\left(\frac{m\pi}{2a}\right)}{j\omega\mu_0 ab\left(\left(\frac{m\pi}{2a}\right)^2+\left(\frac{n\pi}{b}\right)^2\right)}\iint E_y \cos\left(\frac{m\pi}{2a}(x'+a)\right)\sin\left(\frac{n\pi}{b}y'\right)dx'dy'$$

$$B_{mn} = \frac{2\varepsilon_{m}\left(\frac{n\pi}{b}\right)}{\gamma_0 ab\left(\left(\frac{m\pi}{2a}\right)^2+\left(\frac{n\pi}{b}\right)^2\right)}\iint E_y \sin\left(\frac{m\pi}{2a}(x'+a)\right)\cos\left(\frac{n\pi}{b}y'\right)dx'dy' \tag{3.4.30}$$

... ...

where

ε_m =1 for m = 0

and ε_m =2 for m ≠ 0

After substituting Ψ and Φ in Eqn. (C6-4a), the magnetic field component H_x can be obtained as

$$H_x = A_0\left(e^{j\beta_0 z} - \rho e^{-j\beta_0 z}\right) + \sum_{m=1}^{\infty}\sum_{n=1}^{\infty}\left(A_{mn}\gamma_{mn}\left(\frac{m\pi}{2a}\right)\sin\left(\frac{m\pi}{2a}(x'+a)\right)\cos\left(\frac{n\pi}{b}y'\right) - j\omega\varepsilon B_{mn}\left(\frac{n\pi}{b}\right)\sin\left(\frac{m\pi}{2a}(x'+a)\right)\cos\left(\frac{n\pi y'}{b}\right)\right)e^{-\gamma_{mn}z} \quad \text{(3.4.31)}$$

where A_0 is the amplitude of the principal TEM mode, β_0 is the free space wave number, ρ is reflection coefficient of the TEM-T half at the open mouth, and A_{mn} and B_{mn} are given by Eqn.(3.4.30). Therefore, H_x can be expressed in terms of the integral of the aperture electric field $E_y(x', y')$ on the aperture. The expression for H_x can also be obtained in terms of the aperture electric field (according to Huygens' principle) as follows

$$H_x(x,y) = \frac{2j}{4\pi\omega\mu_0}\iint dx'dy' E_y(x',y')\left(k^2 + \frac{\partial^2}{\partial x^2}\right)\frac{e^{jkr}}{r} \quad \text{(3.4.32)}$$

the multiplier 2 in the numerator is due to the image effect of the flange at the face. It is to be noted here that (x′,y′) denotes a point at the open mouth of the TEM-T half and (x,y) denotes a point in free space, so $r = \left[(x-x')^2 + (y-y')^2 + z^2\right]^{\frac{1}{2}}$.

Due to the continuity of the tangential components of the magnetic field at the boundary, this H_x at the aperture (z = 0), is equal to that obtained through Eqn. (3.4.31). However, to determine A_O, it is necessary to express E_y in terms of H_x. The electric and magnetic fields are related as

$$-j\omega\varepsilon E_y = \frac{\partial H_x}{\partial z} \quad \text{(3.4.33)}$$

thus

$$E_y = -\frac{\beta_0}{j\omega\varepsilon}A_0\left(e^{j\beta_0 z} + \rho e^{-j\beta_0 z}\right) + \frac{\gamma_{mn}}{j\omega\varepsilon}\sum_{m=1}^{\infty}\sum_{n=1}^{\infty}\left(A_{mn}\gamma_{mn}\left(\frac{m\pi}{2a}\right)\sin\left(\frac{m\pi}{2a}(x'+a)\right)\cos\left(\frac{n\pi}{b}y'\right) - j\omega\varepsilon B_{mn}\left(\frac{n\pi}{b}\right)\sin\left(\frac{m\pi}{2a}(x'+a)\right)\cos\left(\frac{n\pi y'}{b}\right)\right)e^{-\gamma_{mn}z} \quad \text{(3.4.34)}$$

From this expression of E_y it is possible to find A_o in terms of electric field at the open mouth of the TEM-T half (z=0), as follows

$$j\omega\varepsilon E_y(x',y') = -\beta_0 A_0(1+\rho) + \gamma_{mn}\sum_{m=1}^{\infty}\sum_{n=1}^{\infty}\left(A_{mn}\gamma_{mn}\left(\frac{m\pi}{2a}\right)\sin\left(\frac{m\pi}{2a}(x'+a)\right)\cos\left(\frac{n\pi}{b}y'\right)\right.$$
$$\left. - j\omega\varepsilon B_{mn}\left(\frac{n\pi}{b}\right)\sin\left(\frac{m\pi}{2a}(x'+a)\right)\cos\left(\frac{n\pi y'}{b}\right)\right) \tag{3.4.35}$$

The normalized impedance of the TEM-T half at its open mouth is given by,

$$Z_{norm} = \frac{1+\rho}{1-\rho} \tag{3.4.36}$$

where the normalization is made in terms of the characteristic impedance of the rectangular coaxial structure of the TEM-T half which is 50 Ω in the present analysis. Substituting for A_o from Eqn. (3.4.35) in (3.4.31), and equating (3.4.31) and (3.4.32) at the aperture, and then comparing with (3.4.36), one can obtain

$$Z_{norm} = \frac{j\omega\varepsilon E(x',y') - \Lambda'(m,n)}{\beta_0\left[\frac{j}{2\pi\omega\mu_0}\iint dx'dy'E(x',y')\left(k^2+\frac{\partial^2}{\partial x^2}\right)\frac{e^{jkr}}{r} + \Lambda(m,n)\right]} \tag{3.4.37}$$

where, $\Lambda'(m,n)$ is the term containing the summation of two infinite series of m and n of the R.H.S of Eqn. (3.4.35) and $\Lambda(m,n)$ is the similar term of R.H.S of Eqn. (3.4.31). They have arisen because of the higher order modes. A simplified expression can be derived by substituting for $E(x', y')$ from Eqn. (3.4.12) into Eqn. (3.4.37).

The double integration of the denominator of Eqn. (3.4.37) represents integration over the aperture of the open mouth of the TEM-T half, i.e. x varying from $-a$ to a and y varying from $-b$ to b and because of the symmetry the integrations can be performed over one quarter and then the result should be multiplied by 4 in order to get the total integration over the aperture.

3.4.4.3 Gain

The gain of an antenna can be expressed in terms of the directivity (where directivity is measured in the direction of maximum intensity) and the radiation efficiency as follows:

$$G = \eta_r D \tag{3.4.38}$$

where the radiation efficiency η_r arises as there are some ohmic losses on the antenna structure. For most aperture antennas the ohmic losses are very small, so $\eta_r \approx 1$ and therefore $G \approx D$ [151, pp. 394]. Obviously the assumption is that the antenna is matched to the feed network.

3.5 NEAR H-FIELD SIMULATION BY Q-LOOP ANTENNA

In the present analysis a newly developed quasi-shielded probe called Q-loop is used for the purpose of simulating near H-field on the MUT sheet. A full loop antenna produces dominant H-field in its near region; the characteristics of such field, and the similarity of the field produced by Q-loop antenna are discussed in the following sub-sections. A few other important parameters of this new antenna are also analyzed in this context.

3.5.1 CHARACTERISTICS OF NEAR H-FIELD SOURCE

An ideal example of low impedance field is the radiated field available in the near region of a small loop antenna. The radiated field of a small loop of radius a ($a \leq \lambda/10$) carrying a uniform current $I_0 e^{j\omega t}$ can be expressed as [15]:

$$\begin{aligned} H_r &= \frac{\pi a^2 I_0 e^{j(\omega t-\beta r)} \cos\theta}{4\pi r}\left[\frac{2j\beta}{r}+\frac{2}{r^2}\right] \\ H_\theta &= -\frac{\pi a^2 I_0 e^{j(\omega t-\beta r)} \sin\theta}{4\pi r}\left[\beta^2-\frac{j\beta}{r}-\frac{1}{r^2}\right] \\ E_\phi &= -\frac{j\omega\mu_0 \pi a^2 I_0 e^{j(\omega t-\beta r)} \sin\theta}{4\pi r}\left[j\beta+\frac{1}{r}\right] \end{aligned} \tag{3.5.1}$$

It is evident from the above equations that at a large distance where $r>>\lambda$, terms containing $1/r^2$ and $1/r^3$ may be neglected compared to the term containing $1/r$. Thus in the far field region the radiated field of a loop antenna is TEM containing only H_θ and E_ϕ components. Close to the loop, the terms in $1/r^2$ and $1/r^3$ dominate over the $1/r$ terms, and the region is known as its "near field". In this region magnetic field has both radial and polar components, the electric field, on the contrary, has the azimuth component only. Thus the wave appears to be transverse electric (TE) in nature. At the same time the impedance of this EM wave in this region is smaller than that of the plane wave (hence a low impedance wave). The field distribution and the wave impedance is shown in Fig. 3.19(a) and (b).

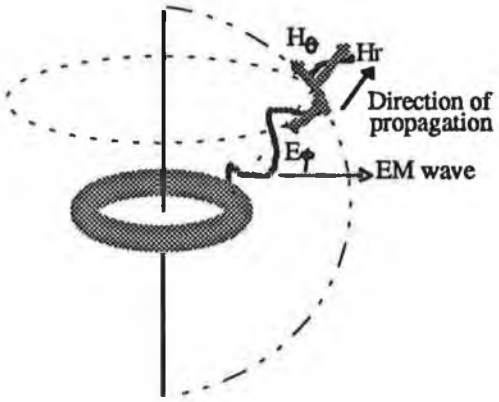

(a)

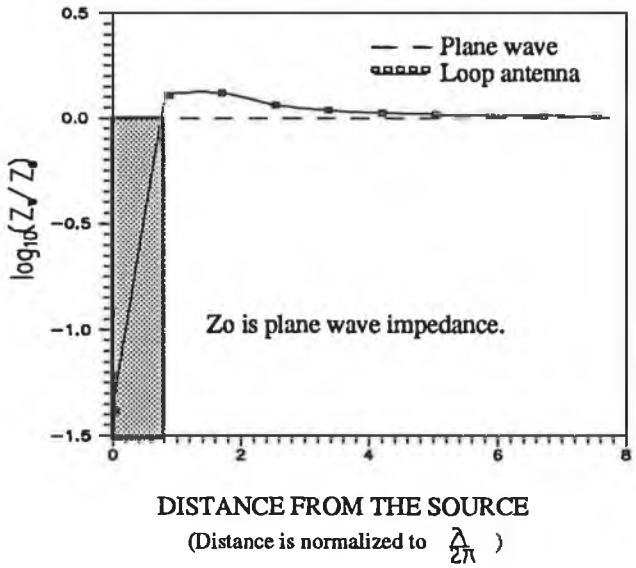

(b)

Fig. 3.19 (a) Radiated field in the near region of a loop antenna (b) Wave impedance of this field (Shaded region represents the low impedance wave).

3.5.2 Q-LOOP ANTENNA AS NEAR H-FIELD SOURCE

Reflectors can improve the directional property of an antenna as well as amplifying radiation from it, viz. a large flat metallic sheet reflector can convert a bi-directional antenna into an unidirectional one. With two such flat sheets intersecting at an angle $<180^{o}$, a sharper radiation pattern can be achieved. This arrangement, referred to as Krauss reflector when designed to have a corner angle of 90^{o}, acts as a retroreflector [126, Chap. 12]. An interesting observation is that a quarter of a loop, placed in front of

a 90^{o} Krauss reflector is equivalent to a complete loop in free space. The systems are equivalent only in a sense that the fields in front of the reflector are identical but at the same time there would be no field components available behind the reflector.

The field pattern of such an antenna system can be studied analytically as follows: the field due to the arc (quarter of a loop) is calculated first and then applying image theory the images of the arc are determined. The effect of these images on the field of the original quarter loop are then superimposed by a method similar to pattern multiplication. The approach is described in the following sections.

3.5.2.1 Images of a Quarter Loop In front of a Corner Reflector

The well known boundary condition of a vanishing tangential component of electric field at the surface of a good conductor constitutes the basic principle of reflection. The reflection behaviour of a Krauss reflector can easily be determined by employing image theory, which states that an ideal dipole oriented normal in front of a perfect ground plane can be replaced by the dipole itself and an image dipole, equidistant from the ground plane, oriented normal to it and carrying the same current in the same direction as the original one, both in free space. It also states that the image of an ideal dipole oriented parallel to the ground plane will be an equidistant dipole, oriented parallel but carrying an equal amount of current in the opposite direction to the original one. The perfectly conducting infinite ground plane in the image theory is of course an idealization. The perfectly conducting assumption is valid when good conductors such as aluminium or copper are used and, generally speaking, if the conducting plane extends beyond the source by several times the length of the source and if the source is not too far away from the conducting plane, then infinitely large plane assumption can also be applicable.

Krauss [126, Chap.12] analyzed the problem of a dipole oriented parallel in front of a 90^{o} corner reflector. Klopfenstien [152] tried it for arbitrary orientation of the dipole. Both of them suggested three images for one dipole to satisfy the boundary conditions as mentioned above. The same analysis can be extended for a quarter loop also, assuming that the quarter loop is composed of infinitesimal dipoles of length $ad\phi$ (such as the dipole at A shown in Fig. 3.20). Image theory straight away refers to the two images at A1 and A2 because of the reflectors OL and OL1. If we take the corner line as a reflector then the third image A3 is to be considered. Progressing in this way along the quarter loop, each infinitesimal dipole element of the arc would have three

images and eventually that would yield the other three quarters of the loop as the images of the original one. Hence the quarter loop in front of the corner reflector is equivalent to a complete loop in free space.

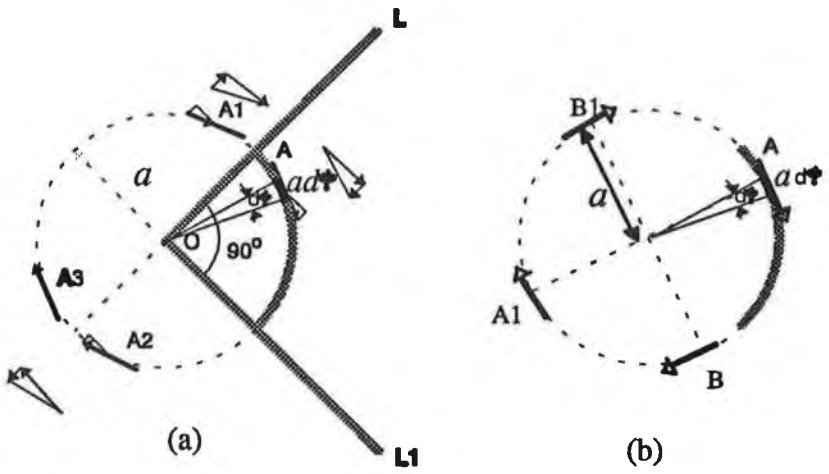

Fig. 3.20 (a) Images of an infinitesimal dipole in front of a corner reflector.
(b) Coplanar pairs of dipole orthogonal to each other.

However, image theory also states that the effect of the image would be experienced only above the ground plane and beneath the ground plane is the shadow region. Thus the Q-loop behaves as a complete loop only in front of the reflector with negligible field (ideally no radiation) behind.

3.5.2.2 Effect of the Images

The effect of the images on the radiation pattern of the quarter loop (original) may be analyzed by applying a method similar to the principle of pattern multiplication. This principle suggests that the radiation pattern of an array of similar elements (antennas) is given by the product of the element pattern and the array factor.

Let us consider an array of co-planar two pairs of dipoles (dipoles at points A and A1 and dipoles at points B and B1) as shown in Fig. 3.20(b). Dipoles of the pair are parallel to each other carrying equal and out of phase current while the lines connecting the dipoles of each pair are orthogonal to each other. Such a set of four dipoles is henceforth referred to as "quad dipoles". The far field pattern is computed starting from the formulation of vector magnetic potential and it is evident (see Appendix C8) that whatever may be the orientation of the quad dipoles with respect to the axes of co-ordinates, field intensities would be given by

$$E_{\phi quad} = 2j\beta a\sin\theta . E_{\phi element} \qquad (3.5.2)$$
$$H_{\theta quad} = 2j\beta a\sin\theta . H_{\theta element}$$

where $2j\beta a\sin\theta$ denotes the array factor. Since the quarter loop or $9\theta^{o}$ arc can be assumed to be a collection of infinitesimal dipoles (although oriented at different angles with the axes) as shown in Fig. 3.20, the same analysis can be extended for the original arc and its three similar images. Hence it is essential to find the radiation pattern for the element i.e. for the arc first and then multiply it with the array factor to get the resulting pattern.

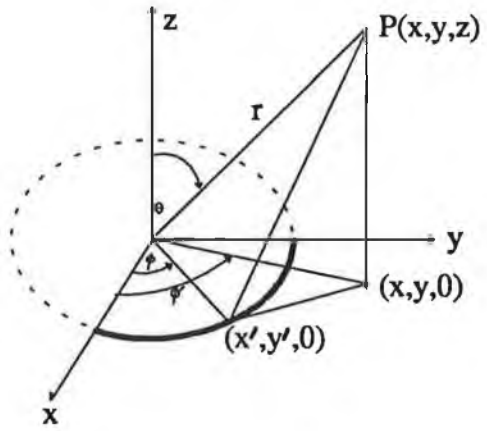

Fig. 3.21 Geometry of the 90^{o} arc of the Q-loop antenna in order to calculate the vector magnetic potential and the radiated field of the arc.

The arc geometry is shown in Fig. 3.21. Vector magnetic potential at a distant point $P(r,\theta,\phi)$ due to the arc is given by (see Appendix C9)

$$\bar{A}_{arc} = \frac{\mu[I]a}{4\pi r}\int_{0}^{\pi/2} e^{j\beta a\sin\theta\cos(\phi-\phi')}d\phi' \qquad (3.5.3)$$

It is difficult to perform the integration analytically but with certain approximations and for a small loop, i.e. $a << \lambda$(at least $a < \lambda/10$) and $\beta a << 1$, the definite integral of (3.5.3) appears to be $\approx \pi/2$(see Appendix C9), thus

$$\bar{A}_{arc} = \frac{\mu[I]a}{4\pi r}.\frac{\pi}{2}\bar{\phi} \qquad (3.5.4)$$

Hence the fields produced by the arc alone can be written as

$$E_{\phi arc} = -j\omega \frac{\mu[I]a}{4\pi r} \cdot \frac{\pi}{2} \qquad (3.5.5)$$

$$H_{\theta arc} = -j\beta \frac{\mu[I]a}{4\pi r} \cdot \frac{\pi}{2}$$

Now substituting (3.5.5) in (3.5.2), the net field in front of the reflector is obtained as

$$E_{\phi} = \frac{\mu\omega[I]a}{4r} \beta a . \sin\theta \qquad (3.5.6)$$

$$H_{\theta} = \frac{\beta[I]a}{4r} \beta a . \sin\theta$$

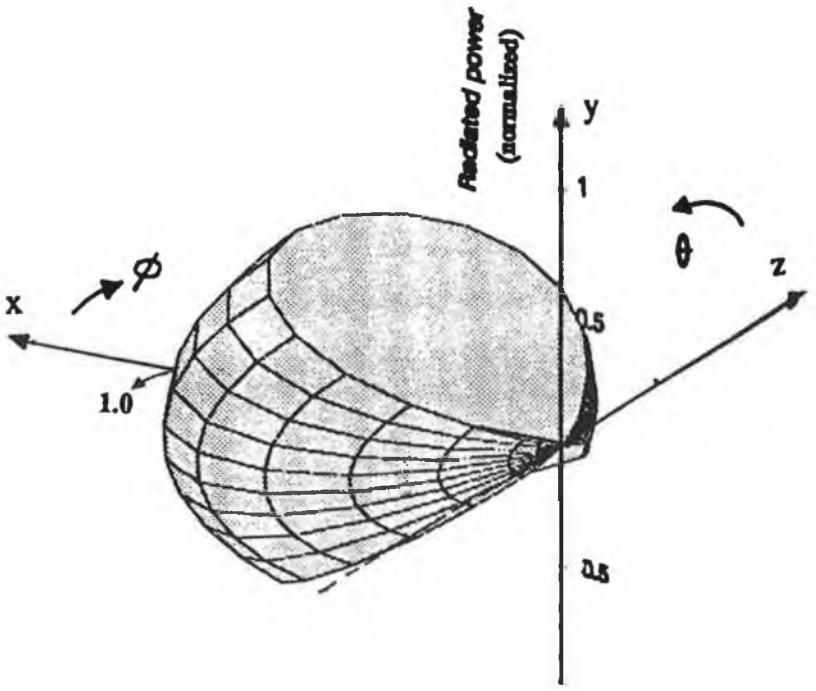

Fig. 3.22 Polar plot of the radiation pattern of the Q-loop antenna (approximate model using the method similar to pattern multiplication principle). The radial axis indicates the radiated power (normalized to the maximum radiated power). The rectangular co-ordinate axes are also shown in the diagram. The pattern is made symmetrical about x-axis by assuming the reflector planes at $\phi = \pm 45^{o}$.

If the co-ordinate axes are chosen such that the loop is in the x-y plane and the reflectors OL1 and OL represent the x-z and y-z planes respectively, then the above field expressions are valid for azimuth angle ϕ from 0 to $\pi/2$ and zenith angle θ from 0 to π as shown in Fig. 3.21 (i.e. in front of the reflector). If the infinite ground plane assumption is valid for the reflectors, there should be neither magnetic nor electric field beyond that quadrant. That is equation (3.5.6) can be re-written as

$$\begin{aligned} E_\phi &= \frac{\mu\omega[I]a}{4r}\beta a.\sin\theta && \text{for } 0\le\phi\le\pi/2 \text{ and } 0\le\theta\le\pi \\ &= 0 && \text{elsewhere} \\ H_\theta &= \frac{\beta[I]a}{4r}\beta a.\sin\theta && \text{for } 0\le\phi\le\pi/2 \text{ and } 0\le\theta\le\pi \\ &= 0 && \text{elsewhere} \end{aligned} \qquad (3.5.7)$$

To illustrate the field variations of (3.5.7), a three dimensional graph of the normalized field amplitude pattern is plotted in Fig. 3.22. These expressions can now be compared with the far field expressions of the complete loop.

3.5.2.3 Comparison with the Complete Loop Antenna

The analysis of the radiation pattern of a loop antenna can be found in most of the texts of antenna as a basic problem. However, following the analysis of Krauss [126, Chap. 6], the generalised expression of the radiated field in the far zone of a complete loop is

$$\begin{aligned} E_\phi &= \frac{\mu\omega[I]a}{2r}J_1(\beta a.\sin\theta) \\ H_\theta &= \frac{\beta[I]a}{2r}J_1(\beta a.\sin\theta) \end{aligned} \qquad (3.5.8)$$

where, [I] = Retarded current at the distant point with respect to the centre of the arc.
$= I_0 e^{j(\omega t-\beta r)}$

I_0 = peak value in time of current (uniform along the arc).

$J_1(x)$ = First order Bessel function of first kind of argument x.

These expressions are exactly the same as the far field expressions of the Q-loop (Eqn. 3.5.6), if small loop approximation is applied to Eqn. (3.5.8) because $J_1(\beta a\sin\theta)$ could be replaced by $\approx \beta a \sin\theta/2$ in that case.

3.5.3 PARAMETERS OF THE Q-LOOP ANTENNA

The antenna parameters, as determined for the TEM-T half radiator in section 3.4.4, are also determined analytically for the Q-loop antenna. Throughout the analysis it has been assumed that the antenna radiates only in front of the reflectors (i.e., the quadrant described by $0 \le \theta \le \pi$ and $0 \le \phi \le \pi/2$) and there is no radiated field behind the reflectors. Moreover the Q-loop is assumed to be small compared to the wavelength.

3.5.3.1 Directivity

Directivity, as stated earlier in section 3.4.4.1, can be determined from a knowledge of the total power radiated by the antenna and its radiation pattern. E_θ and H_ϕ components of the radiated electric and magnetic fields of the Q-loop are given by Eqn. (3.5.7). If these field expressions are substituted in Eqn. (3.4.24) and the integration, indicated in Eqn. (3.4.26) performed with θ varying from 0 to π and ϕ varying from 0 to $\pi/2$, one can obtain the total radiated field for the Q-loop antenna. Since in the analysis it is assumed that the radiation is confined within the limit of θ and ϕ as mentioned above, the total radiated power, P_r is found to be

$$P_r = \frac{5\pi^2\beta^4 a^2 I_0^2}{2} \tag{3.5.9}$$

while the maximum radiation intensity is

$$U_m = \frac{15\pi\beta^4 a^4 I_0^2}{4} \tag{3.5.10}$$

Substituting for P_r and U_m in Eqn. (3.4.27), one obtains the directivity of the Q-loop antenna as

$$D_{Q-loop} = 6 \tag{3.5.11}$$

If we compare the directivity of the quarter loop with that of a complete loop antenna in free space, it is found to be

$$D_{Q\text{-}loop} = 4.D_{loop} \tag{3.5.12}$$

because the directivity of a complete loop antenna is 3/2 (small loop approximations).

3.5.3.2 Input Impedance

The elements that would contribute to the total input impedance of the Q-loop antenna can be modelled by the equivalent circuit shown in Fig. 3.23. Different elements of the circuits can be expressed by the following set of equations (development of the expressions are given in Appendix C10):

R_r is the radiation resistance of the Q-loop antenna and is given by

$$R_r = 5\beta^4(\pi a^2)^2 \tag{3.5.13}$$

which is one quarter of that of a complete loop antenna.

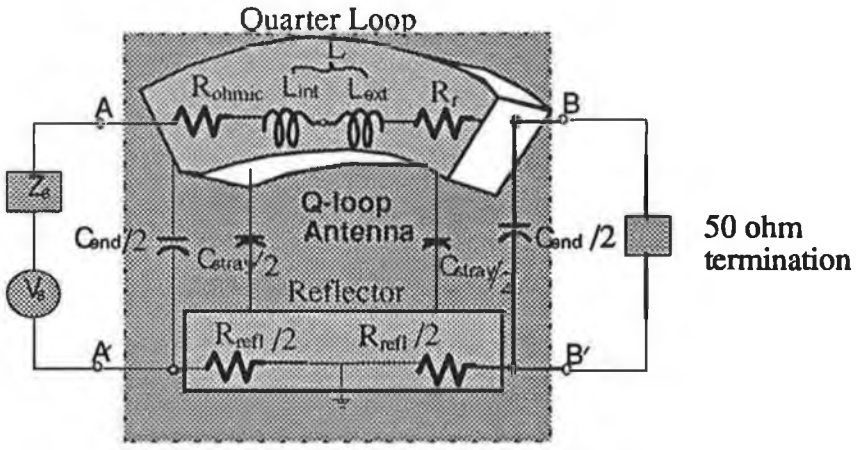

Fig. 3.23 Equivalent circuit of the Q-loop antenna. Distributed parameters such as the capacitance, inductance and resistances are shown as lumped elements to simplify the analysis.

Ohmic resistance of the quarter loop,

$$R_{ohmic} = \frac{\pi a}{8d}\sqrt{\frac{\omega\mu}{2\sigma}} \tag{3.5.14a}$$

Ohmic resistance of the reflector,

$$R_{ref} = \frac{a}{(w+t)}\sqrt{\frac{2\omega\mu}{\sigma}} \tag{3.5.14b}$$

Internal inductance of the quarter loop,

$$L_{\text{int}} = \frac{\mu_0 a}{16} \tag{3.5.15a}$$

External inductance of the quarter loop,

$$L_{ext} = \frac{\mu_0 a^2}{2} \int_0^{\pi/2} \frac{\cos\theta}{\sqrt{\left[\left(\frac{d}{2}\right)^2 + 2a\left(a - \frac{d}{2}\right)(1-\cos\theta)\right]}} d\theta \tag{3.5.15b}$$

Capacitance between the flat end of the quarter loop and the reflector

$$C_{end} = \varepsilon_0 \varepsilon_r \frac{2d^2}{t_n} \tag{3.5.16a}$$

Stray capacitance between the quarter loop and the reflector

$$C_{stray} = \sqrt{2}\varepsilon_0 d \ln\left(\sqrt{2}+1\right) \tag{3.5.16b}$$

In the above sets of equations, a is the radius of the quarter loop, d is the dimension of the square cross-section of the rod that constructs the quarter loop, *w* and *t* are the width and thickness of the reflector, ε_r is the relative permittivity of the nylon gasket (between the reflector and the quarter loop) and t_n is the depth of this gasket.

The input impedance of the Q-loop antenna is the impedance looking into the terminals AA′. The model has been simplified by expressing the internal and external inductances as lumped elements instead of distributed parameters and the capacitances as lumped elements at the two ends.

3.5.3.3 Gain

The gain of the antenna can be determined from its directivity and efficiency. Directivity of the Q-loop antenna is given by Eqn. (3.5.11) and the radiation efficiency of this antenna may be derived from the radiation resistance and the ohmic resistance of the Q-loop antenna. Thus the gain of this antenna is

$$G_{Q-loop} = \eta_r D_{Q-loop} \tag{3.5.16}$$

where η_r is the radiation efficiency of the antenna and is given by

$$\eta_r = \frac{R_r}{R_r + R_{ohmic} + R_{ref}} \tag{3.5.17}$$

R_r, R_{ohmic} and R_{ref} are given by Eqns. (3.5.13) and (3.5.14). Eqn. (3.5.16) describes the gain of the antenna provided the antenna is matched.

3.6 CONCLUDING REMARKS

Standard field simulation is the key element in achieving meaningful SE data, but is very difficult to establish in an on-line measurement system with limited space considerations. The fields simulated by the three different original (proposed) antennas have been analyzed. The results of these analysis have been compared with the ideal characteristics of uniform plane wave, high impedance and low impedance wave respectively.

In case of VCLA, the plane wave emerging from the lens is not uniform. The nonuniformity of illumination, however, can be reduced significantly by proper design of the lens. Edge diffraction and the infringement of probable indirect-path signals may distort the theoretical (section 3.4.2.2) high impedance field available with the TEM-T cell test device in an actual environment. However, introducing appropriate correction factors, these effects could be minimized. Similar effects would likely to be experienced with the application of the Q-loop antenna as well, but by proper design of the reflector, these effects could also be minimized.

Thus despite the fact that the theoretical analysis (based on simplifying assumptions) of the EM fields produced by the selected test devices yield satisfactory results, many other important factors are to be considered in their design and application to obtain appropriate SE data.

Chapter 4

SYSTEM DESIGN

DESIGN AND CONSTRUCTION OF VCLA (PROPOSALS)
DESIGN AND CONSTRUCTION OF TEM-T CELL
DESIGN AND CONSTRUCTION OF Q-LOOP ANTENNA
FABRICATION OF FRAMES FOR MEASUREMENT SYSTEMS

4.1 INTRODUCTION

The generation of standard test fields, which fulfil the requirements of emission and susceptibility measurements, largely depend on the strict maintenance of the design specifications of the test device. Transforming guided waves into free-space waves and vice versa involve many important parameters of the test device(s) that are to be considered with due attention if standard EM waves (such as plane waves, high and low impedance waves) are desired at a particular location. For example, the selection of material type, dimensions and shape of the wave guide, antenna and feed structure must be determined carefully in order to get reliable output as well as to make efficient use of them in the complete measurement system. Moreover, the guided waves may be well defined, but as mentioned before, for the sake of simplicity of the measurement system, the selected test devices are to be incorporated into a non-contacting free space environment and as a result the analysis becomes more complicated with the possibility of inclusion of background noise and indirect path signal into the test field. Thus some special features have to be included in the design to account for these effects.

The V-conical antenna (VCA) is simple to design as only two angular dimensions are needed to be maintained carefully [105], but its feed network must be well-designed so that the requirement of a point source at the tip of the cone can be fulfilled approximately. Moreover, the lens antenna which is to be used in conjunction with the VCA to simulate a far-field situation, requires careful design analysis to minimise reflections from the lens-air interface as well as to obtain the uniformity of the plane wave in front of it.

Although the design specifications of the TEM cell are well documented [153], the development of its modified form as the TEM-T cell is relatively new. In the design of a TEM-T cell care must be taken to ensure the existence of a TEM wave at the open face of the transmitting half of the cell in the specified frequency range. In addition to that the gap which is to be provided between the flanges and the test sheet introduces errors and thus calls for further improvement analysis.

Being a newly developed instrument, the Q-loop demands more detailed analysis of its specifications. Particularly the size of the quarter loop for efficient radiation in the desired frequency range, the size of the reflectors so that image theory holds and the feed network to maintain uniformity of the current through the arc are the important features for

consideration. Again, the diffraction effects due to the sharp edge of the reflectors may distort the field type simulated by the Q-loop. The effect of this edge scattering can be reduced by applying the rolled edge technique proposed by Burnside *et al.* [154].

Furthermore, special frames must be designed to carry out the on-line SE measurements employing the aforementioned test devices. Fortunately, a typical SE measurement system does not involve many sophisticated instruments, and the instruments necessary to construct such a measurement system are more or less the same for the three different situations. However, in the present application, automated data acquisition is essential which dictates the use of computer controlled instruments.

Design and constructional details of the test devices for far field simulation are discussed in the next section. Section 4.3 and 4.4 describe the design analyses of the TEM-T cell test device and of the Q-loop antenna. The fabrication details of the frames for holding the test devices in the on-line SE measurement fixtures are given in section 4.5. Section 4.6 describes the instruments and accessories that are necessary for the complete measurement system.

4.2 TEST DEVICE FOR FAR-FIELD SIMULATION

As mentioned earlier, a VCLA set is used to simulate a far-field situation in the present application. The main constittuents of a VCLA set is a VCA and a lens antenna. The proposed VCLA set that could be used in the present application is shown in Fig. 4.1. The design and constructional details of the VCA and the lens antenna are described in the following subsections separately.

4.2.1 V-CONICAL ANTENNA

A pair of VCAs is essential, where one acts as a transmitter and the other as a receiver. The size of the antenna is dictated chiefly by the sheet width of the MUT. If the diameter of the base of the cone is very small compared to the width of the MUT, the test result would represent only a very small portion of the MUT. On the contrary if it is made very large, the size of the lens would be colossal incurring manufacturing complexity. Moreover to maintain a narrow apex with large base diameter, the height of the cone would be awkwardly large. Thus a compromise is to be made.

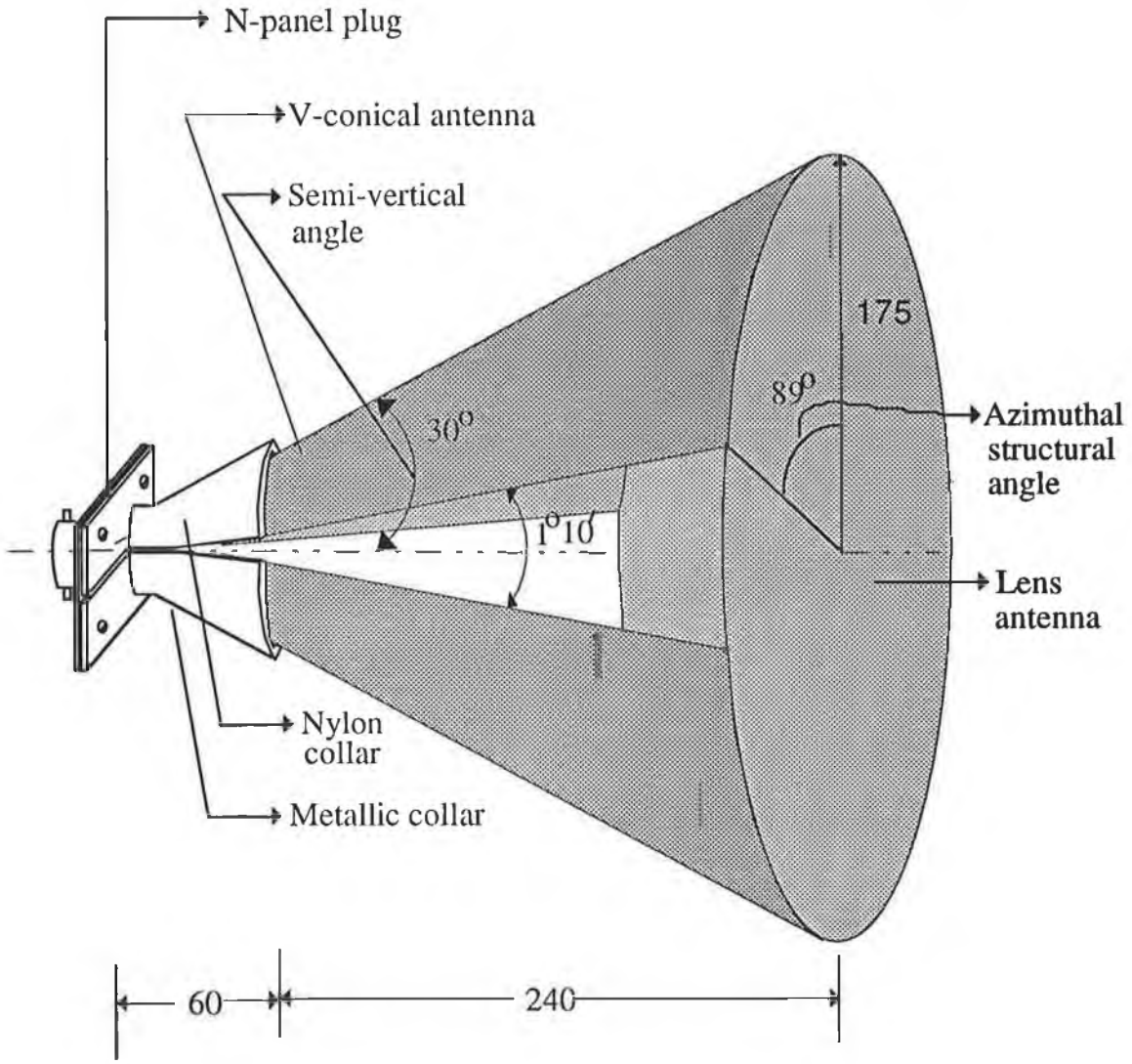

Fig. 4.1 V-conical-lens antenna set for far field SE measurement. All the dimensions are in mm and the diagram is not drawn to scale. Section at the middle is exagerated in the diagram to make it distinct.

4.2.1.1 Design Parameters

In fact the two angles, namely the semi-vertical angle and the azimuthal structural angle are mainly the parameters that are to be selected through calculation for desired field structure and strength.

4.2.1.1.1 Semi-vertical angle

This angle is to be determined by the requirement of the diameter of the base of the cone and by its height. The diameter of the base can be fixed by the width of the test sheet. It is desirable to make it as wide as to cover the whole width of the sheet so that it can give a complete assessment of the shielding capability of the test material. The width of a sheet in a typical production process varies from 60 to 100 cm. The length and volume of the cone would be excessively large even if its base were equal to the minimum sheet width. As a compromise the base could be chosen to be half the width of the sheet. In that case the measurements would relate to approximately 50% of the sheet, which is probably adequate for a typical on-line monitoring system.

With the base diameter selected, the narrower the semi-vertical angle the longer the VCA would be. Complexity of the mounting fixture and greater difficulty in manufacturing are the major drawbacks in making the VCA long. Thus it is desirable to keep it as short as possible. Obviously manufacturing a cone with a very wide semi-vertical angle is also not desirable from the mechanical handling point of view. Thus a compromise is to be made. For the present application the aspect ratio h/D (where h is the height of the cone and D is the diameter of the base) is selected to be very close to unity. If the base diameter is 35 cm, and the semi-vertical angle is 30^{o}, then the height would be 30 cm thus satisfying the above aspect ratio requirement.

4.2.1.1.2 Azimuthal structural angle

The characteristic impedance of the antenna is dependent on the azimuthal structural angle, denoted by ϕ_0. The input impedance of the antenna is given by [105]

$$Z_{in} = \frac{\eta_0}{2} \frac{K(\cos\phi_0)}{K(\sin\phi_0)} \qquad (4.2.1)$$

where K(k) is the complete elliptic integral of first kind of modulus k. η_0 is the free space intrinsic impedance. It is desirable to make Z_{in} as close as possible to 50 Ω. With trial and error calculations using Mathcad® it is possible to determine some value for ϕ_0 which will give Z_{in} very close to 50 Ω. The sample calculation is included in Appendix D1. It has been found that for $\phi_0 \geq 89^{o}$, Z_{in} becomes approximately 50 Ω. Of course, ϕ_0 must be less than

90^{o}. With such a large value of ϕ_0, there is another advantage in that the leakage of the test field and the possibility of infringement of the indirect path signal into the test device will be very small.

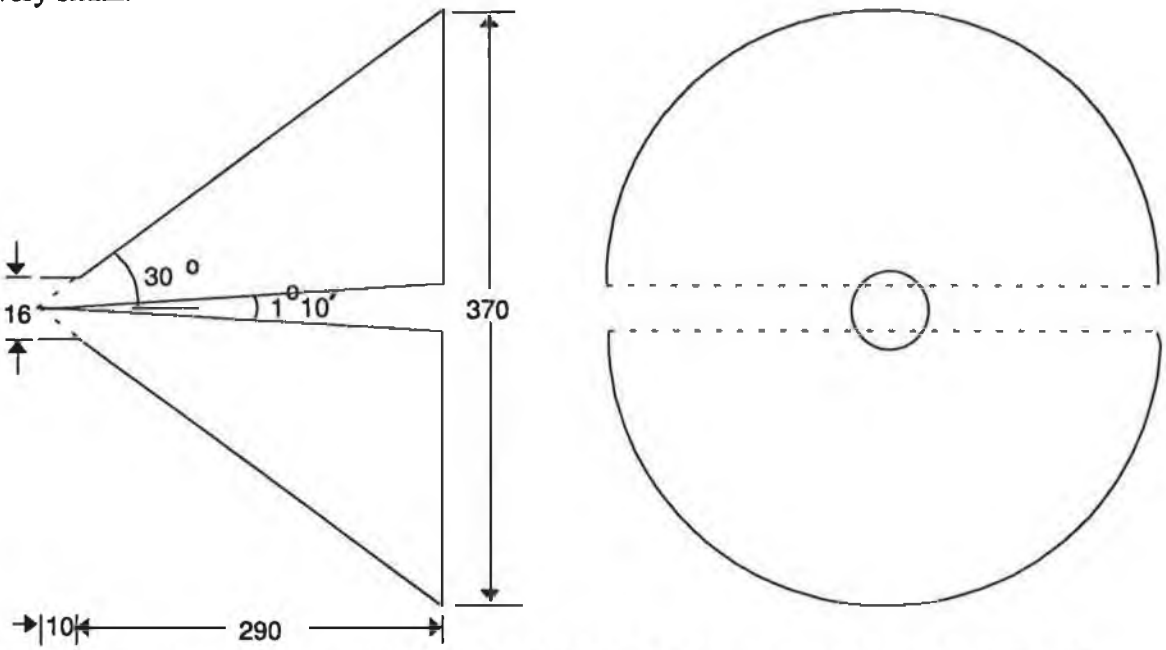

Fig. 4.2 Front and side elevation of the VCA. All the dimensions are in cm and the diagram is not drawn to scale.

4.2.1.2 Construction

Although the design of the VCA appears to be simple, the construction of a conical structure with very stringent angular specifications is quite difficult. However, the conical structure may be fabricated from sheet metals or it may be machined from a block of material. However, sheet metal forming is preferable as it does not involve much machining and wastage of material. Thus reduces the cost of both material and labour.

4.2.1.2.1 Selection of material

Three metals were considered, aluminium, copper and steel. Aluminium, although falling between the other two in conductivity, is recommended for reasons of cost, availability and workability.

The selection of the thickness of the sheet is not crucial. Adequate shielding capability and the ease of mechanical handling are the factors to be considered. Aluminium sheet of thickness 0.2-0.3 mm could be chosen which satisfies both the requirements.

4.2.1.2.2 Fabrication of the cone

Since there would be a longitudinal section at the middle of the cone, it would be easier if it is constructed into two halves although joining them at the end may be very difficult. The alternative is to form a complete cone out of a semi-circular sheet and then cut a longitudinal tapered slot at the middle (meeting the requirement of azimuthal structural angle, $\phi_o = 89^o$). The slant height of the cone will be the radius of the semicircle. This slant height of the cone can be determined from the semi-vertical angle, height of the cone and the radius of the base. The calculations are given in Appendix D2. Slant height of the cone is 36.64 cm.

A strong conical frame is essential to hold the shape the cone. Even a small frame (conical structure of low height, say 1/6 of the height of the VCA) would be strong enough to retain the shape of the cone. This frame should be composed of two symmetrical halves (see Fig. 4.3). One half could be machined from a block of aluminium while the other half from a block of nylon. The tapered end of this frame should be terminated with a rectangular flat face which could be bolted to the N-panel plug. The transition between the tapered end of the conical frame and its flat face could be made by providing a cylindrical collar. A sectional view of this frame/collar is shown in Fig. 4.3. Other reinforcing straps (e.g. nylon) may be attached at intervals along the length of the cone (see Appendix D2).

4.2.1.2.3 Feed arrangement

The centre stud of the coaxial N-panel plug can be soldered to one half of the V-cone while the other half of the V-cone is connected to the outer conductor of the plug through metallic collar. The collar provided at the tapered end of the V-cone (to retain its shape) is composed of two halves as mentioned before. The nylon half is bolted to the V-cone half which is connected to the centre stud of the panel plug as shown in Fig. 4.3. The metallic half of the collar is bolted to the V-cone half that is to be connected with the outer conductor of the panel plug. The centre stud of the panel plug is soldered to the V-cone half through a short wire. Since the diameter of this wire (1 mm) is much smaller than the shortest wavelength (30 cm), the apex of the V-conical antenna is close to a point.

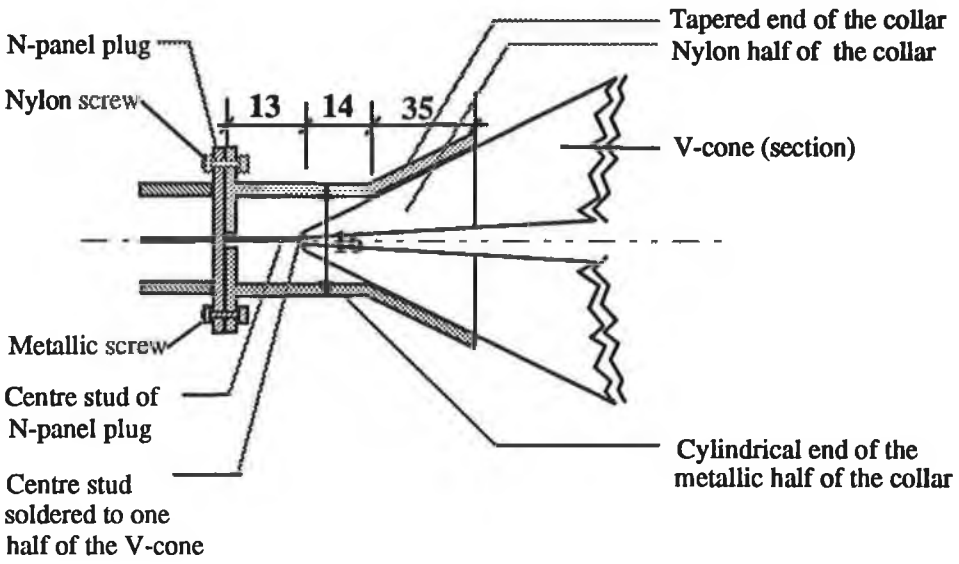

Fig. 4.3 Feed arrangement of the VCA. All the dimensions are shown in bold face and they are in mm. Threads of the N-panel plug are not shown in the diagram. Diagram is not drawn to scale.

4.2.2 LENS ANTENNA

In the VCLA assembly shown in Fig. 4.1, the VCA is used for simulating a spherical wave front of TEM wave which is then transformed into a plane wave front by the lens antenna fitted at the face of the V-cone.

A plano-convex lens is essential for the purpose. The spherical TEM waves from the VCA would be incident on the convex face of the lens and plane waves would then emerge from its flat face. The design and constructional details of the lens antenna are described in the following sub-sections.

4.2.2.1 Design Parameters

Whatever may be the constituent material, a lens can be designed on the basis of Fermat's principle, which states the equality of electrical path length of different rays. In Fig. 4.4, the origin of the co-ordinate axes is chosen at the vertex of the cone and the X-axis is the axis of the cone. Thus in Fig. 4.4, in the plane of the paper, according to Fermat's principle

$$\frac{R}{\lambda_0} = \frac{L}{\lambda_0} + \frac{x-L}{\lambda_l} \qquad (4.2.2)$$

where λ_0 and λ_l are the wavelength in free space and in the lens material rsepectively,

$$R = \sqrt{(x^2 + y^2)}$$

and

$$y^2 = (n^2 - 1)x^2 - 2xnL(n-1) + (n-1)^2 L^2 \qquad (4.2.3)$$

where

n = refractive index of the lens material = λ_0/λ_l

Equation (4.2.2) represents a hyperbola. In polar form we can express R as [126, chap.16]

$$R = \frac{(n-1)L}{n\cos\theta - 1} \qquad (4.2.4)$$

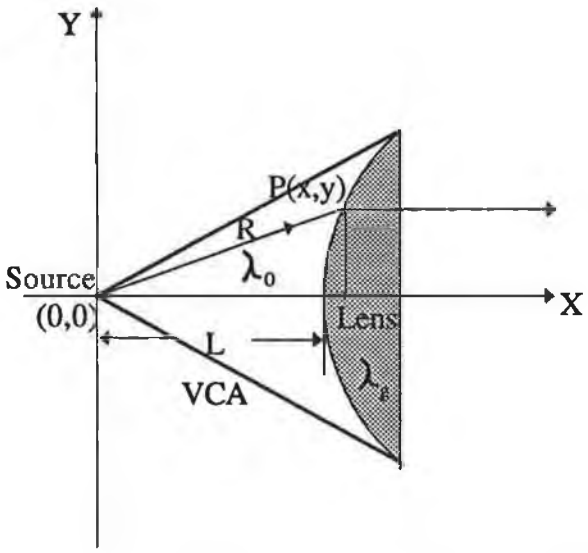

Fig. 4.4 Geometry of the lens antenna fixed at the face of a VCA. The origin of the coordinate system is at the vertex of the VCA and the focal length of the lens plus its depth is the height of the cone.

Referring to Fig. 4.4, the distance L is the focal length of the lens. One of the major design criteria is that this length plus the depth of the lens should be equal to the height of the cone. Moreover, to fit the lens at the mouth of the V-cone antenna, it is essential that the diameter of the flat face of the lens is equal to the diameter of the base of the cone.

Thus the three important design criteria of the lens are: (a) the curved face of the lens should be a hyperbola such that any point on it obeys Eqn. (4.2.3) if expressed in rectangular co-ordinates or Eqn. (4.2.4) if expressed in polar form; (b) the focal length of the lens plus its depth should be equal to the height of the cone; and (c) the diameter of the flat face of the lens should be equal to the diameter of the base of the cone. Moreover in section 3.3.2.1, limitations of lens antennas were mentioned and it is essential to overcome those limitations, if the lens is to be used for the present application. A short account of these requirements are given below.

4.2.2.1.1 Minimizing Reflections from the Lens Interface

It is desirable that the reflection from the interface of the lens and medium of the primary antenna should be as small as possible, so that the EM wave incident on the lens remains unperturbed. It is the impedance mismatch at the interface which causes reflection. Hence if the impedance of the lens can be made as close as possible to the impedance of the medium in which the antenna is embedded, reflection could be maintained within a tolerable limit.

4.2.2.1.2 Uniformity of Field Emerging from the Lens

The plane wave emerging from the right side of the lens produces a secondary pattern with maximum radiation in the direction of the axis. The shape of the secondary pattern is a function of both the aperture A and the type of illumination. A mathematical model for this aperture pattern distribution can be established as follows.

Let the field intensities at the flat face of the lens be E_{m0} and E_{y0} at the axis and at a height y above the axis respectively. Again if we let the corresponding incident field intensities at the curved face be E_{mi} and E_{yi} respectively, from lens geometry (refer to Fig. 4.4) we know that

$$\frac{E_{yi}}{E_{mi}} = \frac{n\cos\phi - 1}{n - 1} \qquad (4.2.5)$$

where, $\phi = \sin^{-1}(y/R)$. Now due to the penetration loss suffered by the EM wave inside the lens, field intensities at the flat face would be given by

$$E_{m0} = E_{mi}e^{-\alpha t_0}$$
$$E_{y0} = E_{yi}e^{-\alpha t} \qquad (4.2.6)$$

where $t_0 = R_m\cos\phi_m - L$ and t is given by

$$t = \frac{(n-1)L(\cos\phi - \cos\phi_m)}{(n\cos\phi_m - 1)(n\cos\phi - 1)} \qquad (4.2.7)$$

In Fig. 3.10, the distribution has been shown for a Nylon 6® (polyamide) lens. However, in order to simulate perfectly the far field condition it is essential that the plane wave emerging from the plano face of the lens be uniform.

4.2.2.2 Construction

The shape of the lens which can be used in front of the VCA would be a section of a spherical hyperbola and the origin (i.e. the vertex of the cone), it can be assumed to be a point source at the focus of that hyperbolic surface. The lens may be machined from a bulk material using a numerically controlled (NC) machine.

4.2.2.2.1 Selection of material

Lenses can be constructed of non-metallic dielectrics, metallic parallel plates or artificial dielectrics. Dielectric materials, such as nylon or polystyrene are preferable in that a bulk piece of such a material can be readily machined to give the particular hyperbolic shape.

Metallic plate lenses, although they do not require any specially designed material (aluminium or copper sheet can be used), every single constituent plate requires specific and individual dimensions. Furthermore, attachment to the open face of the VCA is very difficult as a constant separation between the plates is to be maintained. In case of artificial dielectric, the constituent material itself has to be designed and manufactured following some stringent conditions.

A nylon or polystyrene lens, although, preferable from a machinability point of view, does not satisfy the design requirements mentioned in sections 4.2.2.1.1 and 4.2.2.1.2 which is evident from Fig. 3.10. The nonuniformity of the secondary field pattern in front

of the lens can be reduced significantly if a lossy dielectric is used instead of nylon. The illumination pattern for an Eccogel® lens is shown in Fig. 4.5. Such a lens, however, cannot improve the reflectivity situation because the permittivity of this lossy dielectric is 2.0-j0.051, but its permeability is very close to unity and as a result its intrinsic impedance is close to that of polystyrene.

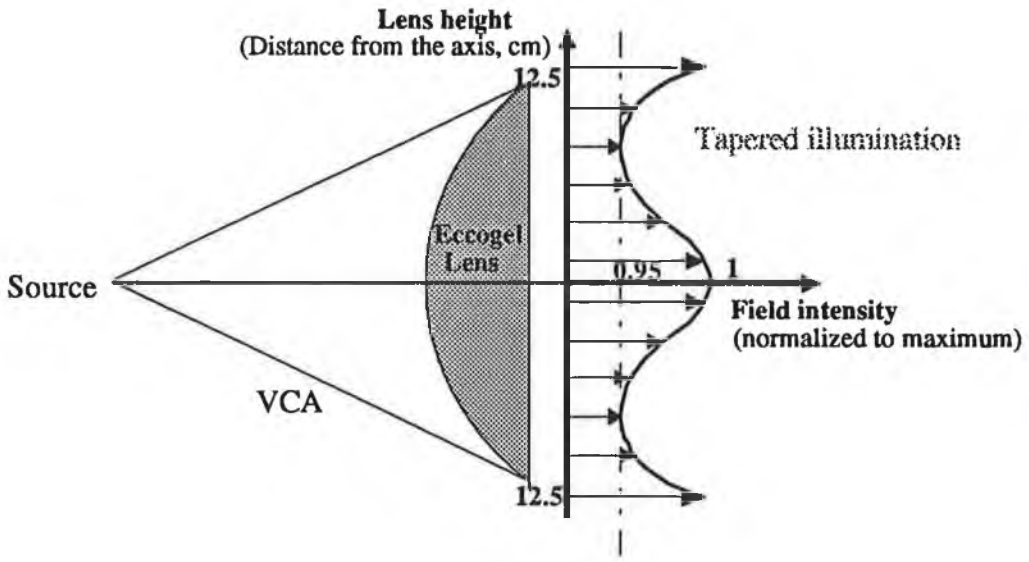

Fig. 4.5 Tapered illumination available in front of a Eccogel® lens. Normalized field intensity profile is shown by the locus of the arrow heads (refer to Appendix D4 for calculations).

A magneto-dielectric material which has the ratio of permittivity and permeability very close to unity might eliminate the reflectivity problem, and because of the EM absorption property it might also contribute to the uniformity of the plane wave emanating from the flat face of the lens. A wide variety of such magneto-dielectric materials is possible. However, changes in the constitutive properties have significant effect on the uniformity, attenuation and dimension of the lens even when $|\varepsilon| = |\mu|$.

It has been observed (see Appendix D3) that for higher values of the constitutive properties, the thickness of the lens reduces but better uniformity of the output field can still be achieved. Thus it is preferable to select some magneto-dielectric material which has higher values of permittivity and permeability but the ratio very close to unity.

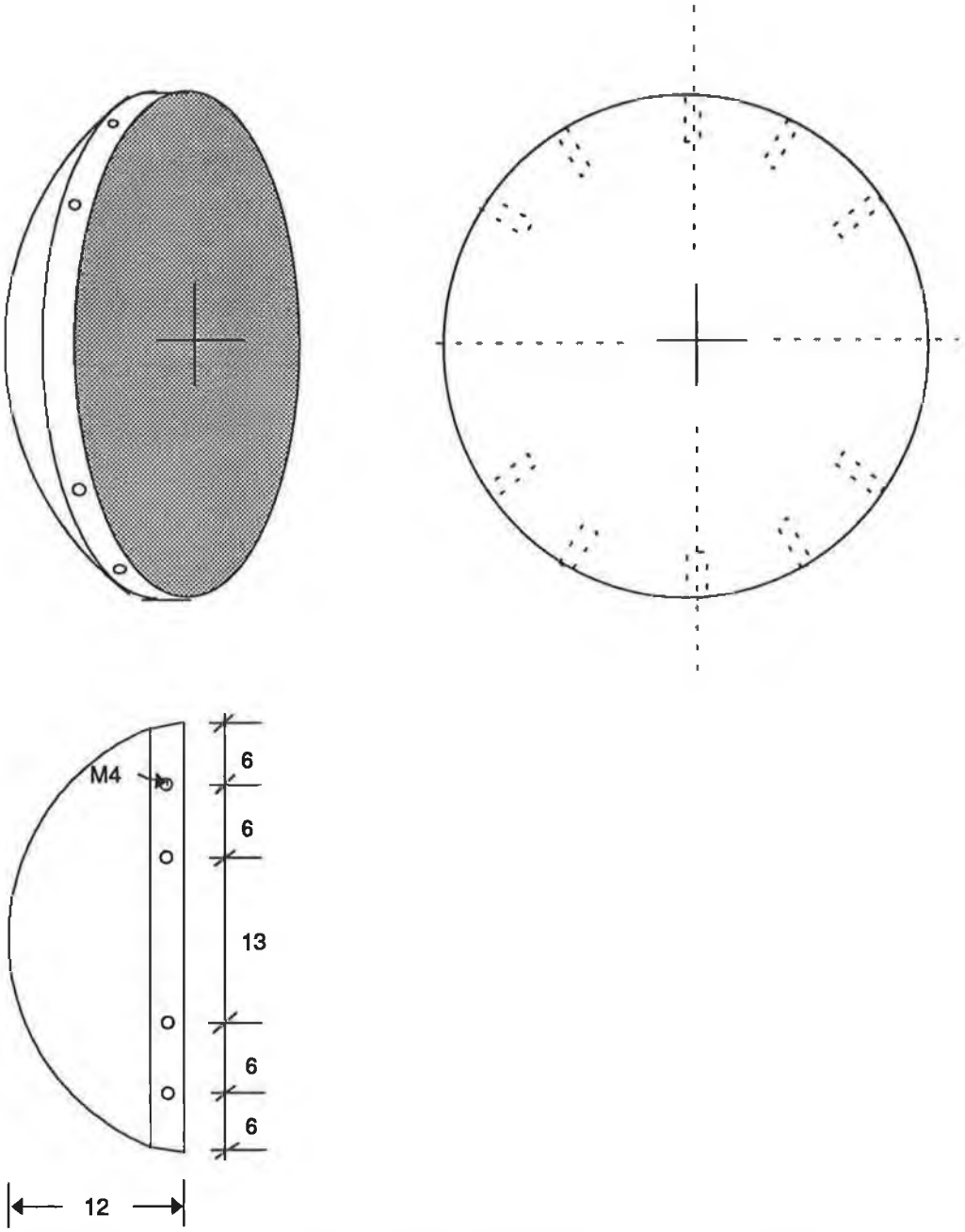

Fig. 4.6 Constructional details of the dielectric lens. All the dimensions are in cm and the diagrams are not drawn to scale.

4.2.2.2.2 Fitting onto the VCA

There should be a frustum (section of a cone) section near the flat face of the lens antenna so that the VCA can be screwed onto that section. The dimension of that frustum section

should be such that it push-fits into the VCA. The structure is proposed in Fig. 4.6. Around the frustum, threaded holes are to be provided radially for screwing the VCA with the lens (screw positions are shown in the diagram). Obviously nylon screws are to be used.

4.3 TEST DEVICE FOR HIGH IMPEDANCE FIELD SIMULATION

A TEM-T cell has been used in the present application in order to measure high impedance field SE. The features to be considered in designing a TEM-T cell are identical to those of a TEM cell. A TEM cell is a section of expanded rectangular coaxial transmission line (RCTL) tapered at each end to match ordinary coaxial line. The design considerations of a TEM cell have been discussed in some greater details in reference [16].

4.3.1 DESIGN CONSIDERATIONS

The two halves of the TEM-T cell test device are identical and are illustrated in Fig. 4.9. Selection of the dimensions shown, involves the consideration of trade-offs between width of the sample, characteristic impedance, frequency range and uniformity of the generated field.

4.3.1.1 Width of the MUT sheet

As the test sheet is continuously moving in an ongoing production process, its length can be assumed to be infinite. Therefore only the width and thickness of the sheet have to be considered in selecting the dimensions of the test device. It is essential that the width of the sample be large enough compared to the dimensions of the cell so that direct capacitive coupling between the flanges of the two halves can be avoided. Again the dimensions of the cell cannot be made very small because in that case the test results would refer to only a small fraction of the width of the test sheet.

However, one can reasonably assume that the fringing fields which cause direct capacitive coupling between the flanges can be minimised if the cell width is half the width of the sheet and if the TEM-T cell is centrally located accross the sheet width. Moreover in that case the measurements would refer to atleast 50% of the sheet.

4.3.1.2 Characteristic Impedance

Usually the cell is connected with 50-Ω source or receiving systems. It is desirable to keep the characteristic impedance very close to 50-Ω, so that maximum power can be transferred. In the present case we have allowed ±1% deviation from 50-Ω. However, in the non-contacting configuration of the test device for on-line SE measurement, which is referred to as modified TEM-T cell, the input impedance of the transmitting half does not remain equal to this characteristic impedance.

The characteristic impedance of the cell may be expressed in terms of the distributed capacitance per unit length of the cell, C_0, by [155]:

$$Z_0 = \eta_0 \frac{\varepsilon_0}{C_0} \qquad (4.3.1)$$

where ε_0 (= 8.852×10^{-12} F/m) is the air permittivity.

An expression for C_0 may be formulated through conformally mapping the rectangular outer conductor and the septum into a parallel plate capacitor configuration as described by Crawford *et al.* [156] and the computation may be performed numerically. However, if the aspect ratio is small, i.e., $b/a \leq 1$, and if $w/b \geq 1/2$, then an approximate expression for C_0/ε_0 may be obtained [157] as

$$\frac{C_0}{\varepsilon_0} = 4\left[\frac{w}{b} + \frac{2}{\pi} ln\left(1 + \coth\frac{\pi g}{2b}\right)\right] \qquad (4.3.2)$$

where a, b and w are the half width, half height of the cell and half width of the septum respectively, and g is the gap between the septum and the side wall of the cell.

Thus from Eqn. (4.3.2), if the width of the cell is larger than its height and the gap between the side walls and the septum is smaller than the half width, the characteristic impedance becomes independent of the cell width. If a characteristic impedance value of 50-Ω is desired, then one requires $C_0/\varepsilon_0 = 7.54$. A set of values for a, b and w may be determined (using a short computer program) based on (4.3.2), in order to meet this requirement.

4.3.1.3 Operating Frequency Range

In the theoretical analysis of the TEM-T cell as an open ended rectangular coaxial transmission line, it was mentioned that the existence of a TEM wave at the open mouth of the TEM-T transmitting half largely depends on the higher order modes that can be generated in the cell even in the absence of the discontinuity i.e., because of the cell dimensions and due to the gap perturbation. Thus the design considerations of reducing the generation of higher modes in the TEM cell are equally applicable in the design of the TEM-T cell as well.

It is observed that the appearance of higher order modes in a TEM cell depends on the size of the cell. Tippet's chart [157], as shown in Fig. 4.7, provides an easy means of determining the cut-off frequencies of the gap perturbed higher order modes appearing in a TEM cell in terms of the width of the cell and the septum while taking cell width to height ratio as a parameter. Note that this estimation is based totally on the cross section of the cell whose length is assumed to be infinitely long. In reality, the cell is finite and the two ends are tapered; thus the actual measured cut-off frequencies are somewhat different from this theoretical estimation. The resonance frequency, f_{res} , associated with a mode of cut-off frequency , f_c, can be found from the following expression:

$$f_{res} = [f_c^2 + (c/d)^2]^{1/2} \qquad (4.3.3)$$

where c = $3x10^8$ m/s is the speed of light, and d in meters the resonance length. Again, because of the tapered sections at the two ends, the resonance length is not well defined. As a first approximation, an average "overall cell length" is usually taken as the resonance length [158].

The TE_{01} and TE_{10} are the most likely other modes to appear in a TEM cell even at low range of frequencies. It is important to note that the first-order TE modes do not become significant until approaching a resonant frequency. Again, if the septum of the cell is centered symmetrically, the odd-order TE modes are not excited in the empty cell (these modes may exist when equipment to be tested is placed in the cell). Thus the upper useful frequency can exceed the multimode cut-off frequency of the first higher order mode, but should be less than this mode's associated resonant frequency.

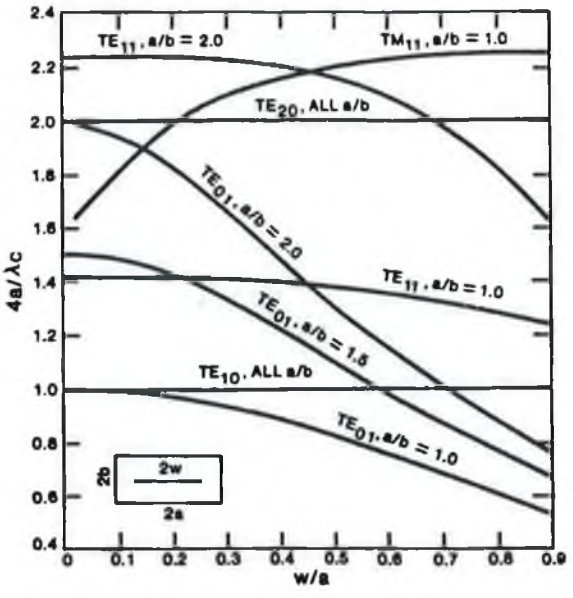

Fig. 4.7 Cut-off wavelengths of the first few higher order gap-perturbed modes in a TEM cell as a function of the aspect ratio (a/b) of the cell and the width of the septum. Adapted from [16, pp. 392].

Fig. 4.8 Photograph of one half of the TEM-T cell (looking into the cell). Septum and dielectric support is shown in the diagram.

Thus the length of the TEM-T cell in clamped configuration (two halves tightly clamped together), should be chosen (following Eqn. (4.3.3), since in this configuration the TEM-T cell is almost like a TEM cell) such that the appearance of resonance of the first higher order mode would be at a frequency above the desired highest operating frequency of the cell.

4.3.1.4 Uniformity of the Generated Field

The analysis of the TEM-T cell presented in section 3.4.2 was based on the assumption that the field at the aperture of the open mouth of the TEM-T transmitting half is uniform. Thus it is essential to ensure the uniformity of the generated field inside the cell. Apart from the discontinuity at the middle, a TEM-T cell is an expanded section of rectangular coaxial transmission line (RCTL) and as such the field is likely to be uniform. Nonetheless, non-uniformity of the field may result due to the tapered ends which are provided for connecting the cell to ordinary coaxial lines. The longer the ends (or in other words the less steep the ends) would be, the lower the non-uniformity results. Furthermore if these ends are made less steep, the length of the cell becomes longer which in turn decreases the resonance frequency of the first higher order mode. As a result, the operating frequency range becomes smaller. In manufacturing TEM cells, the usual practice is to make the length of each tapered end greater than half of the width of the cell. This practice can be followed in designing TEM-T cell halves as well. Another factor, that is to be considered to maintain the uniformity of the field distribution, is the ratio of the septum width to the width of the cell. The field distribution inside the cell for a large number of different values of the above ratio have been studied by Hill [179] and the optimum ratio is shown to be between 0.6 and 0.7 .

4.3.2 CONSTRUCTION

The external view of the one half of a TEM-T cell is shown in Fig. 4.8. The side elevation and the plan of the cell are shown in Fig. 4.9. A medium-size prototype has been designed and developed for on-line SE measurement. Half the width of the MUT sheet is chosen as the width of the cell. The on-line SE of a Polyethylene Terephthalate (PET) laminate and an aluminium laminate samples (defined later in section 5.2.2) were to be tested and these samples were 60 cm wide. Hence, the flange width was chosen to be 30 cm. The height of the cell was selected to be half the width and as mentioned earlier in section 3.4.2.1, such a cell of dimensions 30×15 cm can be readily operated without generating any higher order

mode even up to 1 GHz. The length of the cell is chosen according to Eqn. (4.3.3) so that the operating frequency can be up to 1 GHz. The width of the septum was selected as 20 cm on the basis of the requirements of maintaining a characteristic impedance of 50 Ω throughout the cross-section of the cell and the uniformity of the field distribution inside the cell.

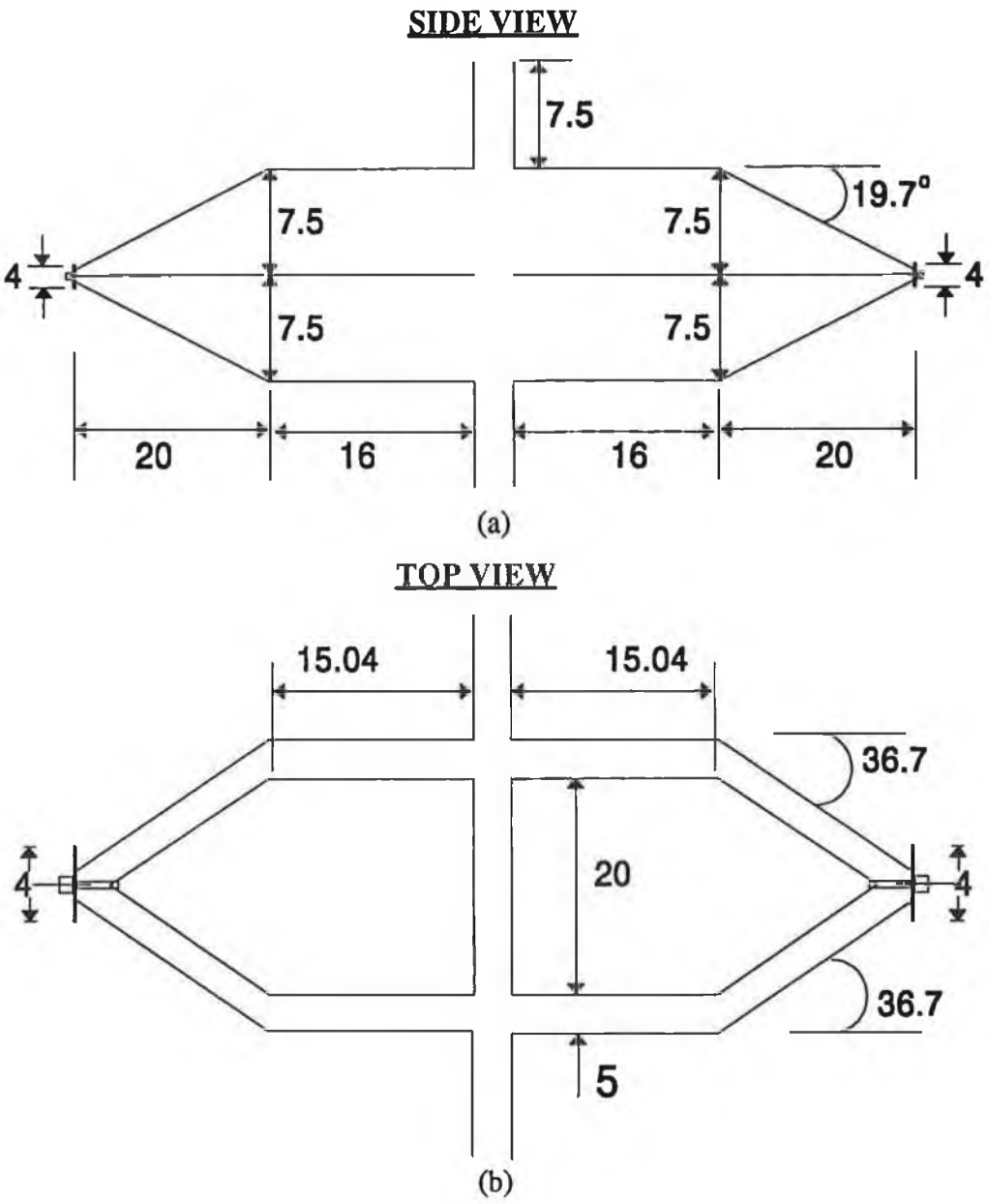

Fig. 4.9 Mechanical design of the TEM-T cell. All the dimensions are in cm and the sketches are not drawn to scale. (a) Side elevation of the cell and (b) Plan of the cell.

4.3.2.1 Process of Fabrication

For a large cell it is essential to build a skeleton or frame [153] on which the metal sheets are to be mounted and that skeleton must be fabricated from material with the lowest possible dielectric constant to minimize the effects of these members on the characteristic impedance of the cell. In addition it is important that the material should be electromagnetically transparent. Wood, nylon or any good quality plastic can be used.

Another alternative is to mould each half of the TEM-T cell completely and in that case the performance would definitely be better than the other configurations, as there would be no probable paths (joints and seams) of EMI leakage. However, this would be an expensive process.

Smaller cells can be built without a frame, requiring more extensive sheet metal work. Each half of the cell can again be divided into two quarters as shown in Fig. 4 of reference [103]. Rivet joints or welded joints, depending on the material and thickness of the sheet, may be employed to bind the two quarters in forming each half of the cell.

The TEM-T cell constructed for this project is of moderate size and has been designed to be manufactured from sheet metals without any frame. Properly formed metallic sheets are welded to give the particular shape.

4.3.2.2 Selection of Material

The coaxial structure of the TEM-T cell (except at the discontinuity at the middle) would serve as a shield against unwanted EM radiation from inside the cell. If the outer conductor of the TEM-T cell is maintained at earth potential then outside the cell there is neither an electric field, nor a magnetic field, since there is equal and opposite current flow in the two conductors of the cell. There is therefore minimal possibility of EMI leakage from inside the cell.

To assess EMI from external sources on the field inside the cell, consider the normal incidence (most severe case) of plane waves on the walls of the outer conductor. The shielding effectiveness offered by the cell wall to such incident waves can be

determined by Eqn. (D6-1) of Appendix D6. The expressions for absorption, reflection and correction factors are presented there in that Appendix and the SE offered by different metallic sheet as functions of frequency and sheet thickness are plotted. It may serve as a guide in selecting the material for constructing a wall of the TEM-T cell with adequate shielding capability against background noise.

E- and H-field shielding and the composite of the two are shown in Appendix D6 for aluminium, copper and steel (sheet thickness 0.5 mm). Steel, although, less effective against E-field, is the best against H-field and far field. Materials used by different commercial organizations to manufacture TEM cells are listed in the same Appendix. Thick copper sheet (as shown in Table D6-1) is not easy to handle mechanically and chromate (or cobalt) coated aluminium are not cost effective for manufacturing a single cell. Standard steel is thus recommended for manufacturing the TEM-T cell in the present application.

4.3.2.3 Thickness of the sheet that constructs the TEM-T cell

It is obvious that the thicker the sheet used, the better the shielding performance would be. Of course, one can not select a sheet which is arbitrarily thick, one has to consider several other factors, such as ease of mechanical handling, cost and availability and matching with the dimensions of the cell.

In Fig. D6-3, the composite shielding effectiveness of steel sheet of various thickness is shown as a function of frequency. It is evident from the figure that even at a low frequency of 10 kHz, shielding offered by a steel sheet of thickness 0.5 mm is well above 200 dB, which is excellent.

Light weight is also desirable for the test device as it will be easier for assembling the device in any orientation, vertically or horizontally, depending on the position of the MUT sheet. Although not applied in the system described here, light weight would be essential if it were necessary to have the test device moving continuously.

The available thinnest steel sheet was 0.7 mm thick and it was used for constructing the outer conductor of the cell. Mechanical handling was easier and the cell is strong enough even with this thin sheet.

The centre conductor or septum should be as thin as possible for two reasons. Firstly it is to be suspended from a N-plug which is connected by an end plate with the outer conductor (refer to Fig. 4.12). Nevertheless, the septum is supported to the wall of the cell by dielectric clamps but they are very small. Secondly, a thick septum would cause more fringing fields thus causing the internal field pattern to differ widely from TEM and would affect the characteristic impedance as well. Hence 0.7 mm thick sheet is suggested for the centre conductors as well.

The flanges should be more substantial, because they are exposed to more mechanical impact than the side walls. Hence 1 mm thick sheet was chosen for the flanges. They were not welded to the open mouth of the two halves of the TEM cell, because welding would cause warping in them (especially, if thin sheets are used). Thus flanges were bolted to the shallow collar at the open mouth of the TEM-T cell halves. Fig. 4.10(a) shows the collar and the screw positions on it for one half of the cell. As thicker sheet is used, aluminium, instead of steel, was used for constructing the flanges. One of the flanges is shown in Fig. 4.10(b).

4.3.2.4 End Plate and Feed Arrangement

As discussed earlier the cell is tapered at both ends to match with ordinary 50 Ω coaxial connectors. As the upper limit of the operating frequency is 1 GHz, it is desirable to use UHF connectors such as the N-connectors at both ends of the cell. In order to mount the N-panel plug at the end of the cell, a flat end plate is essential as part of the outer conductor.

The tapered end of each half is cropped along a plane transverse to its length, maintaining the length of the cell as required by the design criteria of the resonance length of first higher order mode, mentioned earlier in section 4.3.1.4. It is shown schematically in Fig. 4.11. A thick flat plate (6 mm thick) with a hole at the centre of dimensions shown in Fig. 4.12(a) is then welded as shown. Thick plate is chosen so that warping due to welding can be minimized.

A N-panel plug (chassis mounting plug) is then tightly screwed onto this end plate as shown in Fig. 4.12(b). The septum of the cell is extended (by brazing) with a short length of copper tube at its narrow end. The inner diameter of the copper tube is such that the centre stud of the panel plug push -fits into the copper tube ensuring good electrical contact.

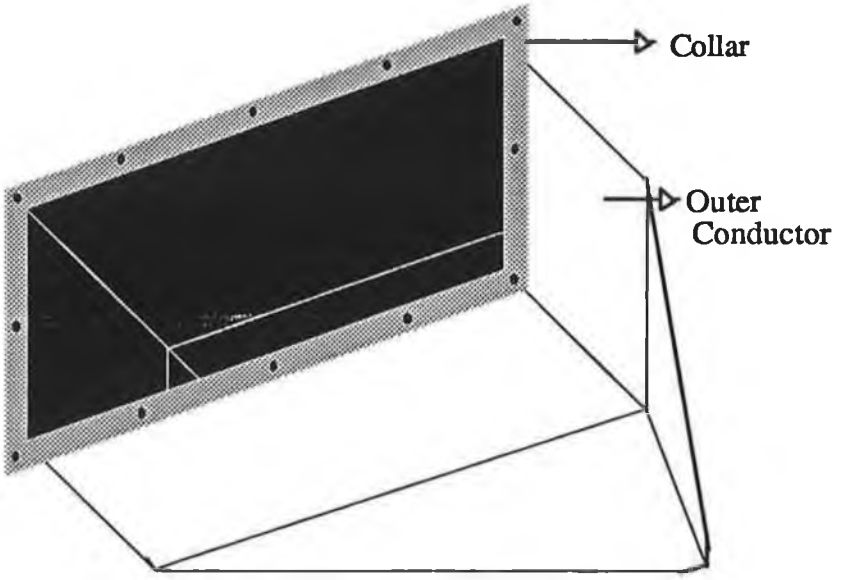

(a)

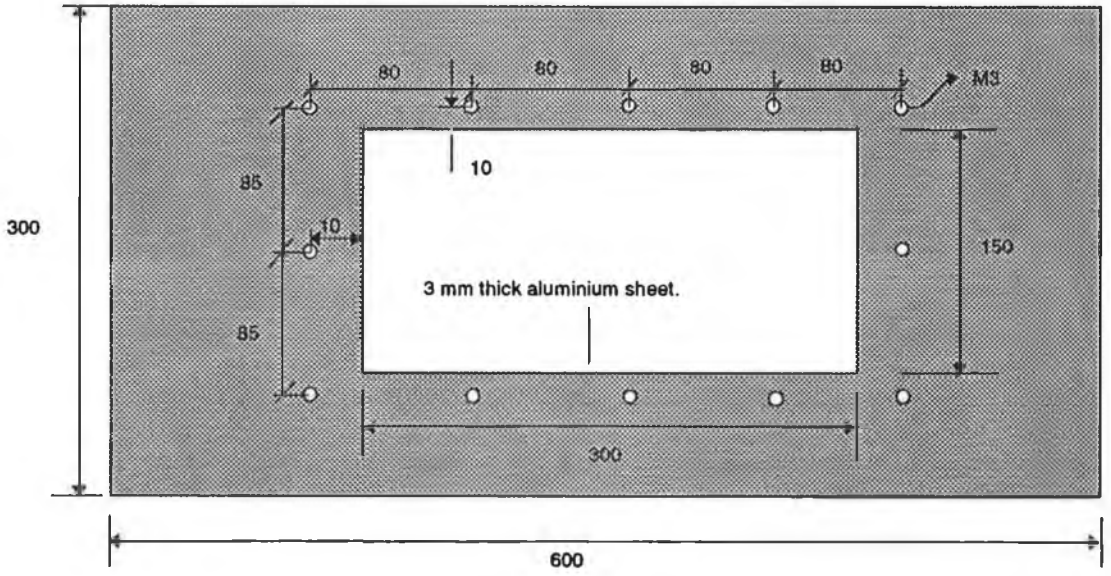

(b)

Fig. 4.10 Detail design of the flange and its mounting onto the open mouth of the outer shell of the TEM-T cell half. (a) The shallow collar of the outer shell and the screw positions are shown and (b) Aluminium flange and the screw positions. All the dimensions are in mm and the diagram is not drawn to sacle.

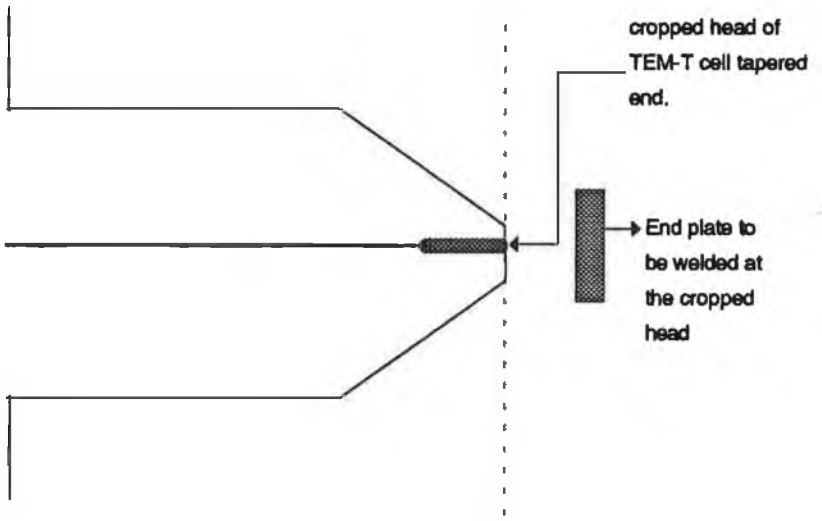

Fig. 4.11 Arrangement for mounting an N-plug at the tapered end of a TEM-T cell half. The cropped head at the tapered end is shown through a dotted line at that section.

4.4 TEST DEVICE FOR LOW IMPEDANCE FIELD SIMULATION

A newly developed Q-loop antenna is employed in the present application for low impedance field SE measurement. The major components of a Q-loop are the quarter of a loop, the corner reflector and the feed arrangement for the antenna. Their design and constructional details are described separately in the following subsections.

4.4.1 QUARTER OF A LOOP

It has been established theoretically that the quarter of a loop when mounted on a 90^{o} corner reflector, behaves as a complete loop in front of the reflector. Thus the design features of a complete loop are equally applicable for such a quarter of a loop, except that one has to consider the ease of mounting it on the reflectors and the end connections with coaxial connectors.

4.4.1.1 Design Considerations

The basic criteria in designing a loop antenna is the radiation efficiency and radiated power in the desired operating frequency range. It is evident that both the radiation efficiency and

radiated power depend on the size of the loop. Obviously, the mean loop radius and the cross-section dimension(s) of the loop are the only features to be designed.

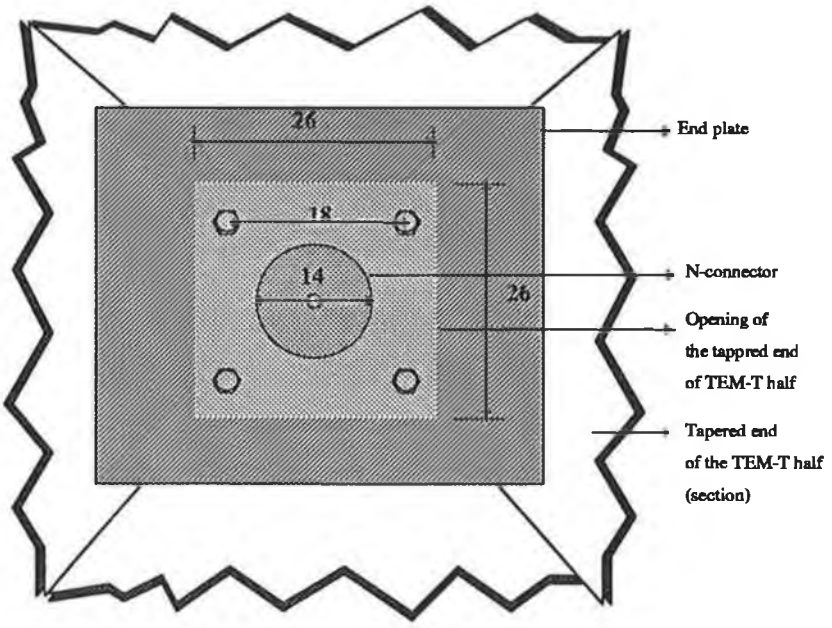

(a)

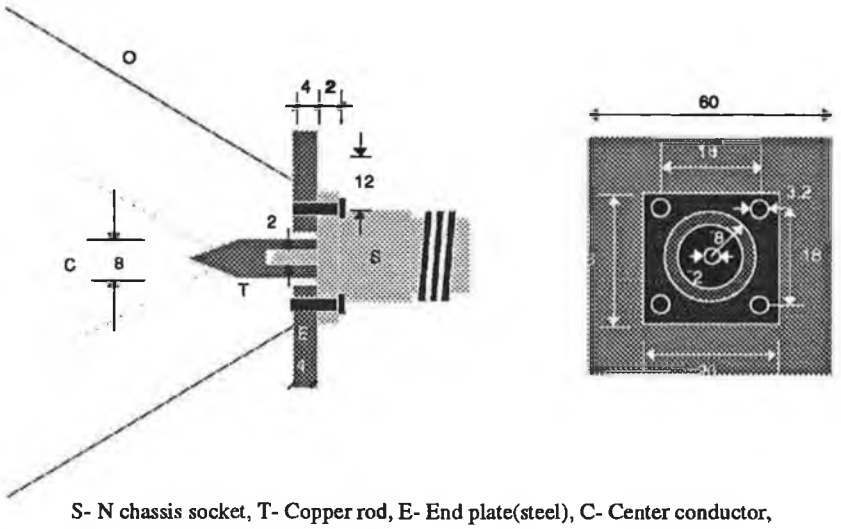

S- N chassis socket, T- Copper rod, E- End plate(steel), C- Center conductor,
O- Outer conductor..

(b)

Fig. 4.12 End plate and the end connection of the TEM-T cell. All the dimensions are in mm and the diagrams are not drawn to scale. (a) Configuration of the end plate (b) End connection of the TEM-T cell half with the N-plug.

4.4.1.1.1 Mean loop radius

Radiated power and radiation efficiency as functions of mean loop radius have been plotted at different frequencies in Fig. D5-1 of Appendix D5. From the figure it is evident that both the radiation efficiency and the radiated power of a loop antenna increase with increase in mean loop radius. However, for the present application a moderate size is to be chosen for the reasons described earlier in designing the VCLA and the TEM-T cell. The width of the MUT, as mentioned in section 4.3.1.1, dictates the width of the opening of the corner reflector on which the quarter loop would be mounted. If the diagonal of the square reflector is 30-35 cm, the length of its each arm would be 20-25 cm. Thus in order to provide enough clearance it is desirable that the loop mean radius should be half the length of each arm.

Obviously, a larger loop would be required to develop a large amount of radiated power at lower frequencies (Fig. D5-1). However, at frequencies near and above 100 MHz, a loop of mean radius 10 cm can produce sufficient radiated power. Thus the mean radius of the loop has been selected as 10 cm.

4.4.1.1.2 Shape of the loop cross-section

A solid square cross-section is chosen as the shape of the loop cross-section. As the quarter of the loop has been machined from a large block of the material, the ease of machining was a pivotal argument in deciding such shape. Moreover, fixing the quarter loop to the reflector is easier with square face sections at each end.

4.4.1.1.3 Dimension of the loop cross-section

The cross-sectional dimension(s) of the wire(or rod), that would be used for constructing the loop, is also an important factor in controlling radiation efficiency and radiated power when the mean diameter of the loop is fixed.

Since the quarter loop is machined to have a square cross-section, only one dimension must be determined. It has been observed (Appendix D5) that with the increase in this parameter, both the radiated power and the radiation efficiency increase up to a certain limit, and then they start decreasing. In Fig. D5-2 of Appendix D5, the effects of

the dimension of the loop cross-section on the radiation efficiency and radiated power have been plotted as functions of frequency.

From Fig. D5-2(a) it may be inferred that the maximum radiation efficiency can be achieved with a 18 mm square within the frequency band of 100-1000 MHz but from Fig. D5-2(b), it is obvious that the maximum radiated power is available with squares of different sizes at different frequencies. Making a compromise between maximum radiation efficiency and maximum radiated power within frequency band of 100-1000 MHz, it was decieded to select the optimum dimension of 15 mm. This has an added advantage that it providing enough room for mounting the BNC panel connectors at the ends of quarter loop where it meets with the sides of the corner reflector.

4.4.1.2 Construction

Bending any metal rod of square (or circular) cross-section as a 90^{o} arc is very difficult, particularly if the rod is thick (such as 15 mm square). Creeping of the rod and springing back to the original shape are the two major problems in such forming. Thus it is advisable to machine the desired shape from a rectangular block of aluminium. Specific dimensions of the quarter of the loop and the screw positions for end connections at its two flat ends are shown in Fig. 4.15(a). The sectional view of the quarter loop is shown in Fig. 4.15(b).

4.4.1.2.1 Selection of material

The ease of machining is the major criteria in selecting the material for constructing the quarter loop. It has to be a metal of very high conductivity. Copper or aluminium could be used. Although copper is a better conductor than aluminium, machining aluminium is easier and aluminium is cheaper as well. As a result blocks of aluminium were machined to make the quarter loops.

4.4.2 REFLECTOR

Reflectors improve the directional property as well as the gain on an antenna. In the current application another purpose of the reflector is to provide a quasi-shielded test environment for the test device. The design and construction are simple apart from the measures that are to be taken, to reduce edge diffraction.

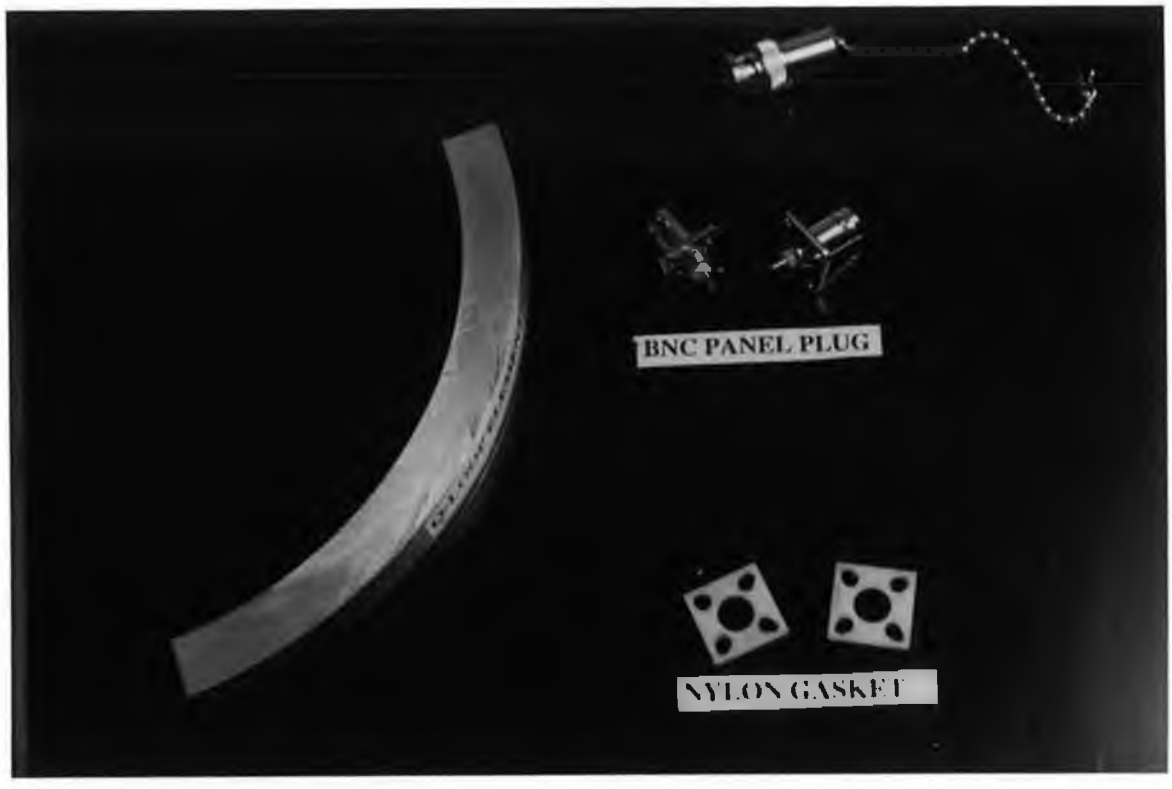

Fig. 4.13 Photograph of the Q-loop element of the Q-loop antenna. Connectors and gaskets are shown in the diagram.

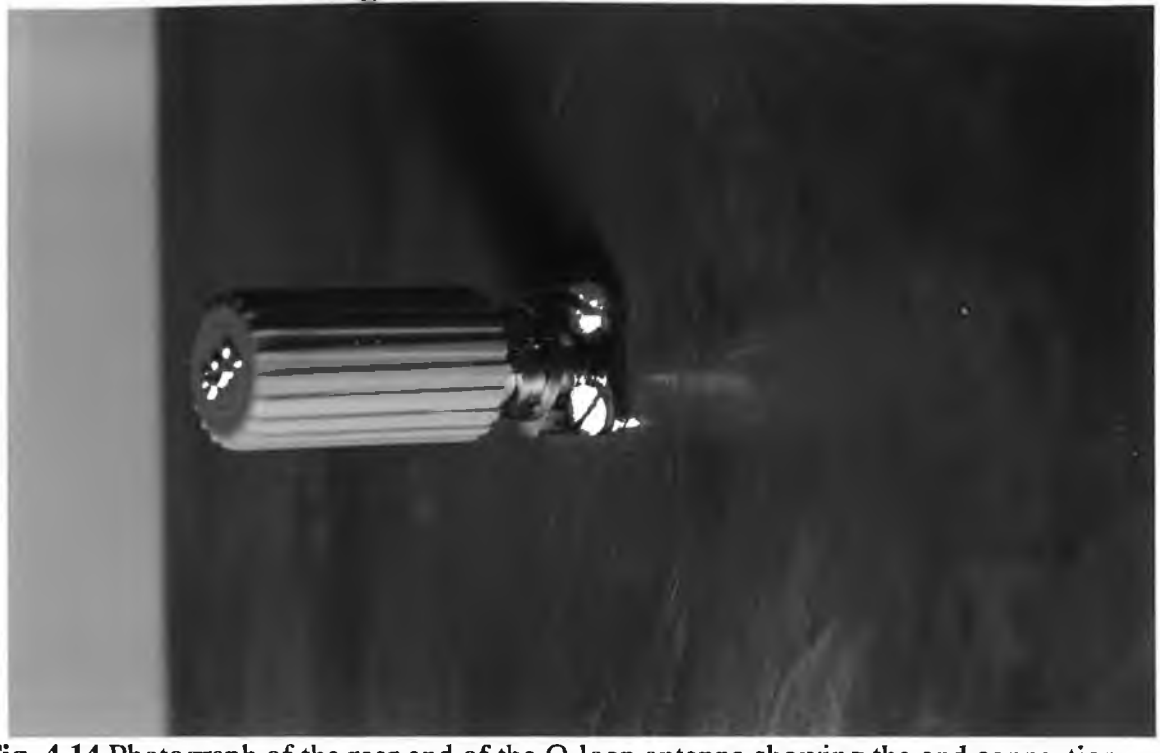

Fig. 4.14 Photograph of the rear end of the Q-loop antenna showing the end connections.

4.4.2.1 Design Considerations

The most important factor in designing a reflector is that it is to be large compared to the source antenna so that the image theory holds. The theory holds for infinitely large ground planes (reflectors). In practical designs, it is assumed that if the dimensions of the reflector are six to ten times larger than the source antenna, image theory can reasonably be applied.

Two pairs of reflectors were designed. One pair for SE measurement and the other pair for antenna measurements. For SE measurement, as described in the next chapter, it is essential that the MUT is in the near field region of the antenna and as such short reflectors were used. Antenna measurements, on the contrary, were performed mostly in the far field region, as described in chapter 6, and in order to get rid of the edge diffraction, long reflectors were built. In both the cases, however, the width of the reflectors were the same and it was about six times the mean radius of the quarter loop antenna.

4.4.2.2 Construction

Any metallic sheet of good conductivity can be a very good reflector. Copper or aluminium sheet can be used. In our application, aluminium sheet has been selected for constructing the reflectors. As reflection is the main objective that is to be achieved from the reflector, even very thin sheet can be used. Obviously, it should be strong enough, so that it remains straight in any orientation. Thus the reflectors were made of 2 mm thick sheet.

The width of the reflectors were 60 cm. The length of the arms was different for the two different sets. The length of each arm of the reflectors that were used for SE measurement, was 25 cm (up to the edge, excluding the curvature and the flat extensions) so that the MUT can be placed in the near field region of the Q-loop even up to 300 MHz.). The reflectors which were used for antenna measurements, had arm length 60 cm (excluding the curved portion and flat extensions). The diagram of the larger set of reflectors are shown in Fig. 4.16.

The reflector can be constructed by joining two flat sheets at an angle of 90^{o} but thin aluminium sheet was selected as bending a large sheet is a simple way of constructing the square reflector.

4.4.2.2.1 Reducing the effect of edge diffraction

Due to the sharp edge of the reflectors, the region behind the sheet reflector would not be a full shadow region. There would be some radiated field in this region as well which may be explained with the Geometrical Theory of Diffraction (GTD). The pattern in this region is effectively that of two weak line sources, one along each edge [159].

The diffracted radiation into the shadow region can be minimised by modifying the sharp edges of the reflectors into rolled edges and Burnside *et al.* [154] have demonstrated that a curvature of radius > $\lambda/4$ where, λ is the longest operating wavelength, at the edge of the reflectors can reduce the edge scattering significantly. Moreover, wrapping the edges with some absorbing materials could further reduce these effects [126, pp. 549].

Thus in order to reduce the edge diffraction, near and above 100 MHz, the edges of the reflectors were curved with a radius of curvature > 75 cm. However, no absorbing material was wrapped around this edges, because effective absorbers at this low frequency range are seldom available and very expensive.

4.4.2.2.2 Fixing the Quarter loop on to the reflector

The reflector is the ground plane and thus it should be electrically isolated from the quarter loop. Hence it is essential to mount it (quarter loop) onto the reflector putting some insulating gasket or pad in between. A thin block of nylon with a hole at the center (to pass the BNC panel jack) is used for this purpose. There is a groove in the block at the top so that the flat end of the quarter loop push-fits there. The quarter loop is then screwed on to the reflector with long nylon screws. The design of the end connections along with the screw positions for the panel jacks are illustrated in Fig. 4.17.

4.4.3 FEED ARRANGEMENT

It is essential that uniform current would flow through the quarter loop. A simple arrangement can be made by feeding through one end of the quarter loop and connecting a load at the other end. Care must be taken to feed the antenna in a RF tight way. 50 Ω BNC panel connectors are fitted at both ends. One of them provides the I/O port and the other

end is terminated with a 50 Ω coaxial load. The illustration of the rear end of the Q-loop antenna shows in details the feed arrangement and the load connections (refer to Fig. 4.14).

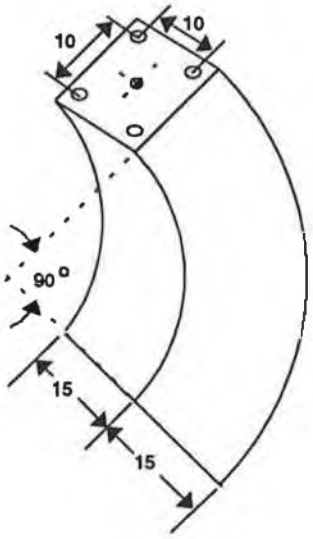

(a)

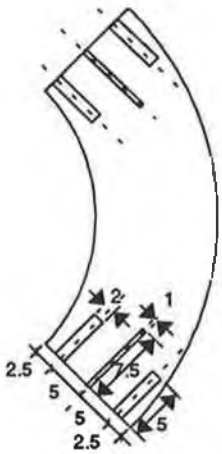

(b)

Fig. 4.15 Detail design of the Quarter of a loop. The screw positions for end connections and hole for penetrating the centre stud of the panel jack have also shown (a) Isometric view (b) Sectional view. Dimensions along the width and depth are exaggerated for better understanding. All the dimentions are in mm.

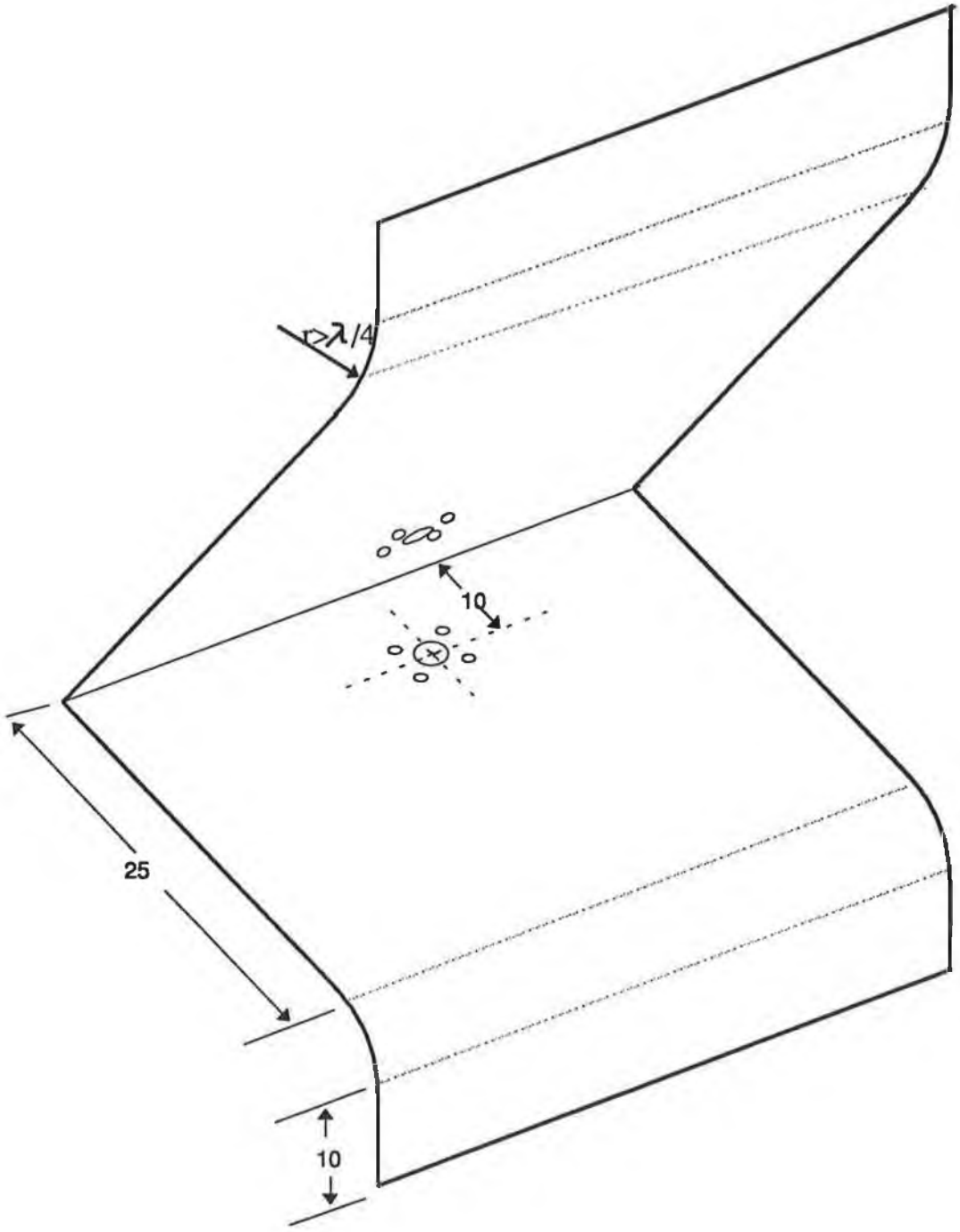

Fig. 4.16 Design of the 90^{o} corner reflector. The recommended material is aluminium sheet of thickness 2 mm. Curvature made for reducing the effect of edge diffraction is also shown, $\lambda = 3$ meter for the longest operating wavelength in the current application. All the dimensions are in cm and the diagram is not drawn to scale.

The input impedance of the Q-loop antenna may be altogether different from 50 Ω. However, it is not necessary to deliver maximum power to the load, the basic requirement is to maintain a uniform current through the quarter loop.

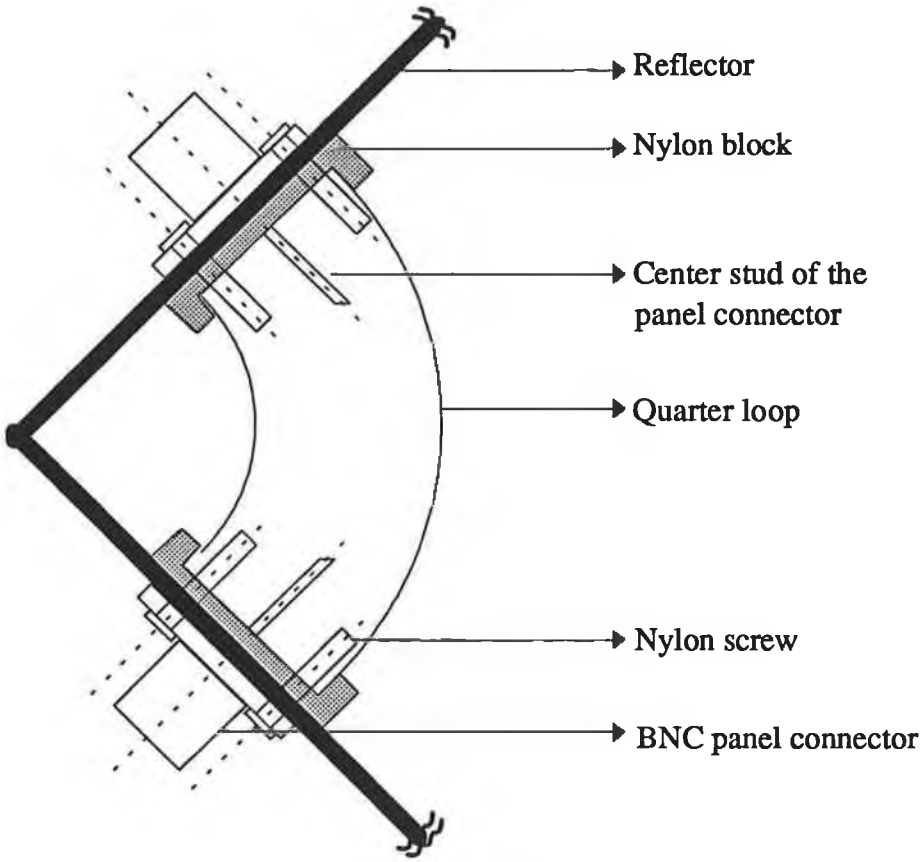

Fig. 4.17 Detailed diagram of the end connection of the quarter loop with the reflector and the panel connector. The nylon gaskets are shown which maintain electrical separation between the quarter loop and the reflectors.

4.5 FRAMES FOR HOLDING THE TEST DEVICES

IL measurement is the basic principle of determining SE with the aforementioned test devices as stated earlier in chapter 2. Thus it is essential to mount a pair of each antenna in a face to face position to construct the test devices. Moreover to simulate on-line SE measurement situation, some mechanism (may be as an integral part of the holding frame) is necessary to move the MUT sheet through the gap between the pair of antennas with a moderate speed.

Since the structure of all three test devices is different separate frames had to be fabricated for each of them. They had to be similar in a sense that holders for the pair of devices should be in the frame and the same mechanism of moving the MUT sheet could be applied for all of them. It is desirable that they be made from wood or some strong dielectric material, so that they do not behave as an EM scatterer around the test devices.

4.5.1 FRAME FOR HOLDING THE VCLA ASSEMBLY

The frame may have the structure of a typical optical bench. There should be movable curved holders on wooden vertical uprights, whose position can be monitored from a scale fixed at the base of the frame. These curved holders may be made of metallic sheets and they can be screwed to the VCA wall. An schematic diagram of the frame is shown below in Fig. 4.18. The whole frame is to be made from timber.

4.5.1.1 Mechanism for moving the MUT sheet in between the pair of test devices

If a separate mechanism irrespective of the frame structure can be developed for moving the MUT sheet in between the pair of test devices, the same structure can then be applied for on-line SE measurement with all three test devices.

For on-line SE measurement, the MUT is to be passed between the gap of the two halves with a moderate speed. That can be accomplished by a separate roller assembly. In this application, the MUT sheet was moved manually. Two pairs of vertical uprights held a pair of revolving rollers as shown in Fig. 4.19. The rollers were made of nylon. The distance between the two pair of uprights is adjustable. The gap between the two uprights of each pair is the same and is only slights wider than the MUT. The MUT sheet can be clamped with the rollers at its two ends and can be passed between them. The horizontal cantilever supports held "fixed rollers" (as indicated in the diagram) which allow the portion of MUT sheet between the two halves of the test device to remain vertical while moving. The handle is provided to move the MUT sheet manually. These movement can easily be made motor operated.

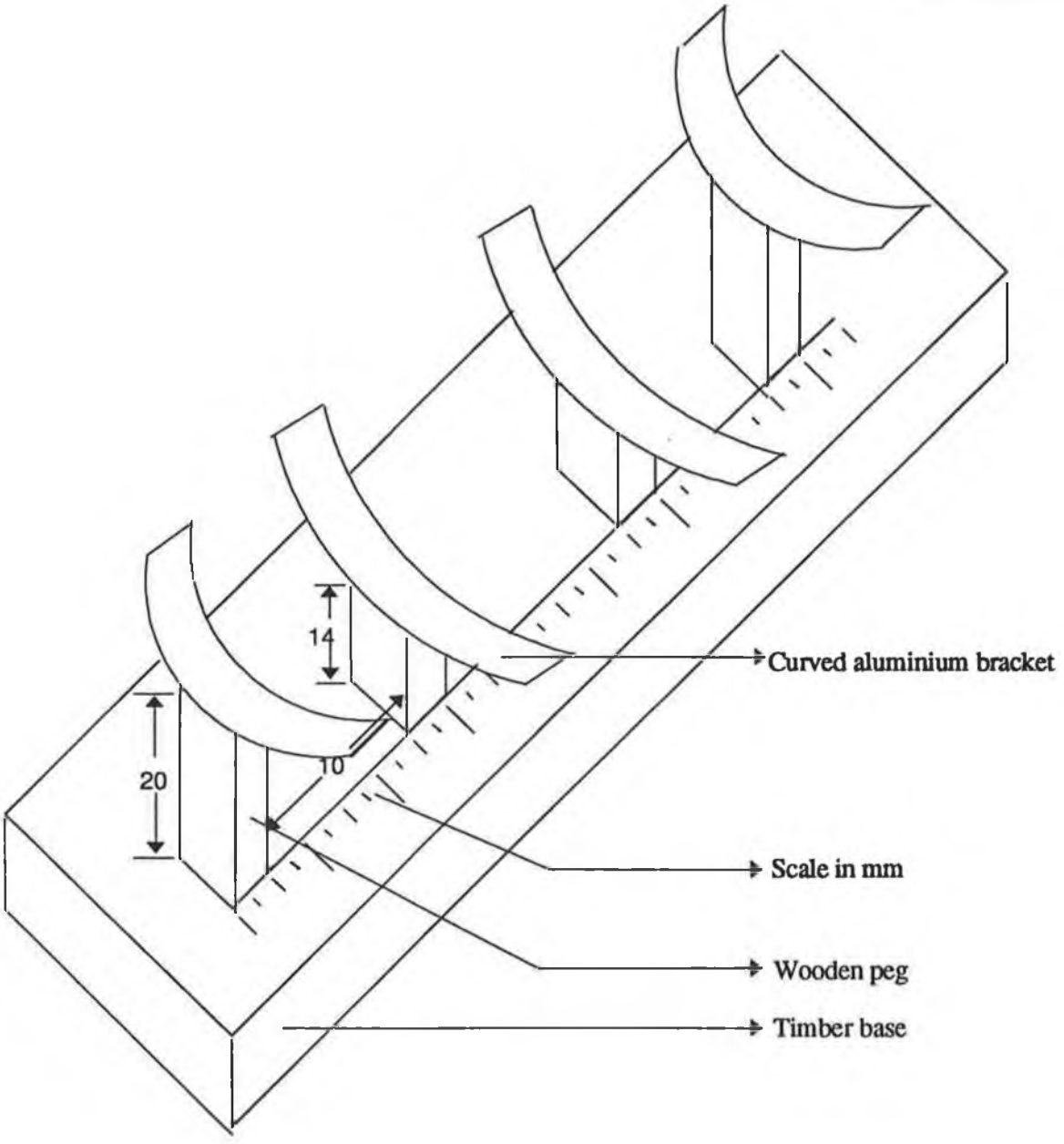

Fig. 4.18 Bench for holding the pair of VCLAs for on-line SE measurement. All the dimensions are in cm and the diagram is not drawn to scale.

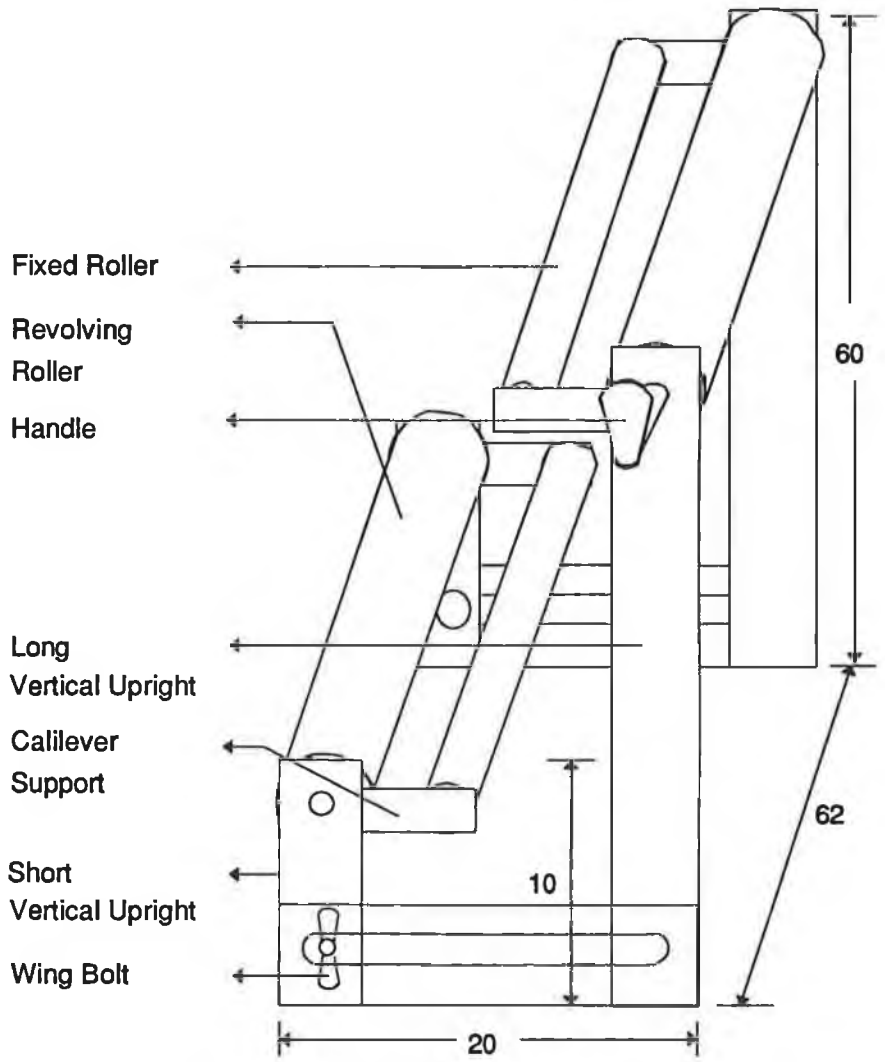

Fig. 4.19 Mechanism for moving the MUT sheet in between the two halves of the test devices. All the dimensions are in cm and the diagram is not drawn to scale.

4.5.2 FRAME FOR HOLDING THE TEM-T CELL

Two different holders were made for the TEM-T cell. For clamped stationary measurement (CSM), the cell was placed in a vertically upright position, in order that the self weight of the upper half of the cell could be exploited to press tightly the MUT sheet onto its bottom half. In case of non-contacting stationary measurement (NCSM) and on-line SE measurements, the cell halves were placed horizontally in face-to-face position.

4.5.2.1 Frame for holding the TEM-T in CSM

A hollow wooden cubical truss structure was used to hold the bottom half of the TEM-T cell. The tapered end of the cell half passes through the box and its (cell half's) neck fits tightly to the frame. Care must be taken to keep the connector at the lower end accessible. The frame is shown in Fig. 4.20(a).

The MUT is placed on the open mouth of the bottom half and the other half of the cell is positioned on the MUT so that the flanges align properly. The top half tightly presses the MUT onto the bottom half.

4.5.2.2 Frame for holding the TEM-T in NCSM

A horizontal podium was built for each half of the cell. The two podiums were connected to each other through horizontal bars at each side as shown in Fig. 4.20(b). The horizontal bars are slotted at the middle and there is a scale fitted at one bar. The gap between the two halves can be changed and the scale reads the separation between the two halves directly.

In on-line SE measurement configuration, the same movement mechanism, described earlier in section 4.5.1.1, can be applied fitting that mechanism with the above mentioned horizontal frame.

4.5.3 FRAME FOR HOLDING THE Q-LOOP ANTENNA

The very structure of the corner reflector of the Q-loop antenna suggests a V-grooved structure for holding it. As mentioned earlier for TEM-T cell, two separate frames are built for holding the Q-loop pair, one for stationary measurement and the other for on-line SE measurement. However, no extra frame is to be built for on-line SE measurement, as the TEM-T cell frame can be used with little modification.

In case of stationary measurement, a wooden box with V-grooves on both sides is provided for the Q-loop antenna which is to be placed at the bottom. Two vertical uprights are attached to the two sides of this box. The other Q-loop of the pair can be placed on top of the triangular wooden blocks fitted at the end of the vertical uprights as shown in Fig. 4.21(a).

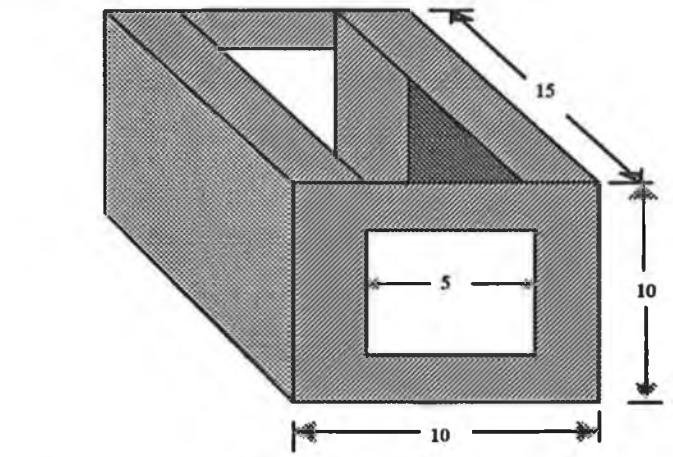

(a)

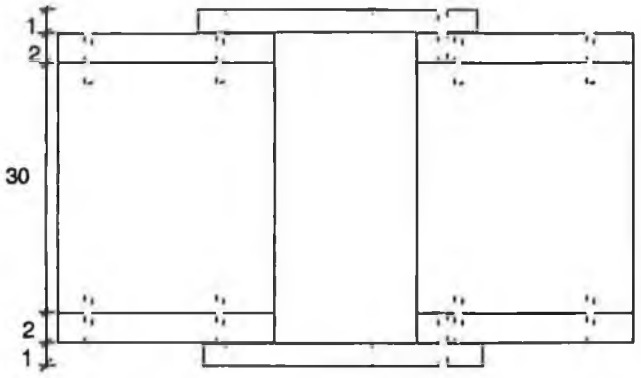

PLAN

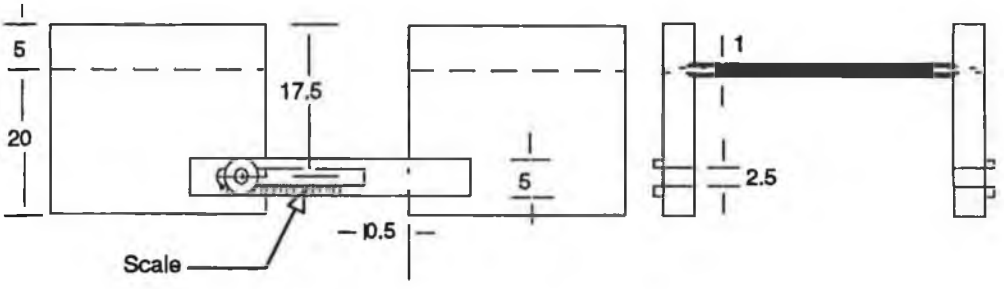

SIDE ELEVATION FRONT ELEVATION

(b)

Fig. 4.20 Frame for holding the TEM-T cell for SE measurement (a) Holder for clamped stationary measurement (b) Holder for non-contacting stationary measurement and on-line SE measurement. All the dimensions are in cm and the diagrams are not drawn to scale.

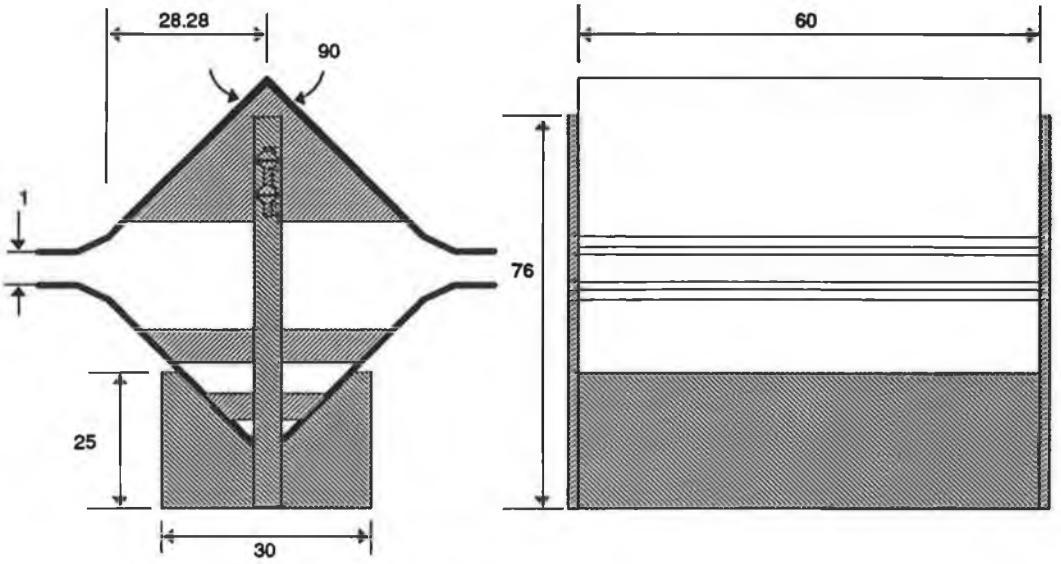

(a)

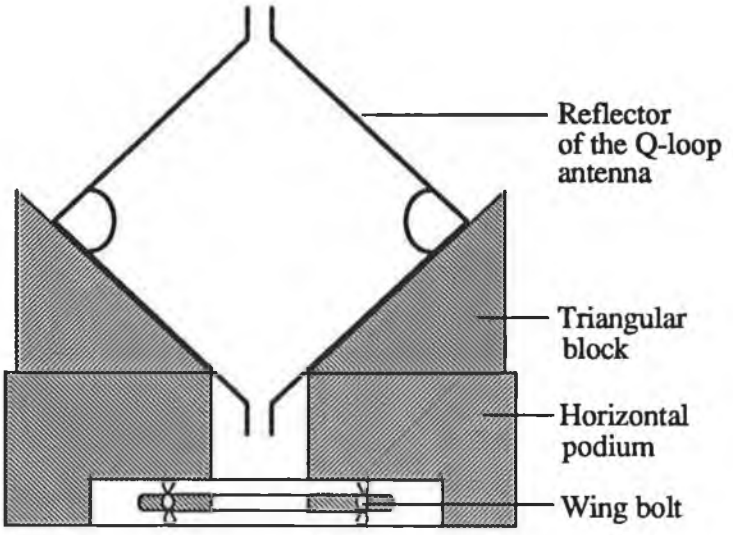

(b)

Fig. 4.21 Frame for holding the Q-loop antenna pair for SE measurement. (a) Wooden frame for stationary measurement. (b) Modified form of the TEM-T cell frame for holding the Q-loop pair in on-line SE measurement configuration. All the dimensions are in cm and the diagrams are not drawn to scale.

On-line SE measurement can be performed by placing the pair of Q-loops on the horizontal podium frame built for the TEM-T cell test device which was described earlier in section 4.5.2.2. A triangular (right-angled triangle) wooden support is clamped to each of the

horizontal podiums as shown in Fig. 4.21(b). The reflector of the Q-loop antenna is then clamped to the slanted face of this triangular support and this would arrange the Q-loops horizontally in a face-to-face position. The mechanism of movement of the MUT sheet is then fitted into the system to get on-line SE data.

4.6 INSTRUMENTS AND ACCESSORIES

Fortunately, the SE measurement techniques applied in the present application do not involve any sophisticated instruments and accessories. The basic set of instruments are the same for all three test devices. The major instruments are the signal generator to feed signal into the transmitting half of the test device and the spectrum analyzer or EMI receiver to record the signal strength at its (test device's) receiving half.

Depending on the test devices, some accessories, such as amplifiers and attenuators may be necessary. Some output devices, such as plotter, pen recorder, memory card are also important to display and record the test results.

However, for on-line SE measurement, computer controlled automated data acquisition is particularly important in order to achieve adequate speed and accuracy, in which case the major instruments should have computer interfacing capability.

A brief discussion of the instruments and the accessories employed in the current application is given below. Most of these instruments are commercially available and the detailed specifications can be obtained from the manufacturers. Only the relevant features are mentioned.

4.6.1 SPECTRUM ANALYZER

A Chase ADVANTEST R3361A spectrum analyzer was used. This instrument uses a synthesized technique to cover a wide frequency band of 9kHz to 2.6 GHz. It also offers high-performance functions such as the 1Hz-resolution frequency setting function and 1Hz-resolution frequency counter function. The analyzer has an internal controller function, parallel I/O, and GP-IB interface for line connection and automatic measurement. The following are the relevant important features of this spectrum analyzer:

* Wide frequency range: 9 kHz to 2.6 GHz
* Total level measurement accuracy of ±1 dB (typical)
* Central frequency and start/stop frequency setting with 1 Hz resolution by synthesizer technique
* Internal tracking generator
* 50-ohm input impedance
* 120 dB display range
* GP-IB interface (as standard)
* Direct plotting function

The R3361A has an internal tracking generator (TG) and the 120 dB dynamic -range display guarantees a 110 dB dynamic measurement range for frequency characteristic measurement with this generator. A log sweep is also available.

4.6.2 SIGNAL GENERATOR

The Hewlett-Packard Model 8657B sysnthesized signal generator was used. It has a carrier frequency range of 100 kHz to 2060 MHz. Frequency resolution is 1Hz. Its output amplitude is levelled and calibrated from +13 to -143.5 dBm. The HP 8657B has precise power levels from +7 to - 143.5 dBm (114 dB μV to 36.5 dB μV) with over range to +17 dBm at decreased accuracy. The carrier frequency, output amplitude, and modulation functions can be remotely programmed via the Hewlett-Packard Interface Bus (HP-IB).

4.6.3 POWER AMPLIFIER

The Amplifier Research 5W1000 power amplifier was used as an amplifier in the input stage. It is a broadband solid-state amplifier providing linear operation over the spectrum from 500 kHz to 1000 MHz. The power rating of the amplifier is 5 watts, and it has the important features like instantaneous bandwidth, flat output, and immunity to even worst case load mismatch.

4.6.4 PRE-AMPLIFIER

A Chase ADVANTEST preamplifier model R14601 was used at the input of the spectrum analyzer in order to amplify the received signal. The operating frequency range of this

preamplifier is 9 kHz to 1 GHz. The gain is 25 dB or more and almost flat. The I/O impedance is approximately 50 Ω and the I/O connectors are N-type.

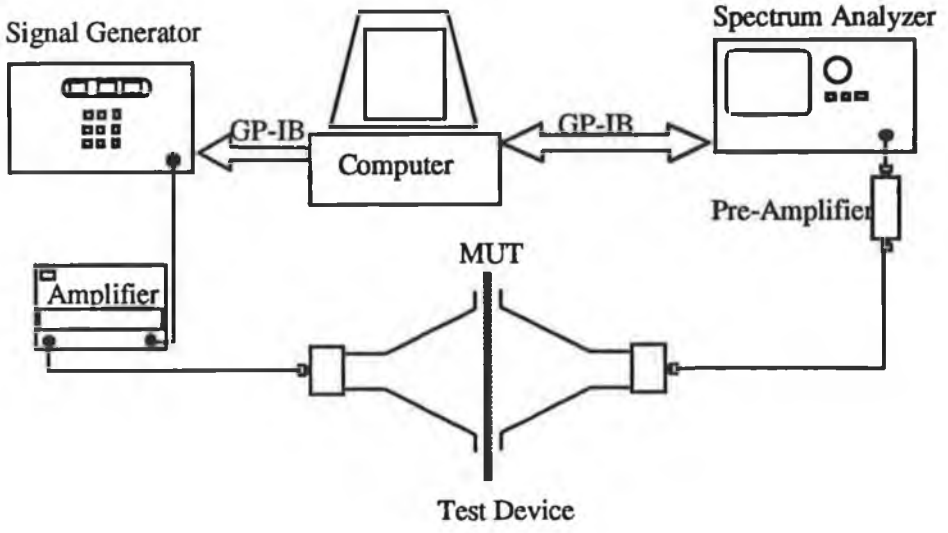

Fig. 4.22 Block diagram of the automated on-line SE measurement system. A generalized diagram is shown which is applicable for all three test devices.

Several other peripheral equipment, such as a PC to control the automated data acquisition and a plotter HP5584B (to get the plot of the received signal strength directly from the output of the spectrum analyzer) were used. The block diagram of the overall automated measurement setup is shown in Fig. 4.22.

4.7 CONCLUDING REMARKS

The design and constructional details of the newly developed EMC antennas and the test devices for SE measurements (employing these antennas) have been described. VCLA has not been constructed as mentioned earlier at the beginning of this thesis, yet the design features are presented. The proposed design and constructional procedure of this device, although they may need some modifications in the practical manufacturing, provide a thorough guideline for satisfying the requirements of on-line SE measurement system.

There is obviously some design flexibility in the frames for holding the test devices and as such the actual frames of Q-loop antenna are a bit different from that described in this

chapter. The common movement mechanism for moving the MUT sheet, is specially designed for the flexible PET laminate sheet (sample #1) which of course, is not applicable for conductive composites that are not flexible. However, the main purpose of this study is to observe the effect of the movement of the MUT sheet in a moderate speed on the recorded SE data. Thus the speed is the main consideration, not how it was achieved.

Finally the major instruments and accessories employed for on-line SE data acquisition have been described. There are several other accessories and test facilities which were used for antenna measurements that had been performed in the EMC laboratory of Power Electronics Ireland of the University of Limerick. They will be described later in chapter 6.

Chapter 5

SE MEASUREMENT

OFF-LINE SE MEASUREMENT AND TEST RESULTS
ON-LINE SE MEASUREMENT AND TEST RESULTS
CALIBRATION OF THE TEST DEVICES
CALIBRATED TEST RESULTS
COMPARISON WITH THE PREDICTED SE

5.1 INTRODUCTION

The SE of planar sheet-like conductive plastic materials against near field sources was measured. The developed test devices measure the SE in a situation that attempts to reconstruct the on-line environment likely to prevail in the manufacture of such plastics. Near E-field measurements have been carried out with the modified TEM-T cell. Q-loop antennas have been employed for near H-field measurement.

The developed antennas produce the desired field in a quasi-shielded environment requiring some calibration factors to be introduced into the test results to obtain reliable SE data. The test devices are calibrated by taking into account the background noise, indirect path signal infringement and radiation loss. Special measurements are thus essential to estimate appropriate correction factors and these can be introduced prior to recording the test results in course of automated measurement.

The proposed regularly filled (FSS like filling) conductive plastic sample [160] was also tested in order to verify the predicted improvement in their SE values over conventional filled conductive composites (where the conductive fillers are randomly distributed).

Test results of the near field SE measurements are presented in section 5.2 where the discussion on the automated measurement system is also included. Section 5.3 introduces the tests and data processing necessary to calibrate the test devices. All these test results are then compared with the predicted SE values and analytical models of the test configurations in sec 5.4.

5.2 SE MEASUREMENT

The frequency range covered was from 10 MHz to 1 GHz for most of the samples. However due, mainly, to the calibration inaccuracies at frequencies lower than 100 MHz, it was not possible to get very accurate SE data during on-line measurements, thus the lower range of frequency was selected to be 100 MHz for on-line measurements. For the TEM-T cell the upper frequency limit was found to be 1 GHz because above that frequency higher order mode resonances occur causing distortions to the test field. Thus the device is incapable of simulating standard high impedance field above that frequency.

Low impedance field SE measurements were taken from 10 MHz to 1 GHz. However at the lower range of frequencies, the same problem of calibrating the test device, as was observed with the TEM-T cell, was quite evident with the Q-loop as well. Furthermore, at frequencies above 300 MHz, this test device failed to estimate the SE of good quality shields.

The estimated SE values of most of the sample materials used were found to be less than 100 dB. Thus the dynamic range of 100 dB for the test system was adequate. The test devices and the instrumentation used in the measurement system were capable of providing a dynamic range of that level.

Near field SE data differs widely from far field data in a sense that far field SE data includes attenuation due to reflection, absorption and successive re-reflections inside the MUT sheet while near E-field suffers attenuation due mainly to reflection and near H-field suffers attenuation due mainly to absorption.

5.2.1 BASIC PRINCIPLE OF THE MEASUREMENT PROCEDURE

The basic principle of insertion loss (IL) measurement, which is applied in most of the SE measurement techniques (refer to section 2.4), has also been applied with test devices in the present application.

The purpose of these SE measurement procedures is to quantitatively measure the IL that results from introducing the test sample. Power from a transmitter (P_t) is coupled to a receiver, first with no material present (P_r) in order to establish a reference reception level, and then with the sample in between them (P'_r). In each case the input power of the transmitter is held constant.

$$\text{Insertion loss} = \text{SE} = 10\log_{10}\frac{P_r}{P'_r}$$

$$= 10\log_{10} P_r - 10\log_{10} P'_r$$

$$= P_r(dBm) - P'_r(dBm) \qquad (5.2.1)$$

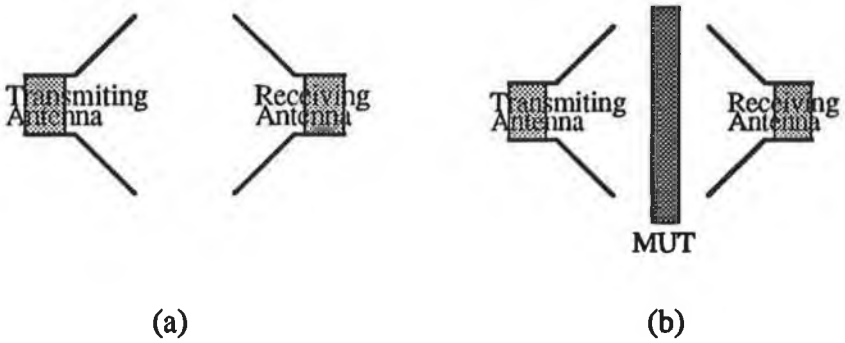

Fig. 5.1 Basic arrangement for SE measurement. (a) Reference measurement (b) IL measurement.

5.2.2 TEST SAMPLES

A wide variety of conductive composite materials is available as mentioned earlier. Attempts have been made to investigate the SE values of each type. A few samples of surface metallized plastics were chosen. A representative material was chosen from the variety of filled conductive composites and a sample of flexible laminate was also tested. Principally the measurements were taken on four different samples. In addition the shielding capability of the newly proposed regularly filled conductive plastic (RFCP) was also measured and to demonstrate the improvement in SE over randomly filled conductive plastics a few other samples were made and tested.

5.2.2.1 Polyethylene terephthalate (PET) laminate

Commercially available PET laminate, consisting of 0.07 mm copper foil backed by 0.075 mm thick polymer [161] was selected as a sample of flexible laminates, henceforth referred to as sample #1. This laminate, is flexible but highly resilient. Total sample thickness was 0.16 mm. The sample used for clamped stationary measurement was 300 mm wide and 610 mm long. A 2 meter coil of this laminate of width 610 mm was used for on-line SE measurement.

5.2.2.2 Aluminium laminate

A sample specially made by pasting aluminium microfilm using super adhesive glue (Araldit® 2005A of Ceiba-Geigi) on an ABS (Acrylonitrile Butadiene Styrene) sheet, was taken as one kind of metal plated plastic. In electroless plating, metal films of thickness 10-20 μm are the most common. The thickness of the aluminium foil used was

measured to be 16 μm. Thus apart from the mechanical properties of the coating this sample represents the shielding behaviour of a typical electroless plated plastic material. The ABS sheet was 2 mm thick and 400×800 mm in size. This sample will be referred to as sample #2.

5.2.2.3 Vacuum coated plastic

Aluminium coated ABS sheet using the vacuum metallization technique (courtesy of TOP TECH Ireland Ltd.) known as the ELAMET® coating process [162] is another type of sample which was tested. ELAMET® is a special high vacuum metallization process. Batches of plastic parts are masked, exposing only the areas that require metallization, and are mounted on customised fixtures. These are then placed in a vacuum chamber, where pure aluminium pellets are vaporised, under controlled conditions. The aluminium, in a gaseous form, then adheres to the exposed plastic areas, forming a very strong bond between the metal and the plastic.

This process is successfully used by manufacturers of the shielded enclosures for sophisticated electronic equipment like computers, digital and telecommunication equipment.

The thickness of the ABS sheet was 2 mm and the coating thickness was 2 micron. The size of the sample was chosen to be slightly larger than the flange dimension of the TEM-T cell. This is indicated as sample #3.

5.2.2.4 Carbon loaded PVC

Finally as a filled conductive plastic a carbon black loaded PVC sheet designated as sample #4 was also tested (Sample supplied by Athlone Extrusions Ltd). This type of conductive plastic has been developed with a special morphology and a low carbon black content. The polymer matrix is composed of PVC. The electric properties remain very stable at elevated temperatures and relative humidities. Tests were carried out up to 80° C and 80% relative humidity [163]. According to the supplier 7% carbon black was loaded into the PVC polymer base. Potential applications of such materials are for electric heat carriers, permanently anti static parts, electrodes for electro-deposition painting, electrodes for electrosynthesis and shields against electromagnetic radiation. Sample thickness was 2 mm. The size of the sample was the same as the flange of the TEM-T cell.

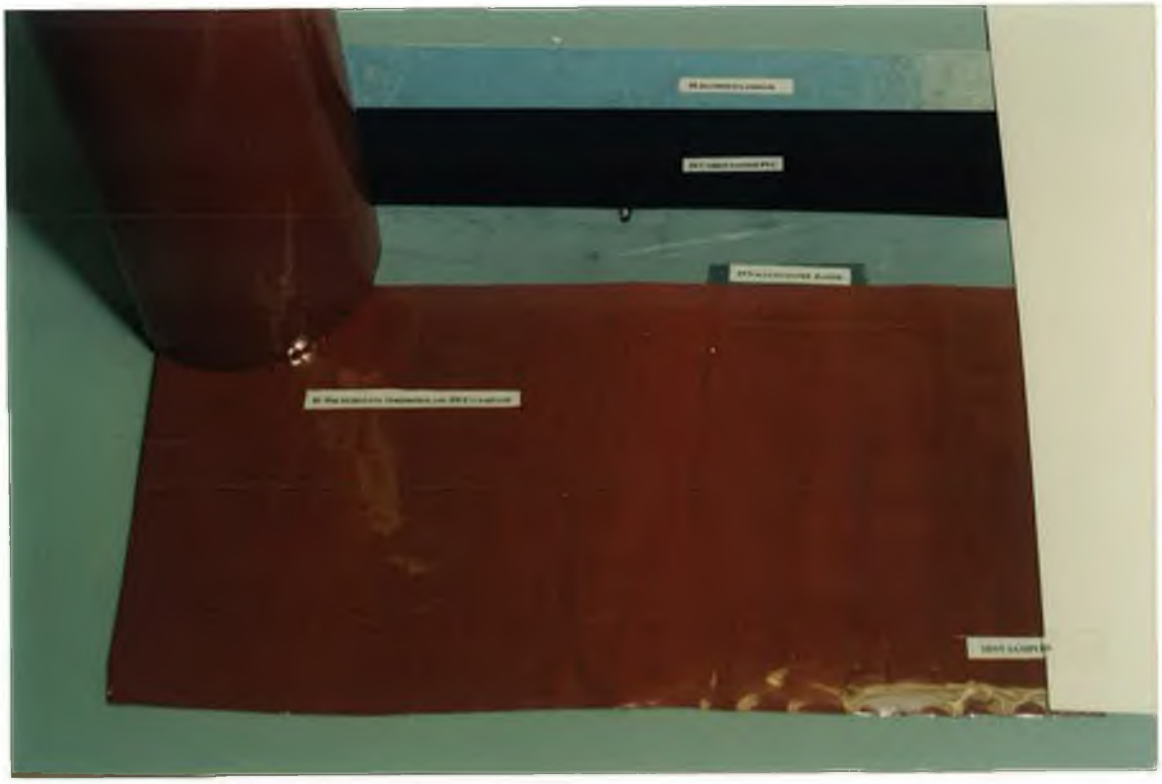

Fig. 5.2 Photograph of the test samples

5.2.2.5 Sample preparation for measurements on RFCP

The theoretical model of the shielding capability of the proposed regularly filled (FSS like filling) conductive plastic (RFCP) has been presented in chapter 3. In order to determine its SE experimentally and to compare this test results with that theoretical model as well as with the SE of available filled composite in which the flakes are randomly distributed, the following four different samples were prepared.

A regular array of thin copper strips was developed on a printed circuit board (PCB) as shown in Fig. 5.3(a), henceforth referred to as sample #5a. Because of the unavailability of large size PCBs, a 30x15 cm board was used (the selection of this particular size is dictated by the size of the open mouth of the TEM-T cell test device). Analytically it was found that the maximum reflection occurred approximately around quarter wavelength long elements although it depends on several other factors such as inter element separation, angle of incidence and type of the incident wave. Element size was selected to be 5 cm long and 2 mm wide which (theoretically) should allow observation of resonance near 2 GHz. A large element size could not be accommodated with the board size available. Although some higher order modes are known to be generated inside the TEM-T cell above 1 GHz, these are limited to two or three. Thus it

was assumed that the frequency range for this measurement could be extended to 2 GHz without incurring serious errors in the results. Sample #5b was prepared with a random distribution of the copper strips on a same size (30x15 cm) PCB and is shown in Fig. 5.3(b). The dimension of each element and the total number of elements were the same as before. As the samples do not cover the flanges at the open mouth of the TEM-T cell, a special sample holder was made from 3 mm thick perspex sheet, with dimensions equal to those of the flanges. At the centre of the holder there is a rectangular slot of 30x15 cm to fix the samples. For reference measurement a PCB of the samples' size with all the copper removed from it was used to study the effect of the dielectric substrate on the reflection coefficient. This is referred to as sample #5c. To normalize the reflection coefficient with that of a continuous copper screen as was done in the theoretical analysis, another 30x15 cm PCB was taken without removing any copper from it. This is referred to as sample #5d.

Fig. 5.3 Photograph of the test samples 5a-d.

5.2.3 AUTOMATED MEASUREMENT

In section 2.2.2, the importance of introducing automated instruments in susceptibility and emission measurements has been noted. In particular, for on-line SE measurement of

a conductive composite within its production cycle, the introduction of automated measurement is mandatory to make the speed of data acquisition and manipulation satisfactorily fast. The necessity of such automation through computer controlled systems is also obvious for the adjustment of the real-time data using the appropriate calibration factors determined prior to recording the test results.

A block diagram of a test system is shown in Fig. 4.22. For the work reported in this thesis a HP8657B synthesised signal generator and a Chase ADVANTEST R3361A spectrum analyzer have been used. The spectrum analyzer has a built-in swept frequency function generator as well. With the test set-up illustrated in Fig. 4.22, it is essential to maintain synchronous operation of the signal generator and the spectrum analyzer at each frequency. The listing of a simple computer program which measures the SE of a material starting from frequency of 100 kHz up to 1 GHz in three different steps with the test set-up shown is presented in Appendix E1. However, for simplicity of the test procedure and for maintaining synchronism mostly the built-in function generator of the spectrum analyzer was used.

5.2.4 PLACEMENT OF THE MUT SHEET BETWEEN THE TEST DEVICES

For the test devices employed in the present analysis the near field region was determined where they could provide the desired field pattern and while placing the MUT sheet care has been taken to maintain this distance.

Placing the MUT sheet very close to the test device indeed reduces the possibility of indirect path signal infringement and the distortion of the test field due to background noise, which will be described in the following subsections. Very close spacing between the test sheet and test device thus produces a quasi-shielded environment which is essential for the measurement of SE against EMI.

5.2.4.1 Position of TEM-T halves w.r.t the MUT sheet

The main purpose of placing the MUT sheet very close to the TEM-T halves is to simulate the incidence of high impedance field in the test region. From Fig. 3.14(b), it is evident that the field in front of the TEM-T transmitting half remains predominantly electric up to a distance of $2\pi r / \lambda \approx 1.2$. Thus for a 30 cm long EM wave (frequency 1 GHz), one can obtain high impedance field up to 6 cm away from the transmitting half of the cell.

With the closest possible spacing the immunity against background noise can be significantly improved. If the separation is comparable even with the smallest operating wavelength, ambient noise can affect the test results severely. However, in the present analysis, the smallest operating wavelength was 30 cm and the separation was maintained ≤ 3 cm, thus this effect may be neglected. EMI coming parallel to the sheet (as shown in Fig. 5.4) can affect test results adversely because in that case the flange and the test sheet or the flanges of the two halves might act as parallel plate wave guide for the incoming EMI.

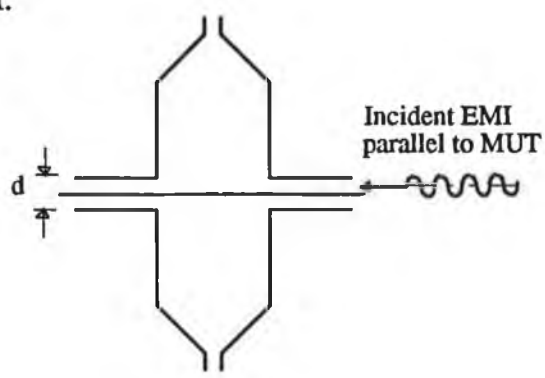

Fig. 5.4 The possibility of the incidence of EMI on the test location.

Even in that case the smaller the separation the shorter the cut-off wavelength of the propagating higher order modes (The cut-off frequency of the first higher order propagating mode is 5 GHz with the aforementioned separation). Thus, keeping the separation between the two halves smaller in turn reduces the exposure of the test region to EMI. There are several other reasons for keeping the separation smaller, which are discussed below.

It can be demonstrated from the analysis of the field in front of the TEM-T half, described in section 3.4.2.2, that as the observation plane moves away from the aperture of the open mouth, the field magnitudes decrease in both the transverse and axial components. Similar results has been shown by Fan *et al.* [164] with an open ended circular coaxial line. Thus in order to provide a considerable amount of field strength at the test location it is essential to keep the TEM-T cells very close to the MUT sheet.

The upper frequency limit of the test fixture is set primarily by the gap between the two halves of the TEM-t cell. The gap should be sufficiently small so that the open end of the radial line (which model the flanges in the fixture described later in section 5.4.1.2) does not radiate [143] a significant amount beyond the perimeter of the flanges

(-4a ≤x≤4a and -4b≤y≤4b where a and b are half width and half height of the cell respectively).

The lower frequency limit of the technique depends mainly on the capacitance between the centre conductors (septum). At lower frequencies, the transmission coefficient becomes very small, because the capacitive coupling between the septum is very small. As it is necessary to keep the septum very thin to maintain a TEM mode in the cell, one must resort to close separation of the septum to provide better capacitive coupling between them. Otherwise the inaccuracies in measuring the small amount of transmitted power would limit the lower frequency of operation [143].

Strictly speaking, the assumption of the existence of only TM_{0n} higher order modes in the region of discontinuity holds only if the spacing between the two halves is much smaller than half the wavelength [85, Chap. 9], even though the structure is axisymmetric. For smaller spacing modes are possible with circumferential variations but no axial variations. Thus it is another reason to keep the spacing very small.

5.2.4.2 Position of Q-loop antennas w.r.t the MUT sheet

The design of the Q-loop antennas assumed the use of large reflectors (image theory requires that they be infinite). For low impedance field SE measurement it is essential to put the MUT in the near field region of the transmitting antenna and for applying the insertion loss principle the receiving antenna should also be in the near field region of the transmitting one. Hence the large reflectors were replaced by smaller reflectors so that the simulation of low impedance field on the MUT sheet and on the receiving antenna at the shortest possible wavelength could be insured.

The wave impedance of the field produced by the Q-loop as demonstrated in Fig. 3.19, exhibits that the low impedance field exists up to a distance r, where $2\pi r/\lambda \leq 1$. Thus for a 1.5 meter long EM wave (200 MHz) the Q-loop elements should be placed within a distance of ≅20 cm from each other. Hence the Q-loop elements are mounted on corner reflectors with 25 cm arm length. The flat extended faces of the reflectors of the two antennas are separated by only 1 cm. The MUT sheet is placed at the middle i.e., at a distance of 5 mm from these flat faces.

Moreover with closer spacing of the two Q-loop antennas a quasi-shielded test environment could be established as was demonstrated in case of TEM-T cell device.

5.2.5 HIGH-IMPEDANCE FIELD MEASUREMENT

The TEM-T cell was originally designed to obtain SE data by clamping the MUT sheet between the two flanges. This measurement will be referred to as clamped stationary measurement (CSM). It is assumed that the data obtained by CSM are to be taken as the best available SE values for any sample and for the purposes of comparison and for convenience will be referred to henceforth as "actual" SE data.

For on-line SE data acquisition a gap has to be provided between the test device and the MUT. The MUT sheet was placed stationary between the two halves of the TEM-T cell with a gap and this arrangement is termed as non-contacting stationary measurement (NCSM). Finally the MUT sheet had to be moved in order to simulate the on-line situation and this is referred to as on-line measurement (OLM).

5.2.5.1 CSM Against High-impedance Field

The MUT sheet was sandwiched between the flanges of the two halves of the TEM-T cell maintaining close electrical contact between them The center conductors were in contact with the sheet. Hence it can be inferred that there would be negligible radiation loss in this test configuration. EM wave incident on the sheet suffers attenuation mainly due to the shielding offered by it and as the incident field is predominantly electric in nature this shielding is mainly due to the reflection of the wave from the surface of the MUT sheet. Thus it should give actual near E-field SE data. The experimental set-up was as shown in the block diagram of Fig. 5.5.

A reference measurement was done by placing the base unmetallized plastic (or polymer) material in the cell. The thickness of this base plastic sheet was taken to be the same as the MUT sheet.

The reception behaviour of the cell with this reference sample is shown in Fig. 5.7. It exhibits the capacitive coupling nature of a regular increment of 20 dB per decade of frequency of the receiving signal. Although not very significant, some distortions from linearity are evident at frequencies above 700 MHz. The sample was not clamped tightly with the flanges which left some gap between the test sample and the flanges. At the higher range of frequencies there may be some leakage even through this small gap.

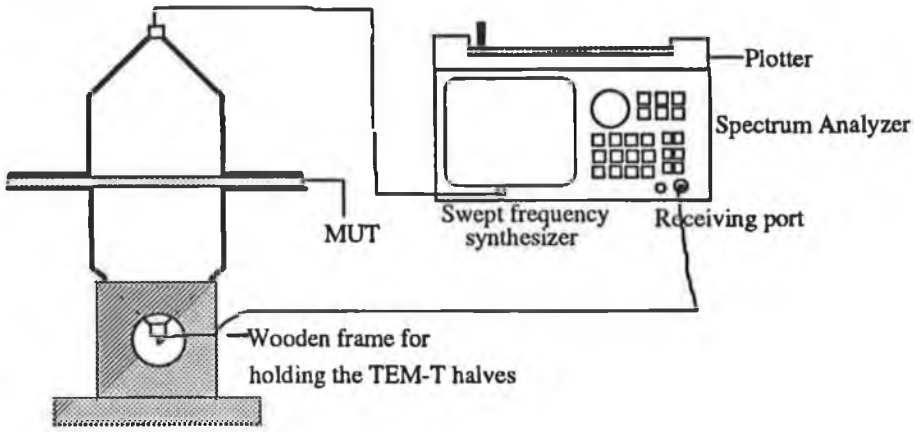

Fig. 5.5 Schematic diagram of the SE measurement system using TEM-T cell test device.

For measuring the SE of the test samples, they are then sandwiched between the flanges. The same set of measurements starting from an exciting frequency of 10 MHz to 1 GHz were taken with four different samples. These test results are then compared with the reference measurement to get the SE data of the samples. The SE values of the four different samples are shown in Fig. 5.7. This comparative measurement has another advantage in that the cable attenuation need not be taken into account as it is being cancelled out.

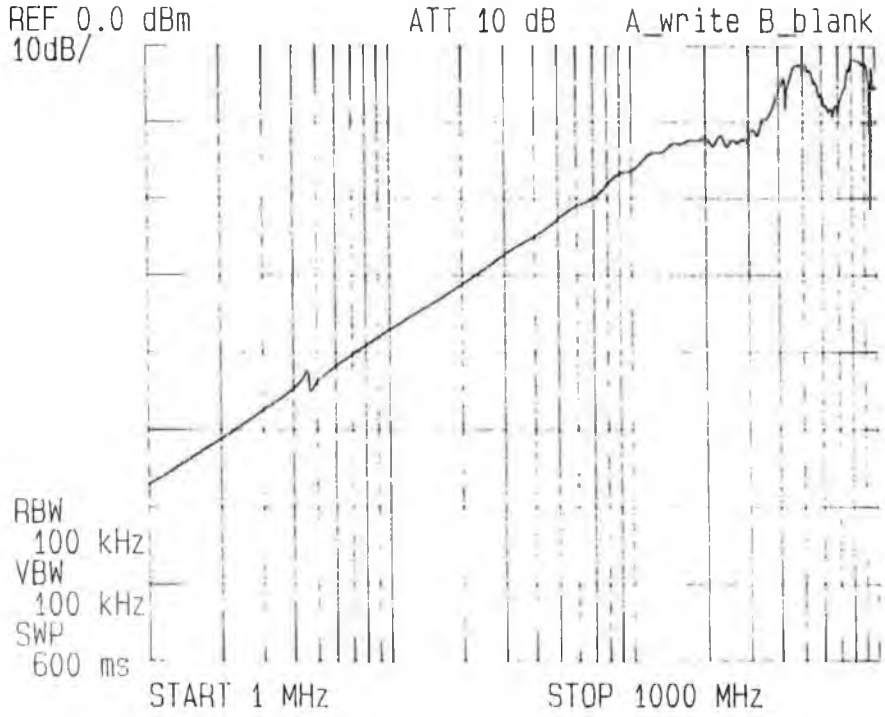

Fig. 5.6 Reference reception level of the TEM-T cell in CSM configuration. Trigger level (input signal strength) is 0.0 dBm.

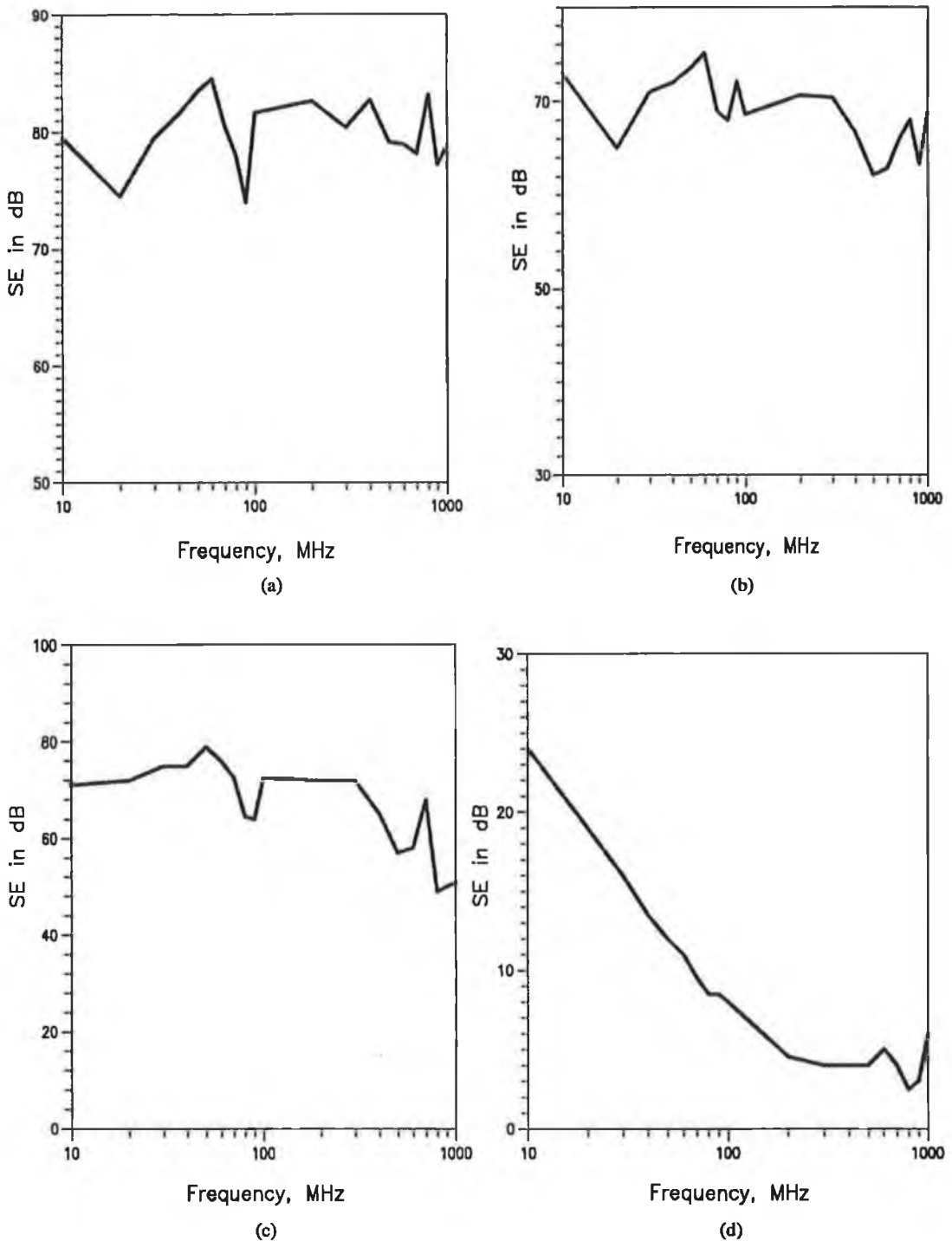

Fig. 5.7 Clamped stationary SE data with TEM-T cell (a) SE of sample #1 (PET laminate) (b) SE of sample # 2 (Aluminium foil glued onto the ABS sheet) (c) SE of sample #3 (Vacuum coated aluminium) (d) SE of sample #4 (Carbon loaded PVC).

5.2.5.2 NCSM Against High-impedance Field

This is the transition from closed test fixture for laboratory measurement to open test fixture necessary for on-line measurement. The MUT was placed stationary in a holder halfway between the two halves of the TEM-T cell.

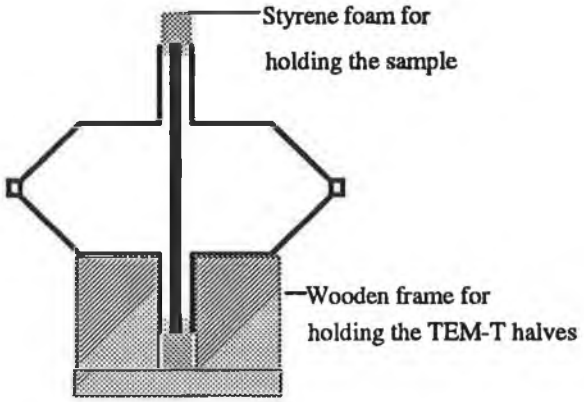

Fig. 5.8 Schematic diagram of the test device and sample position for non contacting stationary measurement (connections to the spectrum analyzer are not shown).

The gap between the two halves of the TEM-T cell was maintained at 3 cm in order to ensure near field distance and other requirements as discussed earlier in section 5.2.4. The schematic diagram of the test device and the position of the MUT is shown in Fig. 5.8. For ease of mounting, the two halves were placed horizontal instead of vertical.

A reference measurement was taken with the empty cell maintaining 3 cm gap between the two halves. The reception behaviour at this situation is plotted in Fig. 5.9.

For SE measurement of the MUT sheets the test samples were then placed in the gap and power received in each case for a swept frequency range from 10 MHz to 1 GHz was recorded in dBm. The SE data obtained in this way are plotted in Fig. 5.10 and are clearly lower than those obtained in CSM.

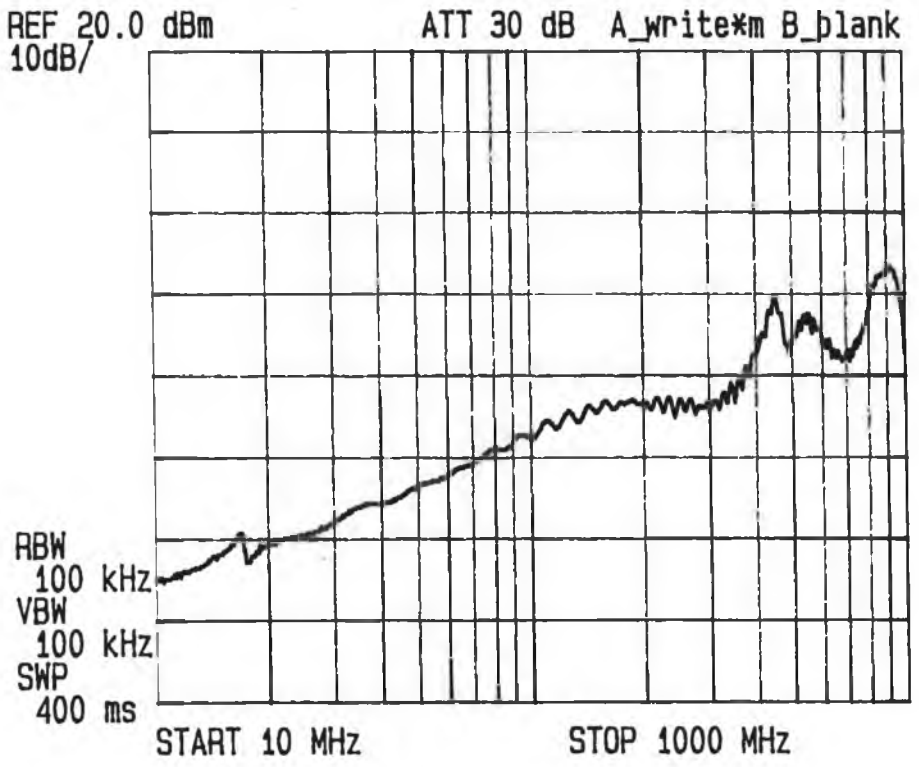

Fig. 5.9 Empty cell reception level of the TEM-T in NCSM configuration. Gap between the two halves was 3 cm. Trigger level (input signal strength) is 0.0 dBm.

5.2.5.3 OLM of SE against high impedance field

There may be wide variety of situations in a practical production run of polymer based conductive composite materials. In the present analysis a particular example has been chosen where the conductive composite material at a final stage of its production would pass over some rollers in planar sheet form at which point the developed techniques would be employed to monitor its shielding capability (see Figs. 1.4 and 1.6). A continuous data acquisition process is proposed for this purpose in which the test device remains stationary and the sheet passes through it. If a swept frequency signal generator were used, this technique would provide a continuous SE data of the sample over the complete range of frequency.

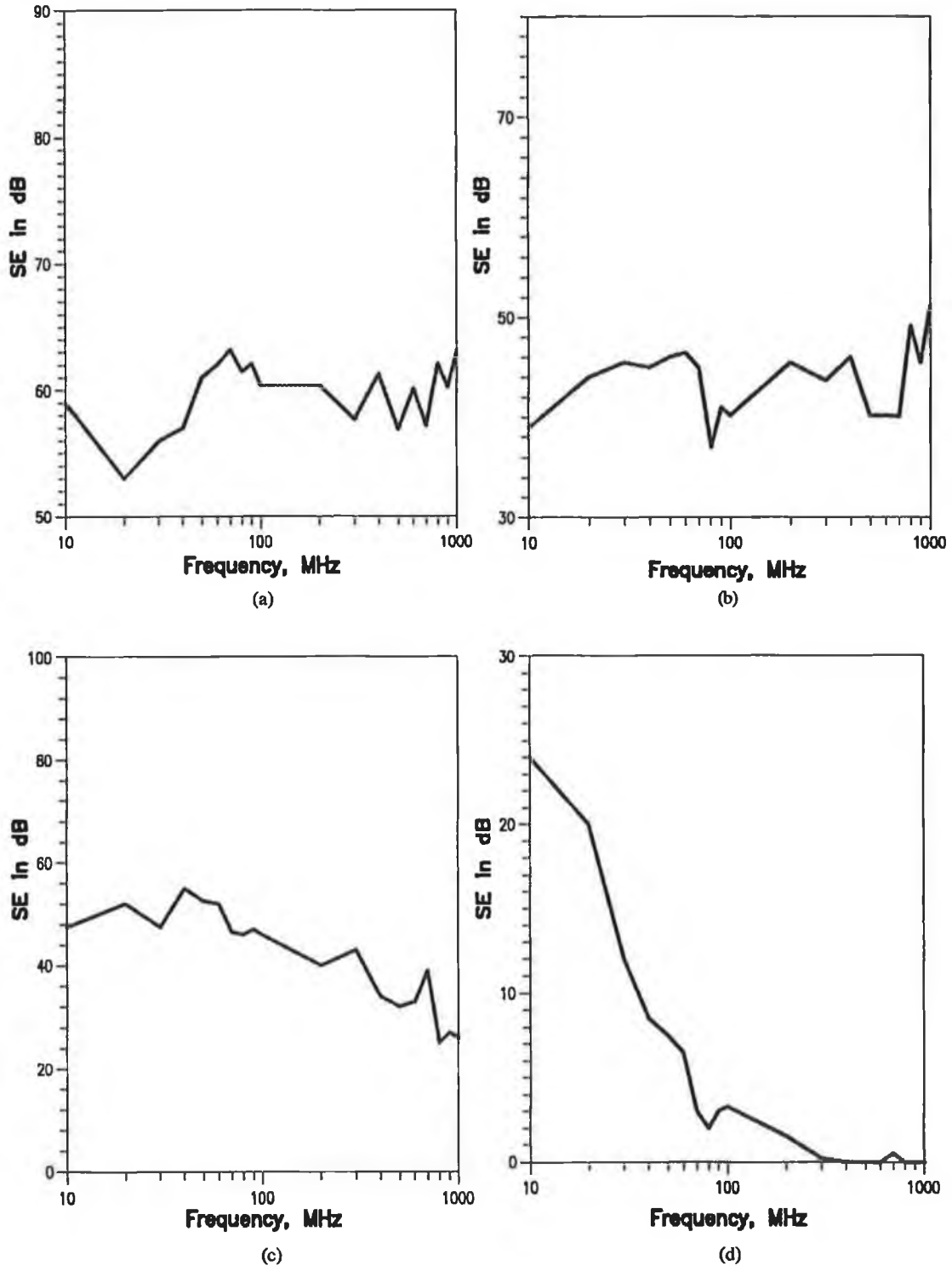

Fig. 5.10 Non contacting stationary SE data with TEM-T cell (a) SE of sample #1 (PET laminate) (b) SE of sample # 2 (Aluminium foil glued onto the ABS sheet) (c) SE of sample #3 (Vacuum coated aluminium) (d) SE of sample #4 (Carbon loaded PVC).

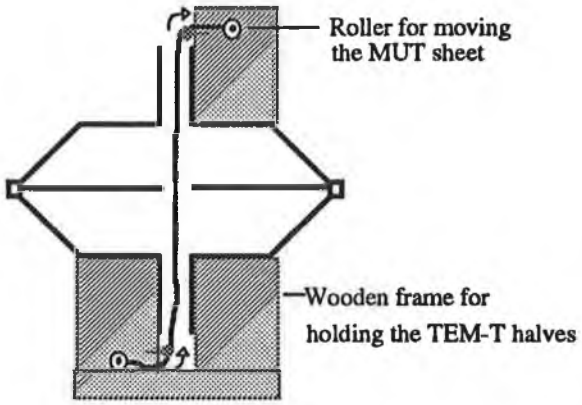

Fig. 5.11 Schematic diagram of the test device and motion of the sample for on-line measurement (connections to the spectrum analyzer are not shown).

The speed of the MUT is not important. This is shown in section 5.2.7. The only effect which might arise due to its motion, is the wavering of the sheet and this, it was thought, might cause a fluctuation in the received power level. Thus a (moderate) speed of 1 cm/s was given to the sheet in order to simulate the situation of on-line measurement. The schematic diagram of the test configuration is shown in Fig. 5.11.

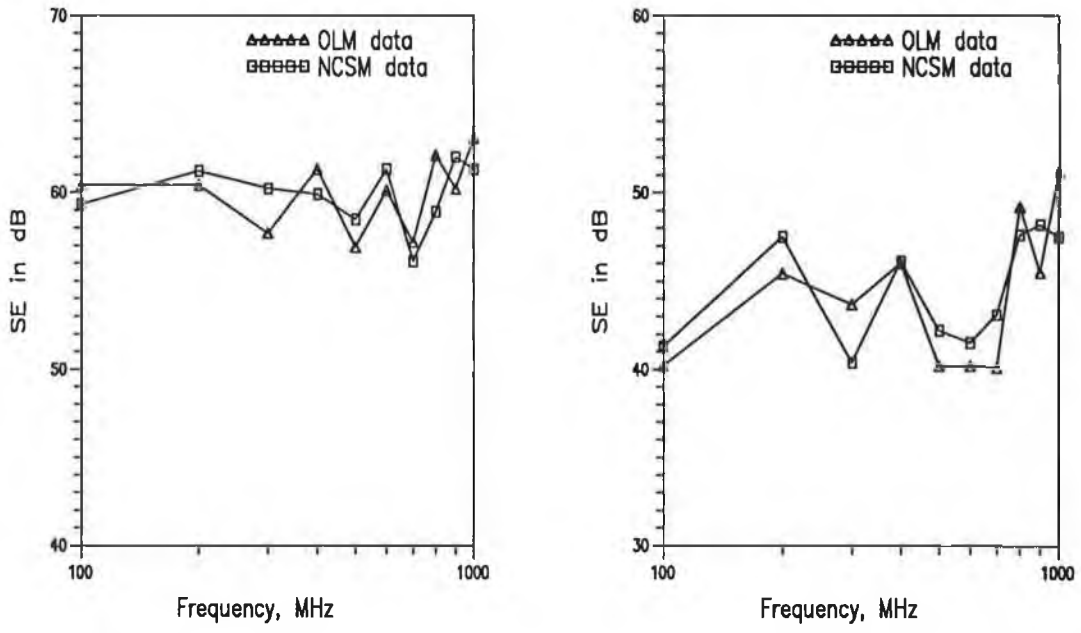

(a) (b)

Fig. 5.12 OLM data with the TEM-T cell (a) SE data for sample #1 (b) SE data for sample #2 . Corresponding NCSM data is shown in the figure for comparison.

A swept frequency measurement was taken from 10 MHz to 1 GHz with the MUT moving through the gap. Unfortunately sufficiently long lengths of all sample material, that would have allowed for a substantial simulated production run, were not available. Long samples of the PET laminate (sample # 1) and the specially made aluminium laminate (sample # 2) were available. So the OLM data were taken only with them. SE data has been calculated by subtracting these test results from empty cell reception levels in NCSM (since the distance between the two halves of the TEM-T cell were the same in both NCSM and OLM) and are plotted in Fig. 5.12.

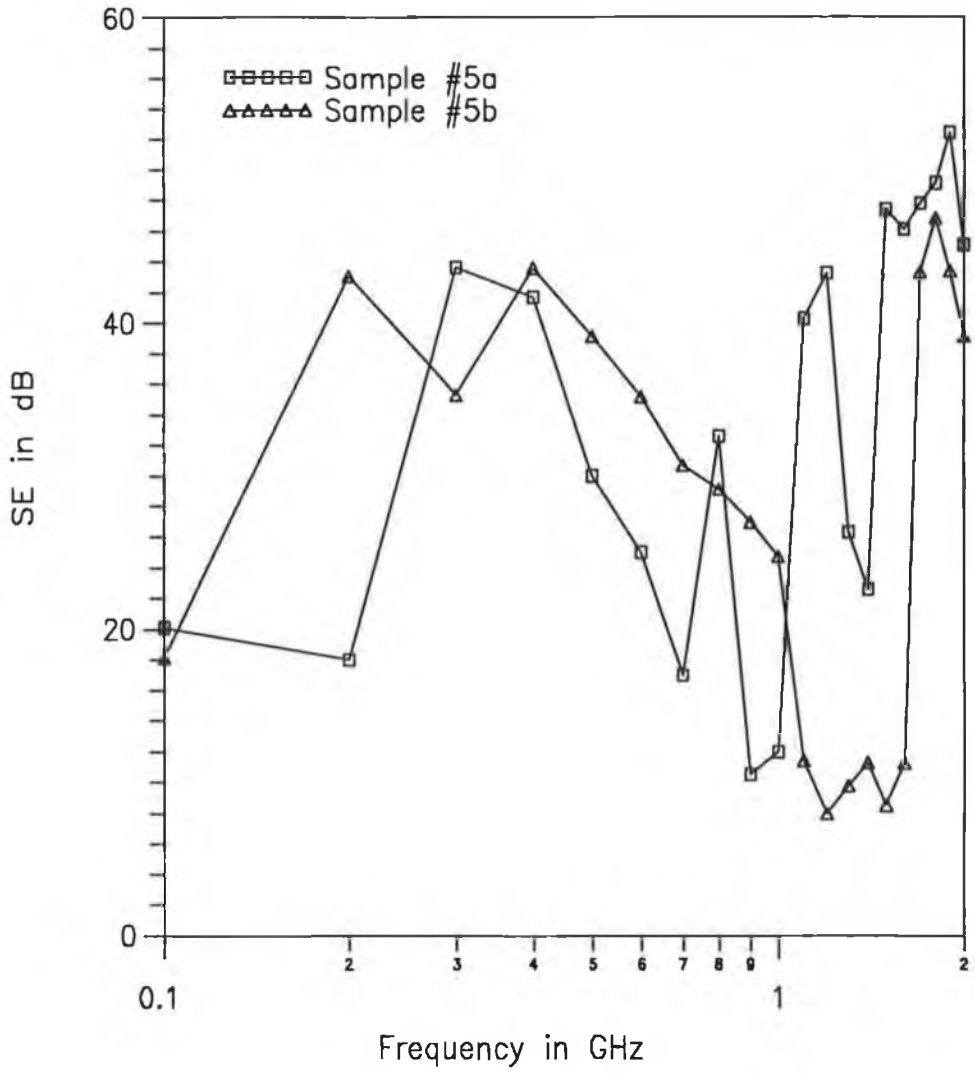

Fig. 5.13 SE of the RFCP sample (sample #5a) and sample #5b (in which the copper strips are randomly distributed in order to simulate an ordinary filled conductive composite). TEM-T cell test device has been used in clamped stationary measurement configuration (as shown in Fig. 5.5) to measure SE.

5.2.5.4 SE measurement of the RFCP

The test arrangement was similar to that shown in Fig. 5.5 (TEM-T cell in CSM configuration). Reference measurement was done at first with sample #5c, by placing it in the sample holder and sandwiching this in between the flanges of the cell. Starting from 100 MHz, measurements of attenuation were performed up to 2 GHz in steps of 100 MHz. Similar measurements were made for #5a, #5b and #5d samples. The test results are plotted in Fig. 5.13. If we compare the power received with sample #5a to the reference measurements with sample #5c, it can be inferred that the attenuation suffered by the signal is mainly due to the reflections from the array of conducting strips. SE values obtained with sample #5a and sample #5b were normalized with that obtained with sample #5d.

5.2.6 LOW-IMPEDANCE FIELD MEASUREMENT

In describing the constructional details of the Q-loop antenna in chapter 4, it was mentioned that the corner reflectors are open at the two edges. Thus unlike TEM-T cell there is no way that this test device can be employed in a closed form test fixture and obviously no such test data as the CSM are possible. However, stationary measurement with a small gap between the pair of antennas should yield good estimates of the shielding capability of the MUT against low impedance field. Some calibration corrections would obviously be necessary.

5.2.6.1 Stationary Measurement

By stationary measurement with the Q-loop antenna, it obviously means non-contacting stationary measurement (NCSM). The two antennas were placed very close to each other leaving a very small gap in between the flat extended faces of their reflectors to get reference data. The test arrangement is shown in Fig. 5.14.

The signal was fed at one end of the transmitting Q-loop and the other end was terminated with a coaxial load (refer to the more detailed description of section 4.4.3). The power received at the receiving Q-loop was recorded using a spectrum analyzer connected at one of its terminals while its other end was also terminated at a coaxial load. The reference reception level is shown in Fig. 5.15. A swept frequency measurement from 10 MHz up to 1 GHz was performed and the test results (SE data) are plotted in Fig. 5.16.

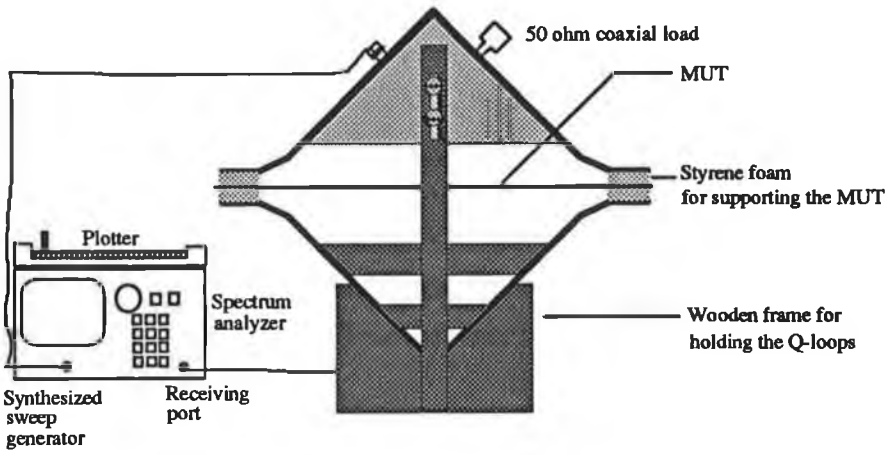

Fig. 5.14 Placement of the Q-loops and the MUT sheet for stationary measurement of low impedance field SE.

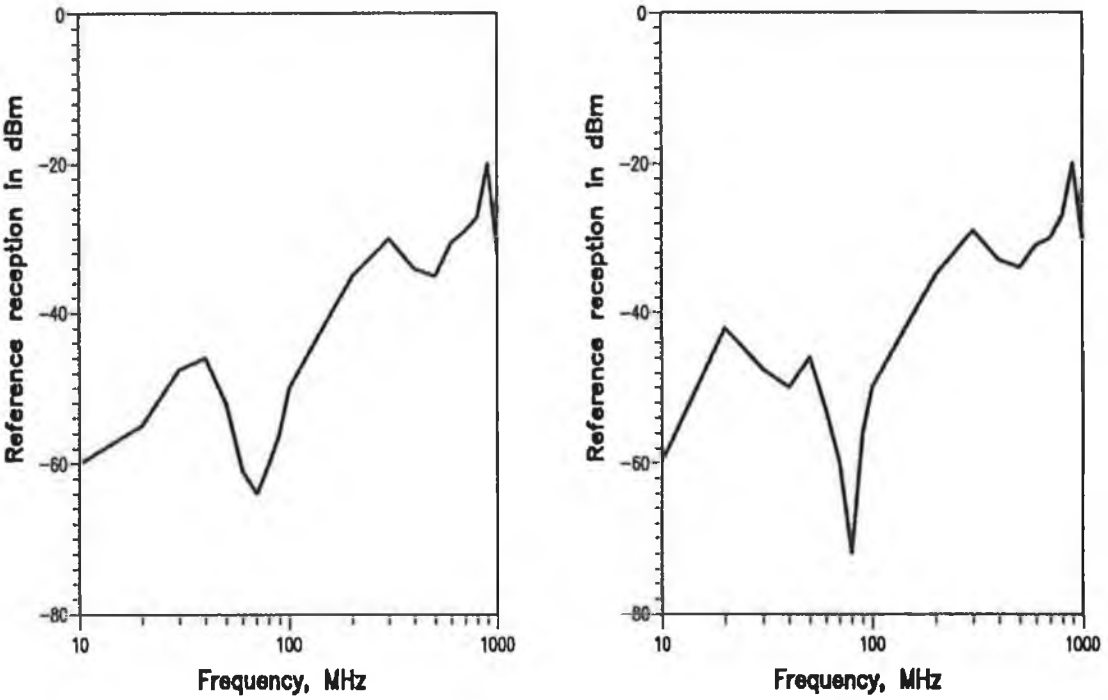

Fig. 5.15 Reference reception behaviour of the Q-loop antenna. No sample present in between the pair of Q-loop antennas. Gap between the flat faces of the reflectors of the pair is 5 mm; (a) In normal room (b) In absorber lined chamber.

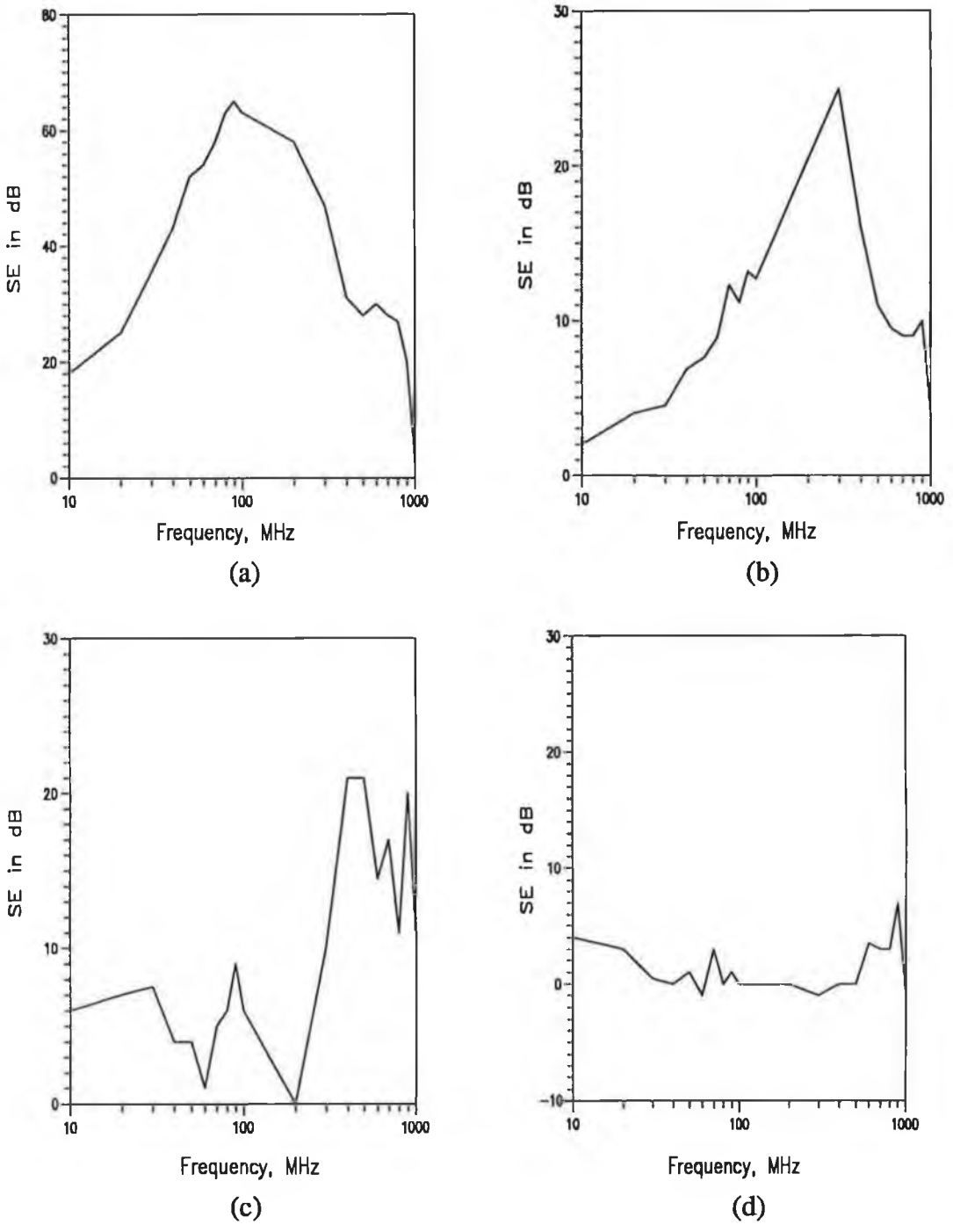

Fig. 5.16 Low impedance field SE data through stationary measurement using Q-loop antenna (a) Sample #1, (b) Sample #2, (c) Sample #3 and (d) Sample #4.

5.2.6.2 OLM against Low-Impedance Field

For OLM the relative position of the Q-loops was maintained as before, and the MUT sheet was moved through the gap between them. The MUT sheet was driven at the same speed of 1 cm/s as was the case in section 5.2.5.3.

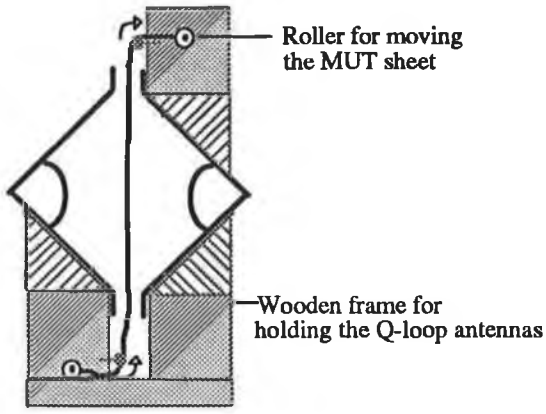

Fig. 5.17 Test configuration and the movement of the MUT sheet for on-line measurement of low impedance field SE (electrical connection are not shown).

In fact, the same movement mechanism as was used for high impedance field SE measurement was applied. The schematic diagram of the test system is depicted in Fig. 5.17. The test results are plotted in Fig. 5.18.

5.2.6.3 Low impedance field SE measurement of the RFCP

Measurements similar to those discussed in section 5.2.5.4 were taken with the Q-loop antenna test device as well. None of the two samples (sample #5a and #5b) could attenuate the low impedance field of the transmitting Q-loop antenna. Low impedance field is principally attenuated by absorption loss into the material. Of course some absorption losses would be there due to the loss resistances of the conducting strips but these would be negligible.

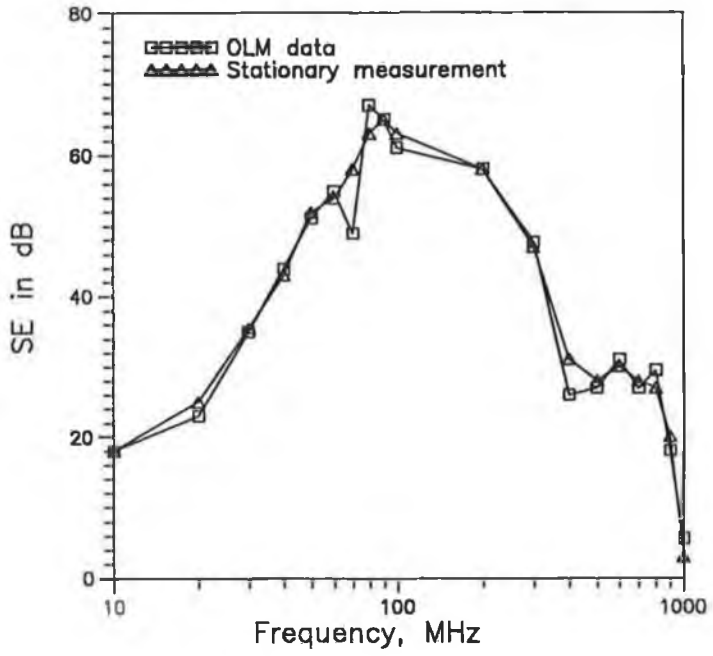

(a)

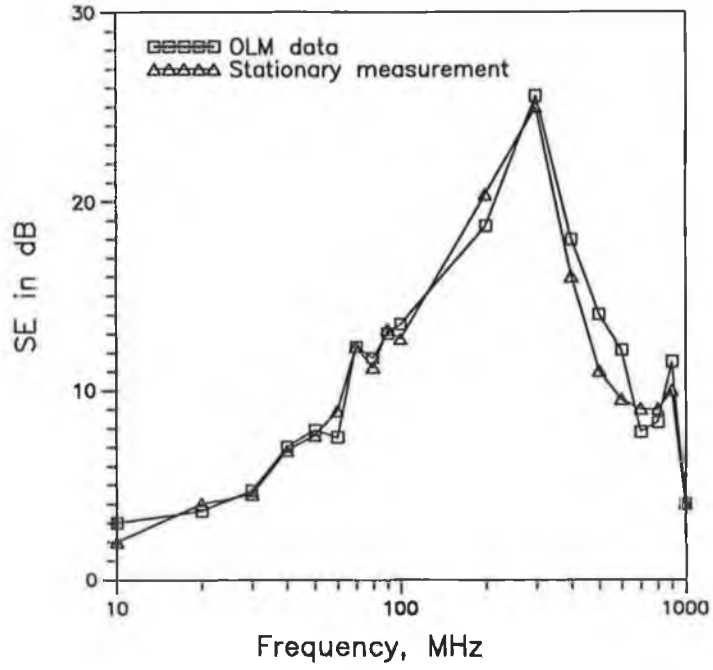

(b)

Fig. 5.18 Low impedance field SE data through OLM using Q-loop antennas, (a) Sample #1 and (b) Sample #2. The stationary measurement data are also shown for comparison.

5.2.7 EFFECT OF MOVEMENT OF THE MUT ON SE MEASUREMENT

It is important to investigate whether the movement of the MUT sheet might result in any change of the incident EM field on it in on-line SE measurements. The interaction of plane electromagnetic waves with interfaces moving with uniform velocity has been studied by numerous investigators [165]-[170]. These investigations show that the movement of the plane should not produce any change in the incident field pattern as long as its speed is not comparable with the speed of light.

Thus it can be assumed that the error would be negligible if we neglect the effect of movement of the test sheet on SE data predicted with a motionless surface. Since the velocity of propagation of an EM wave is the same for either plane waves or high/low impedance waves in free space, the above assumption is equally applicable for the high/low impedance field measurements as well.

5.3 CALIBRATION OF THE TEST DEVICES

The leakage of test fields and infringement of indirect path signals to the test receiver in case of non-contacting measurements employed in the present analysis for OLM were manifested in the form of recorded SE values of the MUT being lower than actual.

Corrections for indirect path signal infringement depend on the particular test environment whereas the wavering effect may appear in the same form irrespective of the test site.

5.3.1 CALIBRATION OF TEM-T CELL

The SE data, obtained in the OLM configuration with the TEM-T cell, differ significantly from the actual SE values of the MUT. As will be shown later in section 5.4.1.1, in CSM it is possible to get the high impedance field SE data of the sample with sufficient accuracy. If the SE data available through this measurement (Fig. 5.7) is compared with that obtained through OLM (Fig. 5.12), a significant difference of 20-30 dB is quite evident.

In fact, NCSM values for SE are also lower than actual by 20-30 dB. The difference in SE values obtained through NCSM and OLM is rather small and variable

(variation is ± 3-5 dB). Thus the major variation in test results is reported while changing from the closed test fixture of CSM to the open test fixture of NCSM.

The reduction of received power level in reference measurement with NCSM can be explained from the analytical model established in section 5.4.1.2. The gap in this test configuration would increase the impedance of the capacitive coupling between the two centre conductors. This would also be the case with the radial transmission line. Consequently the larger impedance mismatch would reduce the transmission of power to the receiving half.

5.3.1.1 Correction for Radiation loss

Because of the gap maintained between the TEM-T halves and the MUT sheet, the TEM-T transmitting half starts radiating in to free space especially at the higher range of frequencies where the dimensions of the cell are not small compared to the wavelength. At the lower range of frequencies the transmitting half would not be radiating and all the energy is concentrated in the fringe or reactive field of this half (where the receiving half of the cell is placed).

The approximate radiation pattern of the TEM-T half shown in Fig. 3.17 gives an indication that the radiation is predominantly within the boundary of the flange. Similar observations are reported by Fan *et al.* [164] where they have noted that the field strength reduces significantly just beyond the perimeter of the outer conductor of the coaxial structure. Still a significant amount of radiated field may exist in a region beyond the flanges. A test conducted by the National Defence Research Institute of Sweden [54] demonstrated that the axial discontinuity in a coaxial structure (such as a TEM cell) causes the maximum possible leakage through that path.

An assessment of the radiation loss can be made analytically by computing the power received by a hypothetical perfect absorber (with dimensions equal to those of the MUT) located in front of the TEM-T cell transmitting half in place of the MUT. This, when compared with the total power available at the open end of this TEM-T half, gives approximately the loss encountered by radiation.

The EM field at the aperture of the open mouth of the TEM-T transmitting half is expressed by Eqns. (3.4.2) and (3.4.7). Real power (average power) content in that EM field can be calculated by

$$P_{av} = \frac{1}{2}\mathrm{Re}\int_S (\vec{E}\times\vec{H}^*).d\vec{S} \qquad (5.3.1)$$

where the integration surface is the aperture. Again the power incident on a sheet having dimensions equal to that of the MUT sheet and placed at a distance of z=1.5 cm (the position of the MUT in NCSM) from the open mouth of the TEM-T half (refer to Fig. 3.12 for geometry of the radiating TEM-T half) can also be computed by performing similar operations with $\vec{E}$ and $\vec{H}$ vectors given by Eqn. (3.4.11) (which gives the expression of those vectors in front of the TEM-T transmitting half) and the integration is to be performed over the area of the MUT sheet. In case of a hypothetical absorber (as mentioned above) all the incident power would be absorbed, thus this latter power level when compared with that calculated before gives an assessment of the radiation loss. However at the desired frequency range, this would not be very significant.

5.3.1.2 Correction for Indirect path signal infringement

The intensity of the indirect-path signal reaching the receiving half of the TEM-T cell principally depends on the presence of EM scattering objects around the test system. In particular, metallic walls, objects and ground planes can introduce significant error due to severe reflections.

An EM wave emanating at large angles (with the axis of the TEM-T half) can strike the receiver after being reflected back from a nearby metallic object or may be reflected at large angles from the MUT surface and then be re-reflected, from other EM scatterers, to the receiver (refer to Fig. E3-1 of Appendix E3). Background noise can also be a source of such infringement.

However, a test can be carried out by placing the SE measurement system inside an ordinary room (which simulates a typical industrial environment) and comparing the data obtained with those from similar measurements performed inside an anechoic chamber. The amount by which the received signal strength exceeds that in the absorbing room considered to be the worst possible infringement caused by the indirect-path signal.

5.3.1.3 Correction for Wavering effect of the moving MUT sheet in OLM

Wavering of the test sheet (random displacements at right angles to directions of motion) can be studied by moving it up and down (or to and fro) within a particular band height

(or width) in the gap between the two halves of the TEM-T cell. Statistical analysis of the fluctuations in the received signal strength can give a better understanding of the possible error caused by wavering and a correction factor may thus be included in the analysis to rectify the SE data.

The variability of a data set fluctuating around a mean is statistically expressed by the standard deviation, σ (to avoid confusion with the conductivity, σ the standard deviation is denoted by bold face font).

In order to measure the variability of the OLM data w.r.t the NCSM data, the standard deviation of the difference is calculated and it is found to be only 2 dB (approximately) in case of sample #1. Compared to the SE value of 75-85 dB, this spread is negligibly small.

The wavering would change the position of the MUT sheet in the gap (farther or closer to the transmitting half than 1.5 cm). So the effect of wavering was studied by the following tests.

The MUT was placed closer to the transmitting half and then closer to the receiving half. Although the difference in received power level was not very prominent, in general it was observed that as one moved farther from the transmitting half, the recorded SE value decreased.

As the wavering of the MUT sheet in OLM is random it is hard to predict the exact situation whether it is moving nearer to the transmitting half or farther at a particular frequency or frequency range. However, if the mean variation of the above two cases w.r.t the NCSM data is added to the OLM data an overall improvement in the recorded SE data (much closer to the NCSM data) can be observed. The standard deviation of the OLM data (after such corrections) w.r.t the NCSM data is found to be 1.11 dB (a sample calculation is given in Appendix E2).

5.3.2 CALIBRATION OF Q-LOOP ANTENNA FOR OLM

From the radiation pattern of the Q-loop plotted in Fig. 3.22, it can be seen that radiation is confined within one quadrant of the azimuth ($0^o \leq \phi \leq 90^o$) and polar ($|\theta| \leq 45^o$) angles i.e., mostly within the quadrant covered by the Krauss reflector. Thus the leakage of the test field through radiation is negligibly small. Moreover as the MUT and the receiving

antenna were positioned strictly in the near field region of the transmitting antenna, the field in and around the test location was predominantly reactive not radiative. Thus this test device was calibrated to take into account the following two corrections.

5.3.2.1 Correction for Indirect path signal infringement

A test similar to the one mentioned earlier with the TEM-T device can be conducted to assess the amount of the error that can be introduced in this way. The test device was placed in an ordinary room with some metallic objects around to simulate a typical industrial environment and the power reaching the receiver recorded. The test device was then placed in a four-walled absorber chamber as shown in Fig. 5.19[1]. The absorbers were chosen such that they are capable of absorbing significantly the EM wave even of the largest possible wavelengths transmitted by the antenna.

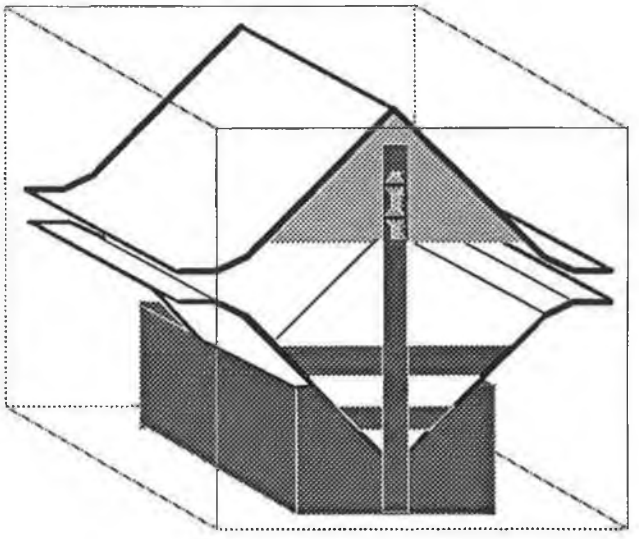

Fig. 5-19 Q-loop antenna test device in four walled absorber room to estimate the effect of the indirect path signal infringement and background noise. To show the Q-loop test device in the room walls are shown transparent.

The low impedance face of the absorber was placed inside while the high impedance face was placed outside, thus the outgoing EM waves from the test device (which can strike the nearby scattering object) were mostly absorbed and at the same time the incoming EMI were reflected.

[1] In fact, no significant improvement in test data was observed by performing the experiments in an anechoic chamber and therefore, this alternative approach of four-walled chamber was attempted.

The absorbers used in this test were ECOSORB® EN79 whose reflectivity profile as function of frequency is shown in Fig. E4-1 (Appendix E4). Fig. E4-1 illustrates the poor reflectivity level in the lower range of frequencies (from 10-100 MHz) of this absorbers. Thus the test can not be expected to yield good results in this range. This is a major limitation of calibrating the test devices at low frequency.

5.3.2.2 Correction for Wavering effect of the moving MUT sheet

The SE values shown in Fig. 5.18 when compared with respective data of stationary measurement of Fig. 5.17, a fluctuating variation of 3-5 dB is quite evident, and this is because of the wavering effect of the MUT in OLM. In order to measure the variability of the OLM data w.r.t the data obtained through stationary measurement, the standard deviation of the difference is calculated and it is found to be only 1.4 dB and 1.0 dB in case of sample #1 and sample #2 respectively. Compared to their low impedance field SE value of 30 dB or above, such spreads are very small.

However, the procedure described earlier in case of TEM-T cell for calibrating it against wavering effect is repeated for Q-loop antenna and the correction factor is added to the OLM data to calibrate it. Standard deviations of the differences in this case were found to be 0.4 dB and 0.3 dB with the above two samples respectively.

5.3.3 CALIBRATED SE DATA

Correction factors necessary to introduce into the OLM results to obtain reliable SE data in two different (TEM-T cell and Q-loop) cases have been described in the previous section. Following those procedures one can obtain improved SE data directly from on-line measurements through automated data acquisition which is discussed below.

5.3.3.1 Calibrated SE data with TEM-T cell

Four correction factors are to be introduced into the SE data obtained through OLM in order to calibrate the test results. They are namely: the correction for radiation loss, correction for increased transmission loss, correction for indirect path signal infringement and the correction for wavering effect as mentioned in section 5.3.1. To calibrate the NCSM data only the last correction factor is not necessary.

A study of the correction factors, determined theoretically or experimentally, reveals that the main deference between the CSM and the NCSM data is caused by the indirect path signal infringement. Nevertheless the other factors such as the radiation loss and increased transmission loss also contribute to the difference but not very significantly. In order to give an estimate of the amount of indirect path signal infringement error, the NCSM data in an ordinary room and in an anechoic chamber for each sample are plotted on the same graph as shown in Fig. 5.20 (a)-(d).

The radiation loss being negligibly small even up to 200 MHz, the calculation of the error that might result due to this loss is computed from 200-1000 MHz according to the formula discussed earlier in section 5.3.1.1. The correction factor varies from 0.5-2 dB. The error that might be caused by increased transmission loss are estimated through measurements of the power transmission coefficients with and without the MUT in front of the TEM-T half for each sample (see the discussion of section 5.4.1.2) and it is found to be less than 2 dB even in the worst possible case of sample #1.

In case of carbon loaded PVC sheet (sample #4), the NCSM data in an ordinary room and in the absorber lined room seemed to have no difference. In fact, there is only a little difference between the CSM data and the NCSM data as well. At the lower frequencies the difference is about 2-3 dB but negligible at higher frequencies.

One possible explanation of this smaller difference can be given through the illustration shown in Fig. E3-1 of Appendix E3. As the SE of this particular MUT is very low, there will be less reflection of the EM wave incident on its surface and as a result even in an ordinary room the possibility of indirect path signal infringement on to the test receiver is small. Nevertheless, the influences of background noise or radiated EM waves which may come back to the receiver are not affected by the lower SE values of the sample and as such attributing the large difference (from 20-30 dB in case of other samples to only 0-2 dB in case of sample #4) only to the less reflection is not reasonable enough. Hence for this particular sample the calibration experiments were inconclusive.

In case of sample #1 through #3, it has been observed that a major part of the difference between the CSM data and the NCSM data is due to this error, because there were more reflections from their interfaces which increase the possibility of indirect path signal infringement.

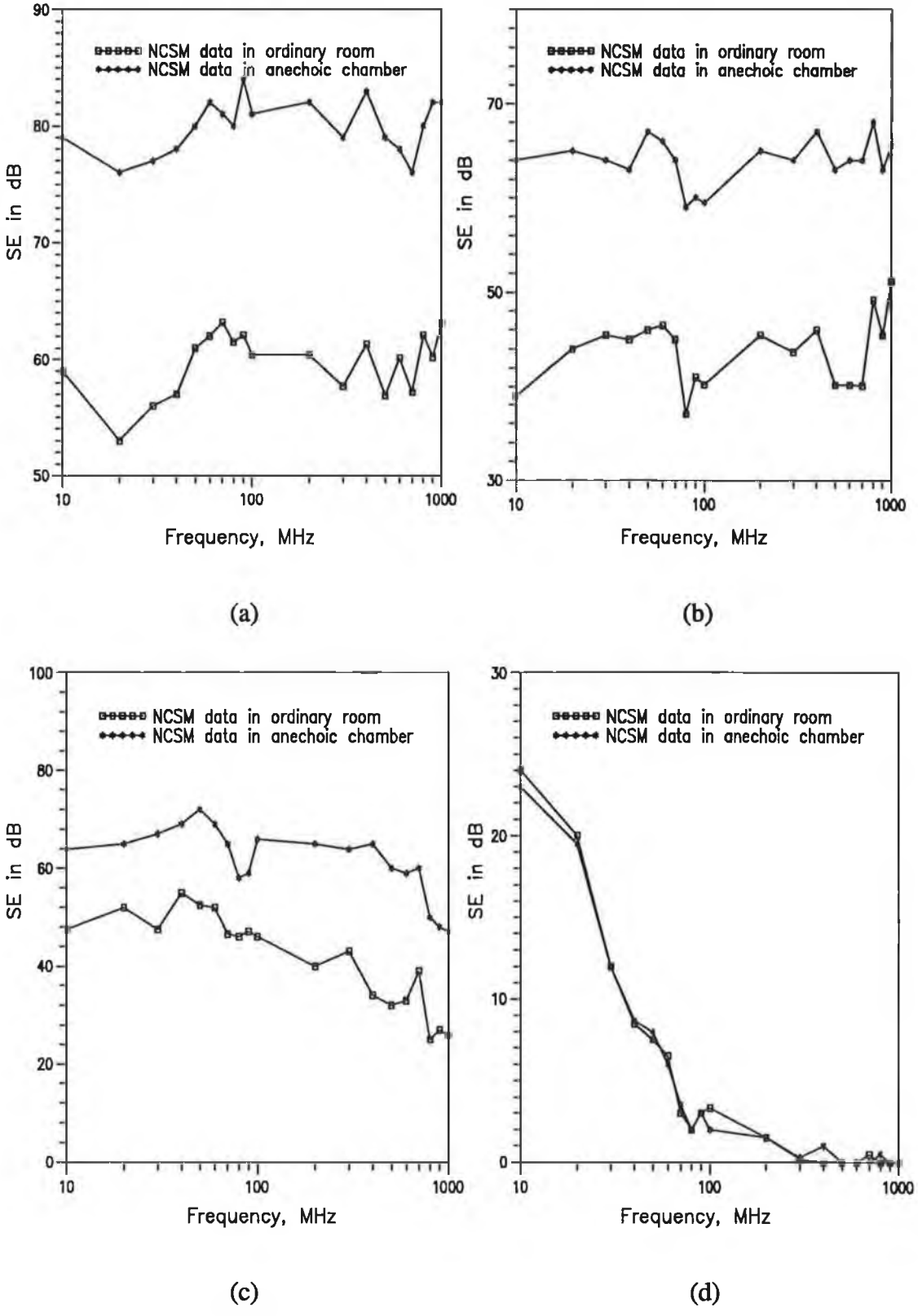

Fig. 5.20 SE measurements in NCSM configuration with TEM-T cell in an ordinary room and in anechoic chamber (a) sample #1, (b) sample #2, (c) sample #3 and (d) sample #4.

In Fig. 5.21 the relative weighting of the correction factors for each sample has been shown graphically. Correction factors (at a frequency of 100 MHz) to be introduced are plotted in that figure. Correction factor due to wavering depends on the stiffness of the sample and was the largest in case of the least stiff sample (#1). Correction due to increased transmission loss is a function of the reflectivity of the sample and the larger the reflectivity of the sample, the greater the correction factor is (see Fig. 5.21). The radiation loss factor, being computed following the analysis of section 5.3.1.1, is the same irrespective of the samples.

It is evident that except the radiation loss none of the correction factors is the same for all four samples. Thus before applying this test device for on-line SE measurement, it is essential that the calibration should be done with a sample material of the MUT and in the test environment where this technique would be employed.

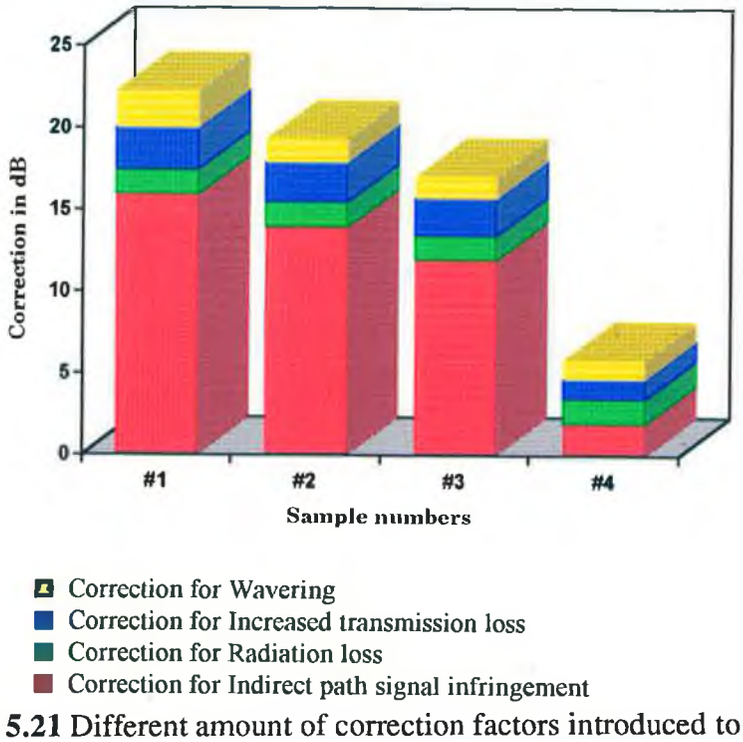

Fig. 5.21 Different amount of correction factors introduced to calibrate the OLM data with TEM-T cell to estimate the actual SE values of the samples.

It is to be noted here that for samples having poor SE values, the lower values of calibration factors for indirect path signal infringement available with the aforementioned calibration experiments are not well explained, as has been mentioned earlier in section 5.3.3.1 for sample #4. Hence further investigation is necessary on the calibration procedure to apply this test system for measuring the on-line SE of such samples.

The calibrated SE data (after introducing these correction factors into the OLM data) are plotted in Fig. 5.22 for sample #1 and #2. The uncalibrated and calibrated results are together for comparison. Uncalibrated results are found to be 20-30 dB lower than the calibrated ones; it is thus clear that the calibrated OLM data is within 5-7 dB of the CSM data (which represent the actual SE of the sample).

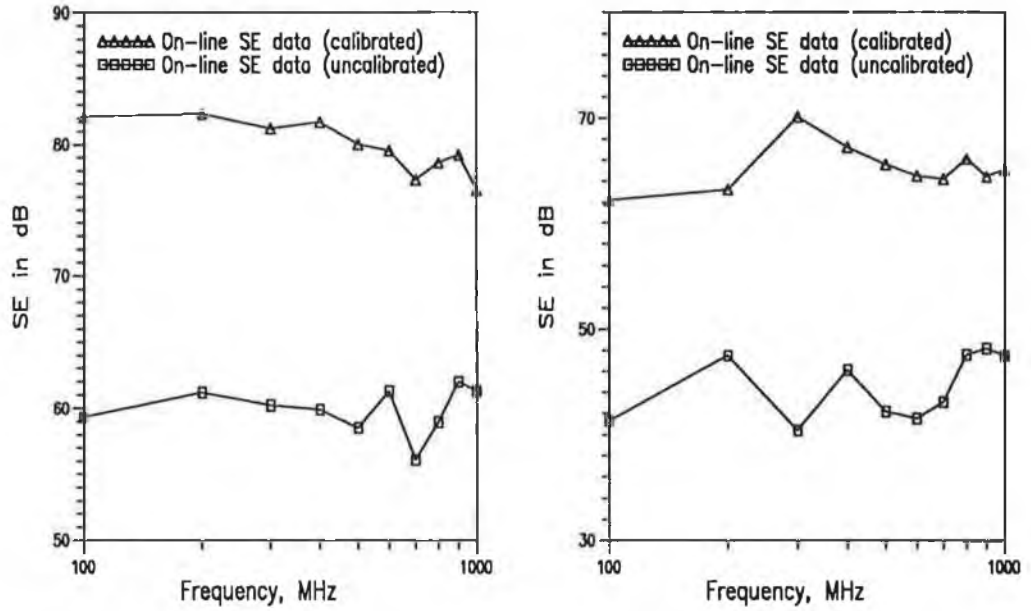

(a) (b)

Fig. 5.22 Calibrated OLM data (a) Sample #1 (b) Sample #2. Uncalibrated OLM data are also shown for comparison.

From the above discussion, it is evident that the calibration factors are frequency dependent and although it is possible to introduce those factors through the course of automated measurement for a swept frequency range, in a practical production run for on-line characterization of the product it may not be viable to incorporate such frequency dependent correction factors. There is every possibility that the calibrated results at the end may not provide reliable data. Moreover as the correction factors such as those for the indirect path signal infringement and wavering effects are random in nature, it is impossible to get exactly the same set of data at different times, all the other conditions remaining the same. However, they do appear to be bounded and thus instead of attempting such absolute measurements, without loosing a great deal of accuracy (as far as on-line characterization is concerned), the measurement system could be made much simpler by introducing a fixed correction factor irrespective of the frequency.

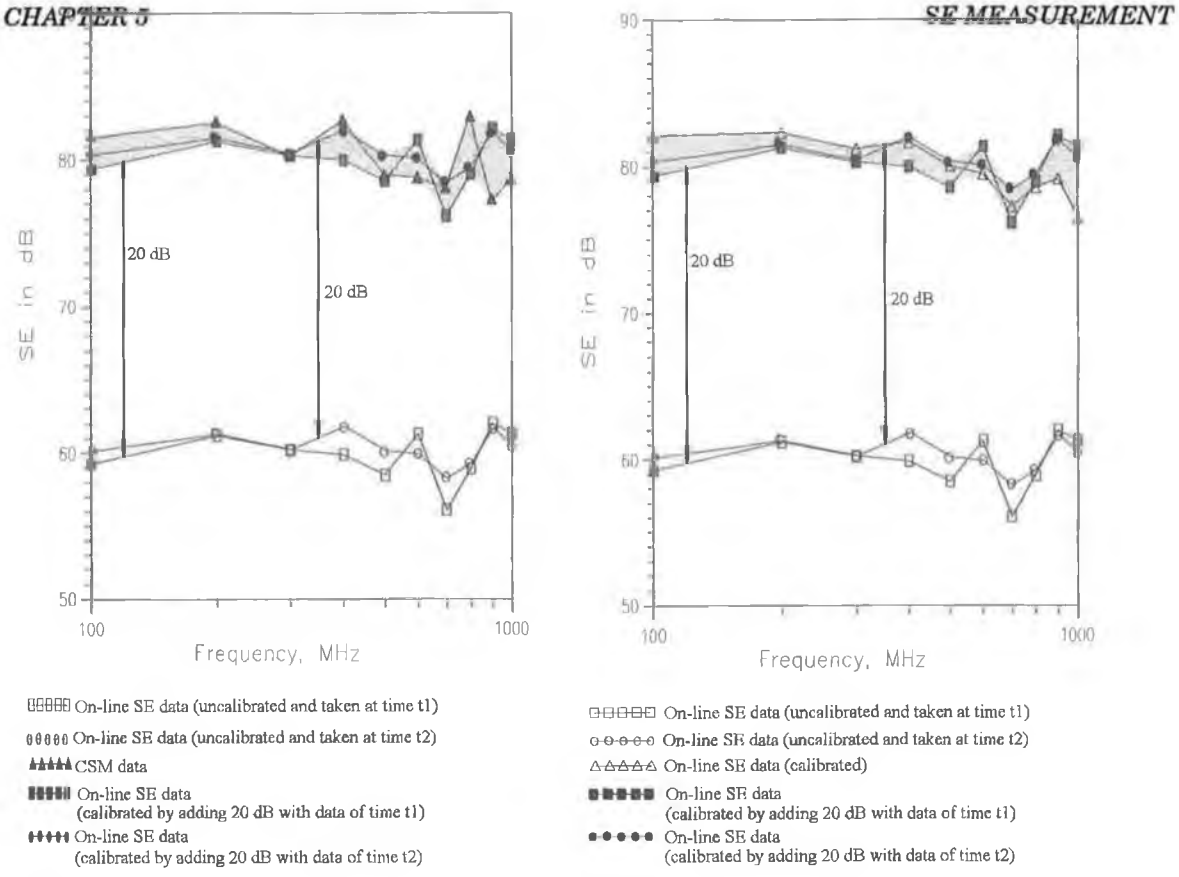

(a) (b)

Fig. 5.23 Calibrated and uncalibrated OLM data for Sample #1 at two different instants. Calibrations using simplified approach are compared, (a) with CSM data and (b) with calibrated OLM data using more involved approach.

It could be shown through the correlation of the CSM data and the calibrated OLM data obtained through such simplified corrections that the resulting SE data lie within a particular band of accuracy. In Fig. 5.23, it has been demonstrated for sample #1. The OLM data taken at two different instants have been calibrated by adding 20 dB at all frequencies and the resulting data are compared in Fig. 5.23(a) with the CSM data and in Fig. 5.23(b) with the calibrated SE data obtained through adding the four different calibration factors (two of them are frequency dependent) as mentioned earlier in this section. The height of the grey band shown in the diagram varies from 3 to 7 dB. Thus if the ambient noise level does not change significantly and the situation of the EM scattering objects around the test site remains almost the same, it may be inferred that for an MUT, like sample #1, the addition of an average correction factor of 20 dB throughout the frequency range with the OLM data would give SE values within a 3-7 dB band of accuracy.

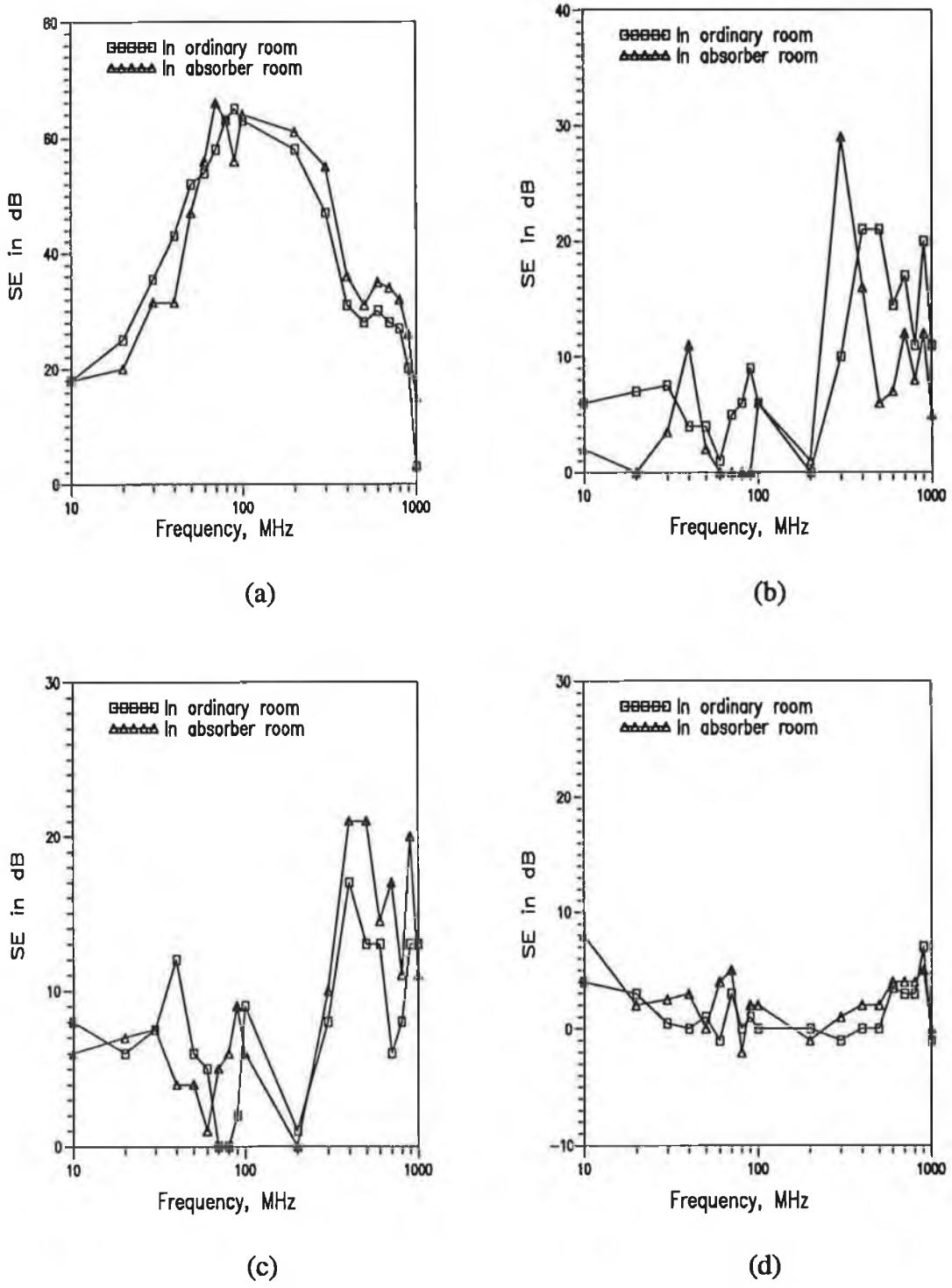

Fig. 5.24 Stationary measurement of the low impedance field SE with the Q-loop antenna in ordinary room and in the four walled-absorber room as shown in Fig. 5.19. (a) Sample #1, (b) Sample #2, (c) Sample #3 and (d) Sample #4.

5.3.3.2 Calibrated SE data with Q-loop antennas

The calibrated OLM data of sample #1 and #2 are plotted in Fig. 5.25 along with the uncalibrated result. Calibrated stationary measurement data for the other two samples are also shown in Fig. 5.24 along with the uncalibrated result. No significant difference can be observed except at higher frequencies (100-300 MHz). At lower frequencies, the calibration could not be performed properly (see section 5.3.2) and as such improvement due to calibration is insignificant.

However, due to less reflection suffered by the low impedance field EM wave incident on the MUT sheet, the amount of indirect path signal infringement error was very small. In case of TEM-T cell this was the main cause of a large difference between the CSM and the NCSM data.

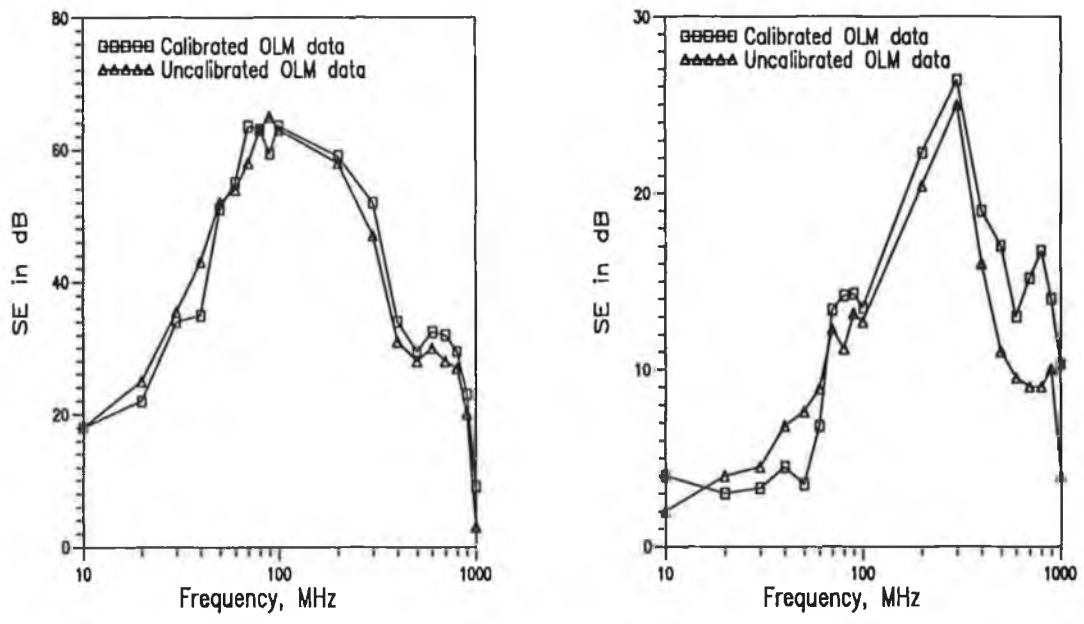

(a) (b)

Fig. 5.25 Comparison of the calibrated OLM data with the uncalibrated one (a) Sample #1 (b) Sample #2.

5.4 COMPARISON WITH THE THEORETICAL RESULTS

Expressions for calculating the SE of different type of conductive plastic materials were presented in section 3.2. It is possible to approximately estimate the SE of the samples used in the measurements through those expressions. The test results will then be compared with these predictions.

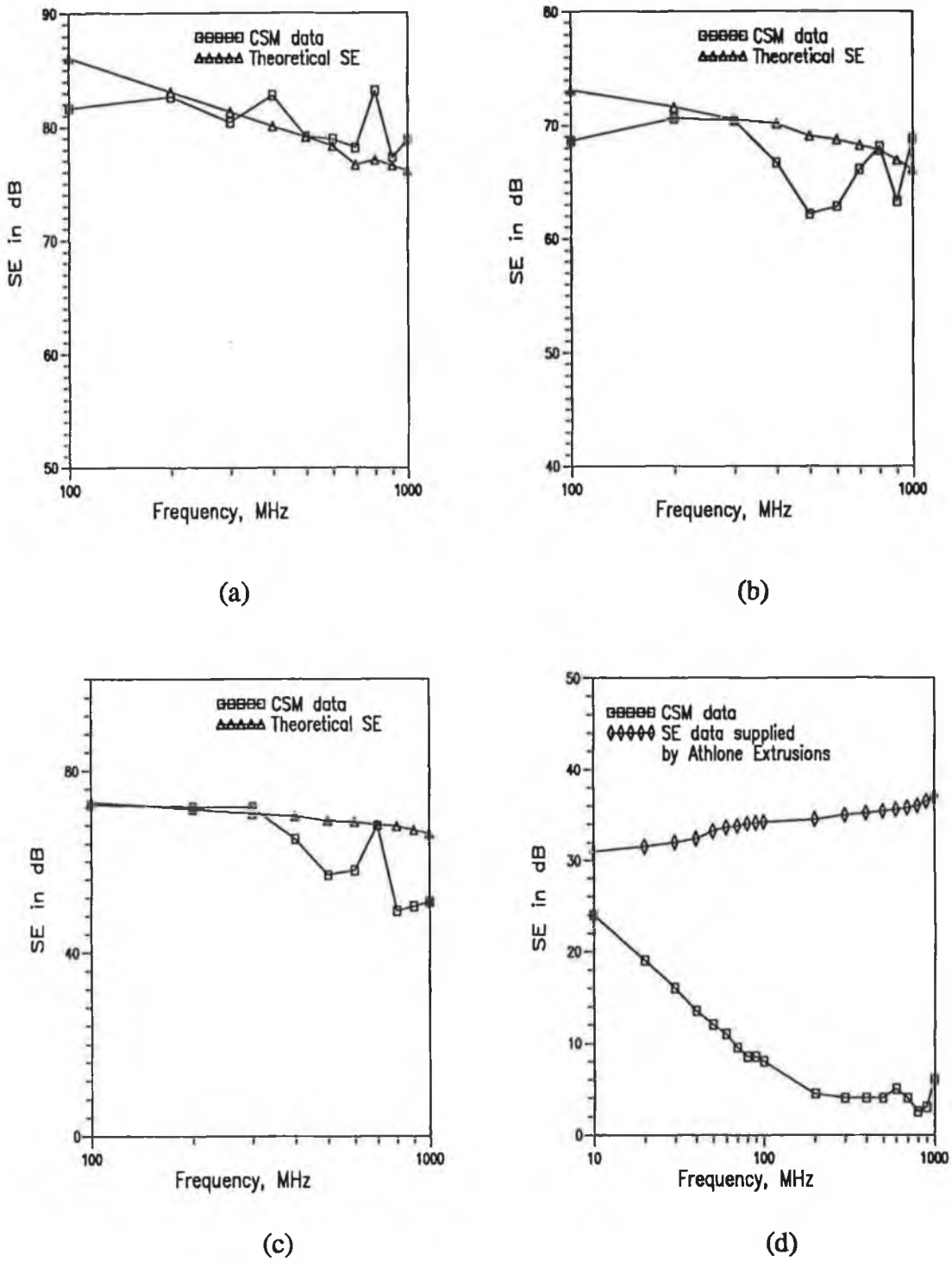

Fig. 5.26 Comparison of the CSM data (using TEM-T cell) with theoretical SE data (a) Sample #1 (b) Sample #2, (c) Sample #3, (d) Sample #4. Only the reflection loss is considered as theoretical SE of the samples. For sample #4, SE data supplied by Athlone Extrusions are re-printed as theoretical SE data.

5.4.1 ANALYSIS OF TEM-T CELL TEST RESULTS

Applying the appropriate boundary conditions for the constituent materials of different samples in the formulas for near E-field SE presented in section 3.2, the theoretical SE values are computed. A negative slope of these SE values when plotted as functions of frequency is quite evident as the reflection loss decreases with frequency almost linearly.

As noted before in section 5.2.5 that CSM data should represent the actual SE of the samples against high impedance field. NCSM and OLM data on the contrary records lower SE values which requires calibration and the calibrated results are discussed in the previous section. In the present section comparative analysis of each individual set of data with the predicted results are presented.

5.4.1.1 Comparative analysis of the CSM data

SE values determined from CSM measurements are compared with the theoretically predicted SE values of the samples #1 through #4 (sample calculations are shown in Appendix E5). The comparison is shown in Fig. 5.26.

In case of sample #1 through #3 the test results are within 5-7 dB of the predicted results. The decreasing trend of the SE values with frequency is also evident from the test results. In case of sample #4, however, it is not possible to estimate its SE values theoretically (discussed in section 3.2.3) but its approximate SE values are available from data provided by the supplier [163]. Indeed the supplied SE was calculated using the ASTM ES 7-83 coaxial method and the thickness of the sheet was 4 mm. This method measures far field SE where the absorption loss is also included and particularly at high frequency the absorption loss becomes predominant and the thicker the sheet the more the absorption loss. If the CSM data are compared with this supplied data it is apparent that they differ widely at high frequency whereas they were close to each other at low frequency where reflection loss is predominant.

5.4.1.2 Analytical model of the TEM-T cell in NCSM configuration.

In NCSM configuration the measurement fixture may be modelled as a pair of sections of coaxial transmission lines coupled through a open circuited radial transmission line and a capacitor as shown in Fig. 5.27. The capacitor models the capacitive coupling

between the centre conductors, and the radial transmission line models the flanges in the fixture.

For empty cell measurement, capacitance is formed between the two centre plates through air. The impedance of the capacitor is

$$Z_c = -j\frac{1}{\omega C_c} \tag{5.3.3}$$

where C_c is the total capacitance developed between the two center plates including the fringing capacitance. A numerical computation of this capacitance is given in Appendix E6.

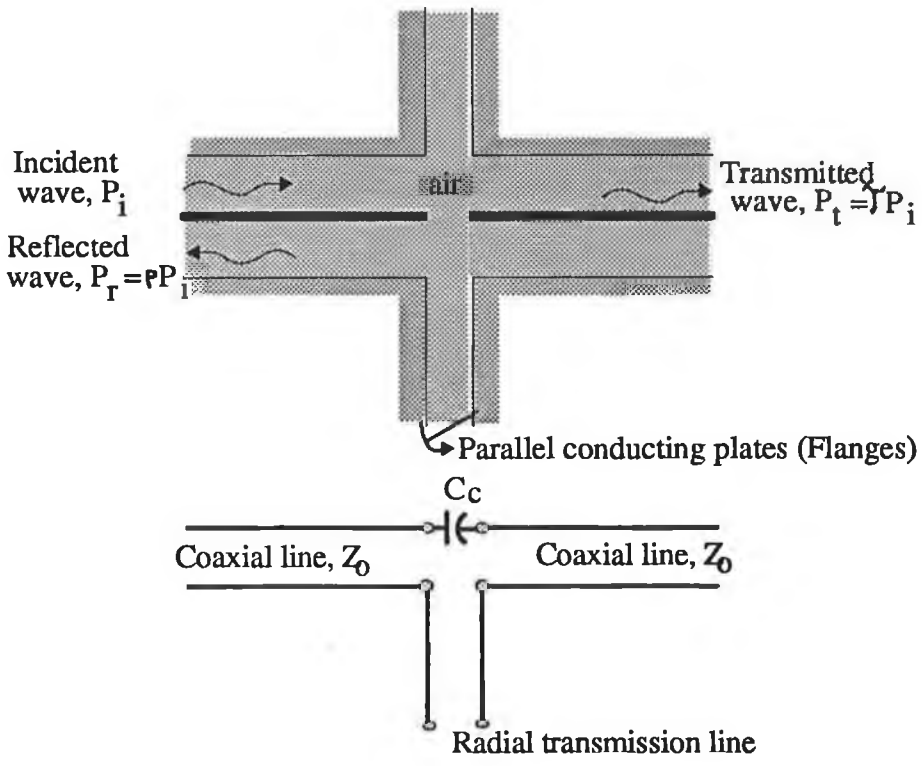

Fig. 5.27 Simplified model and the equivalent circuit for the measurement fixture in non-contacting measurement.

The radial transmission line is formed between the two rectangular flanges at the open mouths of the TEM-T halves. The medium that fills the line is air for empty cell measurement. The radial transmission line is left open, and the open end can be modelled by a perfectly conducting magnetic wall. Even though this model is only approximate, it

is sufficiently accurate for the frequency range of interest particularly when the spacing between the plates is much less than a half of the wavelength [143].

A radial transmission line formed between two parallel plates, each of which is an annular plate between two concentric circles, has been analysed by Ramo *et al.* [85, chap. 9]. The radial transmission line of the present problem is topologically the same as that one. The difference is that annular plates are not between two concentric circles, instead, they are the region between two rectangles with a common centre of gravity along the z-axis (refer to Fig. E7-1 of Appendix E7). With the application of the conformal mapping of multiply-connected regions it is possible to transform this region into an annular region between two concentric circles. Performing this transformation the equivalent radius of the inner and outer circle can be expressed in terms of the dimensions of the rectangles as follows (see Appendix E7 for transformation)

$$\begin{aligned} r_i &\approx 0.251 \text{ meter} \\ r_o &\approx 0.458 \text{ meter} \end{aligned} \tag{5.3.4}$$

Now the input impedance of the radial transmission line is

$$Z_r = \frac{t}{2\pi r_i} \frac{\eta \xi(\beta r_i, r_0 / r_i)}{\beta r_i} \tag{5.3.5}$$

where β is the free space wave number, η is the wave impedance and

$$\xi(\beta r_i, r_0 / r_i) = \frac{E_z}{H_\phi}\left(\frac{\beta r_i}{\eta}\right) \tag{5.3.6}$$

is the normalized impedance at the input of the radial transmission line for TEM wave [85, chap. 9].

The reflection coefficient ρ and the transmission coefficient τ of the fixture are primarily determined from the capacitance between the centre plates whenever $|Z_c| >> |Z_r|$ because so long as this inequality is satisfied, ρ and τ are less sensitive to Z_T than to Z_C; for the frequency range of interest the above inequality holds and the errors in ρ and τ due to the approximation in modelling the open radial line are very small. The empty cell reception behaviour is thus calculated according to the above model and is graphed in Fig. 5.28 along with the experimental results.

Now from the above analysis it is quite evident that as the distance between the two halves increases in NCSM than in CSM the capacitive coupling between the two halves becomes weaker which accounts for lower transmission of power to the receiving half. The lower reception level of Fig. 5.9 (where the gap was 3 cm) than that reported in Fig. 5.6 (where the gap was only 2 mm) can be well explained with this analysis.

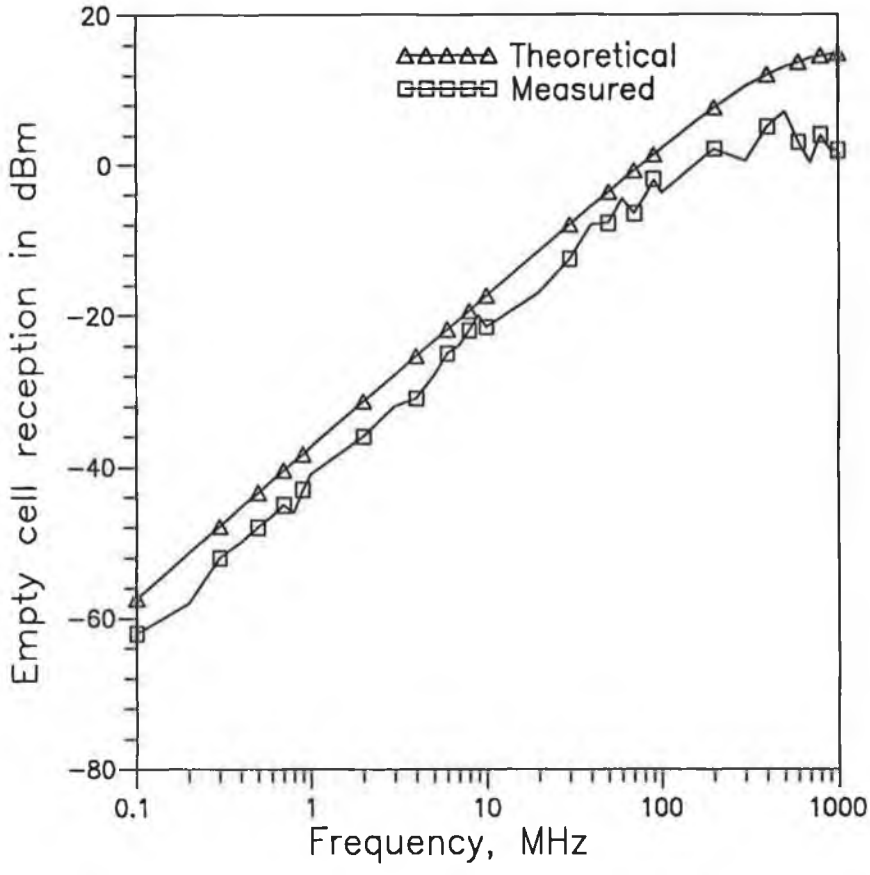

Fig. 5.28 Predicted empty cell reception behaviour according to the analytical model presented in section 5.4.1.2. Measured empty cell reception behaviour is also shown in the figure for ease of comparison. The gap between the two halves is 3 cm.

The above analysis holds for an empty cell but with the MUT introduced, ρ at the open mouth of the transmitting half decreases, resulting in an increase in the transmitted power on to the MUT sheet. This increase is recorded in the form of lower SE value of the sample than the actual (as it is being compared with the power level received by the empty cell). The following example clarifies the situation.

Let the transmission coefficient at the open mouth of the TEM -T half with and without the MUT be τ_o and τ_m respectively, where $\tau_o < \tau_m$. So the corresponding power transmitted in the space between the transmitting half and the position of the MUT are P_{to} and P_{tm} respectively where, $P_{to} < P_{tm}$.

Power at the open mouth of the receiving half without the MUT may be considered as P_{to} (neglecting the radiation loss in free space and infringement of indirect path signal) and the power at the open mouth of the receiving half with the MUT will be

$$P_{ri} = P_{tm} - SE_{MUT} \tag{5.3.7}$$

where, SE_{MUT} is the actual SE of the MUT. On the other hand, in calculating SE through NCSM, one uses

$$SE_{NCSM} = P_{to} - P_{ri} = SE_{MUT} - (P_{tm} - P_{to}) \tag{5.3.8}$$

Since $P_{tm} > P_{to}$, the recorded SE in NCSM is less than the actual SE of the MUT. The difference $(P_{tm} - P_{to})$ can otherwise be represented as $(\tau_m - \tau_o)$ expressed in dB. The value of this quantity is not more than 3 dB and thus not a very significant contributor to the 20-30 dB difference between CSM and corresponding NCSM data.

However, the calibrated NCSM data took account of this effect as well as the other effects such as probable radiation loss and indirect path signal infringement. As a result, these data (calibrated NCSM data) are found to be very close to the predicted SE values as in the case of CSM data.

5.4.1.3 Comparison of the OLM and theoretical data

It is not worth comparing the uncalibrated OLM data with the theoretical SE data because the former do not yield good estimates of the SE of the samples. The calibrated OLM data, as described in the previous section, is however closer to the CSM data and as such they are also closer to the predicted SE values for the above mentioned two samples. The comparison is shown in Fig. 5.29.

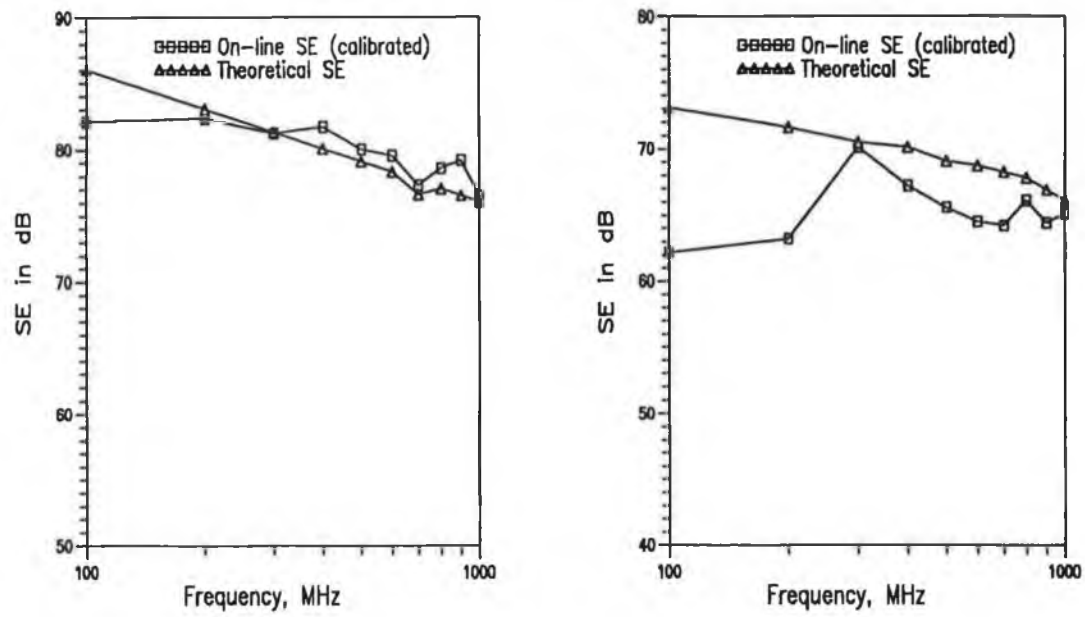

(a) (b)

Fig. 5.29 Comparison of the calibrated OLM data with the theoretical SE data (a) Sample #1 (b) Sample #2. Only the reflection loss is considered as theoretical SE of the samples.

5.4.2 ANALYSIS OF TEST RESULTS WITH THE Q-LOOP ANTENNAS

In section 3.2, separate formulas are presented to predict, theoretically, the SE of conductive plastics against low impedance field. Substituting the values of the intrinsic properties of the constituent materials of different samples in those formulas the respective SE values are computed (sample calculations are given in Appendix E5). These predicted values are compared with the set of low impedance field SE data obtained through measurements in the following sub-sections.

5.4.2.1 Comparative analysis of the stationary measurement

The test results obtained with stationary measurement exhibit negligible SE values of sample #4, poor SE values of sample #3, however, but good SE values of the first two samples. The copper in sample #1 is more conductive than the aluminium or carbon in the other three samples, and therefore sample #1 would be expected to offer the highest attenuation against a low impedance field.

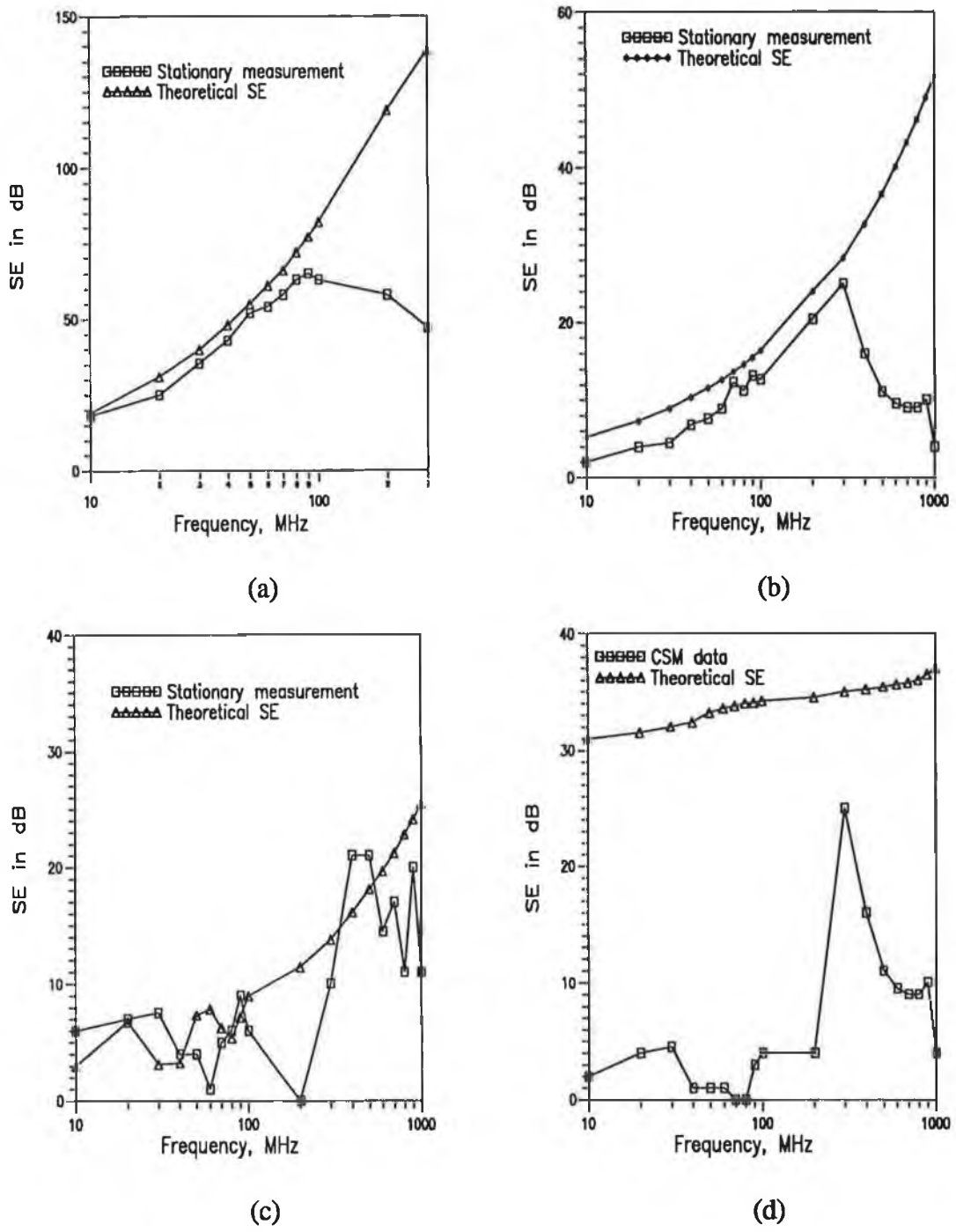

Fig. 5.30 Comparison of the measured low impedance field SE with that predicted theoretically, (a) Sample #1, (b) Sample #2, (c) Sample #3 and (d) Sample #4. Only the absorption loss and the successive re-reflection loss (inside the sample) are considered as theoretical low impedance field SE. In case of sample #4 supplied data by Athlone Extrusions is presented as theoretical SE.

At the lower range of frequencies (10-300 MHz roughly) it is found that the test results are close to the predicted results (refer to Fig. 5.30) but as the frequency increases it seems that the SE of the samples exceed the dynamic range of the test device. In fact at the higher range of frequencies the Q-loop antenna starts radiating in broader patterns and thus the fields do not remain confined within the area of the MUT sheet allowing a larger fraction of the test field to be coupled directly to the receiving antenna and not through the MUT. Obviously the recorded SE values become smaller. In calibrating the NCSM data, it was not possible to consider this factor.

Aluminium foil of sample #2 is thicker than the coated aluminium layer of sample #3 and the lower measured SE values of the latter sample are attributed to this.

Absorption loss is negligible in sample #4 because of the lower conductivity of carbon and as described earlier in section 3.2.3 the major constituent of the SE in such filled composites is the closed network formed by the probable touching fillers, and this is low. It should exhibit some shielding capability due to absorption at high frequency but above 300 MHz, the dynamic range of the test device is exceeded.

5.4.2.2 Comparative analysis of the OLM data

In case of low impedance field SE measurement the calibrated OLM data are very close to the NCSM data (refer to Fig. 5.25). Thus the foregoing analysis of comparing NCSM data with the theoretical predictions can also be applicable for OLM data.

However, if the uncalibrated test results are compared with the predictions, unlike the TEM-T cell test device, one can observe that the Q-loop antenna test device could yield reasonably accurate SE data up to a frequency range of 300 MHz even without calibration.

5.4.3 ANALYSIS OF THE TEST RESULTS CARRIED OUT ON RFCP

It is evident from the test results shown in Fig. 5.13 that the resonance of highest reflectivity occurs near 2 GHz in case of the regular array (sample #5a), which verifies the theoretical observation quite interestingly, but even up to 1.4 GHz no significant amount of reflectivity was noticed. Thus the test result indicates a narrower band of high reflectivity than the predicted one (refer to Fig. 5.31 for comparison).

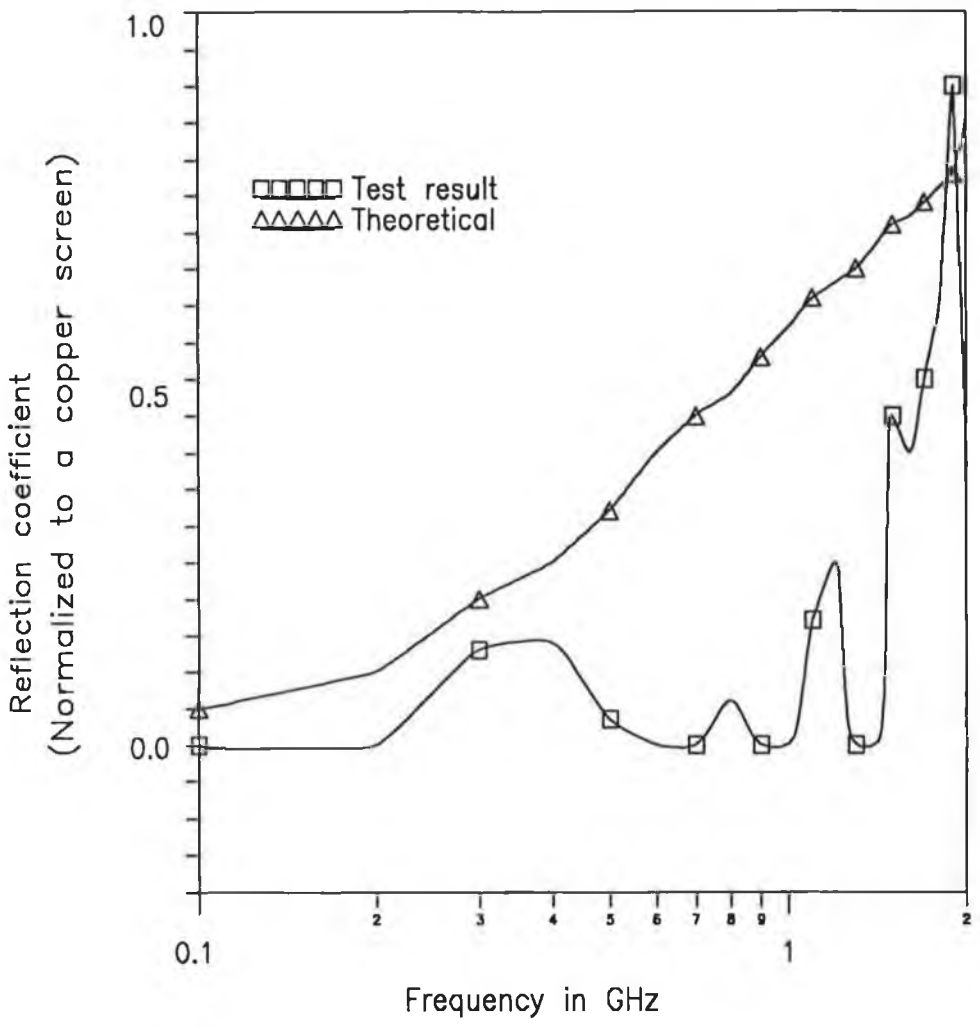

Fig. 5.31 SE expressed in the form of reflection coefficient of the RFCP sample (sample #5a). Theoretical reflectivity computed using the formula presented in chapter 3 and measured reflectivity (as shown in Fig. 5.13) are placed together for comparison.

The improvement in reflectivity (i.e. SE in the present example) for the newly proposed RFCP over that of the randomly filled conductive plastic is quite obvious from the test results. At the lower frequencies sample #5b exhibits better SE than sample #5a, but this is not significant compared to the higher range of frequencies 1.4-2 GHz, where sample #5a showed much higher SE.

In samples #5a and #5b, conducting strips did not form closed loops and therefore the absorption loss was negligible (Some small I^2R loss might be expected from currents circulating within any isolated strip).

5.5 CONCLUDING REMARKS

The SE of a wide variety of materials has been measured, where the test samples are essentially in planar sheet form. Both the closed test fixture and open non-contacting test fixture (that are proposed for on-line measurement) have been used in the measurements. Calibration procedures were described so that the discrepancies in test results that might occur due to the leakage of the test field and due to the exposure of the test devices into the background noise in case of the suggested on-line techniques, can be corrected prior to data acquisition.

The calibration of the modified TEM-T cell for near E-field SE data acquisition proved to be reasonably accurate for samples having moderate or good SE as far as on-line characterisation is concerned. However, for poor shields the calibration is not very justifiable. The Q-loop also yields adequately accurate near H-field SE data up to 300 MHz. Since the OLM data was taken only with two samples, further investigations on a large number of samples are necessary to confirm the reliability of the calibration procedures.

The speed of data acquisition and manipulation are satisfactorily fast to be incorporated into any conductive composite manufacturing process. The test devices are capable of producing only near field shielding data. Thus a complementary test device such as VCLA set for far field SE data acquisition is essential.

The repeatability of the test results with the proposed measurement procedures is a very important feature that requires careful attention. In the concluding chapter, however, this feature is addressed.

Chapter 6

ANTENNA MEASUREMENTS

MEASUREMENT OF ANTENNA RADIATION PATTERNS
MEASUREMENT OF ANTENNA PARAMETERS
COMPARISON WITH THE THEORETICAL PREDICTIONS

6.1 INTRODUCTION

Measurements of the radiation patterns and relevant other parameters of the newly developed antennas are particularly important to show that they possess the essential features for on-line SE measurement and for other EMC applications. These features of the developed antennas have been shown analytically in chapter 3 and their experimental verifications are the contents of this chapter.

Antenna measurements are often tedious and require a proper open site test facility for open area measurements or a specially designed anechoic chamber for in-house measurements. For the higher range of frequencies it is preferable to use an anechoic chamber while for lower frequency ranges open area test sites are more suitable. Important features of these two test locations were briefly reviewed in chapter 2. An anechoic chamber test facility was used for the antenna measurements of this project and the measurements were taken mostly at a frequency of 1 GHz at which the reflectivity level of the chamber was almost negligible.

Throughout the measurement procedure, it is assumed that the antennas can be treated as passive, linear and reciprocal devices. Therefore their radiation properties can be measured in either the transmitting or the receiving mode. Although the pattern of the particular antennas are not definitely known, on the basis of the theoretical analysis it is anticipated that they are directional and this makes the measurement procedures relatively simple.

A fundamental property of any antenna is its radiation pattern which usually refers to the far field distribution. Antenna parameters, such as impedance, directivity, and gain, are enough to characterise the performance of an antenna particularly if it is designed for EMC applications. It is thus essential to measure these figures-of-merit in order to make efficient use of such an antenna.

Measurement of radiation pattern and the results of these measurements are described in section 6.2. Section 6.3 elucidates the measurement procedure and the test results of the three different figures-of merits as mentioned above. In section 6.4 a comparative analysis is presented between the test results and the theoretical models of the pattern and parameters of the antennas under test (AUTs).

6.2 RADIATION PATTERN

The radiation pattern is defined as a graphical representation, usually in the far-field region, of one of the antenna's parameters. For a complete description, the parameters of interest are usually plotted as a function of spherical directional angles θ, φ in all directions in three dimensions. Parameters of interest include amplitude, phase, polarisation, and directivity. The scope of the present analysis covers mainly the amplitude measurements. The directivity can also be derived from the measurements taken. When measuring the SE of planar sheet-like material the phase and polarization parameters of the antenna are effectively unimportant and hence no attempt was made to determine these.

6.2.1 ANECHOIC CHAMBER

All the antenna measurements were performed in the anechoic chamber of Power Electronics Ireland at the University of Limerick. The chamber is designed to operate at frequencies near 1 GHz and above. The chamber is 5 m long , 3 m wide and 7 m high. It is completely lined with absorbing materials ECOSORB® AN27, including the floor (excluding the narrow wooden platform for operator's movement and placement of instruments inside the chamber). There is an access door at one corner of the chamber which is made RF tight with beryllium copper finger springs at the edges. The inner side of the door is also lined with the same absorbing materials.

A photograph of the inside view of the chamber is shown in Fig. 6.1. A rotary turntable is set at one end of the chamber. The motor which rotates the turntable at different specified angles is controlled from the outside of the chamber. Through the motor controller the turntable can be positioned at any angular measure to 1^{o} accuracy.

The ambient noise level of the chamber is recorded through a biconical antenna (BCA) and a log periodic antenna (LPA) at the swept frequency ranges of 30-200 MHz and from 200 MHz to 1 GHz respectively. The ambient noise level inside the chamber was recorded and is plotted in Fig. 6.2. The noise level is negligibly small (ranging from 22 to 35 dBμV/m) except at the lower frequency range of 50-100 MHz and at 460 MHz. At those specific regions it is significantly high (as high as 53.6 dBμV/m). This noise level was recorded with the motor (of the turntable) turned on and if it is turned off this noise almost disappears. Thus the EMI may be due to the motor/motor drive electronics.

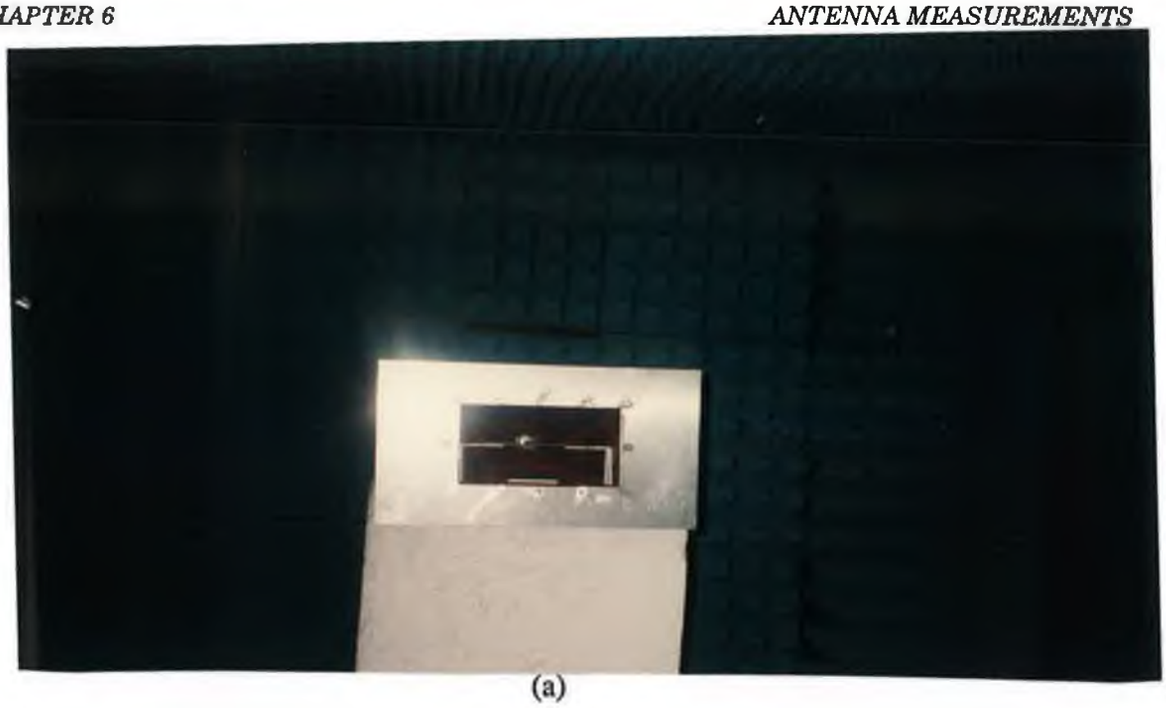

(a)

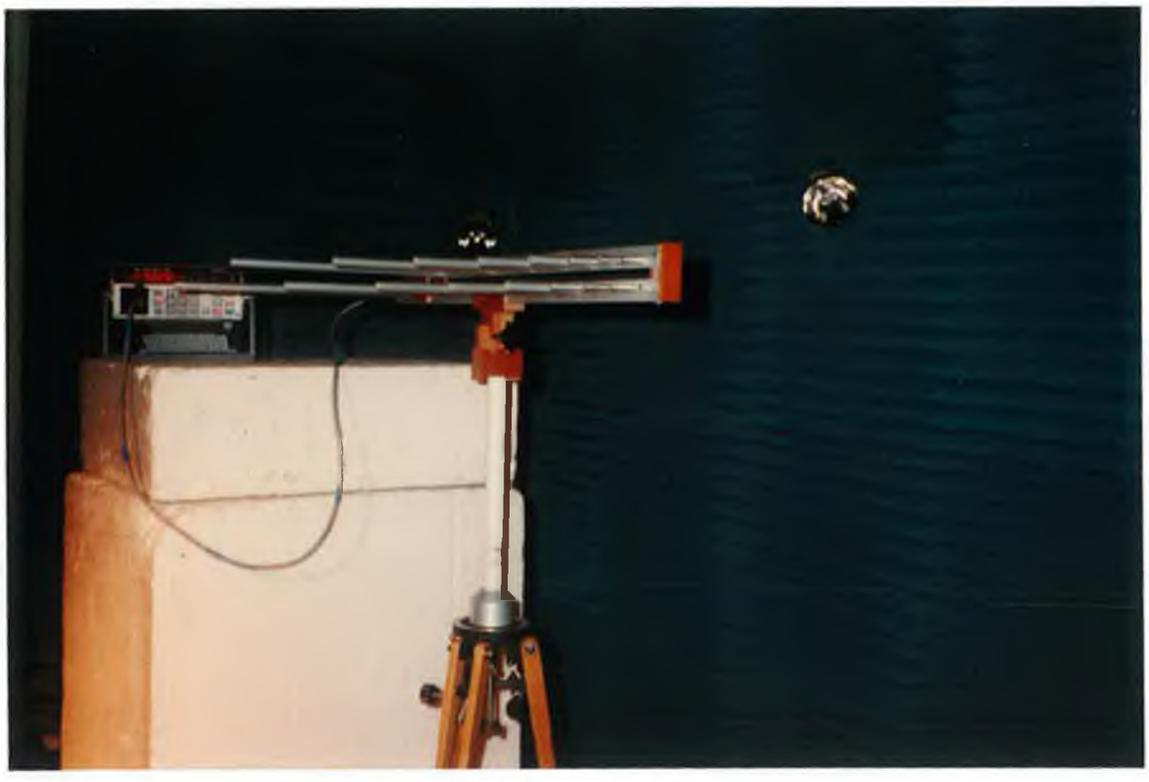

(b)

Fig. 6.1 Photograph of the anechoic chamber of Power Electronics Ireland (PEI), University of Limerick (a) Inside view of the anechoic chamber and (b) Test set-up for the measurement of ambient noise level inside the chamber.

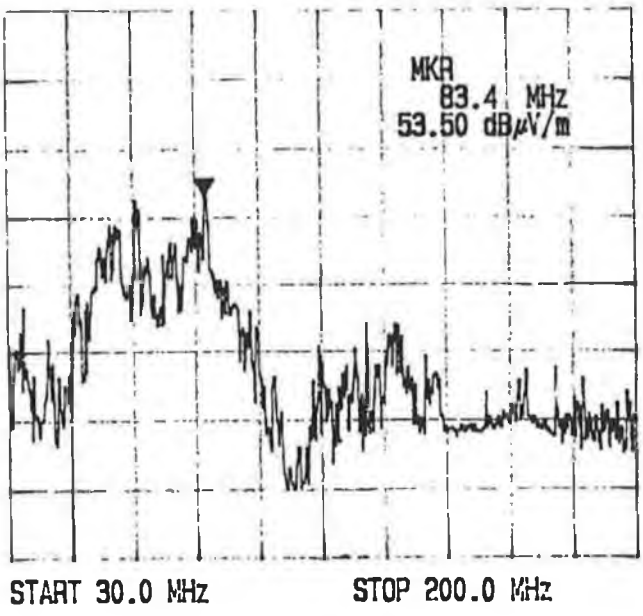

(a)

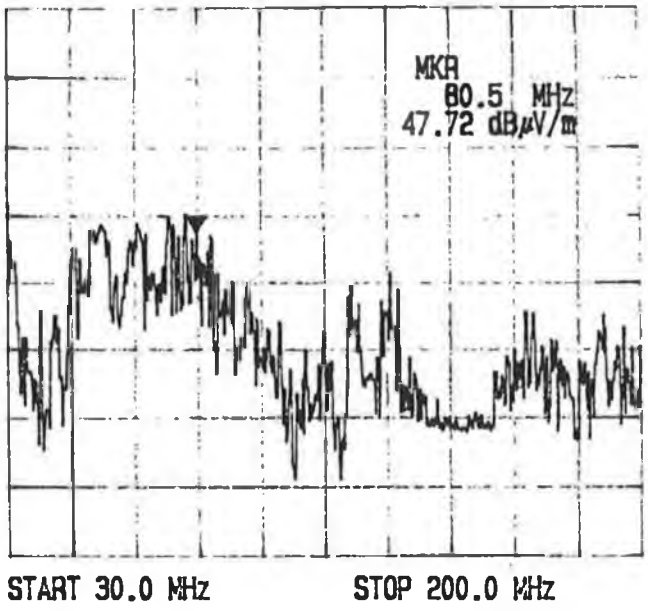

(b)

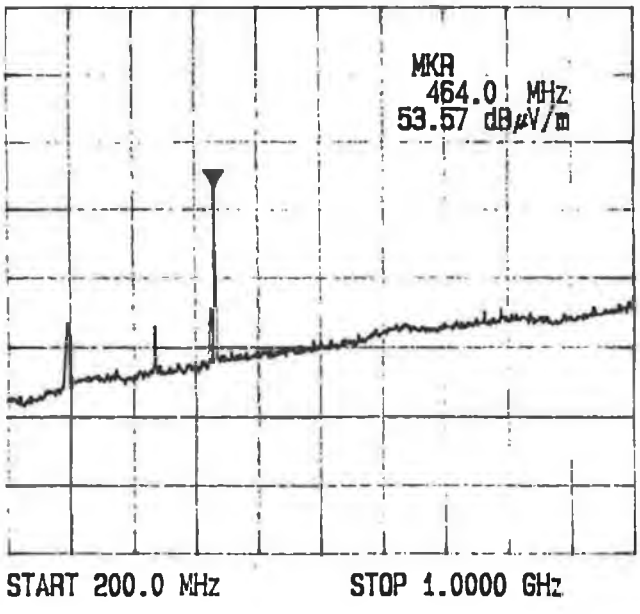

(c)

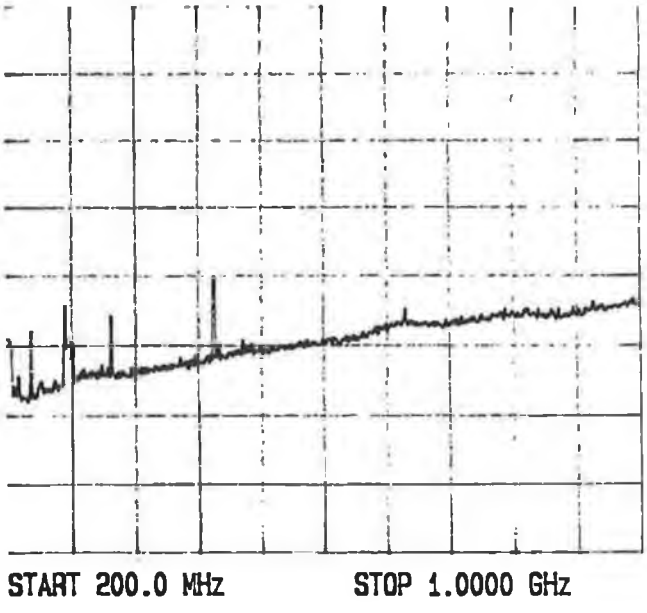

(d)

Fig. 6.2 Ambient noise level inside the chamber (a) With BCA for horizontal polarization (b) With BCA for vertical polarization (c) With LPA for horizontal polarization and (d) With LPA for vertical polarization.

The reflectivity level of the chamber varied from 49% (at 100 MHz) down to 2% (at 1 GHz) and in the microwave range of frequencies it works as almost a completely absorbing (and no echo) chamber. Except for a few measurements (SE measurements for calibrating the test antennas) as described in the previous chapter, most of the antenna measurements were taken at 1 GHz at which the anechoic chamber works very well.

6.2.2 TEST SET-UP

The basic instruments required in determining the radiation pattern of an antenna are another standard antenna, a signal generator and a receiver or power meter. The relatively precise positioning of the test and the standard calibrated antennas are particularly important in case of pattern and phase measurements which necessitates the use of a turntable to rotate the antenna under test (AUT) accurately at different angular positions.

A schematic diagram of the test set-up employed is shown in Fig. 6.3. The AUT acts as a transmitting antenna while the log periodic antenna acts as the receiving one. A synthesised signal generator (Rohde & Schwarz sweep generator and synthesizer model no. 339.001.02) was used to feed 1 GHz signal to the AUT.

6.2.3 MEASUREMENT PROCEDURE

As the AUTs are of directional type with the main beam in a particular direction, two patterns called *principal plane patterns*, bisecting the main beam may suffice to completely describe their radiation pattern. Two sets of measurements were taken. Both the AUT and the LPA are placed for their horizontal polarisation position at the same level, and the AUT is rotated in a horizontal plane by 360 degrees. The readings of the power meter connected with the LPA are recorded on a X-Y plotter. Both the AUT and the LPA are then placed for their vertical polarization position and the AUT is rotated through an angle of 360 degrees in a horizontal plane. The power meter readings are plotted. The X-axis of the plotter recorded the angular movement of the AUT while the Y-axis monitored the received voltage by the power meter in dBV. The relative positioning of the antennas for radiation pattern measurement of the TEM-T half is shown in Fig. 6.4.

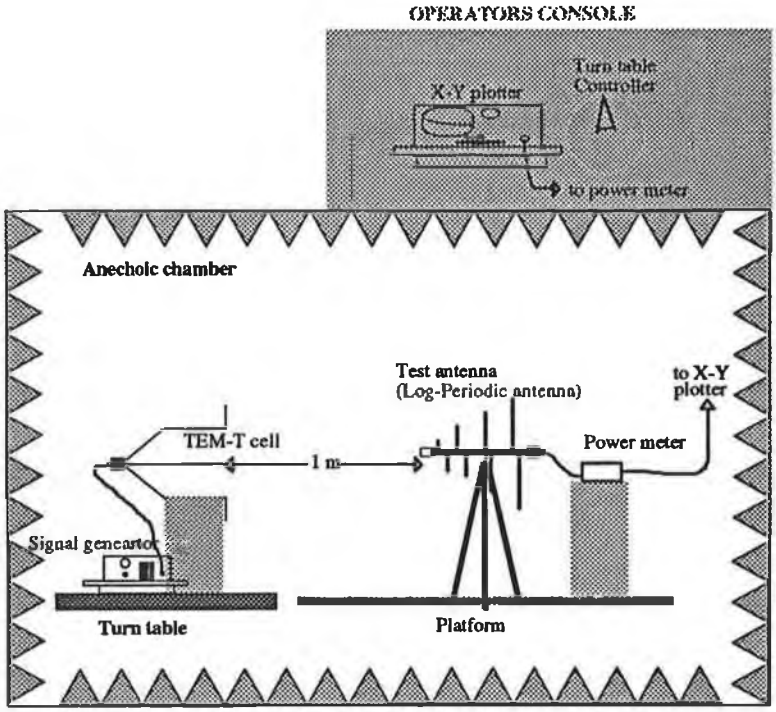

Fig. 6.3 Schematic diagram of the test arrangement for radiation pattern measurement.

6.2.4 TEST RESULTS

The test plots show the radiation patterns of the AUTs as a function of their angular position but at particular planes. In case of horizontal position of both the AUT and the test antenna the plane of observation is the plane generated by ϕ varying from 0 to 360^{o} at $\theta = 90^{o}$ where ϕ and θ represent the azimuth and polar angles respectively. Again for their vertical positioning it represents the plane of observation as $\phi = 90^{o}$ and θ varying from 0 to 360^{o}.

The power meter recorded the voltage received by the LPA (power meter and LPA are matched with 50 Ω impedance) in dBV. Thus the field strength at the test site can be obtained by adding the antenna factor of the LPA (supplied by the manufacturer of the LPA and expressed in dB) to this voltage data. The resulting field strength data are required to be expressed in μV/m in order to plot the radiated field pattern.

A relative power radiation pattern in three dimensions can be plotted from these planar patterns by generating a data file which contains data for radiation intensities at

different values of ϕ for every different value of θ and vice versa. The techniques of generating such data files for the two different AUTs are described below.

6.2.4.1 TEM-T Cell Pattern

The geometry of the TEM-T cell suggests the rectangular co-ordinate system as a suitable one for plotting its radiation pattern. The theoretical pattern plot has thus been shown on a rectangular co-ordinate system. However, the test data were obtained in spherical co-ordinates because it was easier to locate the angular positions with the rotary turntable. Fig. 6.5 shows the output of the X-Y plotter for the TEM-T half where the radiated field pattern is plotted as functions of angular positions θ and ϕ.

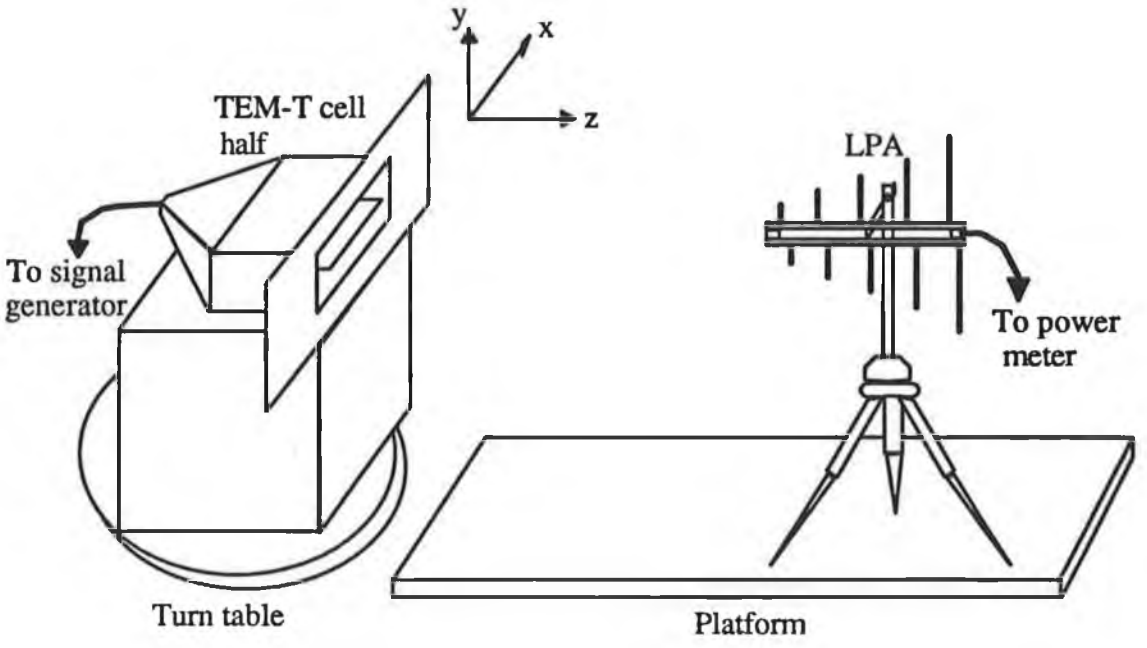

Fig. 6.4 Relative positioning of the TEM-T half radiator and the test antenna (LPA) in vertical polarization mode for radiation pattern measurement.

Fig. 6.6 illustrates how angular positions of the TEM-T half can be related to the x and y co-ordinates. The relationship between these angles and x and y however, is the same and is given by

$$x = (\text{Half length of the TEM-T cell} + 1 \text{ meter}) \times \sin\phi \text{ and} \qquad (6.2.1)$$
$$y = (\text{Half length of the TEM-T cell} + 1 \text{ meter}) \times \sin\theta$$

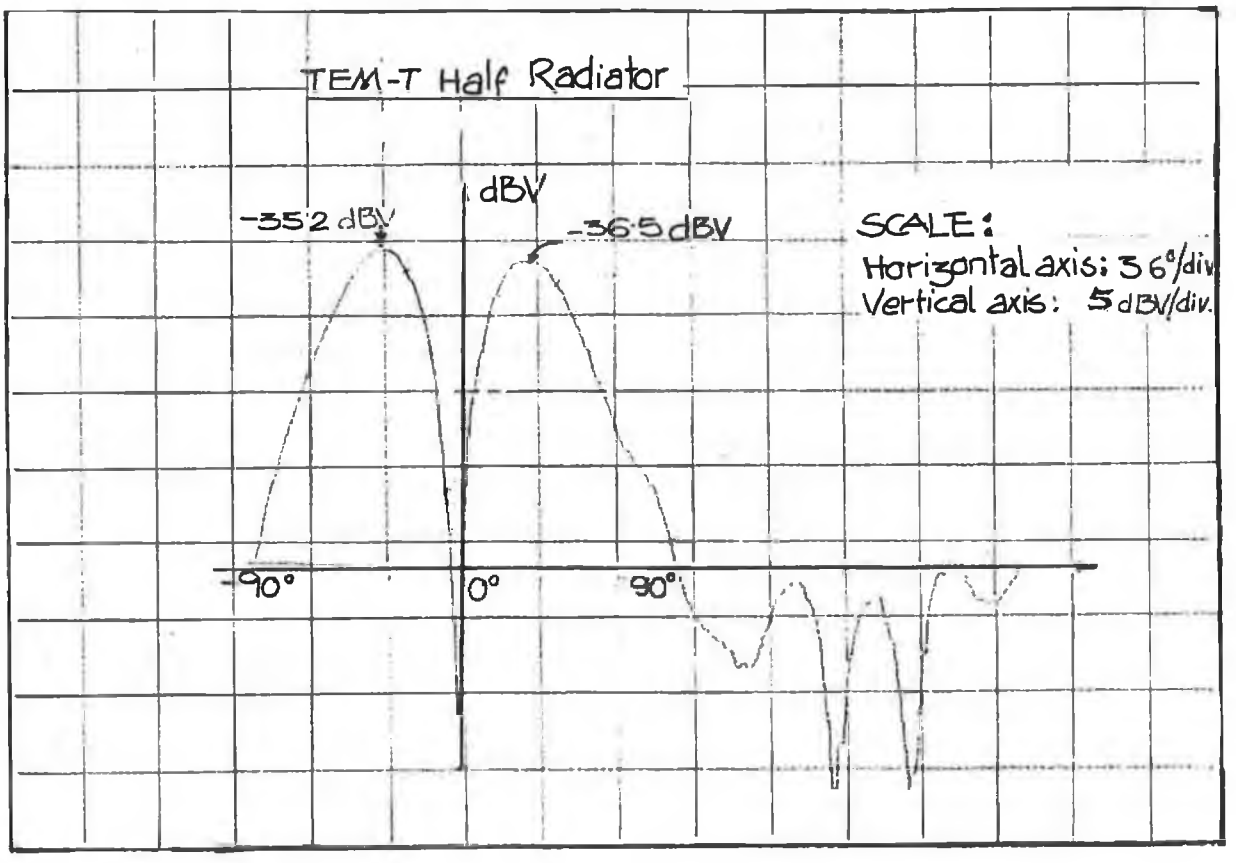

(a)

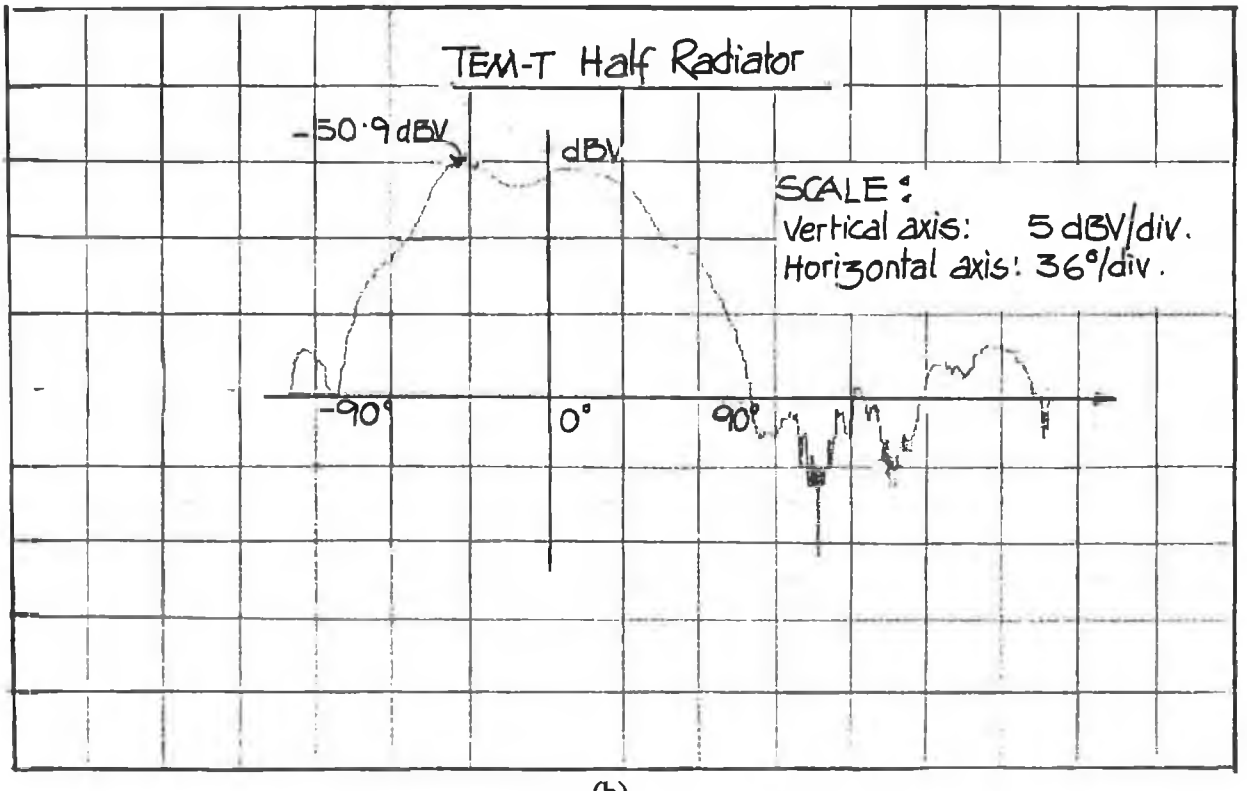

(b)

Fig. 6.5 X-Y plotter output for TEM-T half radiation pattern (a) Horizontal polarization and (b) Vertical polarization.

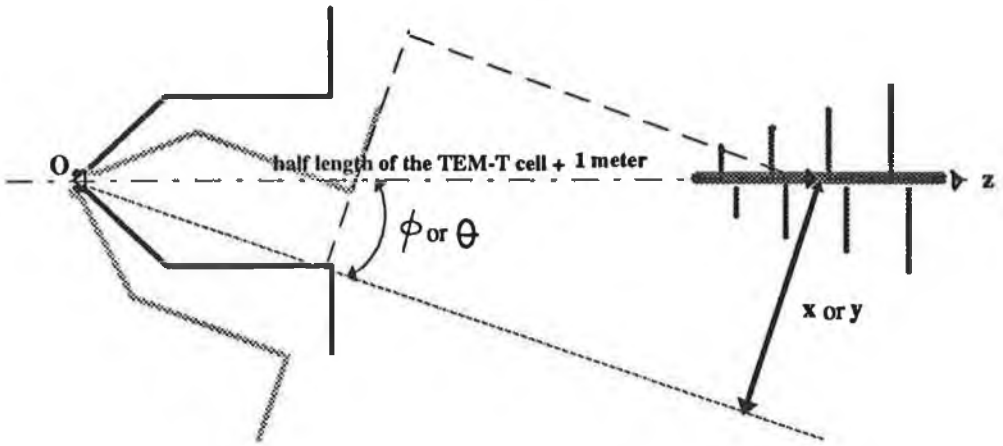

Fig. 6.6 Relation between the angular position and the rectangular co-ordinates position of the test field locations of TEM-T half .

As the TEM-T half has a large flange at its open mouth, it was anticipated that there would be no field behind it and from the radiation pattern shown in Fig. 6.5, it is confirmed that except for a few small shoots, the radiation intensities are almost negligible for angles $360^{o} \leq \phi \leq 180^{o}$ and $360^{o} \leq \theta \leq 180^{o}$. Moreover it can be seen from Fig. 6.6 that for angles greater than 90^{o} or less than -90^{o} the distances x and y are not defined. Thus the radiation pattern was plotted for angles greater than -90^{o} and less than 90^{o} only. This range of angles is assumed to be sufficient since it is much greater than the range considered with the paraxial approximations (i.e. a conical volume with apex angle $\leq 30^{o}$).

The field strength data in μV/m as functions of x and y positions are calculated from the plot of Fig. 6.5 and Eqn. (6.2.1). Each data set has been normalized with respect to the maximum field strength recorded in the respective case. Now the normalized field strength for every value of x (say at $x = x_i$, i = 1,..., m positions) is multiplied by the normalized data for every value of y (say $y = y_j$, j = 1,..., n positions) to give the normalized field strength at every point in space in the form of a m x n matrix (x_i, y_j , i = 1,..., m and j = 1,..., n). These would give the relative field pattern at distance z = 1 m from the open mouth of the TEM-T half. The details of computations are given in Appendix F1. The field pattern is plotted using GT®[174], a graphics software package, and is shown in Fig. 6.7.

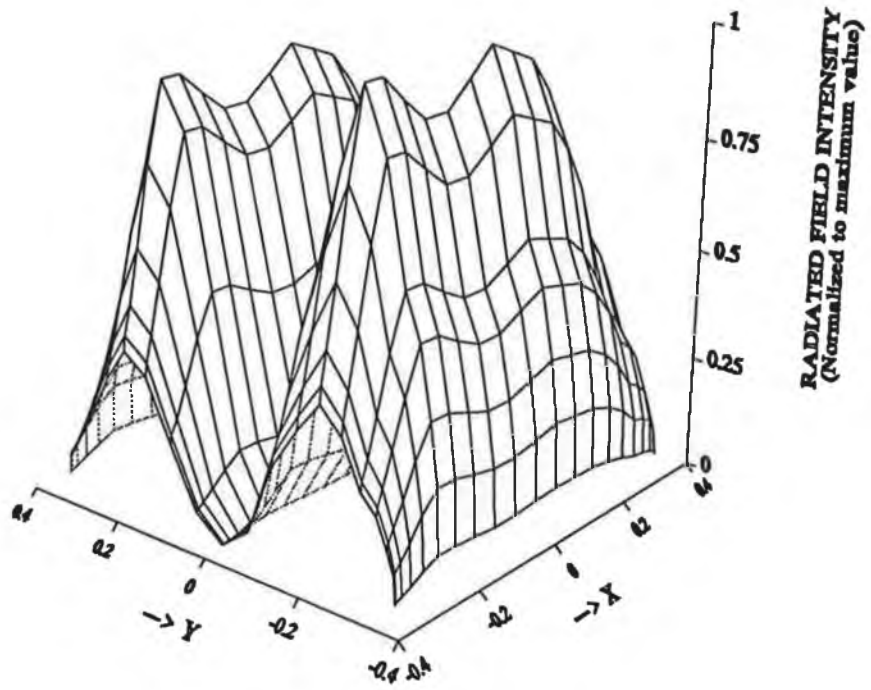

Fig. 6.7 Radiation pattern of the TEM-T half (relative field intensity pattern, experimental). Dimensions along x and y directions are in meter.

6.2.3.2 Q-loop antenna radiation Pattern

A clear picture of the Q-loop antenna radiation pattern can be visualized if it is plotted in spherical co-ordinates. Thus the test data available as the output of the X-Y plotter in the form of the plots of field strength as functions of ϕ and θ positions in two different planes, i.e., at $\theta=90^{o}$ and $\phi=45^{o}$ planes respectively, shown in Fig. 6.8 were combined to get a three dimensional polar plot of the radiation pattern. The theoretical pattern plot has also been shown on a spherical co-ordinate system (refer to Fig. 3.22).

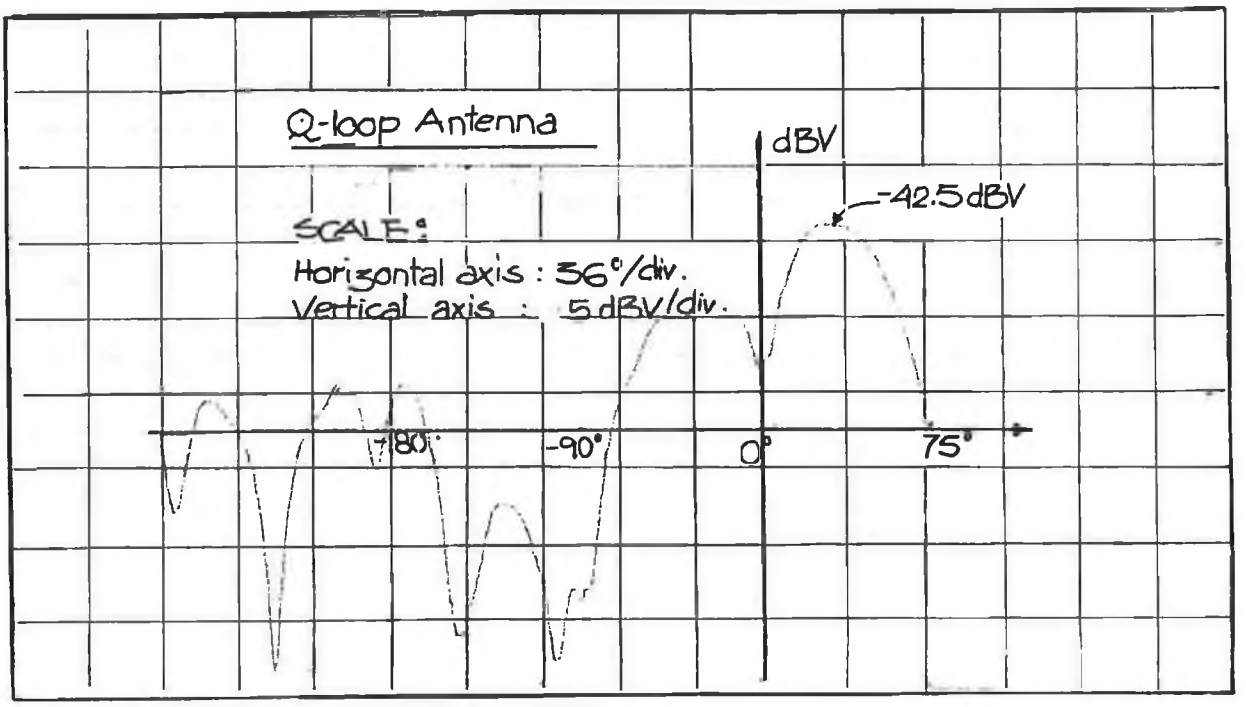

(a)

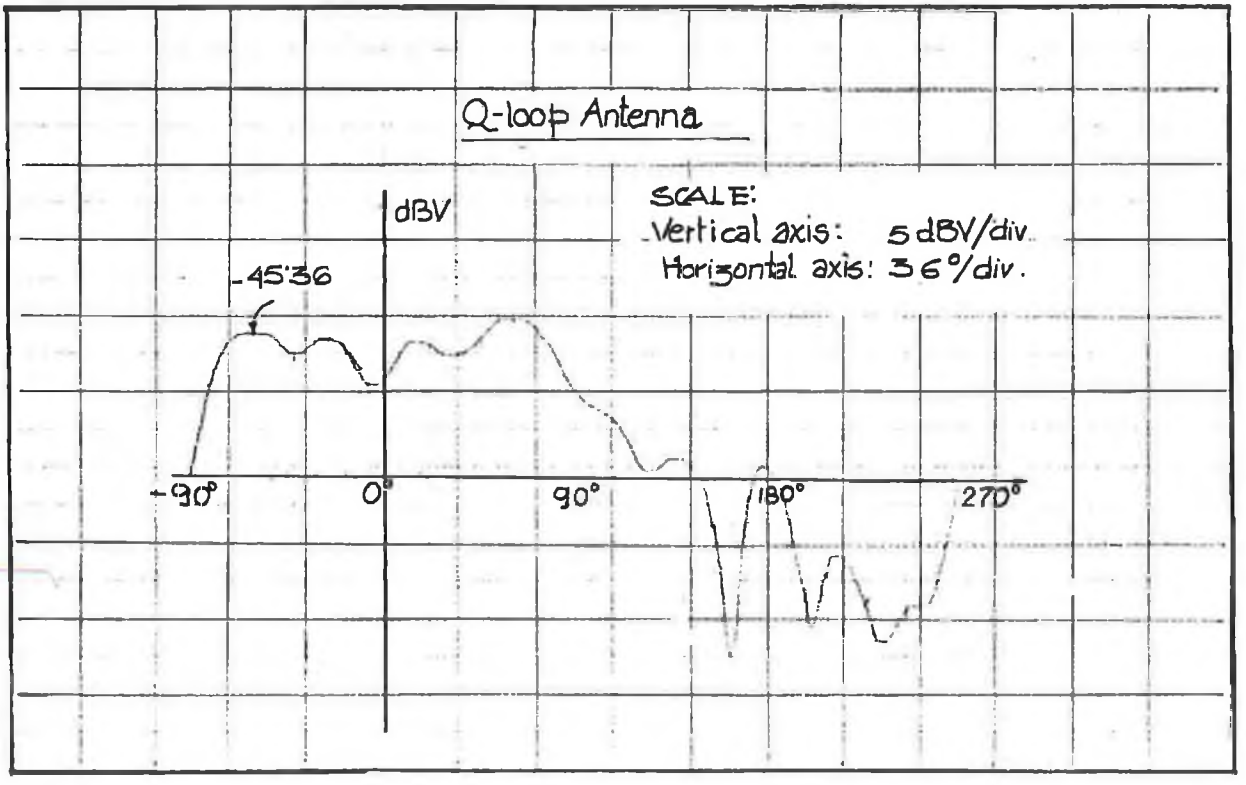

(b)

Fig. 6.8 X-Y plotter output for Q-loop antenna radiation pattern (a) Horizontal polarization and (b) Vertical polarization.

Fig. 6.9 Photograph showing the relative positioning of the Q-loop antenna and the LPA for vertical polarization mode.

The relative positioning of the of the Q-loop antenna and the LPA for radiation pattern measurement is shown in the photograph of Fig. 6.9. It shows the reference directions. The meaning of the angular positions in two different plots (of Fig. 6.8) can also be understood from this photograph.

Because of the large 90^{o} corner reflectors there should not be any field for azimuth angle $|\phi| > 45^{o}$, if the reference is selected as shown in Fig. 6.9. Similarly the field intensities should be negligible in the region ($180^{o} \leq \theta \leq 360^{o}$). Fig. 6.8(a) and (b) also suggest a similar distribution except for a few shoots in those (theoretically) null regions. In order to get an understanding of the relative radiation pattern it is thus enough to plot the pattern for azimuth angle varying from -75^{o} to $+75^{o}$ only and polar angle varying from 0 to 180^{o}. The extension of the plot up to 75^{o} instead 45^{o} in the azimuth direction is because of the considerable field intensities available in the test result (refer to Fig. 6.8) up to that angular position.

The field strength data are expressed in μV/m as functions of ϕ and θ positions from the plots of Fig. 6.8. Each data set has been normalised with the maximum field strength recorded in the respective case as was done with the TEM-T half and following the same procedure as described earlier for TEM-T half the normalized field strength at every point in space was expressed in the form of a m x n matrix (θ_i,ϕ_j, i = 1, ..., m and j = 1,..., n). These would give the relative field pattern at a radial distance r = 3 meters from the centre of the Q-loop antenna. The field pattern is plotted using GT® and is shown in Fig. 6.10.

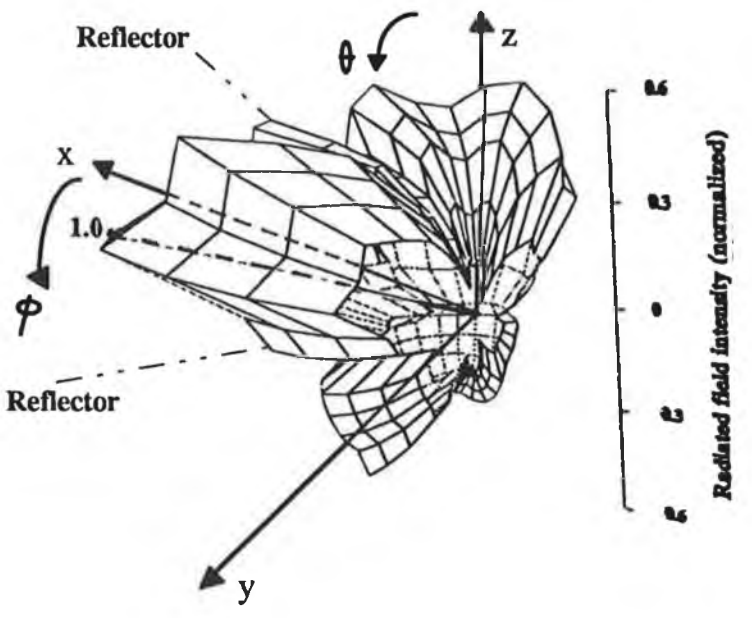

Fig. 6.10 Polar plot of the radiation pattern of the Q-loop antenna (Relative field intensity pattern, experimental). The radial axis represents the normalized radiated field intensity, a scale of which is shown along the z-axis. The rectangular co-ordinate axes are also shown in the diagram.

6.3 MEASUREMENTS OF ANTENNA PARAMETERS

Fortunately, the measurements of the characteristics of interest such as gain, directivity, impedance and VSWR do not involve much sophisticated instrumentation nor a special test environment. The measurements of the above parameters mainly require an anechoic chamber and test antennas as were essential for pattern measurements. Gain of the

antennas was measured in two different ways, directivity was derived from the radiation pattern and only the magnitude of the VSWR was measured. The measurement procedure and analysis of the test results are discussed below.

6.3.1 ANTENNA GAIN MEASUREMENT

Gain is probably be the most important figure-of-merit of an antenna. The relative amplitude-pattern information may be converted into absolute field intensities through information derived from the measurement of antenna gain. It is defined as "the ratio of the radiation intensity in a given direction, to the radiation intensity that would be obtained if the power accepted by the antenna were radiated isotropically. Various techniques, depending on the frequency of operation, are available for measuring the gain of an antenna. Usually free space ranges are used to measure the gain near or above 1 GHz. At lower frequencies the longer wavelengths require larger area to simulate free-space conditions and thus the measurement system becomes complicated.

Two basic methods are commonly used to measure the gain of an electromagnetic radiator in the literature [172-173] on antenna measurement: (a) Absolute gain measurement and (b) Gain transfer measurements. The absolute gain method is used to calibrate antennas that can be applied as standards for gain measurements and it does not require *a priori* knowledge of the gains of the antennas. Gain-transfer methods on the other hand must be used in conjunction with standard gain antennas to determine the absolute gain of the AUT. A calibrated LPA whose absolute gain is known can be employed for this purpose.

6.3.1.1 Absolute Gain Measurements

Among the number of available techniques the simplest one, known as the two antenna method, has been employed to measure the absolute gain of the AUTs. The method is based on Friis transmission formula (described in Appendix F2). It requires an identical pair of each AUT. One of the pair is used as the transmitter and the other as the receiver. The antennas are separated by a distance R, which must satisfy the far-field criterion ($R > \frac{2D^2}{\lambda}$) of each antenna where D is the larger dimension of the AUT and λ is the operating wavelength. The schematic diagram of the test arrangement is shown in Fig.

6.11. The transmitting AUT was rotated until the angular position for maximum reading of the power meter was found.

According to Friis formula for completely identical, polarization matched antennas which are aligned for maximum directional radiation, Eqn. (F2-6) (see Appendix F2) reduces to

$$G_o(dB) = \frac{1}{2}\left[20\log_{10}\left(\frac{4\pi R}{\lambda}\right) + 10\log_{10}\left(\frac{P_r}{P_t}\right)\right] \qquad (6.3.1)$$

where

G_0(dB) = gain of the AUT in dB

P_r = power received by the receiving antenna

P_t = power transmitted by the transmitting antenna

Measuring the powers P_r and P_t and substituting the values of R and λ in Eqn. (6.3.1), the absolute gain of the antenna can be found.

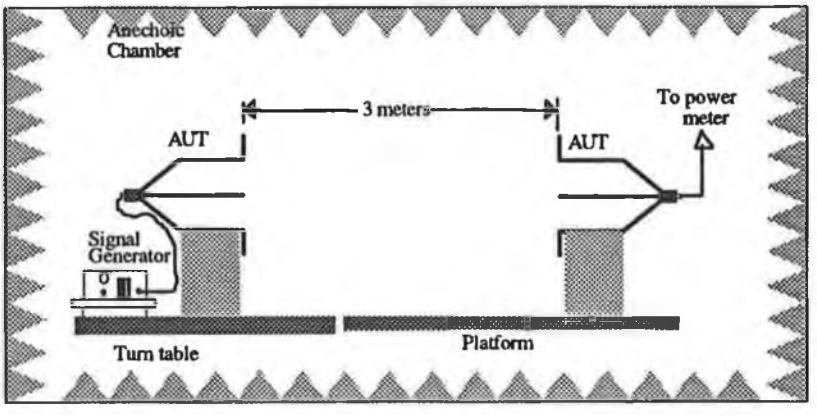

Fig. 6.11 Basic arrangement of the two antenna method of absolute gain measurement.

6.3.1.1.2 Gain of the TEM-T antenna

Power transmitted by the signal generator, P_t = -1.9 dBm

Power meter reading, P_r = -39.2 dBm

R = 3 meters and λ = 0.3 meters (at 1 GHz in free space)

thus from Eqn. (6.3.1)
G_{OTEM-T}= 2.4 dB

6.3.1.1.2 Gain of the Q-loop antenna

The transmitted power, distance between the antennas and the wavelength were the same as above and the power meter reading , P_T = -34.5 dBm. So from Eqn. (6.3.1)
$G_{OQ-LOOP}$= 4.7 dB

6.3.1.2 Gain-comparison Measurements

This method is most commonly used to assess the gain of an antenna. Usual practice is to compare the antenna under test (AUT) with an standard antenna whose gain is known with respect to an isotropic radiator. Initially relative gain measurements are performed, which when compared with the known gain of the standard antenna, yield absolute gain.

The procedure requires two sets of measurements. In a simple test arrangement the AUT is used as a transmitting antenna and the LPA is placed at a distance of 3 m (which fulfils the far-field requirement of both the antennas). Power received by the LPA is recorded. The other antenna of the AUT pair is then placed at the same distance from the AUT and the power received by this antenna is compared with that received by the LPA. As the gain of the LPA is known in dBi (decibel isotropic) the dBi of the AUT can be determined. The basic test set-up is almost the same as shown in Fig. 6.11 except that the receiving antenna is once the LPA and then another AUT.

6.3.1.2.1 Gain of the TEM-T antenna

Power received by the LPA = -46.7 dBm
Power received by the TEM-T half = -50.4 dBm
Gain of LPA = 5.9 dBi
Gain of TEM-T half = 2.2 dBi

6.3.1.2.2 Gain of the Q-loop antenna

Power received by Q-loop antenna = -46.2 dBm

power received by LPA = -44.9 dBm
Gain of Q-loop antenna = 4.6 dBi

The techniques outlined above yield good results provided the AUTs and the standard gain antennas exhibit good linear polarization purity. Errors would be introduced if either of them polarizes with a finite axial ratio. In order to get rid of the effects of multiple reflection interferences and the ground reflections, the measurements were performed at 1 GHz.

6.3.2 DIRECTIVITY MEASUREMENT

The directivity is defined earlier by Eqn. (3.4.23). When the radiation pattern of an antenna is known, that equation may be used to determine the directivity of the antenna. The radiation intensities available from the pattern measurement are averaged over the angle subtended by the sphere and the maximum radiation intensity (which is 1 in the normalised data file created for pattern plotting as described in section 6.2.3) is then divided by this average intensity to get the directivity data.

6.3.2.1 Directivity of the TEM-T half

A computer program (similar to the one used for generating the data file for pattern plotting) is developed in order to compute the directivity of the TEM-T half acting as an antenna. Field intensities at different angular positions around the TEM-T half are taken from the X-Y plotter output shown in Fig. 6.5. These are then averaged over the total angular area measured in degrees square (as shown in Appendix F3). The directivity is just the reciprocal of this average intensity. The polar plot of the radiation intensity profile (from which the average intensity is computed) over the $360^{o} \times 360^{o}$ angular area is given in Fig. 6.12. Through these computations the directivity of the TEM-T half antenna was found to be $\cong 8$.

6.3.2.2 Directivity of the Q-loop antenna

From a similar computer program to above (listing is given in Appendix F3), the directivity of the Q-loop can be calculated. Intensity data is taken from the X-Y plotter output shown in Fig. 6.8. The polar plot of the radiation intensity profile for Q-loop

antenna (from which the average intensity is computed) over the $360^o \times 360^o$ angular area is given in Fig. 6.13. The directivity of the Q-loop antenna as a result of such computations was found to be $\cong 6$.

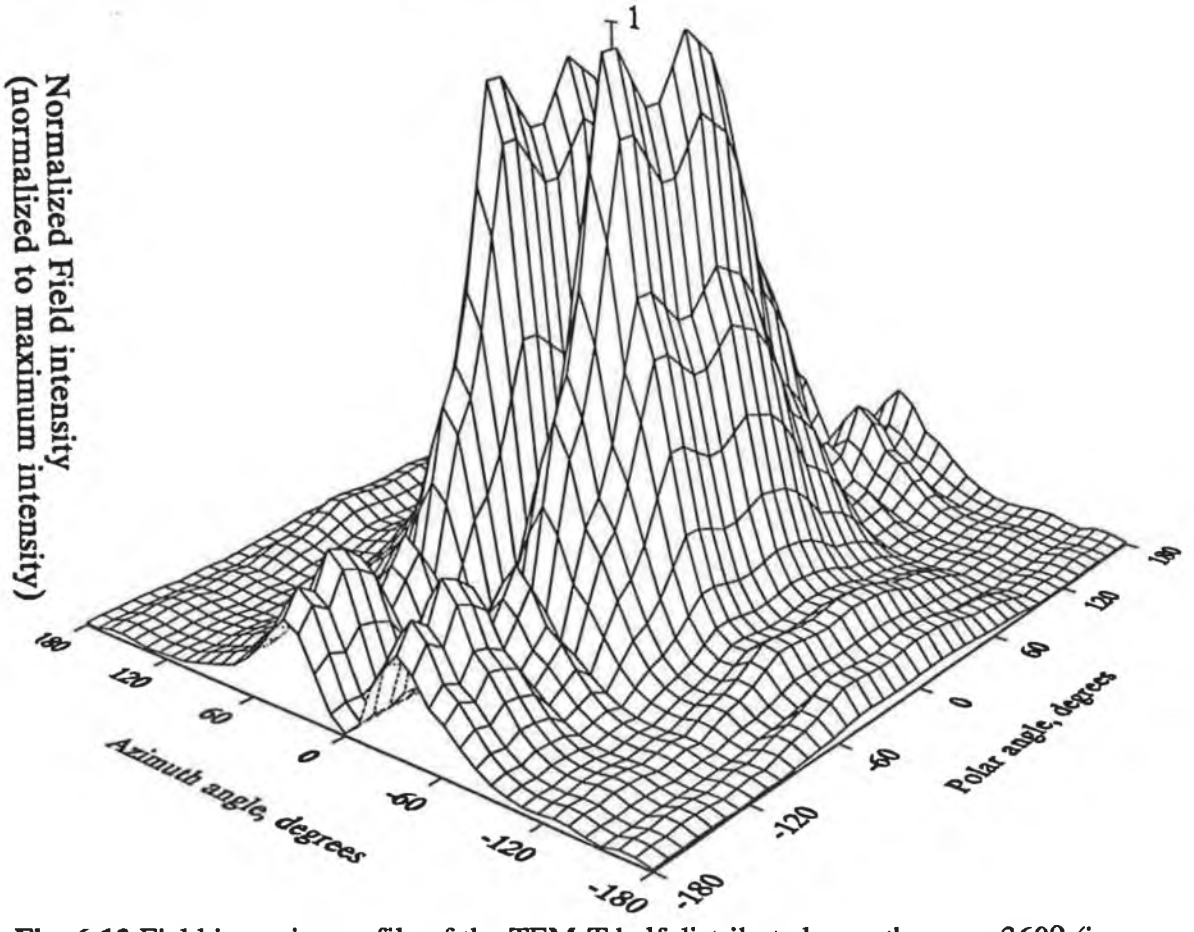

Fig. 6.12 Field intensity profile of the TEM-T half distributed over the area, 360^o (in azimuth direction) $\times 360^o$ (in polar direction). At a distance of 1 m from the TEM-T half and at a frequency of 1 GHz.

6.3.3 TRANSMISSION COEFFICIENT MEASUREMENT

By transmission coefficient is meant the ratio of the transmitted power to the incident power at the input terminals of the antenna. The signal generator, receiver and the co-axial line are assumed to be all 50-Ω system. In fact this ratio is an indirect measure of the impedance mismatch at the input of the antenna with respect to a 50-Ω line. It depends on input impedance of the antenna. Any impedance, Z_A terminating a transmission line will produce a reflected wave with reflection coefficient ρ and a voltage standing wave ratio (VSWR) related as follows

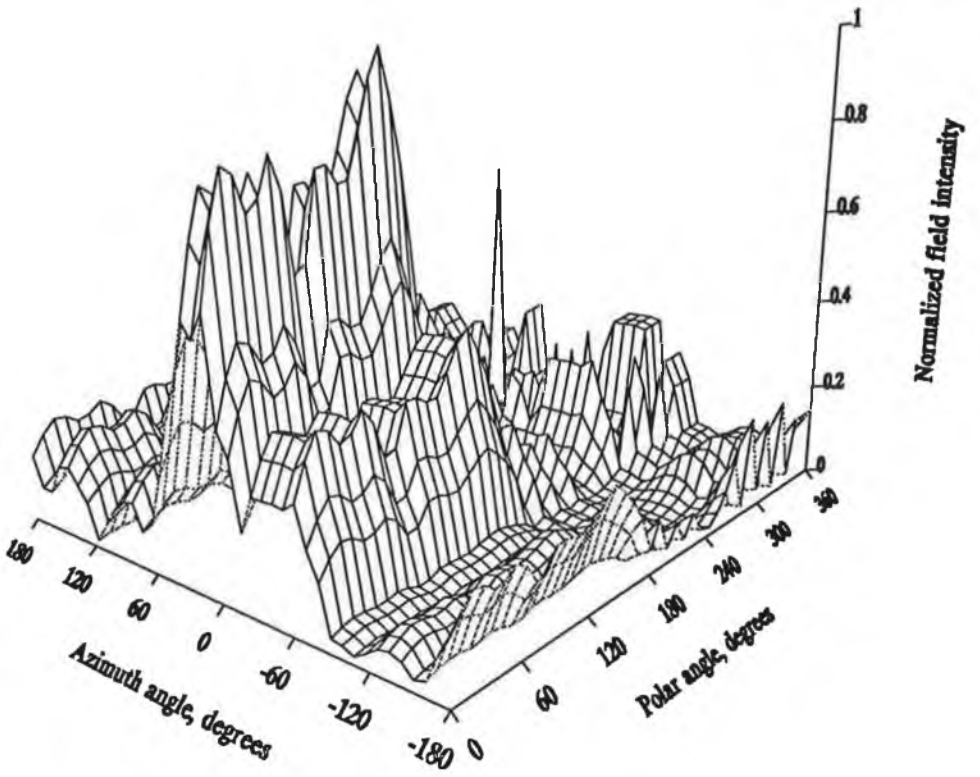

Fig. 6.13 Field intensity profile of the Q-loop antenna distributed over the area, 360^{o} (in azimuth direction) $\times 360^{o}$ (in polar direction) at a radial distance of r = 3 m.

$$\rho = \frac{|\text{reflected voltage}|}{|\text{incident voltage}|} = \frac{Z_A - Z_L}{Z_A + Z_L} = \frac{VSWR - 1}{VSWR + 1} \qquad (6.3.4)$$

where VSWR is the ratio of the maximum to minimum voltage on the line and Z_L is the characteristic impedance of the line. The power transmitted to the AUT from the signal generator is related to the reflection coefficient as

$$P_{trans} = P_{inc}\left(1 - |\rho|^2\right) \qquad (6.3.5)$$

Where P_{inc} is the power fed by the signal generator. Thus if it is possible to measure the ratio of the incident to reflected voltage at the terminal of the AUT with a 50-Ω system, the power transmtted to the AUT can be determined from the above equation.

The reflection coefficient was measured in this case using a directional coupler (HP 778D dual directional coupler) and a power meter. The block diagram of the test set-up is shown in Fig. 6.14.

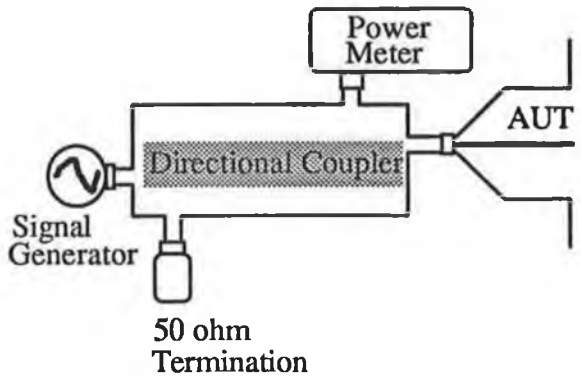

Fig. 6.14 Block diagram of the test arrangement for reflection coefficient (at the input terminals) measurement of the antennas under test.

6.3.3.1 Test Procedure

A signal is fed through a matched signal generator (output impedance 50Ω) to the input port of the bi-directional coupler. The other port on the input side is terminated with a matched load of 50 Ω. A power meter (input impedance 50 Ω) is connected at one of the test ports. At first the other test port is left open and the power meter reading is noted in dBV. Ideally since the other test port is open all the power incident at that port should be reflected back to the power meter, hence it gives the amount of power incident on this port. Then the AUT terminal is connected to this port and the power meter reading is recorded again in dBV. This gives the amount of power being reflected back due to the impedance mismatch (with respect to 50Ω) at the AUT terminals. Thus the ratio of these two readings of the power meter gives the reflection coefficient of the 50Ω line when terminated at the AUT.

6.3.3.2 Power transmission coefficient of the TEM-T cell half

Power meter reading with the output port open V_{ref} = -33.8 dBV
Power meter reading with the AUT at the output port V_{inc} = -38.0 dBV
Thus the reflection coefficient, $|\rho|$ = -4.2 dB

Expressing |ρ| in per unit and from Eqn.(6.3.5), the power transmitted to the input of the antenna at 1 GHz with respect to a 50-Ω system can be found as $P_{trans} = 0.61 P_{inc}$. P_{inc} can be read from the power meter.

6.3.3.3 Power transmission coefficient of the Q-loop antenna

V_{ref} was the same as before and
V_{inc} = -41.0 dBV .
Thus for Q-loop antenna, |ρ| = -7.2 dB and
following the same calculations as before $P_{trans} = 0.81 P_{inc}$.

All the above measurements were also made in the anechoic chamber. Obviously the transmission coefficient is affected by the surrounding objects. If there are metallic objects or EM scatterers near the AUT the reflection coefficient and related parameters would be affected. In the present analysis only the magnitude of the voltage reflection coefficient is given but it is a phasor quantity and hence has phase angles as well. It is possible to measure the input impedance of the AUT if the phase angle of the above quantity were known, however, this is beyond the scope of this work.

6.4 COMPARISON WITH THE THEORETICAL RESULTS

In order to compare the radiation patterns with the test results as described in section 6.2 above, the three dimensional pattern plots are not enough. To demonstrate the similarity or deviations it is essential to show the projections of the three dimensional plots on different planes. The comparative analysis for two different antennas are discussed separately.

6.4.1 COMPARATIVE ANALYSIS FOR TEM-T HALF ANTENNA

The theoretical radiation pattern of the TEM-T half acting as an antenna was shown in Fig. 3.18. Mathematical formulations for determining the antenna parameters are given in section 3.4.4. Those predictions are compared with the test results in the following subsections.

6.4.1.1 Study of Radiation Pattern

In determining the radiation pattern of the TEM-T half theoretically it was assumed that there would be no radiation behind the flanges of the TEM-T half. Moreover with paraxial approximations it was observed that far the field beyond the aperture of the cell ($-2a \leq x \leq 2a$ and $-2b \leq y \leq 2b$, where a and b are the half length and half width of the TEM-T cell), the radiation intensity drops to a negligible value.

In actual measurement of the radiation intensity, some radiated field is detected behind the TEM-T half (zero field there could only be assumed with an infinite flange which was not the case in practice). Furthermore, the outer conductor of the TEM-T cell was assumed to be carrying equal and opposite current to that on the septum but as soon as the cell was sectioned at the middle and left open as an isolated half this assumption does not hold. As a result some leakage current, although minimal, starts flowing through this conductor contributing to the radiation. In front of the flanges the radiation pattern is similar to that plotted theoretically. The spread of the radiation intensity with significant field strength in front is wider in the x -direction than that predicted analytically.

As noted before the comparative pattern behaviour can be seen more clearly through the projections of the 3-D plot in X-Y, Y-Z and X-Z planes. The projection of the patterns (Fig. 3.12 and Fig. 6.7) on the X-Y plane are shown in Fig. 6.15, where it is apparent that the experimental pattern is diffused over a larger area than the theoretical one. In the theoretical analysis it was assumed that the flange is not contributing to radiation but in practice there must be some radiated field due to the leakage current on the flange which results in this wider spread of the intensity.

The dual peak of the projected pattern on the Y-Z plane (as described earlier in section 3.4.3 due to the oppositely directed E-field distribution at the radiating aperture) is as prominent in the experimental pattern (refer to Fig. 6.16(b)) as it was in the theoretical one (refer to Fig. 6.16(a)). However, in the theoretical model because of the simplifying assumptions of vertically directed uniform E-field lines, the distribution is symmetrical while in the experimental pattern the it is not symmetrical. This might have resulted from the lack of proper alignment of the TEM-T septum and the axis of the LPA in vertical polarization mode.

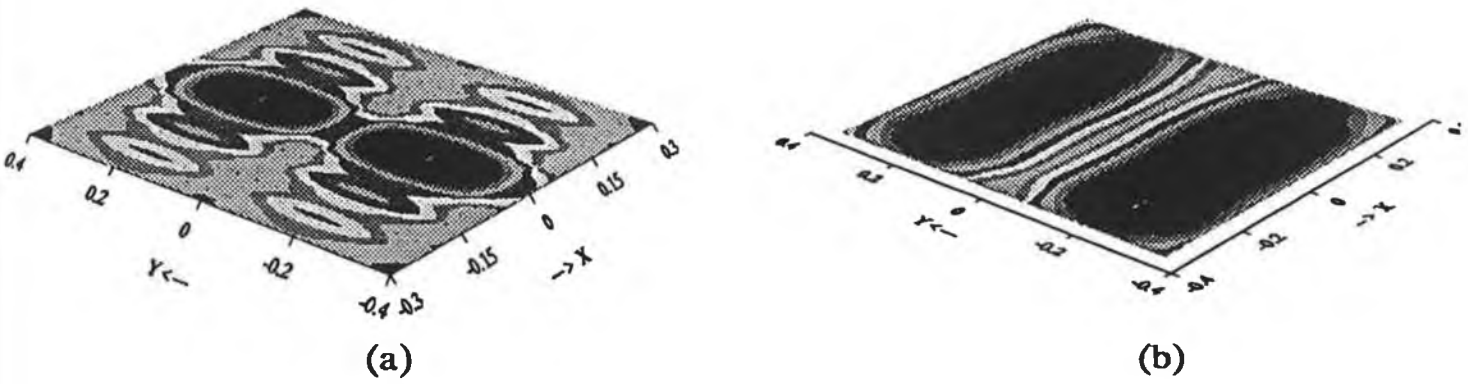

Fig. 6.15 Projection of the radiation pattern of the TEM-T half on X-Y plane (a) Theoretical and (b) Experimental.

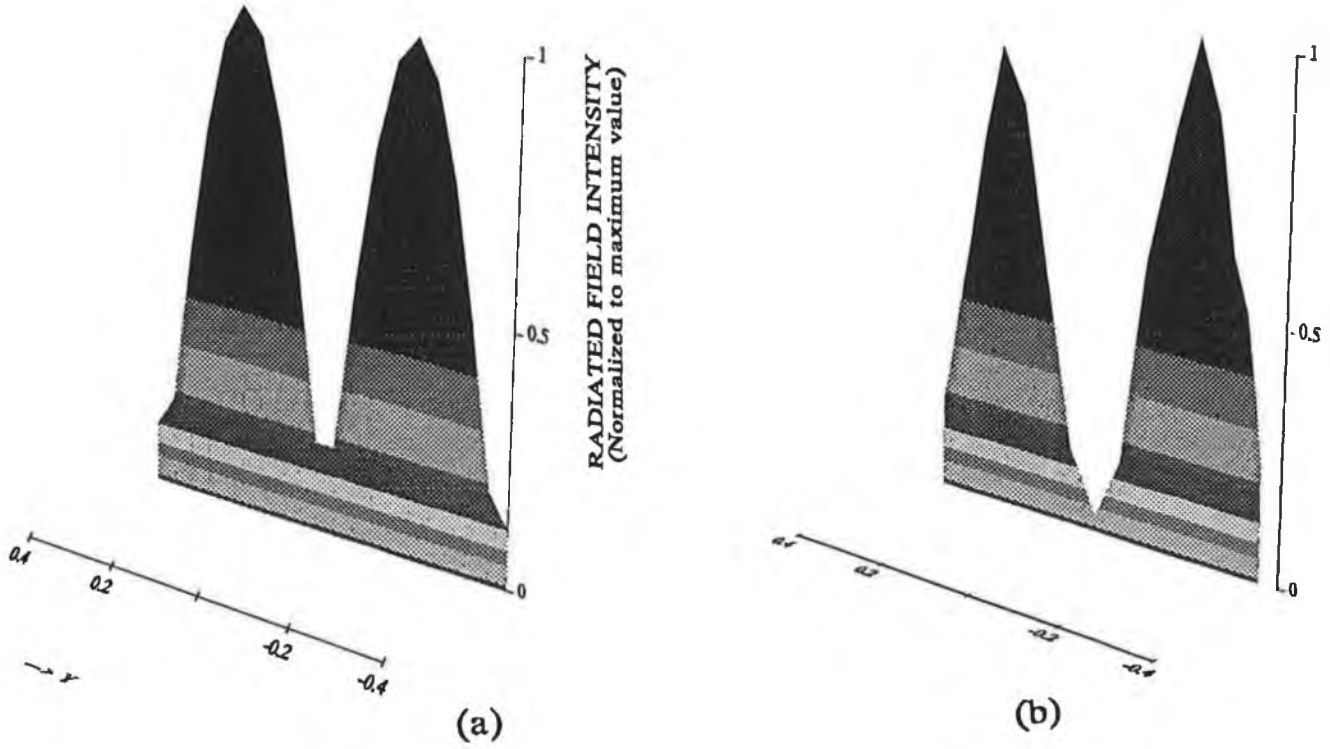

Fig. 6.16 Projection of the radiation pattern of the TEM-T half on **Y-Z** plane (a) Theoretical and (b) Experimental.

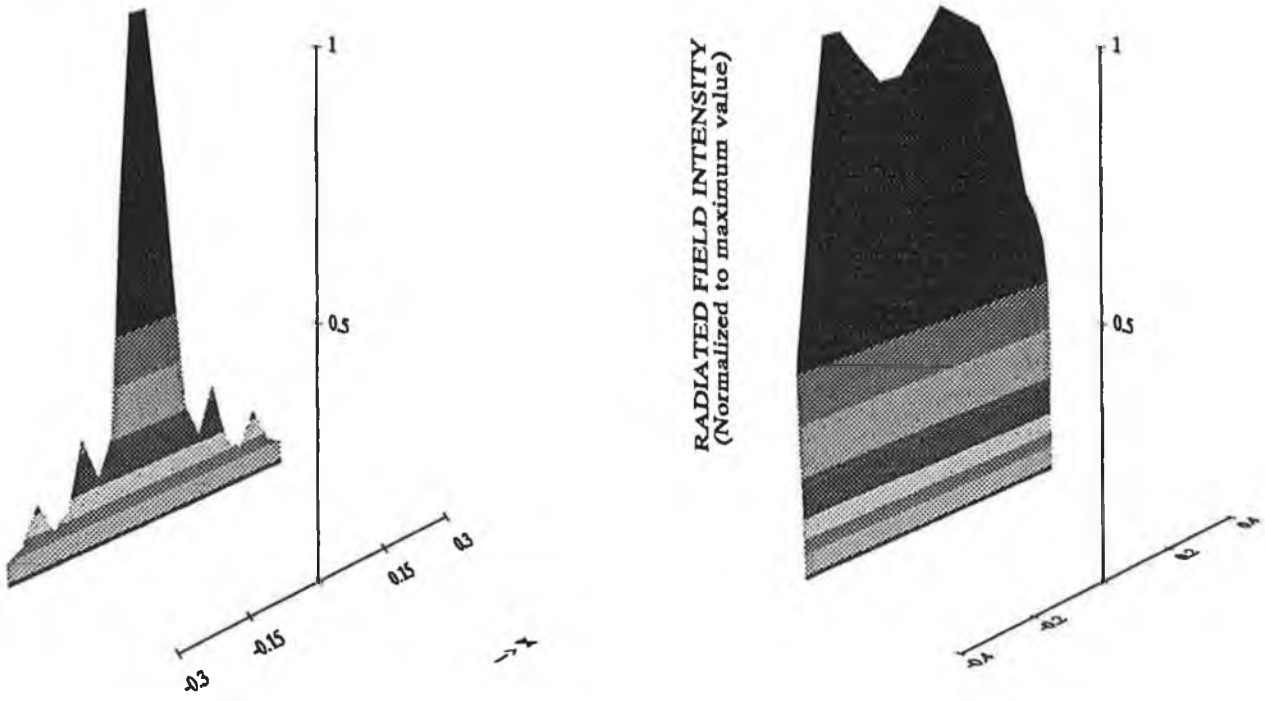

(a) (b)

Fig. 6.17 Projection of the radiation pattern of the TEM-T half on X-Z plane (a) Theoretical and (b) Experimental.

It is interesting to note that, although not very significant, a dual peak shape is also observed in the experimental pattern projection on the X-Z plane but this is completely absent in the theoretical pattern (where a single peak is observed) as shown in Fig. 6.17. This phenomenon may well be explained from the more accurate E-field distribution of the radiating aperture (as plotted in Fig. 3.13) where it is apparent that the E-field vectors are not uniform along x-direction rather they have peaks symmetrical about the z-axis at small values of x. In the approximate theoretical pattern calculation this was neglected and uniform distribution was assumed (refer to Fig. 3.15). The wider spread of the experimental pattern along x-axis is also evident from Fig. 6.17 and it has been explained before.

6.4.1.2 Study of the antenna parameters

Simplifying assumptions are also made in calculating the important antenna parameters analytically as were done in determining the radiation pattern. However, apart from a few exceptions, the test results are very close to the predicted values.

6.4.1.2 .1 Gain

The measured gain of the TEM-T half differs widely from the theoretical gain. From Eqns. (3.4.38), (3.4.26) and (3.4.27), the gain of the antenna is found to be 6 dBi whereas its measured value in both gain measurement techniques were found to be slightly above 2 dBi. As discussed at the end of section 6.3.1 the test results would be erroneous if either the AUT or the standard antenna polarizes with a finite axial ratio. The standard antenna is an LPA thus linearly polarized but the TEM-T half behaves like an open ended wave guide and as such its polarisation may perhaps be elliptic. The discrepancy in the test result may be caused by this polarization mismatch.

6.4.1.2.2 Directivity

Directivity calculation for the TEM-T half was based on assumptions similar to those made for radiation pattern analysis. Thus because of the wider pattern and existence of the field intensity behind the cell, the average intensity was higher in experimental results which appeared in the form of lower directivity value than the theoretical one. The measured directivity of 8 is lower than the predicted directivity of 9.8 (calculated using Eqns. (3.4.26) and (3.4.27)).

6.4.1.2.3 Reflection coefficient at the input terminals of the TEM-T half

Performing the integrations as indicated in Eqn. (3.4.37) and substituting in Eqn. (3.4.36), the input reflection coefficient of the TEM-T half were computed which was $\cong 0.45$. This is smaller than the measured value but not very significantly.

6.4.2 COMPARATIVE ANALYSIS FOR THE Q-LOOP ANTENNA

To compare the three dimensional polar plots of the Q-loop antenna, projections of the patterns on the $\theta=90^{o}$ plane ($|\phi|\leq 180^{o}$) and same on the $\phi=0^{o}$ plane($0^{o}\leq\theta\leq 360^{o}$)are used.

6.4.2.1 Study of Radiation Pattern

The pattern plotted from test results does not differ significantly from the predicted pattern shown in Fig. 3.22 except for some shoots in the (theoretically) shadow region.

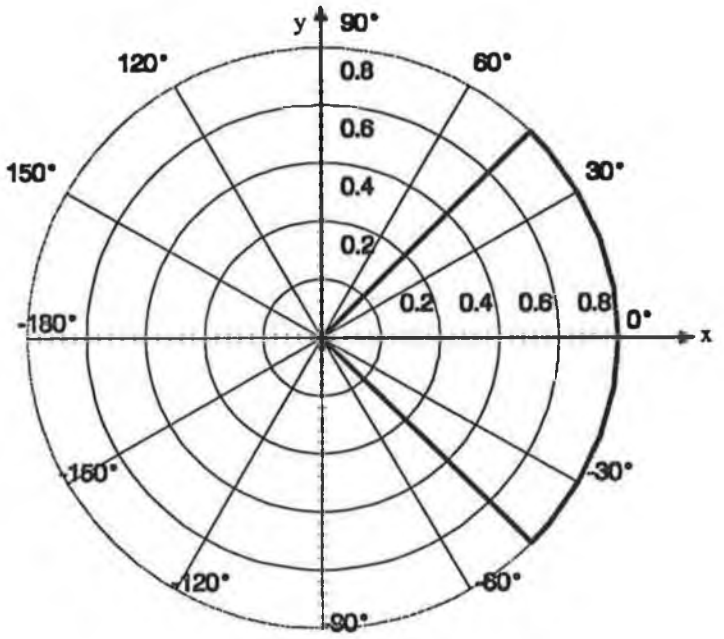

(a)

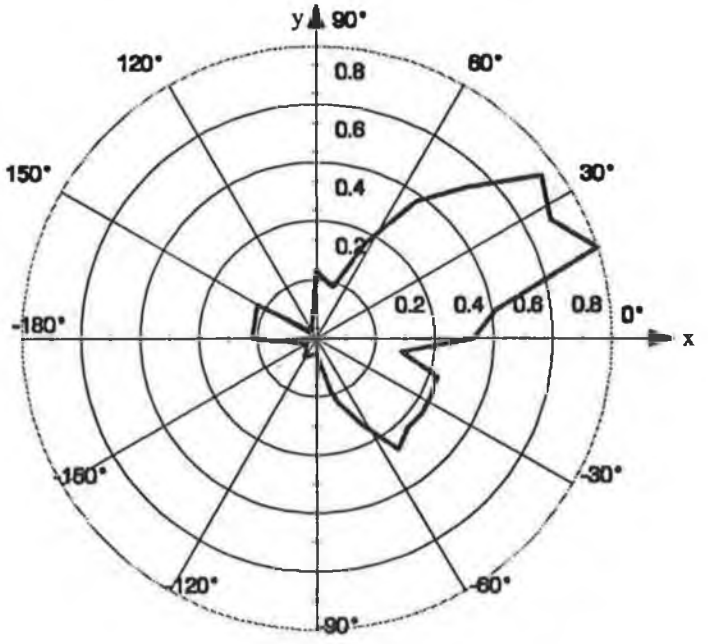

(b)

Fig. 6.18 Planar radiation pattern on $\theta = 90^{o}$ and ϕ varying from -180^{o} to $+180^{o}$
(a) Theoretical predictions and (b) Test results.

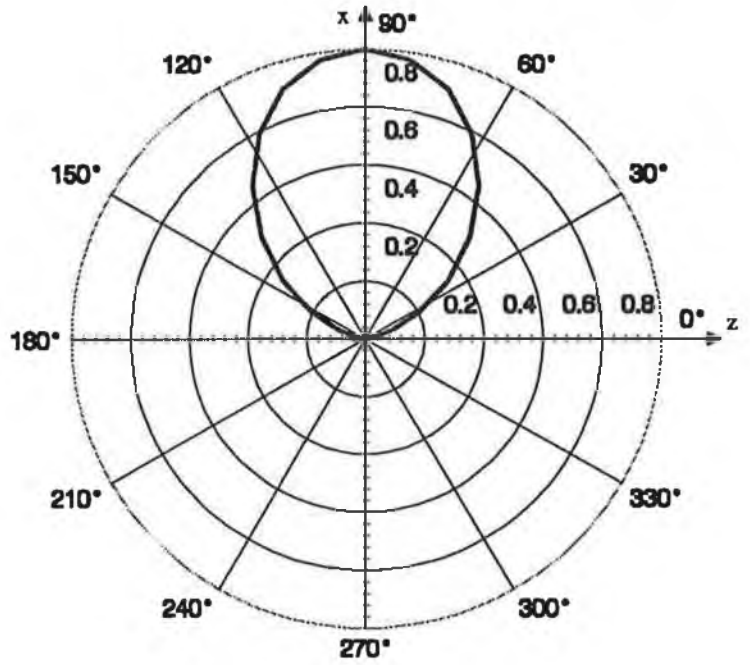

(a)

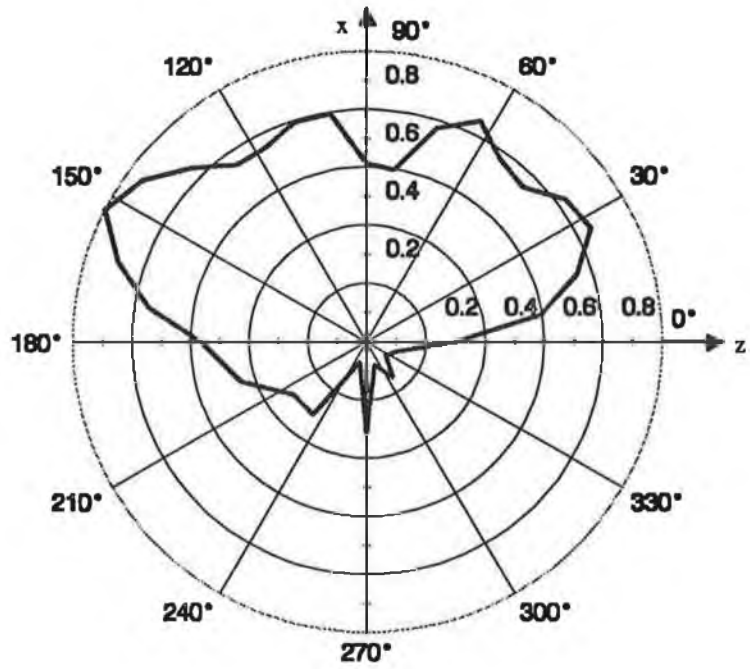

(b)

Fig. 6.19 Planar radiation pattern of the Q-loop antenna on $\phi = 45^{o}$ plane with θ varying from 0 to 360^{o} (a) Theoretical predictions (b) Test results.

The reason for the existence of some field behind the reflector most likely due to the leakage current flowing thorough the reflector which contributes to radiation there.

Two principal discrepancies are noted: the radiated field is spread up to $\pm 75^{o}$ (refer to Fig. 6.18 (b)) instead of $\pm 45^{o}$ as was predicted theoretically (refer to Fig. 6.18(a)) and the distribution is not uniform as anticipated in the theory. These were most probably caused by the edge diffraction and because the size of the reflector which was comparable to the wavelength.

On the $\phi=0^{o}$ plane, the test results show a greater spread (refer to Fig. 6.19(b)) than that observed with the theoretical pattern (as shown in Fig. 6.19(a)) which can be explained as above. The distortion in the shape of the pattern is mainly due to the edge diffraction and the contribution of the reflector leakage currents into the radiated field. The peak intensity in the measured pattern has also been shifted to $\theta=150^{o}$ from the predicted $\theta=90^{o}$ position. For simplicity of the positioning of the Q-loop antenna in vertical polarization mode, one of the sides of the reflector was placed horizontally on a block of polystyrene foam and other side was placed vertically upward.

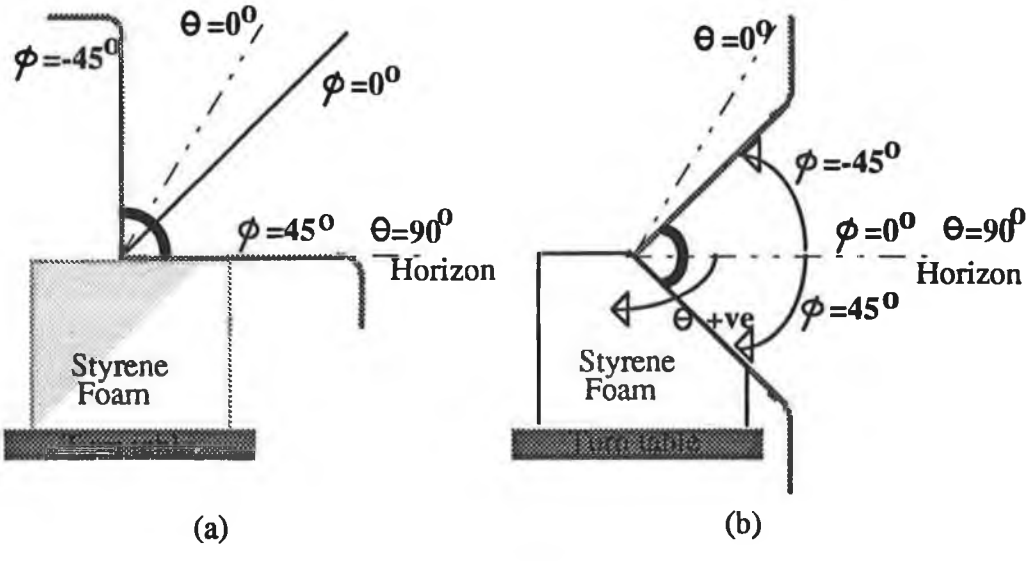

Fig. 6.20 Positioning of the Q-loop antenna in vertical polarization mode. (a) The positioning employed in the measurement (b) Proper positioning.

In fact for positioning the Q -loop symmetrically with respect to the LPA, the sides of the reflector should make $\pm 45^{o}$ with the horizon (Fig. 6.20(b)). This improper positioning (unavoidable in the circumstances) introduces the lack of symmetry in the measured pattern.

6.4.2.2 Study of the antenna parameters of the Q-loop

Important antenna parameters were derived theoretically in section 3.5.3 where some simplifying assumptions were applied, such as that the reflectors act as perfect ground planes, the current distribution on the Q-loop element is uniform and the loop is small compared to the wavelength. Still the test results vary only a little from the predicted values.

6.4.2.2 .1 Gain

Measured gain of the Q-loop antenna is very close to the theoretical gain. From Eqns. (3.5.11), (3.5.13), and (3.5.17) substituting the dimensions of the Q-loop element and the reflector, the gain of the antenna can be calculated. In the present case it is $\cong$ 5.9 dBi (neglecting the reflector losses) and the measured value in two different measurements were found to be 4.7 and 4.6 dBi. which are slightly lower because there must be some losses in the reflector.

6.4.2.2.2 Directivity

Although the directivity calculation of the Q-loop were made with an assumption that there would be no field behind the reflectors, the directivity computed from the test results is almost the same as predicted in Eqn. (3.5.11). There it was found to be 6 with small loop approximations while in section 6.3.2.2 the measured directivity is also 6 (approximately).

6.4.2.2.3 Reflection coefficient at the input terminals of the Q-loop antenna

An equivalent circuit model of the Q-loop antenna is presented in section 3.5.3.2 from which it is possible to predict the input impedance offered by the Q-loop placed in free space. A computer program is developed (listing is included in Appendix F4) which

calculates the impedance and reflection coefficient at the input terminals of the Q-loop when connected to a 50-Ω line. The reflection coefficient $|\rho|=0.415$ computed in this way is very close to $|\rho|=0.4$ found experimentally.

6.5 CONCLUDING REMARKS

The antenna measurements are important in the present perspective only in the context of using the newly developed antennas in EMC measurements. However, in case of SE measurement, it is not very essential to calibrate the test antennas as rigorously as it would be for other applications, such as antennas used for broadcasting purposes or for remote sensing. Thus only a few essential features of the antennas are measured. Relative radiation patterns are studied and compared with predictions. Apart from those anomalies which arise from (simplifying) assumptions made in the development of the theoretical analysis and from measurement inaccuracy, the overall radiation patterns are in good agreement. Except for the measured gain of the TEM-T transmitting half, all other measured values of the parameters are very close to their predicted values.

The reflection coefficient at the antenna input terminals is particularly important in a sense that knowing this parameter in free space and in the presence of the MUT, it is possible to predict the SE of the MUT (especially planar sheet like materials). This is referred to as a future work to be done in the next chapter of this thesis.

An overall good agreement between the theoretical and experimental results with the two newly developed antennas emphasizes the fact that they have the features appropriate for on-line SE measurements. Moreover it also suggests other probable EMC applications of these antennas discussed at the end of this thesis.

Chapter 7

CONCLUSIONS AND REMARKS

CONCLUSIONS
NOTES FOR FURTHER RESEARCH

7.1 CONCLUSIONS

On-line SE measurement of conductive plastic materials during their production process was the objective of this research. Standard field simulation is the starting point of any SE measurement technique, and hence the necessity of an antenna, antenna set or waveguide which could simulate standard EM waves. Unfortunately, waveguides do not provide a non-contacting test facility which is a key issue in developing a simple technique for on-line measurement. Therefore, the choice rests on antennas. The development of the antennas, as part of this research work, resulted from this motivation. This concluding discussion gives an insight about the desirable EMC features met by the newly developed antennas. The discussion is then followed by the remarks on the level of success achieved through the application of these antennas in on-line SE measurements.

7.1.1 PROBABLE USEFUL FEATURES OF THE DEVELOPED ANTENNAS

In the present work three different antennas have been developed. Although the VCLA was not constructed, the design details and relevant properties of this antenna have been demonstrated analytically. The near and far field patterns and other important figures-of-merit of the TEM-T half (acting as an antenna) have been analyzed. Similar analysis have also been presented for the Q-loop antenna. Those parameters of the two antennas have also been measured for comparison with the analytical results. From all these analyses and investigations the following important features (particularly for EMC applications) of the newly developed antennas can be highlighted. Of course they would need further development in construction, improvement in analysis and accuracy in measurements to be considered for application in other EMC measurements.

7.1.1.1 Frequency Range of Operation (EMC range of frequency)

In this work special attention is focussed on the RF range of 20 MHz to 1 GHz [176]. The antennas developed and reported upon in this thesis could successfully be used throughout this frequency range. The VCA is virtually independent of frequency, thus it can operate over this whole range and if the lens antenna is designed following the guidelines described in section 4.2.2, the VCLA assembly could probably be used in this frequency range. Successful application of the modified TEM-T cell has been reported in this work over the above mentioned frequency range.

Measurements have also been taken with the Q-loop antenna from 10 MHz to 1 GHz but above 300 MHz, SE measurement with this antenna did not yield reliable results. However, good results were obtained in case of radiation pattern and antenna parameter measurements at 1 GHz with this antenna which show that it may be suitable for other EMC test purposes.

7.1.1.2 Directional property

The directional property of the VCA has been illustrated in Fig. 3.6. Moreover, when a lens is fitted at the open mouth of the VCA, it has been demonstrated theoretically that the VCLA assembly would radiate parallel beams of EM waves, of course in a region very close to the assembly. It may be suitable for simulating far-field situation in a confined region.

It has been shown theoretically that the TEM-T half ideally radiates in a semi-infinite space, where the potential radiation is available only within a narrow beam soild angle (see Figs. 3.17 and 3.18). Experimental results also indicate a similar pattern (see Figs. 6.7 and 6.12) except for some shoots behind and a wider field distribution in front which could perhaps be attributed to the leakage current flowing through the outer conductor and flange of the TEM-T half.

The Q-loop antenna exhibits better directional property than a complete loop antenna. While a complete loop antenna radiates over a solid annular surface in 360 degrees, it has been demonstrated theoretically that the Q-loop radiates in only one quarter of such a surface (see Fig. 3.22). Experimental observations were also in close agreement with that prediction (refer to Figs. 6.10, 6.17 and 6.18). These useful directional properties available with all three antennas may possibly be exploited in other EMC measurements as well.

7.1.1.3 Improved directivity and Gain

As the two newly developed antennas are of highly directional type, their directivities are much higher than those of other available antennas used for producing high impedance field or low impedance field (such as dipoles or loop antennas). Directivity of the TEM-T half is approximately five times that of a half-wave dipole antenna[1] (directivity of half-wave dipole

[1]Obviously better directivity can be achieved with dipole arrays such as LPA.

is 1.64 [85, chap.12] and that of the TEM-T half is ≈ 8) and the directivity of the Q-loop is four times that of a complete loop antenna (see Eqn. (3.5.14)).

7.1.1.4 Standard field simulation

Most of the antennas can develop uniform plane wave radiation at large distances (the distance is quantified in section 2.2). The distance being impractically large even in case of a frequency as high as 100 MHz, a special antenna set, namely the VCLA, has been designed and proposed in the present work.

The TEM-T was employed to produce a predominant electric field in the near region. Huygens' principle was applied to find the field distribution in the near region of the TEM-T cell. The aperture field was determined with the assumption that only principal TEM mode exists. The field in the near region exhibits high impedance and it is TM in nature (shown in Fig. 3.13) thus it is similar to that produced by an ideal dipole in its near region.

The Q-loop antenna was used to produce predominant magnetic field in the near region. It has been analytically established that in front of the reflectors, the field pattern of the Q-loop antenna is identical to a complete loop antenna and therefore predominantly magnetic in the near region.

7.1.1.5 Ambient noise shielding performance

The VCLA provides a shielded environment for the field generated inside its conical metallic shell. Very close it, the field emerging from the plane face of the lens antenna is confined within a narrow beam and as such less susceptible to ambient noise. The close placement of the MUT between two such VCLA antennas would improve the situation in this respect. The quasi-shielded test environment provided by the TEM-T cell and the Q-loop antennas have been demonstrated both qualitatively and quantitatively in chapter 5.

7.1.1.6 Impedance matching

The input reflection coefficients have been measured for the TEM-T half and for the Q-loop antenna. This coefficient can also be obtained theoretically very easily from the expressions of input impedances. In the determination of the input impedance of the TEM-T half

radiator, the analysis presented by Galej's [150] has been followed. The input impedance of the Q-loop antenna has been modelled using the formulation of Plonsey [177]. Ohmic resistance of the antenna is calculated using Eqn. (2-60) of Stutzman [151] assuming uniform current distribution throughout the length of the arc (quarter loop). The assumption of uniform current distribution is applicable in this case since current is fed through one end and the other end is terminated to a coaxial load. The analytical and measured values of the input reflection coefficients have been compared in Sec 6.5.3.1 and they are in close agreement. This coefficient is particularly important in case of TEM-T cell, since it is possible to express the SE of a planar sheet placed in between the two halves of the cell through this reflection coefficient.

Unfortunately the input impedances of the developed antennas were not matched to the 50 Ω systems (instruments used in the measurements). This feature was not very crucial in case of on-line SE measurements as maximum power transfer was not particularly important. However, specially designed balun networks or tapered transmission lines could be used to match the antennas with 50 Ω systems.

7.1.2 APPLICATION OF THE ANTENNAS IN ON-LINE SE MEASUREMENT

A pair of each antenna set placed face-to-face constitutes a simple free-space technique for SE measurements. One antenna of the pair acts as a source to produce the test field on the MUT sheet while the other acts as a receiver. IL measurement is the basic principle of all the three systems. A comparison of the received signal strength, with and without the MUT in between the antennas, determines the SE of the sample.

A contact-less free-space technique with a quasi-shielded test environment, fast data acquisition, no sample preparation and limited constraints on material thickness and mechanical properties are the desirable features of a SE measurement technique that can be employed for on-line data acquisition. All these features are available with the developed test devices. In this work only prototypes of these devices are constructed. The dimensions of these prototype designs are not necessarily suitable for production purposes. Conformity is maintained among the dimensions of the three test devices.

The TEM-T cell has been designed following the design criteria of a TEM cell (Sec. 4.3). Characteristic impedance, cut-off frequency of higher order mode and uniformity of the

field distribution inside the cell are the important factors to be considered in designing a TEM-T cell. The dimension of the flange was chosen as double the dimensions of the cell, however in practice the larger the dimensions could be made, the better the performance that could be achieved.

Design considerations of a loop antenna are equally applicable in the design of the Q--loop element of the Q-loop antenna. Ensuring maximum radiated power and maximum radiation efficiency over the desired frequency range are the criteria in determining the size and cross-sectional dimension of the Q-loop element. Reflectors constitute the most important part of the Q-loop antenna. Thus care had been taken in designing the reflectors so that image theory could be applied (considerably large reflectors) and diffraction effects minimised. However, in practice this is very difficult to achieve with space constraints.

Despite the fact that the far field SE measurement is equally important, only the near field SE have been measured, since the VCLA test device could not be constructed during the time scale of the project.

The SE of four different samples was measured and in selecting the samples, different categories of the conductive plastics have been represented. Although on-line SE measurement is the main objective, SE was measured in such a configuration only for two of the samples, since samples of adequate length were not available with the other two categories. Nevertheless, prototype systems have been developed and the measured on-line SE, after calibration, has been compared with predicted SE and SE measured through standard laboratory techniques. Good agreement confirms that the developed techniques are applicable in such measurements.

7.1.2.1 Calibration of the Test Devices

Calibration is necessary for each of the test devices in the particular environment where they would be used, since the indirect path signal infringement and background noise are functions of the test site and specific test device. Calibration is also essential for each individual type of MUT, as it has been observed (see Appendix E3 and section 5.3.3.1) that indirect path signal infringement largely depends on the shielding behaviour of each individual category of the MUT.

The reliability of the calibration needs further verifications by carrying the tests over a large number of samples and further investigations are essential as to why the calibration factor due to indirect path signal infringement for poor shields is significantly smaller than that for good shields.

7.1.2.2 Repeatability of the Test Results

Although the repeatability of the test results has not been included in chapter 5, where the test results have been reported, a repeatability analysis can be performed with the test results obtained in three different test locations. Most of the measurements of TEM-T cell were performed in the EMC laboratories of DCU, EOLAS (The Irish Science and Technology Agency) and Power Electronics Ireland (PEI), University of Limerick (UL). The repeatability of those test results can be assessed in terms of variation obtained through the comparison of a wide range of data set. Fig. 7.1 shows the repeatability feature. About 75% of the test data are repeatable within 0-3 dB variation. The variations are less than 10 dB for almost 95% of the test data. Empty cell reception behaviour in CSM and in NCSM, CSM and NCSM SE data for sample #1, 2 and 3 and OLM data for sample #1 and 2 are compared. 19 data points for each set of measurements from 10 MHz to 1 GHz have been considered in computing the variation.

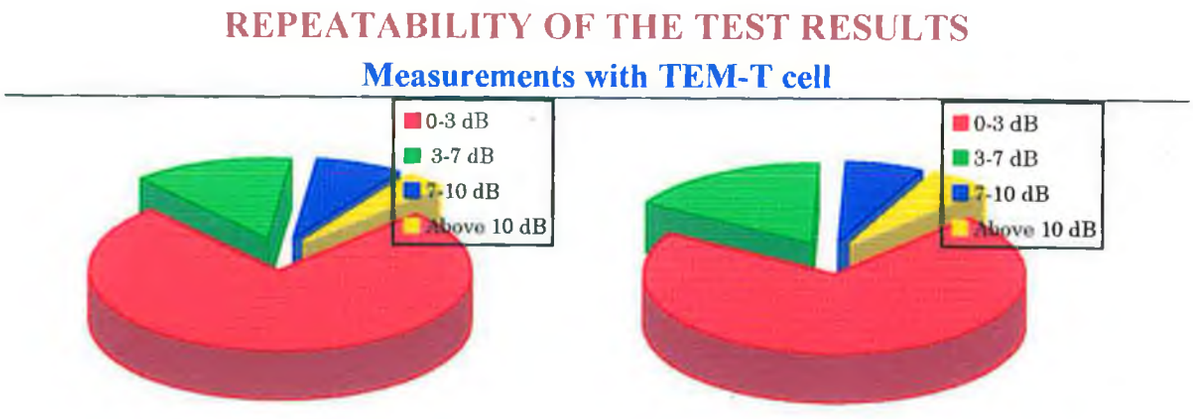

(a) (b)

Fig. 7.1 Pictorial representation of the repeatability of the test results performed in different laboratories. (a) Variation of the test results taken in the EMC laboratory of DCU from those obtained in EOLAS and (b) Variation of the test results taken in the EMC laboratory of DCU from those in PEI, UL.

7.1.2.3 Investigations on RFCP

As a proposed contribution to the field of conductive plastic materials, a new class of filled composite material has been suggested with a two dimensional regular array of conductive flakes (like a Frequency Sensitive Surface (FSS)) in plastic resin. The attenuation of EM waves due to reflection from the conductive flakes arranged in a doubly periodic planar array, typically like an FSS, has been studied both theoretically and experimentally. Experimental verification of the effect of haphazard distribution of the conducting flakes on the reflectivity has also been carried out. It is evident from the test results that the regular distribution of flakes improves the reflectivity compared to the random one.

One notable feature of this new type of material is that the shielding capability which it exhibits due to reflection can be controlled by manipulating the shape, size and separation of the flakes and almost a precise prediction of SE values can be made theoretically prior to manufacturing. This is not at all possible with the available filled conductive composites.

7.2 NOTES FOR FURTHER RESEARCH

In addition to the features covered in the present study, there are other important features of these three newly developed EMC antennas that could constitute interesting research projects. Theoretical analysis of these antennas need further rigorous treatment in order to take into account the practical design limitations. Moreover these antennas may find potential applications in other EMC related areas. A brief discussion on each of them are presented below.

7.2.1 RESEARCH ON VCLA

Apart from the application of VCLAs as test devices for measuring SE of planar sheet-like material during production, they could play an effective role in antenna calibration in a compact range measurement system. Generation of a plane wave particularly at low frequencies (such as 100 MHz) requires large test areas (mentioned earlier in section 3.3.1) which could be minimized by using such antennas.

Since the VCLA can theoretically produce parallel beams of plane wave in a confined region the possibility of reflections from boundary walls and floor reduces in such a

measurement. That means the necessity of lining the wall, floor and roof of a screened room with anechoic or absorbing materials may significantly be reduced and thus it may provide a low cost system for antenna measurements.

Moreover, as the VCA is a hi-fi antenna and the lens in front of it just transforms the spherical wave front into a plane wave front with well defined directivity (if edge diffraction is neglected), the VCLA could be further investigated for use in broadcast applications and in digital communication with high fidelity reception and transmission behaviour.

7.2.2 RESEARCH ON TEM-T CELL

It has been described that each half of the TEM-T cell can be treated as an aperture antenna. The analysis of their behaviour as antennas is performed by assuming them to be flanged open-ended rectangular coaxial transmission line (FORCTL). There may be several other research implications of this newly proposed radiating structure.

7.2.2.1 Application of FEA to find the accurate field distribution on the MUT

Simplifying assumptions such as the presence of the principle mode i.e. TEM, at the aperture were made in developing the radiation model of the FORCTL. In practice, higher order modes are generated due to the abrupt transition of impedance from 50 Ω to 377 Ω at the open mouth of this device. Although these higher order modes are evanescent in nature and exist only very close to the open mouth into the FORCTL, the aperture field is a combination of these modes and the principal TEM mode. Hence more accurate analysis calls for the inclusion of the effect of these modes on the radiated field.

Finite element analysis (FEA) such as that used by Scott [143] in analyzing a similar structure (flanged open ended circular coaxial cell), might be applied to develop a more accurate model of the field distribution on the MUT sheet.

7.2.2.2 Alternate way of SE measurement

It is possible to model the SE of a planar sheet-like sample in terms of the scattering parameters of the TEM-T cell. Theoretical as well as experimental determination of these

coefficients are possible for such a cell with a Hewlett-Packard HP8510B vector network analyzer. SE can then be determined from these quantities using the following analysis.

The TEM-T cell may be considered as a two port network. The scattering parameter S_{11} and S_{12} will give the transmission coefficient T_{12}, which can be utilized to express the SE of the sample as follows:

$$SE = 20\log_{10}|T_{12}| \tag{7.2.1}$$

Since the two halves of the cell are identical, $S_{12} = S_{21}$ and $S_{11} = S_{22}$. Thus T_{12} can be obtained as $T_{12} = S_{11}/S_{12}$. S_{11} can be measured using the network analyzer directly. S_{21} can be obtained through the relation

$$|S_{21}|^2 = \frac{2(P_2)av}{a_1 a_1 *} \tag{7.2.2}$$

where, $a_1 = \frac{V_{1+}}{\sqrt{Z_{01}}}$, V_{1+} is the voltage incident at the input terminal of the TEM-T cell and Z_{01} is the characteristic impedance of the transmitting half of the cell. $a_1 a_1 *$ can be calculated from

$$a_1 a_1 * = \frac{2(P_1)av}{1-|S_{11}|^2} \tag{7.2.3}$$

$(P_1)av$ and $(P_2)av$ are the average power transmitted by the signal generator to the TEM-T cell and average power received by the spectrum analyzer respectively.

7.2.2.3 Application of FORCTL as probe

It has been demonstrated that the TEM-T half acts as a dipole in a quasi-shielded environment. Thus such a device may also be investigated for applying as a near electric field probe in other EMC measurements. Moreover since the smaller size of such devices extends the upper frequency range of operation, it is possible to apply a smaller size of this probe even for microwave applications. However, in such applications, it is not essential that the coaxial structure should be rectangular; a circular coaxial structure can also be applied.

7.2.2.4 Application of the FORCTL as a device for permittivity measurement

An open ended circular coaxial probe has for a long time been used as a test device for measuring the constitutive properties of dielectric materials as described earlier in section 2.4.6. The FORCTL may also be applicable in such measurements. This would permit the use of rectangular test samples which might, in some circumstances, offer some advantage. No other advantage is known to this author.

7.2.2.5 Improvement analysis over pyramidal horn or OEG

Since the field at the aperture of the TEM-T half is TEM instead of TE the radiation pattern and the polarization of the radiated field are better in this case compared to the pyramidal horn antenna or open ended waveguide (OEG) used as antenna. Thus further measurements on the polarization and phase of the radiated field of the FORCTL could be performed. Moreover gain measurements with respect to the standard OEG or horn antennas are also required to ascertain whether any improvement in gain and directivity is achievable with this new type of antenna.

7.2.3 RESEARCH ON Q-LOOP

The Q-loop antenna is a promising type of magnetic field probe, which might be employed as near H-field characterisation of equipment for EM compatibility testing. Only a subset of its features were explored in this work. Rigorous mathematical analysis of the current distribution on the antenna is required to determine the radiation pattern, paying special attention to the edge diffraction effects of the reflectors. A similar analysis [178] for a half loop antenna may be a guide to such modelling.

Furthermore, a family of fractional loop antennas can be derived from the same principle of reflection with the Krauss reflectors having angles lower than 90^{o}.

7.2.3 FURTHER RESEARCH ON RFCP

Although not covered in this study, the developed on-line SE measurement techniques could potentially be employed in improving the SE of the RFCP type materials by manipulating the size and separation of the conductive flakes.

It has been observed that to block adequately the EM wave at RF frequencies, the size of the flakes to be incorporated in the typical moulding process of presently available filled composite materials becomes impractically large. Moreover it would be difficult to maintain a regular array of the flakes using such moulding processes. Hence a different technique would be necessary to fabricate a regular array of conducting strips embedded in plastic to impart improved shielding capability. Thus a trade off is to be studied between the cost differential of the manufacturing of filled composites by the moulding process and the proposed type of filled plastics yet to be developed and the resultant improvement in the shielding capability. With the increasing interest in millimetre wave applications in military and commercial communications [64], very small size flake could play a vital role in preventing spurious radiation at these frequencies in the proposed regular array distribution.

One may argue about the absorption loss available in a filled composite, which would be absent in case of a regular arrangement of strip-like fillers. However this might be achieved by using closed loop patches (circular, square and triangular).

APPENDICES

CONDUCTIVE PLASTICS, A REVIEW

A comparative analysis of the conductive plastics showing their SE values, production cost, applicability and important other properties is furnished in Table A1-1. RFCP is not included in the table as it is still at the conceptual stage.

Table A1-1: **A comparative study of different metallization techniques for plastics.**

(RFCP is not included as it is a new class of material not yet manufactured commercially)

Techniques	Shielding effectiveness (dB)	Conductivity	Adhesion	Environ-mental stability	Uniformity	Application cost per sq. meter	Uses
Electroless plating	70 - 120	Excellent	Good	Fairly good	Uniform	£5.88-£11.7	For military purpose or for sophisticated shielding
Arc spraying	60 - 90	High	Poor	Very good	Hard to coat uniformly for complex shape	£2.8-£7.38	Use has been limited now a days
Vacuum metallization	40 - 70	Good	Poor	Poor	Difficult to obtain uniform coating	£24.07	For low frequency shielding
Conductive paints	30 - 70	Depends on the type of metal filler used	Very good	Good	Difficult to get uniform & effective coating	£1.50	For data processing equipment, computer etc.
Conductive composite	30 - 60	Depends on the type, aspect ratio, and orientation of metal or carbon filler	Not appli-cable	Very good	Not applicable	Not applicable	For computational equipment and information related apparatus etc.
Conductive fabrics	40 - 100	Depends on the type of metal used	Not appli-cable	Depends on the type of metal used	Not applicable	£12.8-£25	For bonding straps, cable shielding etc.
Flexible laminates	60 - 100	Good	Not appli-cable	Good	Not applicable	£1.9-£8.5	For keyboards, printer etc.

SE MEASUREMENT TECHNIQUES, A REVIEW

The available SE measurement techniques are summarised in Table B1-1 showing their dynamic range, type of test fixture, type of field simulation, frequency range, applicability and other important features. Newly developed techniques are not included. Their distinguishing features over the available techniques are discussed in sections 2.7 and 2.8.

Table B1-1: A comparative study of existing SE measurement techniques.

BASIC TEST METHODS VARIABLES OF INTEREST	OPERATING FREQUENCY RANGE	SIMULATION OF INCIDENT FIELD TYPE	TEST SAMPLE REQUIREMENT	COST OF A TEST SYSTEM	TIME REQUIRED TO OBTAIN DATA	REPEATABILITY	DYNAMIC RANGE
MIL-STD 285 TEST METHOD	From a few MHz-1GHz, dependent on MUT and test fixture	Near-field	Sample surface should be smooth and uniform	High	Medium	Poor	50 dB
ASTM ES7-83 DUAL CHAMBER TEST FIXTURE	Measurements from .1 to 1000 MHz has been reported limited by box reson- ance	Near-field	Silver painting at the edges of the sample may be necessary for conductive polymers having resin reach edges	Moderate	Medium	Better than MIL-STD-285 test method [31]	80 dB
CIRCULAR CO-AXIAL HOLDER	dc-1 GHz (upper frequency dependent)[5]	Far-field	annular shaped, machined and silver painted at the edges	Moderate	Medium	poor	90-100 dB
FLANGED CO-AXIAL HOLDER	1 MHz-1.8 GHz(both upper and lower range are system dependent)	Far-field	Circular plate for loaded measure-ment and two different sample for reference measurement, machined and silver painted at least at one side	Moderate	Medium	Better than CC holder but still poor	90-100 dB
TEM-T CELL	1 MHz-1 GHz (E-field) 1 MHz-400 MHz (H-field)	Far-field	No test sample preparation or reference sample preparation is necessary	Moderate	Medium	Better than CC and SC since no contact impedance effect is to be encountered	70-80 dB
TIME DOMAIN	200 MHz-3.5 GHz	Far-field	Very simple but large one for large sheet test fixture, smaller one works but machining and fitting complexity arises	High	Fast	Poor at the low frequency end but good at the high frequency end	50-60 dB
COMPLEX PERMITTIVITY APPROACH	100 MHz-3.5 GHz	Far-field	Simple flat plate but machining is essential	High	Slow	Depends on permittivity data	Independent of the test configuration
DUAL TEM CELL	1 MHz-200 MHz	Near-field: both high impedance and low impedance	A moderate sample size of square shape,but fitting complexities are involved	High	Medium	Good	50-60 dB
TEM CELL IN A REVERBERATING CHAMBER	200 MHZ-1 GHz	Near field: both high impedance and low impedance	Same as DTC	Very high	Very slow	Poor at the low frequency end but good at the high frequency end	90-100 dB
TRANSFER IMPEDANCE APPROACH	Geometry of the test sample depen -dent. Vary from few hund -red MHz to few GHz	Near-field	No machining, reshaping or remodeling is necessary	Low	Moderate	Depends on transfer impedance data	Independent of the test configuration

C1: SE OF SURFACE METALLIZED PLASTIC BY KLIEN'S FORMULA

Klein[108] proposed a mathematical model to determine the SE of electroconductive (EC) coated dielectric slabs. Fig. C1-1 illustrates the geometry. The assumptions employed in deriving this model have been noted earlier in the main text. For normally incident plane wave, SE has been defined as the ratio of the transmitted to the incident electric field intensities. In fact, this can also be termed as the voltage transmission coefficient T_V.

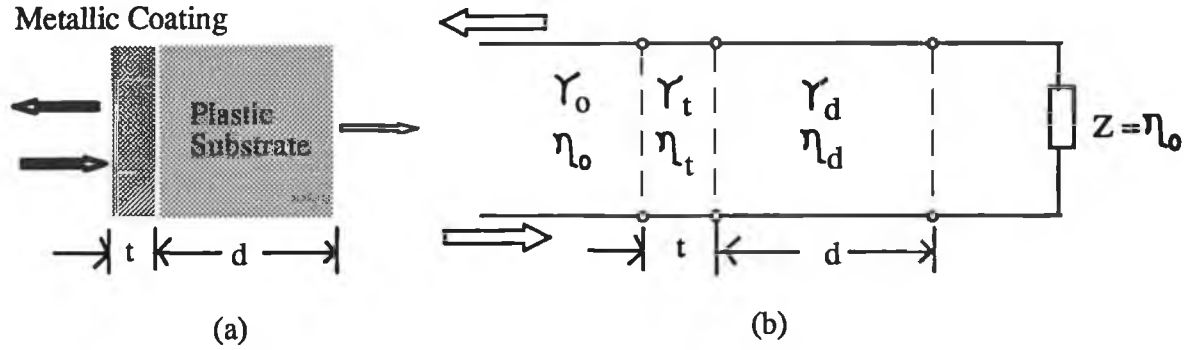

Fig. C1-1: Surface metallized plastic (a) EM shielding results from reflections at impedance discontinuities and absorption in the metal layer. (b) Equivalent transmission-line model including characteristic constants.

However, expressing in dB, SE is given by

$$SE = 10\log_{10}\left[\frac{(1+\varepsilon_r)+(\varepsilon_r-1)\cos(2\beta_d)}{8\varepsilon_r}\left|1+\frac{\eta_0}{R_s}+\frac{1+j\sqrt{\varepsilon_r}\tan\beta_d}{1+j\tan(\beta_d)/\varepsilon_r}\right|^2\right] \qquad \text{(C1-1)}$$

where, ε_r is the relative permittivity of the plastic substrate.

β_d the phase thickness, i.e., the thickness of the plastic substrate expressed in terms of the phase constant of this medium and $\beta_d = 2\pi d/\lambda$,

d the thickness of the substrate in meter.

λ the wavelength of the incident wave in the plastic substrate.

R_S the surface resistance ($\equiv 1/\sigma_f t$) of the metallic coating (paint).

σ_f the film conductivity of the metal (discussed later).

t the thickness of the coating, and

η_0 intrinsic impedance of free space which is 377Ω.

Very thin metallic films have much higher resistivity than bulk metal because of electron scattering from the film surface. If the film thickness is very large compared to the electron mean-free-path, the resistivity is expected to be nearly the same as that of a bulk metal. When the film thickness is on the order of the electron mean-free-path, then the role of electron scattering becomes dominant. Fuchs[10a] and Sondheimer[10b] considered the general form of the solution of the Boltzmann equation for the case of a conducting film and found the film conductivity σ_f in terms of the bulk conductivity σ, the film thickness t, and the electron mean-free-path p:

$$\sigma_f = \frac{3t\sigma}{4p}\left[\ln\left(\frac{p}{t}\right) + 0.4228\right] \qquad \text{for } t<<p \qquad (3.2.2)$$

The surface resistance of conducting films is generally quoted in units of ohms/□ (read as ohms per square) because in the equation of resistance

$$R = \frac{\text{specific resistivity} \times \text{length}}{\text{thickness} \times \text{width}} = \frac{\rho l}{tw} \qquad (3.2.3)$$

when units of length l and width w are chosen to have equal magnitude (i.e., resulting in a square), the resistance R in ohms per square is independent of the dimensions of the square and equals

$$R = \frac{1}{t\sigma_f}\ \Omega/\square \qquad (3.2.4)$$

C2: THEORETICAL SE OF ICP

ICP is a comparatively new class of material and has been shown [8] to be promising in the conductive plastic industry. Since in ICPs, conductive polymeric powder or fibres are blended in base polymer material, it is very difficult to assess their SE theoretically. However, the analysis presented by Colaneri *et al.* [65] can be utilized to get an approximate understanding. The same analysis has been presented here with little modification.

Far -field SE

A planar sheet material of thickness *d*, placed on the x-y plane is shown in Fig. C2-1. The electric field strength E at a distance z into the shield is:

$$E = E_i e^{i(\beta z - \omega t)} \qquad \text{(C2-1)}$$

where $\beta = 2\pi/\lambda$ is the phase constant of the EM wave in the material and ω is its angular frequency, z is the distance measured from the surface of the sheet. Applying the boundary conditions for reflection and transmission of the wave at each of the surfaces of the sheet, an expression of SE can be derived by calculating the ratio of the amplitude of the transmitted field strength to that of the incident field strength. Then with the assumption that $\sigma/\omega\varepsilon_0 >> 0$, which is quite applicable in the present analysis throughout the frequency range of interest (viz; even if σ is as low as 0.1 S/m, then at a frequency of 1 GHz, $\sigma/\omega\varepsilon_0$ is still of order 10^2), one obtains the far-field (normally incident plane-wave) SE as:

$$SE = 10\log\left(\frac{1}{4}\left[\frac{\sigma}{2\omega\varepsilon_0}\left[\cosh\left(\frac{2d}{\delta}\right)-\cos\left(\frac{2d}{\delta}\right)\right]+2\sqrt{\frac{\sigma}{2\omega\varepsilon_0}}\left[\sinh\left(\frac{2d}{\delta}\right)+\sin\left(\frac{2d}{\delta}\right)\right]+2\left[\cosh\left(\frac{2d}{\delta}\right)+\cos\left(\frac{2d}{\delta}\right)\right]\right]\right) \qquad \text{(C2-2)}$$

where $\delta = \sqrt{(2/\mu_0\sigma\omega)}$ is the skin depth of the conductor.

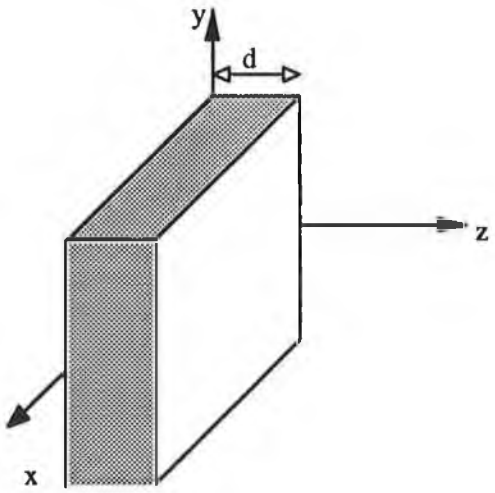

Fig. C2-1 Geometry of a planar shield material consisting of ICP.

For most of the ICPs, the bulk conductivity is in the range 0.1 S/cm-10 S/cm. Under these circumstances, expression (C2-2) has two limits of interest at MHz to GHz frequencies. These limits can be taken as acceptable approximations to (C2-2), depending on whether the frequency is higher or lower than that at which the thickness, d, equals the skin depth, δ. The crossover frequency, ω_c, at which $d = \delta$ is determined from the definition of skin depth as

$$\omega_c = \frac{2}{\sigma\mu_0 d^2} \qquad \text{(C2-3)}$$

For frequencies much lower than ω_c (the case of an "electrically thin" shield, d <<δ), (C2-2) becomes independent of frequency and reduces to:

$$SE = 20 \log(1 + Z_0 sd/2) = 20 \log\left(1 + \frac{Z_0}{2R_s}\right) \qquad \text{(C2-4)}$$

where the expression alternatively in terms of the bulk conductivity, σ, and the surface resistivity, $R_s = 1/(\sigma d)$. For frequencies much above ω_c (i.e., when the thickness of the sheet greatly exceeds the skin depth, d >>δ), (C2-2) reduces to the limiting from:

$$SE = 10 \log\left(\frac{s}{16\omega e_0}\right) + 20\frac{d}{\delta}\log(e) \qquad \text{(C2-5)}$$

The first term on the right of this expression is the contribution to the shielding due to single reflections to the incident wave by the front and back surfaces of the sheet. The second term represents the attenuation by absorption as the wave passes through the sheet.

Near -field SE

Near-field shielding involves a formal analogy between shielding problems and the theory of the reflection and transmission of electromagnetic signals at impedance mismatches in transmission lines. For electric dipole radiation, the wave impedance can be calculated from the expressions for the fields of a radiating dipole. For a source-to-shield distance, r, much less than the free-space wavelength it is given by

$$Z_w = \frac{1}{\beta r} Z_0 \qquad \text{(C2-6)}$$

This expression is valid only up to a source-to-shield distance less than one-sixth the wavelength. In the transmission line analogy, the radiation shield is replaced by a series impedance placed along the transmission line, known as the barrier impedance of the shield. It is given by

$$Z_b = Z_0 \sqrt{\frac{\omega\varepsilon_0}{\sigma}(1+i)} \qquad \text{(C2-7)}$$

With these definitions, the shielding effectiveness can again be calculated by working out the reflection and transmission coefficients for signals propagated along the line. The general result is given by

$$SE = 20\log\left(\frac{k^2+1}{2k}\sinh(\alpha d)+\cosh(\alpha d)\right) \qquad \text{(C2-8)}$$

where $k = Z_w/Z_b$, and $\alpha = (1 + i)/\delta$ is the complex propagation constant. For an electrically thick shield ($d/\delta >> 1$, $\omega >> \omega_c$),

$$SE = 10\log\left(\frac{s}{16\omega e_0 (kr)^2}\right)+20\ \frac{d}{\delta}\log(e)$$

or

$$SE = 10\log\left(\frac{c^2 s}{16\omega^3 e_0 r^2}\right)+20\frac{d}{\delta}\log(e) \qquad \text{(C2-9)}$$

where the fact that $k >> 1$ has been used. The first term on the right-hand side is easily interpreted as the shielding due to reflection, and the second as that due to absorption.

Again for electrically thin samples (As most of those samples of interest here are electrically thin at frequencies of only a few megahertz, this limit is important for the interpretation of shielding data), it can be derived from (C2-8) by making the approximation $k >> 1$, $d/\delta << 1$, and $\omega << \omega_c$ that

$$SE = 20\log\left(\frac{c}{2\omega r}Z_0\sigma d\right) \qquad \text{(C2-10)}$$

C3: FIELD EXPRESSIONS OF V-CONICAL ANTENNA (VCA)

The geometry of the VCA is shown in Fig. 3.5. This is an angular antenna. When the source is located at the origin O, and the boundaries are angularity related, it can be proved that the excited EM wave is in the TEM-mode only and can be expressed in terms of the Hertz scalar function Π_{er}. Field expressions are given here following the analysis of [105].

$$\begin{aligned} E_r &= 0 & H_r &= 0 \\ E_\theta &= \frac{1}{r}\frac{\partial^2\Pi_{er}}{\partial r\partial\theta} & H_\theta &= \frac{j\omega\varepsilon}{r\sin\theta}\frac{\partial\Pi_{er}}{\partial\phi} \\ E_\phi &= \frac{1}{r\sin\theta}\frac{\partial^2\Pi_{er}}{\partial r\partial\phi} & H_\phi &= -\frac{j\omega\varepsilon}{r}\frac{\partial\Pi_{er}}{\partial\theta} \end{aligned} \qquad \text{(C3-1)}$$

where $\Pi_{er} = \Pi(\theta,\phi)e^{-jkr}$ satisfies the Helmholtz equation

$$(\nabla^2 + k^2)\frac{\Pi_{er}}{r} = 0 \qquad \text{(C3-2)}$$

and $\Pi(\theta,\phi)$ satisfies the equation

$$\left[\sin\theta\frac{\partial}{\partial\theta}\left(\sin\theta\frac{\partial}{\partial\theta}\right)+\frac{\partial^2}{\partial\phi^2}\right]\Pi(\theta,\phi) = 0 \qquad \text{(C3-3)}$$

The boundary condition for $\Pi(\theta,\phi)$ can be obtained from the excitation condition

$$\frac{V_0}{2} = \lim_{r\to 0}\int_0^{\theta_0} -E_\theta r d\theta \qquad \text{(C3-4)}$$

Then applying conformal mapping to convert the arcs of the cross-section of the VCA into parallel lines and solving for $\Pi(\theta,\phi)$ one can obtain[105]

$$E_\theta(r,\theta,\phi) = -\frac{V_0}{2b\sin\theta}\frac{\cos\left[\frac{1}{2}\tan^{-1}(Y/X)\right]}{(X^2+Y^2)^{1/4}}\frac{e^{-jkr}}{r} = E_\theta(\theta,\phi)\frac{e^{-jkr}}{r}$$

$$E_\phi(r,\theta,\phi) = -\frac{V_0}{2b\sin\theta}\frac{\sin\left[\frac{1}{2}\tan^{-1}(Y/X)\right]}{(X^2+Y^2)^{1/4}}\frac{e^{-jkr}}{r} = E_\phi(\theta,\phi)\frac{e^{-jkr}}{r}$$

$$H_\theta(r,\theta,\phi) = -\frac{V_0}{2bZ_c\sin\theta}\frac{\sin\left[\frac{1}{2}\tan^{-1}(Y/X)\right]}{(X^2+Y^2)^{1/4}}\frac{e^{-jkr}}{r} = H_\theta(\theta,\phi)\frac{e^{-jkr}}{r} = -\frac{E_\phi(r,\theta,\phi)}{Z_c}$$

$$H_\phi(r,\theta,\phi) = -\frac{V_0}{2bZ_c\sin\theta}\frac{\cos\left[\frac{1}{2}\tan^{-1}(Y/X)\right]}{(X^2+Y^2)^{1/4}}\frac{e^{-jkr}}{r} = H_\phi(\theta,\phi)\frac{e^{-jkr}}{r} = \frac{E_\theta(r,\theta,\phi)}{Z_c}$$

... ... (C3-5)

where Z_c=120π Ω and $\tan^{-1}(Y/X)$ is multivalued when $Y\to 0$:

$$\tan^{-1}(Y/X) = \begin{cases} 0, X > 0 \\ \pi, X < 0 \end{cases} \qquad \text{(C3-6)}$$

X and Y are functions generated by conformal mapping and are given by

$$\begin{aligned} X &= \sin^2\phi_0 - \tfrac{1}{2} + \tfrac{1}{2}\cos 2\phi\cosh 2x_2 \\ Y &= -\tfrac{1}{2}\sin 2\phi\sinh 2x_2 \end{aligned} \qquad \text{(C3-7)}$$

where $x_2 = \ln[\tan(\theta/2)\tan(\theta_0/2)]$

C4: TAPERED ILLUMINATION IN FRONT OF DIELECTRIC LENS

NYLON 6 (Polyamide) LENS

Electrical Conductivity, S/m

$s := 2 \cdot 10^{-13}$

Frequency of operation, Hz

$f := 2 \cdot 10^{8}$

$w := 2 \cdot p \cdot f$

Permeability and Permittivity

$m_0 := 4 \cdot p \cdot 10^{-7}$

$e_0 := 8.852 \cdot 10^{-12}$

$m_r := 1.0$

$e_r := 3.6$

Normal Incidence of Plane wave

$R_m := 25$ **cm**

$n := \sqrt{e_r \cdot m_r}$ **/* Refractive index */**

$q_m := \frac{p}{6}$

$L := \frac{R_m \cdot \left[n \cdot \cos\left[q_m \right] - 1 \right]}{(n-1)}$ **/* Focal length of the lens */**

$|L| = 17.918$ **cm**

$t_0 := R_m \cdot \cos\left[q_m \right] - L$

$i := 0 .. 20$

$q_i := \frac{p}{60} \cdot i - \frac{p}{6}$

$$E_i := \left| \frac{\left[n \cdot \cos\left[q_i \right] - 1 \right] \cdot \left[\exp\left[-a \cdot \left[(n-1) \cdot \frac{L}{\left[n \cdot \cos\left[q_m \right] - 1 \right] \cdot \left[n \cdot \cos\left[q_i \right] - 1 \right]} \cdot \left[\cos\left[q_i \right] - \cos\left[q_m \right] \right] \right] \right]}{(n-1) \cdot \left[\exp\left[-a \cdot t_0 \right] \right]} \right|$$

$$y_i := \frac{(n-1)\cdot L\cdot \sin\left[q_i\right]}{n\cdot \cos\left[q_i\right]-1}$$

Plot of E-field intensity available in front of the lens as a function of Lens height (Normalized to maximum intensity)

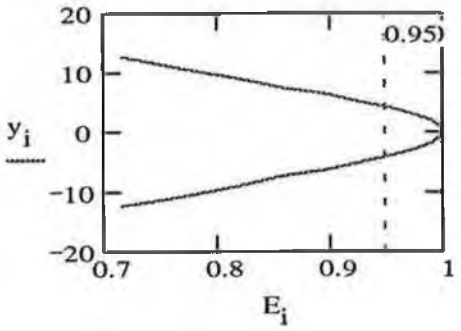

C5: JACOBIAN ELLIPTIC FUNCTIONS FOR COMPLEX ARGUMENTS

The definitions of the necessary Jacobian elliptic functions for complex arguments are presented here from Bowman[184].

$$\begin{aligned} &sn(mz,k) \\ &= sn(mx+jmy) \\ &= \frac{sd_1}{1-d^2s_1^{\,2}} + j\frac{cds_1c_1}{1-d^2s_1^{\,2}} \end{aligned} \qquad \text{(C5-1)}$$

and,

$$\begin{aligned} &dn(mz,k) \\ &= dn(mx+jmy) \\ &= \frac{dc_1d_1}{1-d^2s_1^{\,2}} - j\frac{k^2scs_1}{1-d^2s_1^{\,2}} \end{aligned} \qquad \text{(C5-2)}$$

where,

$$s = sn(mx,k)$$
$$s_1 = sn(my,k'), k' = \sqrt{(1-k^2)}$$
$$c = cn(mx,k) = \sqrt{(1-s^2)}$$
$$c_1 = cn(my,k') = \sqrt{(1-s_1^2)}$$
$$d = dn(mx,k) = \sqrt{(1-k^2 s^2)}$$
$$d_1 = dn(my,k') = \sqrt{(1-k'^2 s_1^2)}$$

where m, k and k′ are defined in section 3.4.2. z(x,iy) is an arbitrary point in the z plane provided, -a≤x≤a and -b≤y≤b. a and b are half the dimensions of the TEM-T cell cross-section.

C6: EM FIELD IN TERMS OF HERTZ POTENTIAL FUNCTIONS

Hertz potential functions, usually denoted by Ψ and Φ, represent the magnitude of magnetic and vector electric potentials of infinitesimally small radiating elements. They are often referred to as auxilliary scalar functions of Hertz vectors denoted by $\vec{\Pi}_e$ and $\vec{\Pi}_m$ where the later terms are related to elementary electric or magnetic currents as[chap.1 of ref. 150]

$$\vec{\Pi}_e = \frac{jI_e d\vec{l}}{4\pi\omega\varepsilon}\frac{e^{j\beta r}}{r} \qquad \text{(C6-1a)}$$

$$\vec{\Pi}_m = \frac{jI_m d\vec{l}}{4\pi\omega\mu}\frac{e^{j\beta r}}{r} \qquad \text{(C6-1b)}$$

where $d\vec{l}$ designates the length of the current element and the direction of current. I_e and I_m are the electric and magnetic currents computed by integrating the corresponding surface current densities along the surface of the conductors in a direction transverse to the current flow.

Hertz vectors obey the vector Helmholtz equations and it is possible to express the radiated electric and magnetic fields in terms of them. The expressions are available in most of the texts on Electromagnetics. For ease of reference, these are repeated here

$$E = \nabla\nabla\cdot\vec{\Pi}_e + \beta^2\vec{\Pi}_e + j\omega\mu\nabla\times\vec{\Pi}_m \qquad \text{(C6-2a)}$$

$$H = \nabla\nabla\cdot\vec{\Pi}_m + \beta^2\vec{\Pi}_m - j\omega\varepsilon\nabla\times\vec{\Pi}_e \qquad \text{(C6-2b)}$$

The electric field components in rectangular co-ordinates can be expressed in terms of their auxilliary scalar functions as [150, chap. 4]

$$E_x = j\omega\mu_0\frac{\partial}{\partial y}\Psi + \frac{\partial^2}{\partial z\partial x}\Phi \qquad \text{(C6-3a)}$$

$$E_y = -j\omega\mu_0\frac{\partial}{\partial x}\Psi + \frac{\partial^2}{\partial z\partial y}\Phi \qquad \text{(C6-3b)}$$

$$E_z = -\left(\frac{\partial^2}{\partial x^2} + \frac{\partial^2}{\partial y^2}\right)\Phi \qquad \text{(C6-3c)}$$

and the magnetic field components

$$H_x = \frac{\partial^2}{\partial z\partial x}\Psi + \frac{\beta^2}{j\omega\mu_0}\frac{\partial}{\partial y}\Phi \qquad \text{(C6-4a)}$$

$$H_x = \frac{\partial^2}{\partial z\partial y}\Psi - \frac{\beta^2}{j\omega\mu_0}\frac{\partial}{\partial x}\Phi \qquad \text{(C6-4b)}$$

$$H_z = -\left(\frac{\partial^2}{\partial x^2} + \frac{\partial^2}{\partial y^2}\right)\Psi \qquad \text{(C6-4c)}$$

C7: HERTZ SCALAR FUNCTIONS FOR TEM-T HALF RADIATOR

Derivation of Hertz scalar functions

The open mouth of the TEM-T cell half is shown in Fig. C7-1. The cross-section of the rectangular coaxial line that construct the cell can also be represented by the same figure. It has been symmetrically divided by the x- axis. Thus it is enough to know the field distribution of one half of that section (i.e., of the region ABHFEG).

For TE modes, the fields in that region can be found in terms of the Hertz scalar function Ψ, which satisfies

$$\left(\nabla_t^2 + K^2\right)\Psi = 0 \qquad \text{In region ABHFEG} \qquad \text{(C7-1)}$$

and $\partial_n\Psi = 0$ on the metal walls, i.e. on GABH and on EF

where ∇_t represents the transverse laplacian and ∂_n represents the normal derivative. H_z (the component of magnetic field along the direction of propagation) is directly proportional to Ψ

and E_x and E_y are proportional to the normal derivative (i.e. $\frac{\partial}{\partial y}$ and $\frac{\partial}{\partial x}$) of H_z (see Eqn. (14) of section 8.2 of [85]). Due to the boundary condition of vanishing tangential component of the electric field on the metal surface, the second part of Eqn. (C7-1) arises.

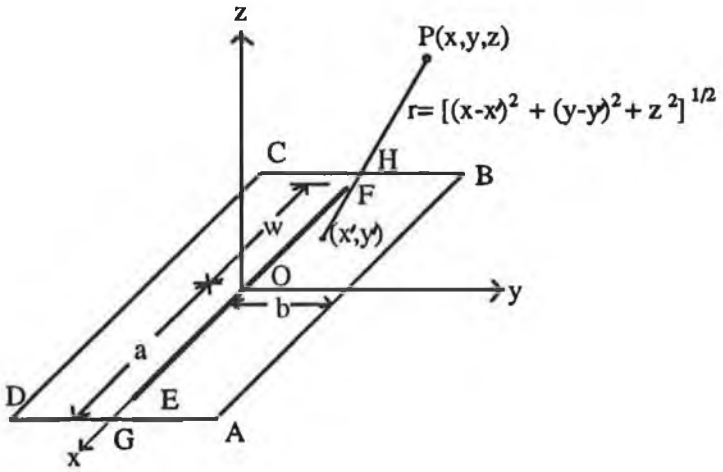

Fig. C7-1 Geometry of the open mouth of the TEM-T half radiator. The thick line indicate the septum. The open mouth is symmetrical about the axes of co-ordinates.

In order to determine Ψ, it is advisable to write it as a superposition of a complete set of basis functions Ψ_{mn} as follows

$$\Psi(x,y) = \sum_{m,n} A_{mn} \Psi_{mn}(x,y) \qquad \text{(C7-2)}$$

A_{mn} are the unknown amplitudes, and the basis functions, Ψ_{mn} must satisfy

$$\left(\nabla^2_t + K_{mn}^2\right)\Psi = 0 \qquad \text{In region ABHFEG(C7-1)}$$

and $\partial_n \Psi_{mn} = 0$ on the metal walls, i.e. on GABH and on EF

$$\left(\nabla^2_t + K_{mn}^2\right)\Psi_{mn} = 0 \qquad \text{In region ABHFEG}$$

$$\text{and} \partial_n \Psi_{mn} = 0 \qquad \text{on the boundary ABHFEG} \qquad \text{(C7-3)}$$

A detailed discussion about the effects of gap perturbation on the properties of these basis functions and on the Hertz scalar function for rectangular co-axial structure can be found in [146]. However, in the present derivation, only the higher order modes that would be generated due to the reflections at the open face of the TEM-T half (not the higher order

modes that would be generated due to gap perturbation) are of interest and as a result a simplified solution of Eqns.(C7-1) and (C7-3) are sought. Assuming a product solution of the form $(A'\cos k_x x + B'\sin k_x x)(C'\cos k_y y + D'\sin k_y y)$ for Eqn. (C7-3) and applying the boundary conditions at the boundary ABHFEG, one can find that B′ and D′ are required to be zero and $k_x = m\pi/2a$ and $k_y = n\pi/b$. Thus the solution of Eqn. (C7-3) becomes

$$\Psi_{mn} = \left(\frac{2}{ab}\right)^{\frac{1}{2}} \cos\frac{m\pi}{2a}(x+a)\cos\frac{n\pi}{b}y$$
$$\text{and } K_{mn} = \left[\left(\frac{m\pi}{2a}\right)^2 + \left(\frac{n\pi}{b}\right)^2\right]^{\frac{1}{2}} \qquad \text{(C7-4)}$$

and the Hertz scalar function Ψ, thus can be expressed as

$$\Psi = \sum_{m,n} A_{mn} \cos\left(\frac{m\pi}{2a}(x+a)\right)\cos\left(\frac{n\pi}{b}y\right) \qquad \text{(C7-5)}$$

In a similar fashion, for TM modes, one can start with the Hertz scalar function Φ, which satisfies

$$(\nabla^2_t + K^2)\Phi = 0 \qquad \text{In region ABHFEG}$$
$$\text{and } \Phi = 0 \qquad \text{on the metal walls i.e. on GABH and on EF} \qquad \text{(C7-6)}$$

E_z is directly proportional to Φ, and due to the boundary condition that the tangential component of the electric field is zero at the metal surface, the second part of Eqn. (C7-6) results. Applying similar reasoning as above, Φ can be expressed as a set of basis functions Φ_{mn} which satisfies an equation similar to (C7-6) except that $\Phi_{mn} = 0$ on the boundary ABHFEG. Starting with the product solution, as above, and then applying the boundary condition one obtains

$$\Phi_{mn} = \left(\frac{2}{ab}\right)^{\frac{1}{2}} \sin\frac{m\pi}{2a}(x+a)\sin\frac{n\pi}{b}y$$
$$\text{and } K_{mn} = \left[\left(\frac{m\pi}{2a}\right)^2 + \left(\frac{n\pi}{b}\right)^2\right]^{\frac{1}{2}} \qquad \text{(C7-7)}$$

and the Hertz scalar function Φ, can thus be expressed as

$$\Phi = \sum_{m,n} B_{mn} \sin\left(\frac{m\pi}{2a}(x+a)\right)\sin\left(\frac{n\pi}{b}y\right) \qquad \text{(C7-8)}$$

C8: VECTOR POTENTIAL OF CO-PLANAR QUAD DIPOLES

Assumptions

- All the lines connecting the dipoles (at A, B, C and D respectively) to the far field point (point of observation, P) are parallel to the radial line to that point (i.e. line OP).
- In distance calculations, any term $\leq a$ is neglected in comparison to r (since $r >> a$) but in phase calculations, those terms would be considered; a is the radius of the loop.
- Since the distances are approximate "=" in the equations of this appendix refers to "≅", but for convenience "=" sign is used in the equations.

In Fig. C8-1, the loop which contains the pairs of dipoles is on the x-y plane. Although the loop should appear elliptic, for better understanding it is drawn as a circle.

Mathematical formulation

Distances from the dipole to the point of observation (refer to Fig. C8-1):

$$\begin{aligned} r_1 &= r - a\cos(\phi' - \phi)\sin\theta \\ r_2 &= r + a\sin(\phi' - \phi)\sin\theta \\ r_3 &= r + a\cos(\phi' - \phi)\sin\theta \\ r_4 &= r - a\sin(\phi' - \phi)\sin\theta \end{aligned} \qquad \text{(C6-1)}$$

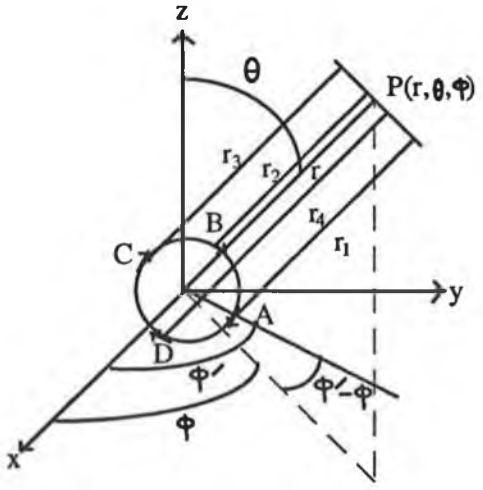

Fig. C8-1 Far field of two pairs of dipoles (co-planar). arbitrarily oriented w.r.t the axes of co-ordinates. Dipoles of each pair are parallel and opposite in phase, while the two pairs are orthogonal to each other.

Vector magnetic potential

Vector magnetic potential at point P due to the dipole at point A is,

$$\overline{A}_A = ke^{-j\beta a\cos(\phi'-\phi)\sin\theta}[\hat{x}\sin\phi' - \hat{y}\cos\phi'] \qquad \text{(C6-2)}$$

where, k is a term containing current and length of the dipole and its distance from the observation point ($\cong r$). $\hat{x}$ and $\hat{y}$ are the unit vectors along x and y directions respectively. Similarly the vector magnetic potentials at point P due to the dipoles at points B through D are,

$$\begin{aligned}
\overline{A}_B &= ke^{j\beta a\sin(\phi'-\phi)\sin\theta}[\hat{x}\cos\phi' + \hat{y}\sin\phi'] \\
\overline{A}_C &= -ke^{j\beta a\cos(\phi'-\phi)\sin\theta}[\hat{x}\sin\phi' - \hat{y}\cos\phi'] \qquad \text{(C6-3)} \\
\overline{A}_D &= -ke^{-j\beta a\sin(\phi'-\phi)\sin\theta}[\hat{x}\cos\phi' + \hat{y}\sin\phi']
\end{aligned}$$

Now the vector magnetic potential at point P due to the pair of dipoles at points A and C is

$$\begin{aligned}
\overline{A}_{A+C} &= k[e^{-j\beta a\cos(\phi'-\phi)\sin\theta} - e^{+j\beta a\cos(\phi'-\phi)\sin\theta}]\times[\hat{x}\sin\phi' - \hat{y}\cos\phi'] \qquad \text{(C6-4)} \\
&= -2jk\sin[\beta a\cos(\phi'-\phi)\sin\theta].[\hat{x}\sin\phi' - \hat{y}\cos\phi']
\end{aligned}$$

if $\lambda \rangle\rangle a$, which is true for a small loop (arc is one quarter of the loop) then $\beta a \langle\langle 1$, the sine of that small argument would be equal to the argument itself. Thus

$$\overline{A}_{A+C} = -2jk\beta a\sin\theta\cos(\phi'-\phi)[\hat{x}\sin\phi' - \hat{y}\cos\phi] \qquad \text{(C6-5)}$$

Similarly,

$$\overline{A}_{B+D} = 2jk\beta a\sin\theta\sin(\phi'-\phi)[\hat{x}\sin\phi' + \hat{y}\cos\phi] \qquad \text{(C6-7)}$$

So the total vector magnetic potential due to the two pairs of dipoles which are orthogonal to each other is

$$\begin{aligned}
\overline{A} &= 2jk\beta a\sin\theta\left[(\sin(\phi'-\phi)\cos\phi' - \cos(\phi'-\phi)\sin\phi')\hat{x} + (\cos(\phi'-\phi)\cos\phi' + \sin(\phi'-\phi)\sin\phi')\hat{y}\right] \\
&= 2jk\beta a\sin\theta[-\hat{x}\sin\phi + \hat{y}\cos\phi] \\
&= \hat{\phi}2jk\beta a\sin\theta
\end{aligned} \qquad \text{(C6-8)}$$

where, $\hat{\phi}$ is the unit vector along ϕ direction. Hence it is evident that whatever may be the orientations of the four set of dipoles (two orthogonal pairs of parallel and opposite in phase dipoles) with respect to the axes of co-ordinates, their vector magnetic potential will be a multiple of $2j\beta a\sin\theta$ of that of a single dipole and the resultant vector magnetic potential would be in ϕ direction.

C9: VECTOR POTENTIAL OF THE Q-LOOP ELEMENT

The geometry of the quarter loop is shown in Fig. C9-1. Refer to that diagram the distance, d can be expressed as

$$d^2 = (r\cos\theta)^2 + QR^2 \qquad \text{(C9-1)}$$

where $QR^2 = RM^2 + QM^2$

$$= RM^2 + (OQ - OM)^2$$

$$= a^2\sin^2(\phi-\phi') + (r\sin\theta - a\cos(\phi-\phi'))^2$$

$$= a^2 + r^2\sin^2\theta - 2ra\sin\theta\cos(\phi-\phi')$$

Thus $d^2 = r^2 + a^2 - 2ra\sin\theta\cos(\phi-\phi')$

or, $d = r\left[1 - \frac{2a}{r}\sin\theta\cos(\phi-\phi')\right]^{1/2}$ (for $r>>a$)

or, $d \cong r$ (for distance considerations) (C9-2)

and $d \cong r\left[1 - \frac{a}{r}\sin\theta\cos(\phi-\phi')\right]$ (for phase calculations) (C9-3)

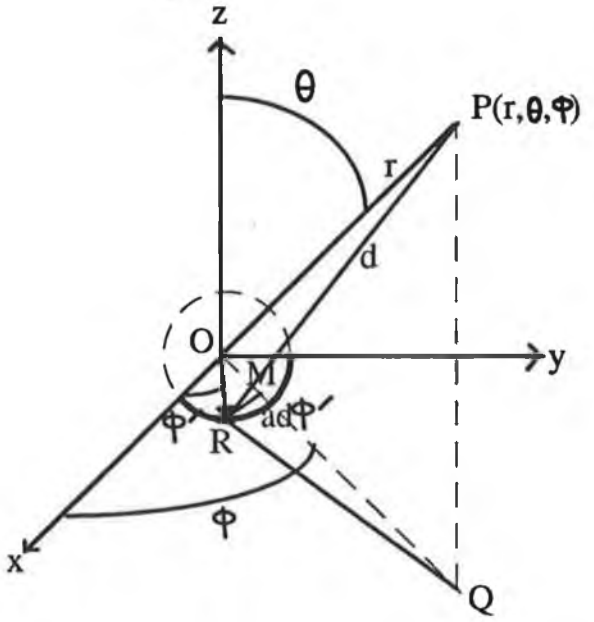

Fig. C9-1 Geometry of the quarter loop. Distance of a dipole of differential length $ad\phi$ at point R from the far field point $P(r,\theta,\phi)$ is indicated as d and a is the radius of the arc.

Vector magnetic potential

Since the current through the arc is in ϕ direction only, so the vector potential at any point in space will be ϕ directed only. Thus by definition [85, chap. 12] the vector potential at point P(r,θ,ϕ) in free space due to the current in the quarter loop is

$$\bar{A} = \frac{\mu[I]a}{4\pi r}\int_0^{\pi/2} e^{j\beta a\sin\theta\cos(\phi-\phi')}d\phi' \qquad \text{(C9-4)}$$

where $[I] = I_0 e^{j(\omega t-\beta r)}$ (retarded current at the centre of the quarter loop (origin of the co-ordinate system) w.r.t the point of observation P)

and I_0 = maximum current in the arc in time.

Evaluation of the integral

An approximate value of the definite integral appearing in Eqn. (C9-4) may be obtained by the following substitutions

let $j\beta a\sin\theta = k$ and $\phi-\phi' = \alpha$, then the definite integral assumes the form

$$\int_0^{\frac{\pi}{2}} e^{j\beta a\sin\theta\cos(\phi-\phi')}d\phi' = \int_{\phi-\pi/2}^{\phi} e^{k\cos\alpha}d\alpha \qquad \text{(C9-5)}$$

If exp(kcosα) is expanded as an infinite series and then integrated term by term,

$$\int_{\phi-\pi/2}^{\phi} e^{k\cos\alpha}d\alpha = \frac{\pi}{2} + \sqrt{2}k\sin\left(\frac{\pi}{4}+\phi\right) + \frac{k^2}{4}(1+\sin 2\phi) + \text{terms containing higher powers of}\left(\frac{k}{2}\right) \qquad \text{(C9-6)}$$

and for a small loop $a \ll \lambda$, i.e. $\beta a \ll 1$. Now since $|\sin\theta| \le 1$, the terms containing k and higher powers of (k/2) in Eqn. (C9-6) may be neglected in comparison to $\pi/2$. Thus the definite integral may be represented as

$$\int_0^{\frac{\pi}{2}} e^{j\beta a\sin\theta\cos(\phi-\phi')}d\phi' \simeq \frac{\pi}{2} \qquad \text{(C9-7)}$$

The above definite integral was evaluated numerically using Mathcad® and good agreement was found.

C10: PARAMETERS OF THE INPUT IMPEDANCE OF THE Q-LOOP

Parameters of the total input impedance of the Q-loop antenna include resistances of the quarter loop and the reflector, inductance of the quarter loop and capacitances between the quarter loop and the reflector. Resistive elements are the ohmic resistances and the radiation resistance.

Radiation resistance

Radiation resistance gives a measure of the radiation efficiency of the antenna and it is given by

$$R_r = \frac{2P_r}{I_o 2} \tag{C10-1}$$

where P_r is the total power radiated by the antenna and $I_o/\sqrt{2}$ is the rms current through the arc. The total power radiated by the antenna is from (3.5.12)

$$P_r = \frac{5\pi^2\beta^4 a^4 I_0^{\,2}}{2} \tag{C10-2}$$

Substituting for P_r from (C10-2) into (C10-1) yields

$$R_r = 5\beta^4(\pi a^2)^2 \tag{C10-3}$$

β is the wave number and a is the loop radaius. The radiation resistance of a complete loop is given by

$$(R_r)_{loop} = 20\beta^4(\pi a^2)^2 \tag{C10-4}$$

Thus the radiation resistance of the Q-loop antenna is one quarter of that of a loop antenna.

Ohmic (loss) resistance

Ohmic resistance for an antenna that carries uniform current is[151, Eqn. (1-184)]

$$R_{ohmic} \approx \frac{l}{w} R_s \tag{C10-5}$$

where l is the length of the antenna and w is the perimeter of the cross-section of the antenna. R_S is the surface resistance[185]

$$R_s = \sqrt{\frac{\omega\mu}{2\sigma}} \qquad \text{(C10-6)}$$

For the quarter loop the length of the arc is $\pi a/2$ and perimeter of the cross-section is $4d$, where d is the length of each arm of the square cross-section of the rod which is used for constructing the quarter loop. Substituting these in Eqn. (C10-5),

$$R_{ohmic} = \frac{\pi a\sqrt{w\mu}}{8\sqrt{2\sigma}d} \qquad \text{(C10-7)}$$

Similarly if it is assumed that uniform current passes through the reflector, the reflector resistance can be represented as

$$R_{ref} = \frac{a}{(w+t)}\sqrt{\frac{2\omega\mu}{\sigma}} \qquad \text{(C10-8)}$$

where w is the width of the reflector and t is thickness of the reflector sheet.

Self Inductance

Self inductance, L of the quarter loop is composed of internal inductance, L_i and the external inductance L_{ext} as

$$L = L_i + L_{ext} \qquad \text{(C10-9)}$$

where L_i is given by[177]

$$L_i = \frac{\mu_0 l}{8\pi} \qquad \text{(C10-10)}$$

l is the length of the arc, thus Eqn. (C10-10) becomes

$$L_i = \frac{\mu_0 a}{16} \qquad \text{(C10-11)}$$

and L_{ext} can be formulated as[177]

$$L_{ext} = \frac{\mu_0 a^2}{2} \int_0^{\pi} \int_0^{\pi} \frac{\cos(\theta' - \theta)}{\sqrt{\left[2a\left(a - \frac{d}{2}\right) + \left(\frac{d}{2}\right)^2 - 2a\left(a - \frac{d}{2}\right)\cos(\theta' - \theta)\right]}} d\theta' d\theta \qquad \text{(C10-12)}$$

with an appropriate change of variables,

$$L_{ext} = \frac{\mu_0 a^2}{2} \int_0^{\pi} \frac{\cos\theta}{\sqrt{\left[\left(\frac{d}{2}\right)^2 + 2a\left(a - \frac{d}{2}\right)(1 - \cos\theta)\right]}} d\theta \qquad \text{(C10-13)}$$

The integration is performed numerically using Mathcad and the calculation is included at the end of this Appendix.

Capacitance

Determination of the capacitance between the flat face of the quarter loop and the refelctor is pretty simple, if the fringing capacitance is neglected and can be expressed as the capacitance between two parallel plates, each of area d^2, placed at a distance of t_n and the medium between is nylon of relative permittivity ε_r. More accurate analysis called for the conformal mapping technique to transform the region between two unequal parallel plates into two equal parallel plates and then express the capacitance which would take into account the fringing field as well (refer to the analysis of Appendix E7).

The stray capacitance between the qaurter loop and the reflector (again neglecting the fringing field) can be approximately formulated as follows:

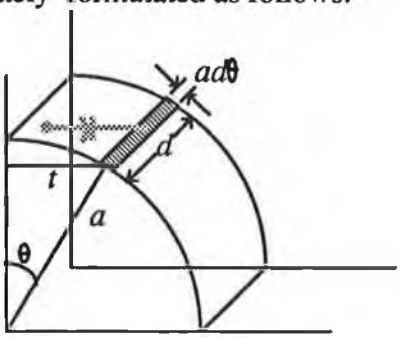

Fig. C10-1 Model of the stray capacitance between the quarter loop and the reflecor of the Q-loop antenna (Fringing capacitance is neglected in the model).

differential arc length is $ad\theta$ and its width is d, thus the area of the differential strip is $dad\theta$. The distance between this strip and the reflector is $\sqrt{2}a\sin\theta$. So the differntial amount of capaciatance

$$dC = \varepsilon_0 \frac{da}{\sqrt{2}a\sin\theta} d\theta \qquad \text{(C10-14)}$$

The total capacitance may be assumed to be twice the capaciatnce between one half of the arc (θ varies from $\pi/4$ to $\pi/2$) and one side of the reflector. Thus the total stray capacitance is

$$\begin{aligned} C_{stray} &= 2\varepsilon_0 d \int_{\frac{\pi}{4}}^{\frac{\pi}{2}} \frac{d\theta}{\sqrt{2}\sin\theta} \\ &= \sqrt{2}\varepsilon_0 d \ln\left(\sqrt{2}+1\right) \end{aligned} \qquad \text{(C10-15)}$$

C11: DETERMINATION OF THE NEAR FIELD OF TEM-T HALF

The formulation of the problem is described in the main text. The computer program that determines the near field distribution in front of the TEM-T transmitting half is listed here. All the subprograms are also listed. A list of the subprograms and their operations is noted in the subprogram called "apincl.h".

```
#include "apincl.h"

static float frequency;    /* frequency in MHz */
static float k;            /* phase constant /meter */
static float zmin;  /* boundary between near and far field in meter */

main()
{
        int n,i,j,l,npts,nptsz;
        float t,Ex,Ey,Ez,Hx,Hy,Hz;
        float theta(float,float,float);
        float phi(float,float);
        float Wave_Impedance(int,float,float,float,float,float,float);
        complex Ephi,Etheta,Er,Hphi,Htheta,Hr;
        complex Exx,Eyy,Ezz,Hxx,Hyy,Hzz;
        float c, omega,lambda;
        float x,y,z,xmax,xmin,ymax,ymin,r;
        FILE *oute, *outh, *outimp;
        oute = fopen("efldm.dat","w");
        outh = fopen("hfldm1.dat","w");
        outimp = fopen("temimp.dat","w");

        printf("Input the number of points at a fixed z plane, npts:\t");
        scanf("%d",&npts);

        printf("Input the number of points in z direction, nptsz:\t");
        scanf("%d",&nptsz);

        printf("Input the frequency of operation in MHz:\t");
        scanf("%f",&frequency);
/*      Provision for computing field at several frequencies are as follows */
/*      for (n = 1; n <= 1; n++){
        frequency = n*100.0;
*/
/*      fprintf(oute,"Frequency in MHz:\t%f\n\n",frequency);
        fprintf(outh,"Frequency in MHz:\t%f\n\n",frequency);
*/

/*      Velocity of propagation of EM wave in meter/sec */
        c = 3.0*pow10(8);
/*      Wave length in meter  */
    lambda = c/(frequency*pow10(6));
/*      Phase constant /meter  */
    k = 2*pi/lambda;
/*      Angular frequency */
        omega = 2.0*pi*frequency*pow10(6);
        complex factor = complex(0.0,omega);

/*      Near and Far Field Radiation Pattern  */
/*      All the distances are in meter  */

        xmax = 2.0*a;
        xmin = -xmax;
        ymax = 2.0*b;
        ymin = -ymax;
        for (l = 0; l<= (nptsz - 1); l++)
```

```
{
        zmin = 0.01;
z = zmin + l*zmin;

printf("z=\t%f\n",z);
for (i = 0; i<= npts; i++)
{
        x = xmin + i*(xmax - xmin)/npts;

        for (j = 0; j<= npts; j++)
        {
                y = ymin + j*(ymax - ymin)/npts;

            r = sqrt(x*x + y*y + z*z);

/*      E-field components in spherical co-ordinates */

                Ephi = (-1.0/epsi)*(cos(phi(x,y))*(pd(Fx,6,x,y,z) + (1.0/z)*Fx(x,y,z))
            + sin(phi(x,y))*(pd(Fy,6,x,y,z)+ (1.0/z)*Fy(x,y,z)));
                Etheta= (1.0/epsi)*(cos(phi(x,y))*((r/z)*pd(Fy,6,x,y,z) + (1.0/r)*Fy(x,y,z))
            - sin(phi(x,y))*((r/z)*pd(Fx,6,x,y,z) + (1.0/r)*Fx(x,y,z)));
                Er= 0.0;
/*      E-field components in rectangular co-ordinates */

                Exx = (Er*sin(theta(x,y,z)) + Etheta*cos(theta(x,y,z)))*cos(phi(x,y))
                        -Ephi*sin(phi(x,y));
                Eyy = (Er*sin(theta(x,y,z)) + Etheta*cos(theta(x,y,z)))*sin(phi(x,y))
                        +Ephi*cos(phi(x,y));
                Ezz = Er*cos(theta(x,y,z)) - Etheta*sin(theta(x,y,z));

                Ex = abs(Exx)*sin(omega*t - arg(Exx));
                Ey = abs(Eyy)*sin(omega*t - arg(Eyy));
                Ez = abs(Ezz)*sin(omega*t - arg(Ezz));
            printf("%f,%f,%f\t%e,%e,%e\n",x,y,z,Ex,Ey,Ez);

/*      H-field components in spherical co-ordinates */

                Hphi = -factor*(-sin(phi(x,y))*Fx(x,y,z) + cos(phi(x,y))*Fy(x,y,z));
                Htheta= -factor*(cos(phi(x,y))*Fx(x,y,z) + sin(phi(x,y))*Fy(x,y,z))*cos(theta(x,y,z));
                Hr= -factor*(cos(phi(x,y))*Fx(x,y,z) + sin(phi(x,y))*Fy(x,y,z))*sin(theta(x,y,z));


/*      H-field components in rectangular co-ordinates */
                Hxx = (Hr*sin(theta(x,y,z)) + Htheta*cos(theta(x,y,z)))*cos(phi(x,y))
                        -Hphi*sin(phi(x,y));
                Hyy = (Hr*sin(theta(x,y,z)) + Htheta*cos(theta(x,y,z)))*sin(phi(x,y))
                        +Hphi*cos(phi(x,y));
                Hzz = Hr*cos(theta(x,y,z)) - Htheta*sin(theta(x,y,z));


                Hx = abs(Hxx)*sin(omega*t - arg(Hxx));
                Hy = abs(Hyy)*sin(omega*t - arg(Hyy));
                Hz = abs(Hzz)*sin(omega*t - arg(Hzz));

        printf("%f,%f,%f\t%e,%e,%e\n",x,y,z,Hx,Hy,Hz);
        fprintf(outimp,"%f\t%f\t%f\t%f\n",z,Wave_Impedance(1,Ex,Ey,Ez,Hx,Hy,Hz),
                Wave_Impedance(2,Ex,Ey,Ez,Hx,Hy,Hz),
                    Wave_Impedance(3,Ex,Ey,Ez,Hx,Hy,Hz));


    fprintf(oute,"%f\t%f\t%f\t%e\t%e\t%e\n",x,y,z,
                Ex,Ey,Ez);
    fprintf(outh,"%f\t%f\t%f\t%e\t%e\t%e\n",x,y,z,
                Hx,Hy,Hz);
    }

  }
}
  fclose(oute);
```

```
    fclose(outh);
    fclose(outimp);
return 0;
}
complex Retard_function(float x,float y,float z,float xprime,float yprime)
{
        float r = sqrt((x-xprime)*(x-xprime) +
                                        (y-yprime)*(y-yprime) + z*z);
        return (complex)  (1.0/r)*exp(complex(0.0,-k*r));

}
```

SUBPROGRAMS

1

```
/* List of header files to be included with the aparture
        radiation programs */

#include <math.h>
#include <stdio.h>
#include <complex.h>
#include <iostream.h>

#include "nr.h"
#include "nrutil.h"
#include "const.h"    /* 2, subprogram to define the constants used */
#include "aprfldm1.h"  /* 3, subprogram to determine the aperture field at the
                                open mouht of the TEM-T half */
#include "current.h"   /* 4, subprogram to determine the equivalent current densities
                                (magnetic cuurent shhet and electric current sheet) */
#include "pddrivr.h"   /* 5, subprogram to drive the routine for partial differentiations */
#include "pdcom1.h"    /* 6, Routine for performing the partial differentiations */
#include "dint1.h"     /* 7, subprogram for performing the double integrations */
#include "radvec1.h"   /* 8, subprogram to compute the vector electric and
                                vector  magnetic potentials */
#include "rfunc.h"     /* 9, subprogram for generating the functions prior to
                                differentiations  or integrations */
```

2

```
/* Definition of the constants used in the program */

#define a 0.15  /* half width of the cell in meter*/
#define b 0.075  /* half height of the cell in meter */
#define w 0.10  /* half width of the septum of the cell */
#define pi 3.141592654
#define epsi 0.000000000008852 /* free space permittivity, Farad/meter */
#define mu 0.000001256   /* free space permiability, Henry/meter */
#define sigma 3.58e7   /* conductivity of aluminium in  Siemens */
```

3

```
#include <math.h>
#include <complex.h>
#include "nr.h"
#include "nrutil.h"
#include "const.h"

#define CA 0.0003
#define pi 3.141592654


void sncndn(float uu,float emmc,float *sn,float *cn,float *dn)
{
        float aa,bb,c,d,emc,u;
```

```
        float em[14],en[14];
        int i,ii,l,bo;

        emc=emmc;
        u=uu;
        if (emc) {
                bo=(emc < 0.0);
                if (bo) {
                        d=1.0-emc;
                        emc /= -1.0/d;
                        u *= (d=sqrt(d));
                }
                aa=1.0;
                *dn=1.0;
                for (i=1;i<=13;i++) {
                        l=i;
                        em[i]=aa;
                        en[i]=(emc=sqrt(emc));
                        c=0.5*(aa+emc);
                        if (fabs(aa-emc) <= CA*aa) break;
                        emc *= aa;
                        aa=c;
                }
                u *= c;
                *sn=sin(u);

                *cn=cos(u);
                if (*sn) {
                        aa=(*cn)/(*sn);
                        c *= aa;
                        for (ii=l;ii>=1;ii--) {
                                bb=em[ii];
                                aa *= c;
                                c *= (*dn);
                                *dn=(en[ii]+aa)/(bb+aa);
                                aa=c/bb;
                        }
                        aa=1.0/sqrt(c*c+1.0);
                        *sn=(*sn >= 0.0 ? aa : -aa);
                        *cn=c*(*sn);
                }
                if (bo) {
                        aa=(*dn);
                        *dn=(*cn);
                        *cn=aa;
                        *sn /= d;
                }
        } else {
                *cn=1.0/cosh(u);
                *dn=(*cn);
                *sn=tanh(u);
        }
}

#undef CA

void field(float x,float y,float *Ex,float *Ey,float *Hx,float *Hy)
{
        complex P0, E0, snz;
        float m,mw,modsq,modulus;
        float uu,muu,val,sn,cn,dn;
        float snmw,s,s1,c,c1,d,d1,septum_width,volt;
        float alpha,alpha1,K1,KK,mx,my;
        float eta,denominator;
        float snx,sny,dnx,dny;

        volt = 1.0;

/*      Plane wave impedance */
```

```
        eta = 377.0;
        m = 21.10;
        modulus = 0.98517245;
        mw = w*m;
        modsq = 1.0 - modulus*modulus;
    sncndn(mw,modsq,&sn,&cn,&dn);
        snmw = sn;
        alpha = snmw;
        alpha1 = alpha*alpha;
        K1=1.0;
        sncndn(K1,alpha1,&sn,&cn,&dn);
        KK = sn;

                mx = m*x;
                sncndn(mx,modsq,&sn,&cn,&dn);
                s = sn;
                c = cn;
                d = dn;


                my = m*y;
                sncndn(my,modulus*modulus,&sn,&cn,&dn);
            s1 = sn;
                c1 = cn;
                d1 = dn;

                denominator = 1 - d*d*s1*s1;

                if ( denominator == 0.0 && y == b)
                        {
                        *Ex = 0.0;
                        *Ey = volt*m/KK;
                        }
                else if ( denominator == 0.0 && y == -b)
                        {
                        *Ex = 0.0;
                        *Ey = -volt*m/KK;
                        }
                else
                        {
                        snx = s*d1/denominator;
        sny = c*d*s1*c1/denominator;
        dnx = d*c1*d1/denominator;
        dny = modulus*modulus*s*c*s1/denominator;

                snz = complex(snx,sny);
                P0 = snmw*snmw - snz*snz;
      E0 = volt*m*complex(dny,dnx)/(sqrt(P0)*KK);

                if (y>=0){
                *Ex = -real(E0);
                *Ey = imag(E0);}
                else{
                *Ex = real(E0);
                *Ey = -imag(E0);
                }

                *Hx = -1.0*(*Ey)/eta;
                *Hy = (*Ex)/eta;
        }
}
```

4

```
#include <math.h>
#include <complex.h>

float Jsx(float xprime,float yprime) /* x-component of the current density
                                        due to magnetic field */
```

```
{
        float Ex,Ey,Hx,Hy;
        field(xprime,yprime,&Ex,&Ey,&Hx,&Hy);
        return -1.0*Hy;
}

float Jsy(float xprime,float yprime) /* y-component of the current density
                                        due to magnetic field */
{
        float Ex,Ey,Hx,Hy;
        field(xprime,yprime,&Ex,&Ey,&Hx,&Hy);
/*      printf("Hx = %e\n",Hx); */
        return Hx;
}

float Msx(float xprime,float yprime) /* y-component of the current density
                                        due to magnetic field */
{
        float Ex,Ey,Hx,Hy;
        field(xprime,yprime,&Ex,&Ey,&Hx,&Hy);
        return Ey;
}

float Msy(float xprime,float yprime) /* y-component of the current density
                                        due to magnetic field */
{
        float Ex,Ey,Hx,Hy;
        field(xprime,yprime,&Ex,&Ey,&Hx,&Hy);
        return -1.0*Ex;
}
```

5

```
/* Double integration of a complex function*/

#include <math.h>
#include <complex.h>

#define a 0.15
#define b 0.075

static float xx,yy,zz;
static float xsav,ysav;
static float (*curr)(float,float);


complex NL(float (*current)(float,float),float x,float y,float z) /* Function subprogram for computation of
                                        Radiation Vectors N & L  */
{
        float xmax, xmin;
        complex s, quad2d(float,float);

                xx = x;
                yy = y;
                zz = z;
                curr = current;

                xmax= a;
                xmin = -xmax;
                s=quad2d(xmin,xmax);
                return s;
        }


complex quad2d( float x1,float x2)
{
        complex qgaus(complex (*func2)(float),float,float);
```

```
        complex f1(float);

        return qgaus(f1,x1,x2);
}

complex f1(float xprime)
{
        complex qgaus(complex (*func1)(float),float,float);
        complex f2(float);
        float y1,y2;            /* ANSI: float yy1(float),yy2(float); */

    y1 = -b;
        y2 = b;
        xsav=xprime;
        return qgaus(f2,y1,y2);
}

complex func(float (*curr)(float,float),float xprime,float yprime,float x,float y,float z)
{
        complex Retard_function(float,float,float,float,float);
/*      printf("x=%f\ty=%f\tz=%f\t going to Rf\n",x,y,z);
*/      return (*curr)(xprime,yprime)*Retard_function(x,y,z,xprime,yprime);
}


complex f2(float yprime)
{
        complex func(float (*curr)(float,float),float,float,float,float,float);
    return func(curr,xsav,yprime,xx,yy,zz);
}

complex qgaus(complex (*funct)(float),float aa,float bb)
{
        int j;
        float xr,xm,dx;
        complex s;
        static float xp[]={0.0,0.1488743389,0.4333953941,
                0.6794095682,0.8650633666,0.97390652};
        static float ww[]={0.0,0.2955242247,0.2692667193,
                0.2190863625,0.1494513491,0.06667134};

        xm=0.5*(bb+aa);
        xr=0.5*(bb-aa);
        s=0;
        for (j=1;j<=5;j++) {
                dx=xr*xp[j];
                s += ww[j]*((*funct)(xm+dx)+(*funct)(xm-dx));
        }
        return s *= xr;
}
```

7

```
/*      Numerical Partial Differentiation  */
#include <math.h>
#include <stdio.h>
#include <complex.h>
#include <iostream.h>


/* driver for the differentiation */

complex pd(complex (*func)(float,float,float),int derv,float x,float y,float z)
{
        if (derv == 1)
        return pdx(func,x,y,z);
        else if (derv == 2)
        return pdy(func,x,y,z);
```

```
    else if (derv == 3)
            return pdxx(func,x,y,z);
    else if (derv == 4)
            return pdyy(func,x,y,z);
    else if (derv == 5)
            return pdyx(func,x,y,z);
            else if (derv == 6)
            return pdz(func,x,y,z);
            else
            {printf("\n No diferentiation is required\n");
            return 0;}

}
```

8

```
/*          Numerical Partial Differentiation  */
#include <math.h>
#include <stdio.h>
#include <complex.h>

#define nval 10
#define tol .00001
static float  hh = 0.001 ;


complex pdxOh2(complex (*func)(float,float,float),float x,float y,float z)
{
            int i;
    float h = hh;
            complex DD[20];
            float EE[20],RR[20];
            complex delx;

            DD[0] = (func(x + h,y,z) -  func(x - h,y,z))/(2.0*h);

    for (i = 1; i<= nval; i++){

                        h = h/2.0;
                        DD[i] = (func(x + h,y,z) -  func(x - h,y,z))/(2.0*h);

                        EE[i] = abs(DD[i] - DD[i-1]);
                        RR[i] = 2.0*(EE[i])/( abs(DD[i]) + abs(DD[i-1]) + tol);

            if((EE[i-1] < EE[i]) || (RR[i] < tol) && (i < nval))
             delx =  DD[i-1];
             else
             delx =  DD[nval];

             }
return delx;
}

complex pdxOh4(complex (*func)(float,float),float x,float y)
{
            int i;
    float h = hh;
            complex DD[20];
            float EE[20],RR[20];
            complex delx;

            DD[0] = (-1.0*func(x + 2.0*h,y) + 8.0*func(x + h,y)
                        -8.0*func(x - h,y) + func(x - 2.0*h,y))/(12.0*h);

    for (i = 1; i<= nval; i++){

                        h = h/2.0;
                        DD[i] = (-1.0*func(x + 2.0*h,y) + 8.0*func(x + h,y)
```

```
                    -8.0*func(x - h,y) + func(x - 2.0*h,y))/(12.0*h);

                    EE[i] = abs(DD[i] - DD[i-1]);
                    RR[i] = 2.0*EE[i]/( abs(DD[i]) + abs(DD[i-1]) + tol);

            if((EE[i-1] < EE[i]) || (RR[i] < tol) && (i < nval))
             delx =  DD[i-1];
             else
             delx =  DD[nval];

            }
return delx;
}

complex pdyOh2(complex          (*func)(float,float),float x,float y)
{
            int i;
      float h = hh;
            complex DD[20];
            float EE[20],RR[20];
            complex dely;

            DD[0] = (func(x,y + h) -  func(x,y - h))/(2.0*h);

      for (i = 1; i<= nval; i++){

                    h = h/2.0;
                    DD[i] = (func(x,y + h) -  func(x,y - h))/(2.0*h);

                    EE[i] = abs(DD[i] - DD[i-1]);
                    RR[i] = 2.0*EE[i]/( abs(DD[i]) + abs(DD[i-1]) + tol);

            if((EE[i-1] < EE[i]) || (RR[i] < tol) && (i < nval))
             dely =  DD[i-1];
             else
             dely =  DD[nval];

            }
return dely;
}

complex pdyOh4(complex (*func)(float,float),float x,float y)
{
            int i;
      float h = hh;
            complex DD[20];
            float EE[20],RR[20];
            complex dely;

            DD[0] = (-1.0*func(x,y + 2.0*h) + 8.0*func(x,y +h)
                    -8.0*func(x,y - h) + func(x,y - 2.0*h))/(12.0*h);

      for (i = 1; i<= nval; i++){

                    h = h/2.0;
                    DD[i] = (-1.0*func(x,y + 2.0*h) + 8.0*func(x,y +h)
                    -8.0*func(x,y - h) + func(x,y - 2.0*h))/(12.0*h);

                    EE[i] = abs(DD[i] - DD[i-1]);
                    RR[i] = 2.0*EE[i]/( abs(DD[i]) + abs(DD[i-1]) + tol);

            if((EE[i-1] < EE[i]) || (RR[i] < tol) && (i < nval))
             dely =  DD[i-1];
             else
             dely =  DD[nval];

            }
return dely;
}
```

```
complex pdyx(complex (*func)(float,float),float x,float y)
{
        int i;
    float h = hh;
        complex D[20];
        float E[20],R[20];
        complex delyx;

        D[0] = 0.25*(func((x + h),(y + h)) - func((x + h),(y - h))
        - func((x - h),(y + h)) + func((x - h),(y - h)))/(h*h);


    for (i = 1; i<= nval; i++){

                h = h/2.0;

                D[i] = 0.25*(func((x + h),(y + h)) - func((x + h),(y - h))
        - func((x - h),(y + h)) + func((x - h),(y - h)))/(h*h);

                E[i] = abs(D[i] - D[i-1]);
                R[i] = 2.0*E[i]/( abs(D[i]) + abs(D[i-1]) + tol);

        if((E[i-1] < E[i]) || (R[i] <= tol) && (i < nval))
         delyx = D[i-1];
        else
         delyx = D[nval];

        }
return delyx;
}

complex pdxx(complex (*func)(float,float),float x,float y)
{
        int i;
    float h = hh;
        complex DD[20];
        float EE[20],RR[20];
        complex delxx;

        DD[0] = (func(x + h,y) - 2.0*func(x,y)
        + func(x - h,y))/(h*h);

    for (i = 1; i<= nval; i++){

                h = h/2.0;
                DD[i] = (func(x + h,y) - 2.0*func(x,y)
                + func(x - h,y))/(h*h);

                EE[i] = abs(DD[i] - DD[i-1]);
                RR[i] = 2.0*EE[i]/( abs(DD[i]) + abs(DD[i-1]) + tol);

        if((EE[i-1] < EE[i]) || (RR[i] < tol) && (i < nval))
         delxx = DD[i-1];
        else
         delxx = DD[nval];

        }
return delxx;
}

complex pdyy(complex (*func)(float,float),float x,float y)
{
        int i;
    float h = hh;
        complex DD[20];
        float EE[20],RR[20];
        complex delyy;
```

```
        DD[0] = (func(x,y + h ) - 2.0*func(x,y)
        + func(x,y - h))/(h*h);

    for (i = 1; i<= nval; i++){

                h = h/2.0;
                DD[i] = (func(x,y + h ) - 2.0*func(x,y)
                + func(x,y - h))/(h*h);

                EE[i] = abs(DD[i] - DD[i-1]);
                RR[i] = 2.0*EE[i]/( abs(DD[i]) + abs(DD[i-1]) + tol);

        if((EE[i-1] < EE[i]) || (RR[i] < tol) && (i < nval))
         delyy =  DD[i-1];
         else
         delyy =  DD[nval];

        }
return delyy;
}
```

9

```
#include <math.h>
#include <complex.h>


complex Nx(float x,float y) /* Function subprogram for computation of
                x-component of Radiation Vector N  */
{
        float Jsx(float,float);
        complex NL(float (*curent)(float,float),float,float);
        return  NL(Jsx,x,y);
}

complex Ny(float x,float y) /* Function subprogram for computation of
                y-component of Radiation Vector N  */
{
        float Jsy(float,float);
        complex NL(float (*curent)(float,float),float,float);
        return  NL(Jsy,x,y);

}

complex Lx(float x,float y) /* Function subprogram for computation of
                x-component of Radiation Vector L  */
{
        float Msx(float,float);
        complex NL(float (*curent)(float,float),float,float);
        return  NL(Msx,x,y);

}

complex Ly(float x,float y) /* Function subprogram for computation of
                y-component of Radiation Vector L  */
{
        float Msy(float,float);
        complex NL(float (*curent)(float,float),float,float);
        return  NL(Msy,x,y);

}

complex Ax(float x,float y) /* Function subprogram for computation of
                x-component of Vector magnetic potential A  */
{
        complex Green_functionmu(float,float);
        return Green_functionmu(x,y)*Nx(x,y);
}
```

```
complex Ay(float x,float y)/* Function subprogram for computation of
                        y-component of Vector magnetic potential A  */
{
        complex Green_functionmu(float,float);
        return Green_functionmu(x,y)*Ny(x,y);
}

complex Fx(float x,float y) /* Function subprogram for computation of
                        x-component of Vector electric potential F  */
{
        complex Green_functioneps(float,float);
        return Green_functioneps(x,y)*Lx(x,y);

}

complex Fy(float x,float y) /* Function subprogram for computation of
                        y-component of Vector electric potential F  */
{
        complex Green_functioneps(float,float);
        return Green_functioneps(x,y)*Ly(x,y);

}
10
#include <math.h>
#include <stdio.h>
#include "const.h"


float theta(float x,float y,float z)
{
        float ro;
        ro = sqrt(x*x + y*y);

        if((z == 0.0) && (ro == 0.0))
        return 0.0;
        else if(z == 0.0 && (ro != 0.0))
        return pi/2;
        else
    return atan(ro/z);
}

float phi(float x,float y)
{
    if((x == 0.0) && (y == 0.0))
        return 0.0;
        else if(x == 0.0 && (y != 0.0))
        return pi/2;
        else
    return atan(y/x);
}

float Wave_Impedance(int i,float Ex,float Ey,float Ez,float Hx,float Hy,float Hz)
{

    if((Ex == 0.0) && (Hy == 0.0) && i == 1)
        return 0;
        else if((Ex != 0.0) && (Hy == 0.0) && i == 1)
    return  10000;
        else if(i == 1)
        return Ex/Hy;

    if((Ey == 0.0) && (Hx == 0.0) && i == 2)
        return 0;
        else if((Ey != 0.0) && (Hy == 0.0) && i == 2)
    return  10000;
        else if(i == 2)
    return  -Ey/Hx;
```

```
    else if((i == 3) && ( sqrt(Ex*Ex + Ey*Ey + Ez*Ez) ==0.0)
            && ( sqrt(Hx*Hx + Hy*Hy + Hz*Hz) ==0.0))
    return  0;
    else if((i == 3) && ( sqrt(Ex*Ex + Ey*Ey + Ez*Ez) !=0.0)
            && ( sqrt(Hx*Hx + Hy*Hy + Hz*Hz) ==0.0))
          return 10000;
          else if(i == 3)
    return  sqrt(Ex*Ex + Ey*Ey + Ez*Ez)/sqrt(Hx*Hx + Hy*Hy + Hz*Hz);

}
```

Note: Part of subprogram 5 has been copied from chapter 4 of Numerical Recipes Example Book (C) by W. T. Vettering *et al.* published by the Cambridge University Press, Cambridge in 1988.

C12: DETERMINATION OF REFLECTION COEFFICIENT OF RFCP SAMPLE

The theoretical derivation of the SE of RFCP is presented in section 3.2.4. The computer program that determines the theoretical reflection coefficient of such a material is listed here. Regular FSS like filling is assumed, where the filler elements are like thin dipoles.

```
#include "fss1inc.h"

#define c 3.0e8 /* speed of EM wave in free space */
#define PI 3.1457
#define epsi0 8.852e-12
#define mu0 12.57e-7
#define llt 0.0

static float beta;
static float omega;
static float l;
static float width;
static float le;
static float Dx;
static float Dy;
static float wavelength;
static float deltal;
static float phi_inc;
static int no_rows;
static int no_cols;
static int i;
static int j;

main()
{
          int freqGHz, no_elements, ang_inc;
          float Rl, Xl, R,freq;
          float K(float,float,complex), geometry(void);
          complex driv_impedance(void);

/* Incident field is plane wave, linearly polarized in y-direction and
  incident at an angle phi_inc */
```

```
/* physical length of each element, 2*l < wavelength
  To avoid grating lobes, Dx and Dy < 0.5*wavelength
                                                but > 0.2*wavelength */
            printf("Input the total no. of elements in the array, N=\t");
            scanf("%d",&no_elements);
      printf("Input the load impedance, Rl=\t");
            scanf("%f",&Rl);
      printf("\t Xl=\t");
            scanf("%f",&Xl);

            no_rows = sqrt(no_elements);
            no_cols = no_rows;
            l = 0.0066;
            Dx  = 0.0089;
            Dy  =2.0*Dx;
            float lblambda;

/* Express l, le, Dx, Dy in terms of wavelength */
            for (ang_inc = 0; ang_inc <= 0; ang_inc++)
            {
                        phi_inc = 10*ang_inc*PI/180.0;

            for (freqGHz = 1; freqGHz <= 10; freqGHz++)
      {
                        lblambda = 0.17 + 0.01*freqGHz;
                        wavelength = l/lblambda;
                        omega = 2*PI*freqGHz*1.0e9;
                        complex Zl = complex(Rl, omega*Xl);
           freq = c/wavelength;
                        beta = 2*PI/wavelength;
/* Provision for expressing l, Dx and Dy in terms of wavelength is kept but
            in the present analysis specific values of the aforementioned
            quantities have been chosen as mentioned before */
/*                      l = 0.5*wavelength;
                        Dx = Dy = 0.5*wavelength;
*/                      deltal = 0.3*l;
                        le = l + deltal; /* ref: fss1*/
/*                      fprintf(fp,"%f\t%f\n",l/wavelength,K(l/wavelength, le, Zl));
                        fprintf("K=\t%f\n",K(l/wavelength, le, Zl));
                        printf("geometry=\t%f\n",pow(geometry(),2));
                        printf("Impd=\t%f\n",pow(abs(driv_impedance()+Zl),2));
*/
/*                      printf("l/lambda=%f\tImpd=%f,%f\n",lblambda,real(driv_impedance()+Zl),
                                    imag(driv_impedance()+Zl));
                        fprintf(fp,"l/lambda=%f\tImpd=%f,%f\n",lblambda,real(driv_impedance()+Zl),
                                    imag(driv_impedance()+Zl));
*/                      R = 1/(K(l/wavelength, le, Zl)*
                                    pow(geometry(),2)*
                                    pow(abs(driv_impedance()+Zl),2));
            printf("%d\t%f\n",freqGHz,R);
            }
            }
            fclose(fp);
return 0;
}

float K(float llambda, float le, complex Zl)
{
            complex driv_impedance(void);
            float Trig(void);

            float Fe1 = (sin(beta*l) -beta*l*cos(beta*le))/(1-cos(beta*le));
            float Fe2 = (1 - cos(beta*le) - Fe1*sin(beta*le))/sin(beta*le);

            return PI*PI*pow(llambda,4)/
                        (3600*pow(abs(Fe1 - Fe2*Zl/driv_impedance()),2)*Trig()*Trig());
}

float Trig(void)
```

```
{
        return (cos(beta*deltal) - cos(beta*le))/sin(beta*le);
}

float geometry(void)
{
        return (Dx/l)*(Dy/l)*pow(cos(phi_inc),2);
}

complex driv_impedance(void)
{
        int epsiok;
        complex Za;
    complex self_impedance(void);
    complex mutual_impedance(void);
/*      printf("i\tj\tRm\t\tXm\n\n");
*/      Za = complex(0.0,0.0);
        for (i = -no_rows/2; i<=no_rows/2; i++)
        {
                for (j = 0; j<=no_cols/2; j++)
                {
                        if(j==0) epsiok = 1; else epsiok = 2;
                        float cs = cos(beta*Dx*j*sin(phi_inc));
                        Za += epsiok*(1-j/(1.0*(no_cols/2)))*mutual_impedance()*cs;
                }
        }
/*      printf("Returning from driv_impedance\n\n");

*/      return Za;
}


complex mutual_impedance(void)
{
        complex ff1(float);
        complex ff2(float);
        complex self_impedance(void);
        complex parallel(float);
        float potscalar, potvector;
        FILE *fp1;
        fp1 = fopen("mutual.dat","w");

        potscalar = beta/(8.0*PI*omega*epsi0*sin(beta*le)*sin(beta*le));
        potvector = -omega*mu0/(8.0*PI*sin(beta*le)*sin(beta*le));

        if((j==0) && (i==0)) return self_impedance();
    else if((i==0) && (j!=0)){
        fprintf(fp1,"%f\t%f\t%f\n", j*Dx/wavelength,real(parallel(j*Dx)),imag(parallel(j*Dx));

        printf("i=%d\tj=%d\tR21=%f\tX21=%f\n", i,j,
                        real(parallel(j*Dx)),imag(parallel(j*Dx));
         return parallel(j*Dx);}
        else{
        complex c1 = compl_intg(ff1, (i*Dy-l),(i*Dy+l));
        complex c2 = compl_intg(ff2, (i*Dy-l),(i*Dy+l));
        return complex(0.0,1.0)*potscalar*c1 + potvector*c2;
        }
}

complex ff1(float y)
{
        complex f1(float);
        return differentiate(f1,y)*sin(beta*(le - fabs(y)));

}

static float y1;
static float y2;
```

```
complex f1(float y)
{
        y1 = y;
        complex Eirsp(float);
        return compl_intg(Eirsp,-l,l);
}

complex ff2(float y)
{
        y2 = y;
        complex Eirvp(float);
        complex compl_intg(complex (*fu)(float),float,float);
        return sin(beta*(le - fabs(y)))*compl_intg(Eirvp,-l,l);
}


complex Eirsp(float yprime)
{
        complex bet = complex(0.0, beta);
        float dist = sqrt(j*Dx*j*Dx + (y1 - yprime)*(y1 - yprime));

        complex retplus = -bet*(le - fabs(yprime) + dist);
        complex retminus = bet*(le - fabs(yprime) - dist);
        return (exp(retplus) + exp(retminus))/dist;
}

complex Eirsp00(void)
{
        complex bet = complex(0.0, beta);
        complex ponm = complex(0.0,beta*(-le - y1 + fabs(y1)));
        complex ponp = complex(0.0,beta*(-le + y1 + fabs(y1)));

        complex ret = exp(bet*y1)*(exp(-ponp) + exp(ponm));
        complex rett = ret*(-EiIntg(-beta*(-l+y1))
                                        +EiIntg(-beta*(l+y1)));
        return rett;
}

complex Eirvp(float yprime)
{
        complex bet = complex(0.0, beta);
        float dist = sqrt(j*Dx*j*Dx + (y2 - yprime)*(y2 - yprime));

        complex retplus = -bet*(le - fabs(yprime) + dist);
        complex retminus = bet*(le - fabs(yprime) - dist);
        return (exp(retplus) - exp(retminus))/dist;
}

complex Eirvp00(void)
{
        complex bet = complex(0.0, beta);
        complex ponm = complex(0.0,beta*(-le - y2 + fabs(y2)));
    complex ponp = complex(0.0,beta*(-le + y2 + fabs(y2)));

        complex ret = exp(bet*y2)*(exp(-ponp) - exp(ponm));
        complex rett = ret*(EiIntg(-beta*(-l+y2))
                                        -EiIntg(-beta*(l+y2)));
        return rett;
}


complex self_impedance(void)
{
        complex prod,Z11;
        complex S(float);
        complex C(float);
                prod = complex(0.0,60.0)/(sin(beta*l)*sin(beta*l));
                Z11 = prod*( 4.0*cos(beta*l)*cos(beta*l)*S(beta*l)
                        -cos(2.0*beta*l)*S(2.0*beta*l)
```

```
                -sin(2.0*beta*l)*(2.0*C(beta*l) - C(2.0*beta*l)));

        return Z11;
}


float intg(float (*fu)(float),float a,float b)
{
        int jj;
        float xr,xm,dx;
        double s;
        static float xx[]={0.0,0.1488743389,0.4333953941,
                0.6794095682,0.8650633666,0.97390652};
        static float ww[]={0.0,0.2955242247,0.2692667193,
                0.2190863625,0.1494513491,0.06667134};

        xm=0.5*(b+a);
        xr=0.5*(b-a);
        s=0.0;
        for (jj=1;jj<=5;jj++) {
                dx=xr*xx[jj];

                s += ww[jj]*((*fu)(xm+dx)+(*fu)(xm-dx));
        }
        return s *= xr;
}


float Cin(float x)
{
        float cinc(float);
        if(x==0.0) return 0.0;
        else{
            return intg(cinc,llt,x);
        }
}

float Cii(float x)
{
        float cinc(float);
        if(x==0.0) return 0.0; /* this is not correct */
        else{
            return 0.577 + log(x) - intg(cinc,llt,x);
        }
}


float Sii(float x)
{
        float sinc(float);
        if(x==0.0) return 0.0;
        else{
            return intg(sinc,llt,x);
        }
}

complex C(float B)
{
        float Cin(float),Sii(float);
        float w = 2*l/10.3;
        float t = w/7.3;

        float width = 0.25*(w+t);
        return log(2.0*l/width)
                - 0.5*Cin(2.0*B)
                - complex(0.0,0.5)*Sii(2.0*B) ;
}

complex S(float B)
```

```
        argm1 = beta*(sqrt(d*d + l*l) -l);
        argm2 = beta*(sqrt(d*d + l*l) +l);
        argm3 = beta*(sqrt(d*d + 4.0*l*l) -2.0*l);
        argm3 = beta*(sqrt(d*d + 4.0*l*l) +2.0*l);
        float cicos = cos(beta*l*(Cii(argm1) + Cii(argm2)));

        return 2.0*(2.0 + cos(2.0*beta*l))*Cii(beta*d)
                - 4.0*cicos*cicos + cos(beta*2.0*l*(Cii(argm3) + Cii(argm4)))
                + sin(beta*2.0*l*(Sii(argm4) - Sii(argm3)
                -2.0*Sii(argm2) + 2.0*Sii(argm1)));
}

float Xpa(float d)
{

        float sicos = cos(beta*l*(Sii(argm1) + Sii(argm2)));

        return -2.0*(2.0 + cos(2.0*beta*l))*Sii(beta*d)
                + 4.0*sicos*sicos - cos(beta*2.0*l*(Sii(argm3) + Sii(argm4)))
                + sin(beta*2.0*l*(Cii(argm4) - Cii(argm3)
                -2.0*Cii(argm2) + 2.0*Cii(argm1)));
}
```

SUBPROGRAMS

1

```
/* List of header files to be included with the FSS1.CPP
        reflection programs */

#include <math.h>
#include <stdio.h>
#include <complex.h>
```

```
{
        float Cin(float),Sii(float);
        return -beta*width
                - complex(0.0,0.5)*Cin(2.0*B)
                + 0.5*Sii(2.0*B) ;
}

float sinc(float x)
{
        return sin(x)/x;
}

float cinc(float x)
{
        return (1 - cos(x))/x;
}

static float argm1;
static float argm2;
static float argm3;
static float argm4;

complex parallel(float d)
{
        float Rpa(float);
        float Xpa(float);
        float mult = 30.0/(sin(beta*l)*sin(beta*l));
        return mult*complex(Rpa(d),Xpa(d));
}


float Rpa(float d)
{
```

```
#include <iostream.h>

#include "diff.h"
#include "complint.h"
#include "exintg.h"


/*          Numerical Differentiation  of a complex function */
#include <math.h>
#include <stdio.h>
#include <complex.h>

#define nval 6
#define tol .00001
static float  hh = 0.005 ;


complex differentiate(complex(*func)(float),float y)
{
        int ii;
    float h = hh;
        complex DD[20];
        float EE[20],RR[20];

        DD[0] = (func(y + h) -  func(y - h))/(2.0*h);

    for (ii = 1; ii<= 2; ii++){

                h = h/2.0;
                DD[ii] = (func(y + h) -  func(y - h))/(2.0*h);

                EE[ii] = abs(DD[ii] - DD[ii-1]);
                RR[ii] = 2.0*EE[ii]/( abs(DD[ii]) + abs(DD[ii-1]) + tol);
                }
                ii = 1;
        while ((EE[ii]>EE[ii+1])  && (ii< nval)){
                h = h/2.0;
                DD[ii+2] = (func(y + h) -  func(y - h))/(2.0*h);

            EE[ii+2] = abs(DD[ii+2] - DD[ii+1]);
                RR[ii+2] = 2.0*EE[ii+2]/( abs(DD[ii+2]) + abs(DD[ii+1]) + tol);
                ii++;}

return DD[ii];
}
```

3

```
#include <complex.h>
#include <math.h>

#define PI 3.1457

complex Eiintg(float x)
{
        int t,todd,teven,lim, fact(int);
        float gamma, si, ci, ssum, csum;
        ssum = 0.0;
        if(x==0.0) return complex(1.0,0.0);
        else{
        gamma = 0.577 + log(fabs(x));
        csum = gamma;
        if(x<0.2)
        {
                si=x;
                ci = gamma;
        }
```

```
        else if (x > 1)
        {
                si = PI/2.0 - cos(x)/x;
                ci = sin(x)/x;
        }
        else
        {
                lim = 3;
                for(t=1;t<=lim;t++)
                {
                        todd = 2*t-1;
                        teven = 2*t;
                        ssum += pow(-1.0,(t-1))*pow(x,todd)/(todd*fact(todd));
                        csum += pow(-1.0,(t-1))*pow(x,teven)/(teven*fact(teven));
                }
                si = ssum;
                ci = csum;
        }

    return complex(ci,si);
        }
}

int fact(int g)
{
        int n;
        int fac = 1;
        if(g==0) fac=1;
        else
        {
        for(n=1;n<=g;n++)
        {
                fac *=n;
        }
        }
return fac;
}
```

4

```
#include <math.h>
#include <complex.h>


complex compl_intg(complex (*fu)(float),float a,float b)
{
        int jj;
        float xr,xm,dx;
        complex s;
        static float xx[]={0.0,0.1488743389,0.4333953941,
                0.6794095682,0.8650633666,0.97390652};
        static float ww[]={0.0,0.2955242247,0.2692667193,
                0.2190863625,0.1494513491,0.06667134};

        xm=0.5*(b+a);
        xr=0.5*(b-a);
        s=complex(0.0,0.0);
        for (jj=1;jj<=5;jj++) {
                dx=xr*xx[jj];

                s += ww[jj]*((*fu)(xm+dx)+(*fu)(xm-dx));
        }
        return s *= xr;
}
```

Note: Part of the subprogram 4 has been copied from chapter 4 of Numerical Recipes Example Book(C) by W. T. Vettering *et al.* published by Cambridge University Press, Cambridge, in 1988.

D1: SELECTION OF THE AZIMUTHAL STRUCTURAL ANGLE

The major design criteria of VCA is that its characteristic impedance should be 50 Ω. The input impedance of the antenna is given by Eqn. (4.2.1). The elliptic integral of the first kind K(k) referred to in that equation is defined earlier in chapter 3. Now according to the design criteria it is possible to form an integral equation

$$0.265 = \frac{\int_0^{\frac{\pi}{2}} \frac{d\beta}{\sqrt{(1-\sin^2\beta\cos^2\phi_0)}}}{\int_0^{\frac{\pi}{2}} \frac{d\beta}{\sqrt{(1-\sin^2\beta\sin^2\phi_0)}}} \quad \ldots \quad \ldots \quad \text{(B1-1)}$$

by letting Z_{in} = 50 Ω on the L.H.S of Eqn. (4.2.1). However, it is very difficult to solve this equation for the unknown parameter ϕ_0 . The Method of Moment (MoM) analysis may be applied but it is tedious and beyond the scope of the present work. However, Mathcad® can be employed to solve this problem using trial and error. The solution procedure is listed below:

Sample calculations for determining the azimuthal structural angle of the VCA

$$\phi := \frac{\pi}{180}, \frac{\pi \cdot 22.5}{180} .. \frac{\pi}{2}$$

$$Z_0 := 377$$

Note the integrations at the numerator are not done exactly up to 90 degrees because in that case the numerical computation does not converge and for the same reason the integrations in the denominator are not started exactly from 0 degrees.

$$\left[2 \cdot \frac{\int_{0.00001}^{\frac{\pi \cdot 0.9995}{2}} \frac{1}{\sqrt{\left[1-[\sin(\phi)\cdot\sin(\beta)]^2\right]}} d\beta}{\int_{0.000001}^{\frac{\pi}{2}} \frac{1}{\sqrt{\left[1-[\cos(\phi)\cdot\sin(\beta)]^2\right]}} d\beta \cdot Z_0}\right]^{-1}$$

652.485
277.093
191.646
133.475
68.53

From the above trial it is observed that we have to start from 67.5 degrees and go above. Note that the angle cannot be more than 90 degrees. Let us start from 75 degrees at step of 5 degrees to 90 degrees.

$$\phi := \frac{\pi \cdot 75}{180}, \frac{\pi \cdot 80}{180} .. \frac{\pi}{2}$$

$$\left[\frac{\int_{0.00001}^{\frac{\pi \cdot 0.9995}{2}} \frac{1}{\sqrt{\left[1 - \left[\sin(\phi) \cdot \sin(\beta)\right]^2\right]}} d\beta}{2 \cdot \int_{0.000001}^{\frac{\pi}{2}} \frac{1}{\sqrt{\left[1 - \left[\cos(\phi) \cdot \sin(\beta)\right]^2\right]}} d\beta \cdot Z_0} \right]^1$$

108.95
94.754
77.604

37.755

From the above trial it is observed that we have to seek for the solution between 85 degrees and 90 degrees.

$$\phi := \frac{\pi \cdot 85}{180}, \frac{\pi \cdot 86}{180} .. \frac{\pi}{2}$$

$$\left[\frac{\int_{0.00001}^{\frac{\pi \cdot 0.9995}{2}} \frac{1}{\sqrt{\left[1 - \left[\sin(\phi) \cdot \sin(\beta)\right]^2\right]}} d\beta}{2 \cdot \int_{0.000001}^{\frac{\pi}{2}} \frac{1}{\sqrt{\left[1 - \left[\cos(\phi) \cdot \sin(\beta)\right]^2\right]}} d\beta \cdot Z_0} \right]^1$$

77.604
73.353
68.53
62.748
54.939
37.755

Thus 89 degrees is the required solution. Since that is the angle for which the characteristic impedance is the closest to 50 ohm. However, we can go further by searching for a more accurate result between 89 and 90 degrees but that would lead us with some fractional value for the angle which is very difficult to maintain during manufacturing.

D2: CONSTRUCTIONAL DETAILS OF THE VCA

The process of constructing the VCA begins with a semi-circular thin aluminium sheet. The slant height of the cone would be the radius of the circle. The sheet is to be marked for 1^o sections at the bottoms and a 2^o section at the middle as shown in Fig. D2-1. The sheet is then folded to give the desired conical structure.

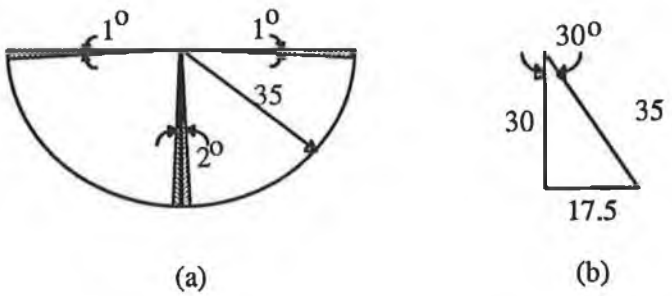

Fig. D2-1 Geometry of the section of the cone and the sheet to construct it. (a) The semi-circular sheet from which the complete cone is to be constructed. The angles should be marked prior to folding and (b) The right-angled triangle, a complete revolution of which around its perpendicular arm constructs the desired conical solid figure. The dimensions of the cone can be ascertained from this diagram.

This conical structure is then pushed into the conical collar to retain the shape. The collar is machined from a block of aluminium. The collar is a frustum(section of a cone) of the desired cone capped with a hollow cylindrical extension. External diameter of the cylindrical portion should be equal to the internal diameter of the N-BNC adopter, which is 1.6 cm. There should be two 2^o tapered sections at the middle of the conical collar as shown in Fig. D2-2 to match with the similar sections of the VCA. M3 size nylon screws and bolts may be used to clamp the VCA to this collar. The screw positions are shown in the figure.

After the cone is fitted to the collar, the desired tapered sections of 2^o at the two sides of the cone can then be cut from the cone to construct the V-cone. In order to make the VCA

strong enough, two more nylon rings can be fitted at distances of 10 and 15 cms from the apex of the VCA as shown in Fig. D2-3. These rings can also be bolted with the nylon screws to the VCA, as was suggested to fix up the collar to the VCA.

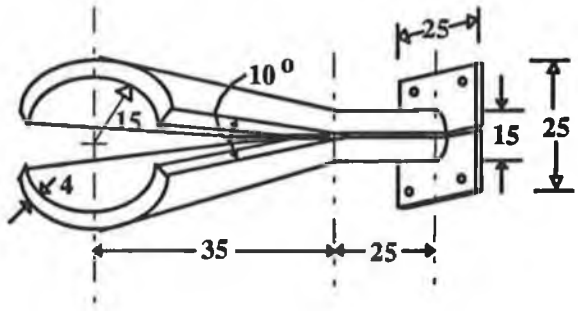

Fig. D2-2 Thick metallic collar to retain the shape of the cone. Cylindrical extension with flat face of the collar is shown. The extension is provided to make electrical connection. Upper half of the collar is made of nylon and the lower half is made of aluminium. All the dimensions are in mm and the diagram is not drawn to scale.

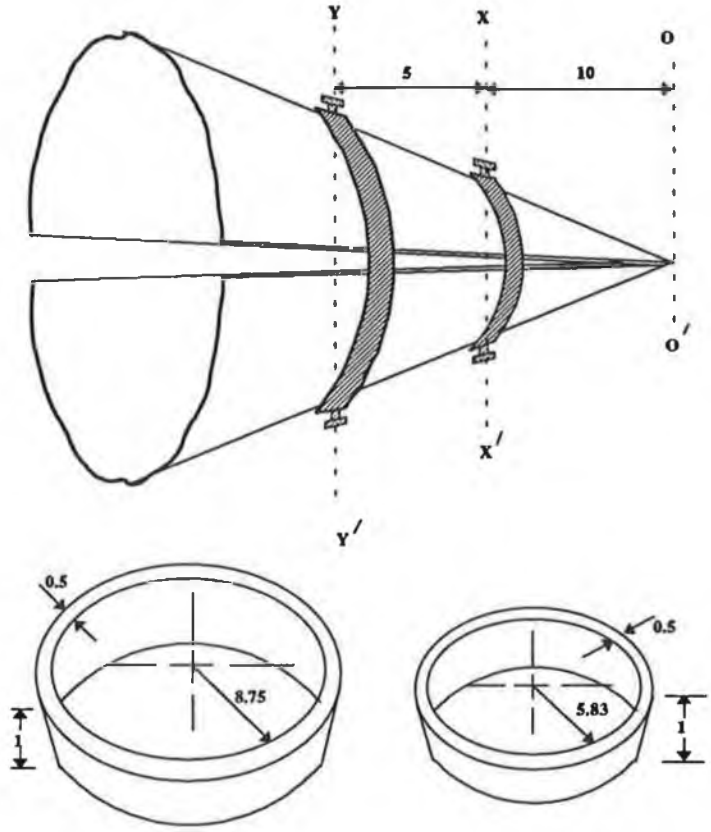

Fig. D2-3 Nylon bands to strengthen the conical structure of the VCA. (a) The position of the bands on the VCA. (b) Dimensions of the bands. The screw positions are also shown in the figure. All the dimensions are in cm and the diagram is not drawn to scale.

D3: FIELD INTENSITY PROFILE IN FRONT OF ECCOGEL LENS

Elemination of nonuniformity of the EM field in front of a lens using lossy dielectrics

Electrical Conductivity, S/m

$s := 10^{-15}$

Frequency of operation, Hz

$f := 2 \cdot 10^{8}$

$w := 2 \cdot p \cdot f$

Permeability and Permittivity

$m_0 := 4 \cdot p \cdot 10^{-7}$

$e_0 := 8.852 \cdot 10^{-12}$

$m_r := 1.0$

$e_r := 2.0 - j \cdot 0.051$ /* Relative permittivity of Eccogel (trade name of a particular product of Emmerson and Cumming Inc., USA */

Absorption Loss:

$a := \mathrm{Re}\left[\sqrt{j \cdot w \cdot m_0 \cdot m_r \cdot \left[s + j \cdot w \cdot e_0 \cdot e_r\right]}\right]$

$a = 0.076$

Normal Incidence of Low Impedance Field

$R_m := 25$

$n := \sqrt{e_r \cdot m_r}$

$q_m := \frac{p}{6}$

$L := \frac{R_m \cdot \left[n \cdot \cos\left[q_m\right] - 1\right]}{(n-1)}$

$|L| = 13.587$

$t_0 := R_m \cdot \cos\left[q_m\right] - L$

$i := 0 .. 20$

$$q_i := \frac{p}{60} \cdot i - \frac{p}{6}$$

$$E_i := \left| \frac{\left[n \cdot \cos\left[q_i \right] - 1 \right] \cdot \left[\exp\left[-a \cdot \left[(n-1) \cdot \frac{L}{\left[n \cdot \cos\left[q_m \right] - 1 \right] \cdot \left[n \cdot \cos\left[q_i \right] - 1 \right]} \cdot \left[\cos\left[q_i \right] - \cos\left[q_m \right] \right] \right] \right]}{(n-1) \cdot \left[\exp\left[-a \cdot t_0 \right] \right]} \right|$$

$$y_i := \frac{(n-1) \cdot L \cdot \sin\left[q_i \right]}{n \cdot \cos\left[q_i \right] - 1}$$

$$R_i := \frac{(n-1) \cdot L}{n \cdot \cos\left[q_i \right] - 1}$$

Plot of E-field intensity as a function of Lens height

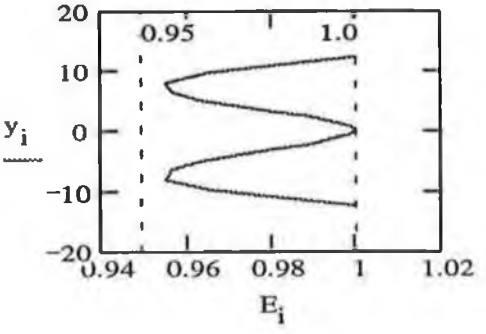

LENS GEOMETRY

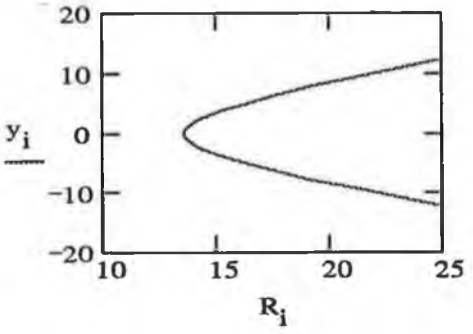

D4: EFFECT OF THE CONSTITUTIVE PROPERTIES ON THE LENS DIMENSION

Electrical Conductivity, S/m

$s := 2 \cdot 10^{-13}$

Frequency of operation, Hz

$f := 2 \cdot 10^{8}$

$w := 2 \cdot p \cdot f$

Permeability and Permittivity

$m_0 := 4 \cdot p \cdot 10^{-7}$

$e_0 := 8.852 \cdot 10^{-12}$

$m_r := 1.0$

$e := 2 .. 10$ /* permittivity is varying from 2 to 10 at steps of unity */

Normal Incidence of Plane wave

$R_m := 25$ cm

$n_e := \sqrt{e \cdot m_r}$ /* Refractive index */

$q_m := \frac{p}{6}$

$L_e := \frac{R_m \cdot \left[n_e \cdot \cos\left[q_m \right] - 1 \right]}{\left[n_e - 1 \right]}$ /* Focal length of the lens */

cm

$t0_e := R_m \cdot \cos\left[q_m \right] - L_e$

8.086
4.575
3.349
2.71
2.311
2.035
1.832
1.675
1.549

/*Thickness of the lens in cm. in higher order of relative permittivity */
/* as relative permittivity is increasing, thickness of the lens is decreasing */

D5: RADIATION EFFICIENCY AND RADIATED POWER OF Q-LOOP

The radiation efficiency and the radiated power of the Q-loop antenna and a complete loop antenna are the same, because if the image effects are taken into considerations the Q-loop behaves like a complete loop. Thus the efficiency and power calculations of a loop antenna are equally applicable for Q-loop antenna.

Radiation efficiency as function of loop radius

The radius of the quarter loop is 10 cm. The efficiency of such a loop antenna is plotted as a function of frequency. It is observed from the curve that the loop radiates efficiently throughout the desired frequency range.

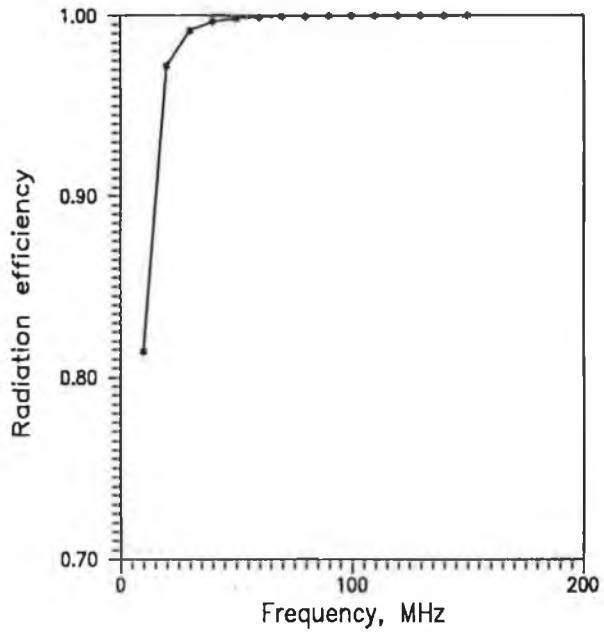

Fig. D5-1 Radiation efficiency of a loop antenna as a function of frequency. Efficiency is expressed in per unit. The efficiency of the loop antenna of diameter, 20 cm is plotted. Above 200 MHz the efficiency is almost unity.

Radiation efficiency as function of rod dimension

The cross-section of the rod used to construct the quarter loop antenna is selected as a square. Fig. D5-2(a) plots the efficiency of that antenna as a function of the length of a side of that square for various values of frequency. It is observed that the efficiency becomes maximum for

an arm length of around 20 mm and for larger arms the efficiency reduces again.

Radiated power as function of the rod dimension

The radiated power as function of the arm length of the square cross-section of the rod is plotted in Fig. D5-2(b) for various values of frequency. From the family of curves it is evident that the power reaches maximum for a certain length of arm and then saturates. For lower range of frequencies, the maximma occur at arm lengths around 10-15 cm and for higher frequencies they occur at larger lengths.

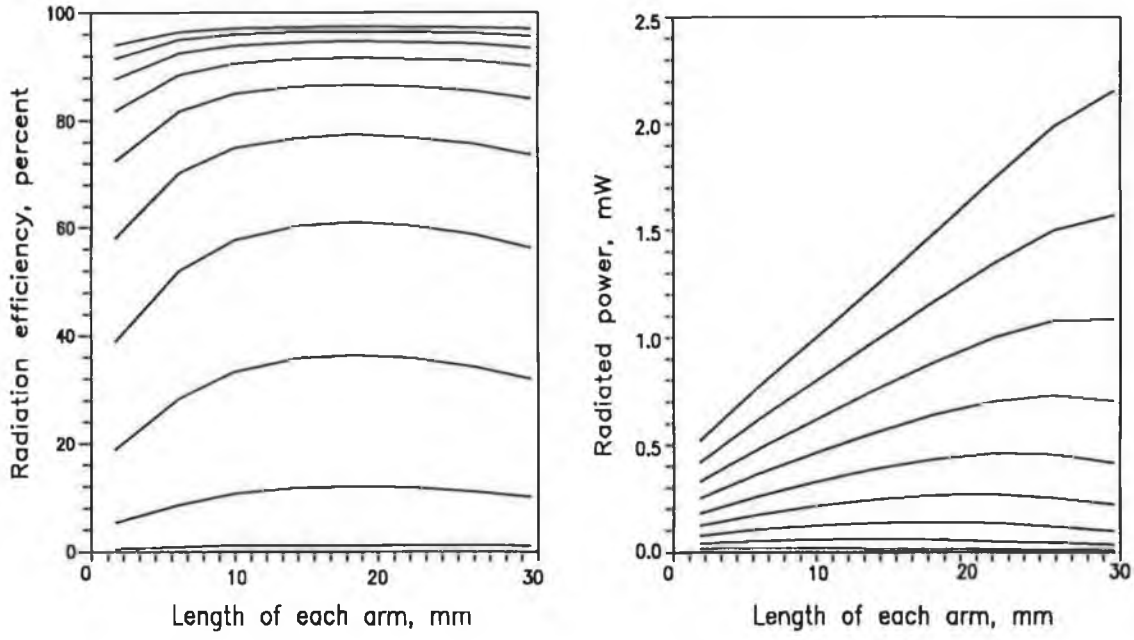

(a) (b)

Fig. D5-2 Radiation efficiency and the radiated power of a loop antenna as a function of the dimension of the rod that construct the loop. Horizontal axis represents the length of each arm of the square cross-section of the rod. (a) Radiation efficiency; bottom curve represents the efficiency at 20 MHz and the next one at 40 MHz and so on up to the top curve at 200 MHz and (b) Radiated power; bottom curve represents the radiated power at 40 MHz and the next one at 60 MHz and so on up to the top curve at 200 MHz.

D6: SE OF METALS, GUIDE TO SELECT FOR THE TEST DEVICES

SE of a plane metallic sheet against normally incident plane wave has been developed theoretically by Schulz et.al.[41] applying transmission line analogy. This analysis is frequently referred to in almost all the texts on EMC. Since metallic sheet is used for manufacturing the

test devices in the present work, it is useful to quote that formula to plot the shielding capabilty of different prospective metal candidates as functions of frequency and their thickness.

$$SE = A + R + B \qquad \text{dB} \qquad \text{(D6-1)}$$

where the absorption loss

$$A = 8.686\sqrt{\omega\mu\sigma}l \qquad \text{dB} \qquad \text{(D6-2)}$$

and the reflection loss

$$R = -20\log_{10}\left|\frac{4k}{(1+k)^2}\right| \quad \text{dB} \qquad \text{(D6-3)}$$

and the correction term for successive re-reflections

$$B = 20\log_{10}\left|\frac{(k-1)^2}{(k+1)^2}e^{2\gamma l}\right| \quad \text{dB} \qquad \text{(D6-4)}$$

In the above set of equations, ω is the angular frequency, μ and σ are the permeabilty and the conductivity of the material, l is its thickness and $k = Z_W/\eta$, η is the intrinsic impedance of the sheet and γ is the propagation constant of an EM wave inside the material.

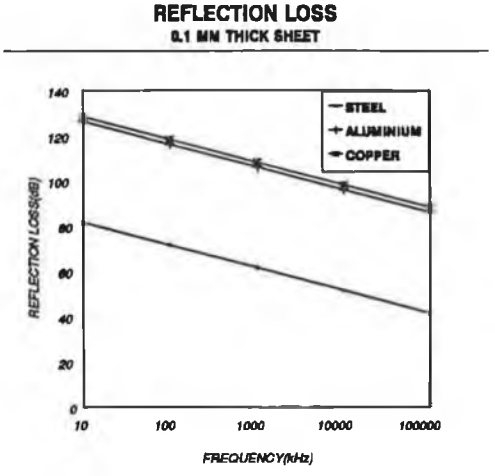

Fig. D6-1 Reflection loss suffered by EM wave while passing through 0.1 mm thick shield of different metals as function of frequncy.

Reflection loss, being a surface phenomenon, is pretty much independent of the thickness of the shielding material. Both absorption and reflection loss mechanisms, however, are dependent on the frequency of the impinging EMI field as is evident from Eqns. (D6-2) and (D6-3).

Eqn. (D6-2) indicates that the reflection loss is more predominent if the shield material is highly conductive and less effective if the shield is ferromagnetic and that low frequency fields are easier to block than high frequency fields. This is shown in Fig. D6-1. Copper and aluminium both have the same permeability, but copper is slightly more conductive, and so provides slightly greater reflection loss to an E-field. Steel is less effective for two reasons. First, it has somewhat elevated permeability due to its iron content, and, second, as tends to be the case with magnetic materials, it is less conductive.

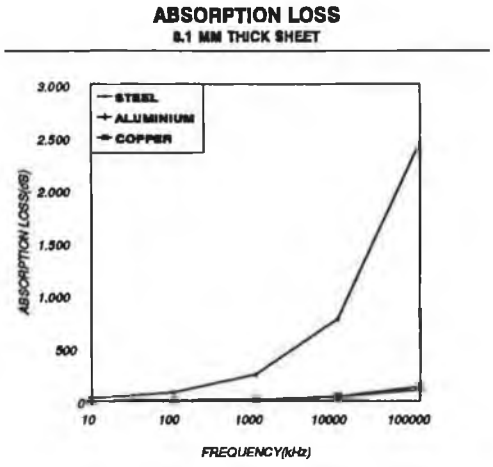

Fig. D6-2 Absorption loss suffered by EM wave while penetrating through 0.1 mm thick shield of different metals as function of frequncy.

On the otherhand, according to (D6-2), absorption loss is more effective at higher frequencies and with shield material that has both high conductivity and high permeability. In practice, however, selecting steel for its high permeability involves some compromise in conductivity. But the increase in permeability more than makes up for the decrease in conductivity, as is evident from Fig. D6-2.

A composite of E-field and H-field shielding is shown in Fig. D6-3. However, this type of data is meaningful only in the far field. In the near field the EMI could be 90% H-field, in which case the reflection loss is irrelevant. It would be advisable then to beef up the absorption loss, by choosing steel. A better conductor than steel might be less expensive but it would also be less ineffective.

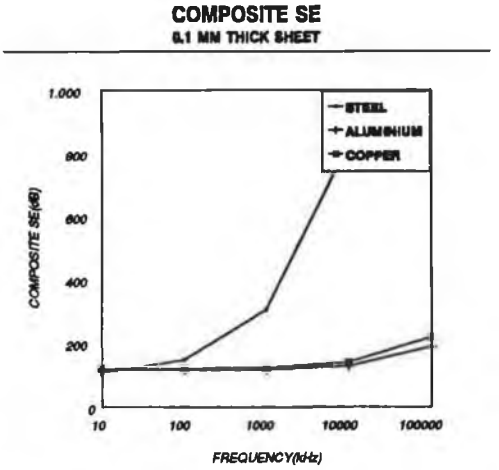

Fig. D6-3 Composite SE of 0.1 mm thick sheet of different metals as function of frequncy. Above 100 MHz, SE of steel becomes immensely high.

TABLE D6-1

Materials used by different commercial organizations in manufacturing TEM cell.

Company	Material used	Remarks
TECKNIT Inc.	Cobalt-caoted aluminum	Coating of coblat improves the H-field shielding
AR Inc. (Amplifier Research)	Chromate-coated aluminium	Coating of chromium improves the H-field shielding
Kansai Electronic Industry	copper (8 mm thick sheet)	Very thick sheet (8 mm) of copper was used

E-field shielding is more effective if the shield material is highly conductive and less effective if the shield is ferromagnetic and that low frequency fields are easier to block than high frequency fields. This is shown in Fig. D6-1. Copper and aluminium both have the same permeability, but copper is slightly more conductive, and so provides slightly greater reflection loss to an E-field. Steel is less effective for two reasons. First, it has somewhat elevated permeability due to its iron content, and, second, as tends to be the case with magnetic materials, it is less conductive.

On the otherhand, H-field shielding (absorption loss) is more effective at higher frequencies and with shield material that has both high conductivity and high permeability. In practice, however, selecting steel for its high permeability involves some compromise in conductivity. But the increase in permeability more than makes up for the decrease in conductivity, as can be seen in Fig. D6-2.

A composite of E-field and H-field shielding is shown in Fig. D6-3. However, this type of data is meaningful only in the far field. In the near field the EMI could be 90% H-field, in which case the reflection loss is irrelevant. It would be advisable then to beef up the absorption loss, by choosing steel. A better conductor than steel might be less expensive but it would also be less effective. Materials used by different commercial organizations to manufacture TEM cell are listed in Appendix D6. Thick copper sheet (as shown in the Table) is not easy to handle mechanically and chromate (or cobalt) coated aluminium are not cost effective for manufacturing a single cell. Ordinary steel sheet was thus recommended for manufacturing the TEM-T cell in the present application.

E1: COMPUTER PROGRAM FOR AUTOMATED MEASUREMENT

A HP synthesized signal generator 8657B is used to feed a signal of amplitude 17.0 dBm (maximum signal strength of the generator) to the input of the test device. Chase ADVANTEST spectrum analyzer R3361A, connected at the output of the test device is picks up the received signal level which is then recorded in an output file. The listing of the computer program is given below:

COMPUTER SUBPROGRAM LISTING

```
/* This is a program to control the HP synthesised signal generator
and the Chase ADVANTEST spectrum analyzer to transmit and receive
signals from 100 kHz to 1 GHz through the test devices which can be
applied for SE measurement */

/* Link this program with appropriate *cib*.obj.  */


#include <stdio.h>
#include <decl.h>


void finderr(void);
void error(void);

extern int ibsta;
extern int iberr;
extern int ibcnt;

/* Application program variables passed to GPIB functions */

char rd[512];          /* read data buffer      */
int sgtr;              /* Hewlett-Packard Signal generator identifier */
int spar;              /* Hewlett-Packard Spectrum Analyzer identifier */

main()
{

  FILE  *output;
  int i, n, freqkhz,freqmhz;

/*  Assign unique identifier to HP signal generator
  "HPSGTR" and store it in variable sgtr. Check
  for error. (ibfind error = negative value returned.)    */

  if((sgtr = ibfind("HPSGTR")) < 0) finderr();

/*  Clear the device and check for error */

  if (ibclr(sgtr) & ERR) error();

/* Write the frequency, amplitude, and modulation setting
  instructions to the HPSGTR.              */

  ibwrt (sgtr,"FR100KZ,AP0DM,AP UV",22);
  if (ibsta & ERR) error();

/*  Frequency increament should be 100 kHz up to 1MHz. */

  ibwrt (sgtr,"FRIS100KZ",9);
  if (ibsta & ERR) error();

/*  Assign unique identifier to Chase ADVANTEST spectrum analyzer
```

```
   "DEV5" and store it in variable spar. Check for error.
   (ibfind error = negative value returned.)     */

   if((spar = ibfind("DEV5")) < 0) finderr();

/* Clear the device and check for error */

   if (ibclr(spar) & ERR) error();

/* Instructions to spectrum analyzer */

   ibwrt(spar, "CF100KZ,SP100KZ,HD0,MK CF",23);

   output = fopen("c:\\grapher\\results\\spectrum.dat", "w");

   fprintf(output, "Frequency in kHz\tAmplitude in dBm\n");

   n = 50;

/* From 100 kHz to 1 MHz at steps of 100 kHz */

   for (i = 0; i < n; i++)
            {
            freqkhz = 100 + i*100;
            if (freqkhz < 1000)
                     {
                     ibwrt(spar,"ML?",3);
                     if (ibsta & ERR) error();

                     ibrd(spar,rd,8);
                     fprintf(output, "%d\t\t\t%s\n",freqkhz,rd);

                     sgtr = ibfind("HPSGTR");
                     if((sgtr
                     = ibfind("HPSGTR")) < 0) finderr();
                     ibwrt(sgtr,"FRUP",4);
                     if (ibsta & ERR) error();

                     spar = ibfind("DEV5");
                     if((spar = ibfind("DEV5")) < 0) finderr();
                     ibwrt(spar, "CS100KZ,CFUP,SP100KZ,MK CF",26);
                     if (ibsta & ERR) error();
                     }

/* From 1 MHz to 10 MHz at steps of 1 MHz*/

            else if (freqkhz == 1000)
            {
            fprintf(output, "Frequency in MHz\tAmplitude in dBm\n");
                     ibwrt(spar, "CS1MZ,SP100KZ,MK CF",19);
                                       }
            else  if ((freqkhz >= 1000) && (i < 19))
            {
                     freqmhz = 1 + (i-10);
                     ibwrt(spar,"ML?",3);
                     ibrd(spar,rd,8);
                     fprintf(output, "%d\t\t\t%s\n",freqmhz,rd);

                     sgtr = ibfind("HPSGTR");
                     if((sgtr = ibfind("HPSGTR")) < 0) finderr();
                     ibwrt(sgtr,"FRIS1MZ",7);
                     if (ibsta & ERR) error();

                     ibwrt(sgtr,"FRUP",4);
                     if (ibsta & ERR) error();

                     spar = ibfind("DEV5");
                     if((spar = ibfind("DEV5")) < 0) finderr();
                     ibwrt(spar, "CFUP",4);

                     if (ibsta & ERR) error();
                     }

/* From 10 MHz to 100 MHz at steps of 10 MHz*/
```

```
        else if (i== 19)
                {
                freqmhz = 10;
                ibwrt(spar,"ML?",3);
                ibrd(spar,rd,8);
                fprintf(output, "%d\t\t%s\n",freqmhz,rd);
                ibwrt(spar, "CS10MZ,SP100KZ,MK CF",19);
                }
        else  if ((i > 19) && (i < 28))
        {
                freqmhz = 10 + (i-19)*10;

                sgtr = ibfind("HPSGTR");
                if((sgtr = ibfind("HPSGTR")) < 0) finderr();
                ibwrt(sgtr,"FRIS10MZ",8);
                if (ibsta & ERR) error();

                ibwrt(sgtr,"FRUP",4);
                if (ibsta & ERR) error();

                spar = ibfind("DEV5");
                if((spar = ibfind("DEV5")) < 0) finderr();
                ibwrt(spar, "CFUP",4);

                if (ibsta & ERR) error();
                ibwrt(spar,"ML?",3);
                ibrd(spar,rd,8);
                fprintf(output, "%d\t\t%s\n",freqmhz,rd);
        }

/* From 100 MHz to 1 GHz at steps of 100 MHz*/

        else if (i== 28)
                {
                freqmhz = 100;

                sgtr = ibfind("HPSGTR");
                if((sgtr = ibfind("HPSGTR")) < 0) finderr();
                ibwrt(sgtr,"FR UP",5);
                if (ibsta & ERR) error();

                spar = ibfind("DEV5");
                if((spar = ibfind("DEV5")) < 0) finderr();
                ibwrt(spar, "CFUP",4);

                ibwrt(spar,"ML?",3);
                ibrd(spar,rd,8);
                fprintf(output, "%d\t\t%s\n",freqmhz,rd);
                ibwrt(spar, "CS100MZ,MK CF",13);
                }
        else  if((i > 28) && (i < 34))
        {
                freqmhz = 100 + (i-28)*100;

                sgtr = ibfind("HPSGTR");
                if((sgtr = ibfind("HPSGTR")) < 0) finderr();
                ibwrt(sgtr,"FRIS100MZ",9);
                if (ibsta & ERR) error();

                ibwrt(sgtr,"FRUP",4);
                if (ibsta & ERR) error();

                spar = ibfind("DEV5");
                if((spar = ibfind("DEV5")) < 0) finderr();
                ibwrt(spar, "CFUP",4);

                if (ibsta & ERR) error();
                ibwrt(spar,"ML?",3);
                ibrd(spar,rd,8);
                fprintf(output, "%d\t\t%s\n",freqmhz,rd);
        }

        else if (i == 34)
        {
```

```
                freqmhz = 700;
                sgtr = ibfind("HPSGTR");
                if((sgtr = ibfind("HPSGTR")) < 0) finderr();
                ibwrt(sgtr,"FRUP",4);
                if (ibsta & ERR) error();

                spar = ibfind("DEV5");
                if((spar = ibfind("DEV5")) < 0) finderr();
                ibwrt(spar, "CFUP",4);
                ibwrt(spar,"ML?",3);
                ibrd(spar,rd,8);
                fprintf(output, "%d\N\t%s\n",freqmhz,rd);
                }

        else  if((i > 34) && (i <= 37))
        {
                freqmhz = 100 + (i-28)*100;

                ibwrt(spar, "CS100MZ,SP100MZ,MK CF",21);

                sgtr = ibfind("HPSGTR");
                if((sgtr = ibfind("HPSGTR")) < 0) finderr();
            /*  ibwrt(sgtr,"FRIS100MZ",9);
                if (ibsta & ERR) error();
                */
                ibwrt(sgtr,"FRUP",4);
                if (ibsta & ERR) error();

                spar = ibfind("DEV5");
                if((spar = ibfind("DEV5")) < 0) finderr();
                ibwrt(spar, "CFUP",4);

                if (ibsta & ERR) error();
                ibwrt(spar,"ML?",3);
                ibrd(spar,rd,8);
                fprintf(output, "%d\N\t%s\n",freqmhz,rd);
        }
        else if ( n >37)
        {
                ibloc(spar);
                sgtr = ibfind("HPSGTR");
                ibloc(sgtr);
                fclose(output);
                exit();
        }
        }
  return(0);
}

void finderr(void)
{
/* This routine would notify you that the ibfind
   call failed, and refer you to the handler
   software configuration procedures.          */

  printf("Ibfind error; does device or board\n");
  printf("name given match configuration name?\n");
}

void error(void)
{
/* An error checking routine at this location would,
   among other things, check iberr to determine the
   exact cause of the error condition and then take
   action appropriate to the application.  For
   errors during data transfers, ibcnt may be
   examined to determine the actual number of bytes
   transferred.                          */

  printf("GPIB function call error:\n");
  printf("ibsta=0x%x, iberr=0x%x,",ibsta,iberr);
  printf(" ibcnt=0x%x\n",ibcnt);
}
```

E2: STANDARD DEVIATION OF THE OLM AND NCSM DATA

The definition of standard deviation is given in eqn. 5.3.2. Using that equation and from the input data files which contain the NCSM and OLM SE data, it is easy to calculate the standard deviations for the first two samples (since OLM data were taken with those two samples only) but it is a lengthy process (if done manually) and as such a computer program is written which performs these operations and the output of that program is represented in tabular form.

COMPUTER PROGRAM LISTING

```
/* This is the computer program to calculate the standard deviation
of the On-line SE data from the NCSM data with the TEM-T cell and the
Q-loop antenna.
_____________________________________________________________________ */

#include <math.h>
#include <stdio.h>


main()
{
        int data,N, sample_no, Test_device, freq;
        float sencsm, seolm, variance, sumse_ncsm, std, mean_sencsm,stddev;
        float seolm1, seolm2, seolmc, variancec, stdc, diff,mean_diff,stddevc;

/*      Test_device = 1 indicates the TEM-T cell and Test_device = 2
        indicates the Q-loop antenna */

/*      Input files */
        FILE *fld11,*fld12,*fld21,*fld22;
/*      Output files */
        FILE *sef;

        sumse_ncsm = 0.0;
        std = 0.0;

/*      N represents the toatl no. of data contents of the input files*/

    fld11 = fopen("c:\\grapher\\results\\sec1std.dat","r");
    fld12 = fopen("c:\\grapher\\results\\qcs1.dat","r");
    fld21 = fopen("c:\\grapher\\results\\sec2std.dat","r");
    fld22 = fopen("c:\\grapher\\results\\qcs2.dat","r");
    sef   = fopen("c:\\hafize\\output\\stddev.dat","w");

/*      freq represents the frequency expressed in 100 MHz */

        for (Test_device =1;Test_device<=2;Test_device++)
        {
        if (Test_device ==1){ N=10;
        fprintf(sef,"Near E-field measurement\n");}
        if (Test_device ==2){ N=19;
        fprintf(sef,"Near H-field measurement\n");}

        for (sample_no =1;sample_no <=2;sample_no++){

        sumse_ncsm = 0.0;
        std = 0.0;
        stdc = 0.0;
```

```
for (data = 1; data<= N; data++) {

if (sample_no ==1){
        if (Test_device ==1)
        fscanf (fld11,"%d\t%f\t%f\t%f\t%f\n",&freq,&sencsm,&seolm,&seolm1,&seolm2);
        if (Test_device ==2)
        fscanf (fld12,"%d\t%f\t%f\t%f\t%f\n",&freq,&sencsm,&seolm,&seolm1,&seolm2);
}

if (sample_no ==2){
        if (Test_device ==1)
        fscanf (fld21,"%d\t%f\t%f\t%f\t%f\n",&freq,&sencsm,&seolm,&seolm1,&seolm2);
        if (Test_device ==2)
        fscanf (fld22,"%d\t%f\t%f\t%f\t%f\n",&freq,&sencsm,&seolm,&seolm1,&seolm2);
        }

sumse_ncsm = sumse_ncsm + sencsm;
variance = (sencsm-seolm)*(sencsm-seolm);
std = std + variance;

diff = -seolm1 - seolm2 + 2.0*sencsm  ;
mean_diff = diff/2.0;
seolmc = mean_diff + seolm;
variancec = (sencsm-seolmc)*(sencsm-seolmc);
stdc = stdc + variancec;
}

mean_sencsm = sumse_ncsm/N;
stddev = sqrt(std/N);
stddevc = sqrt(stdc/N);

fprintf (sef,"%10d  %20.5f %20.5f %20.5f\n",sample_no,mean_sencsm,stddev, stddevc);
}
}

fclose(fld11);
fclose(fld12);
fclose(fld21);
fclose(fld22);

fclose(sef);

return 0;
}
```

TABLE E2-1: Standard deviation of OLM data from NCSM data

Sample #	Average NCSM data (dB)	Standard Deviation, σ (dB)	Standard deviation of calibrated OLM data, σ_c
TEM-T cell test device for near E-field SE measurement			
1	60.10000	1.71552	1.14521
2	44.17500	1.52225	0.38079
Q-loop antenna for near H-field SE measurement			
1	39.39474	1.48785	0.39736
2	10.37368	1.03974	0.33950

E3: INDIRECT PATH SIGNAL INFRINGEMENT AND CORRECTION

There are three major sources of indirect path signal which may be incident on the MUT sheet or on the receiving half of the test device:

(1) The EM wave incident on the MUT sheet at large angles would be reflected at large angles. If there is any metallic object or wall in the vicinity, this reflected wave would again be re-reflected from that wall at very short angle. Thus there is the possibility that this re-reflected wave would come back to the receiving half of the test device. The situation is illustrated in Fig. E3-1. The more the reflections from the surface of the MUT, the larger the error due to indirect path signal infringement. Consequently, it has been observed from the test results for indirect path signal infringement that in case of the PET laminate, this error is the largest and in case of carbon loaded PVC this is the smallest which is shown clearly in Fig. 5.22.

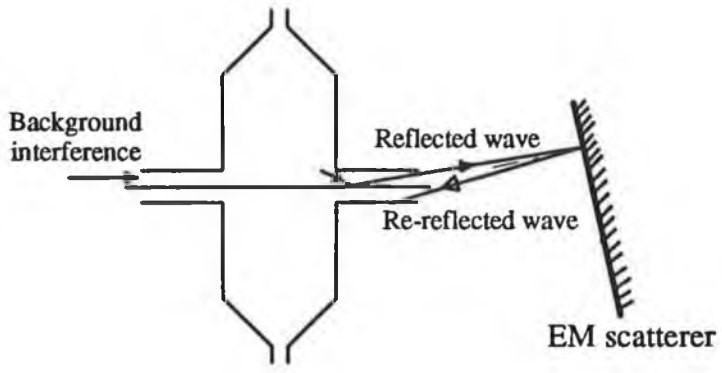

Fig. E3-1 The possibility of the indirect path signal infringement. EM rays incident at wide angles on the MUT are re-reflected from a nearby scatterer and hitting back the receiving half of the test device.

(2) Another major source of indirect path signal infringement is the background noise. Since in NCSM the test device is not completely shielded there exists the possibility that background noise would be incident on the MUT sheet and on the test receiver as well. Thus it may also distort the intended field type on the MUT sheet.

(3) The radiated field from the transmitting half of the TEM-T cell may be reflected back to the receiving half after striking an EM scatterer around.

The effect of all those indirect path signal infringements appear in the form of recording lower SE value of the test sample than the actual.

E4: REFLECTIVITY PROFILE OF ECCOSORB EN79

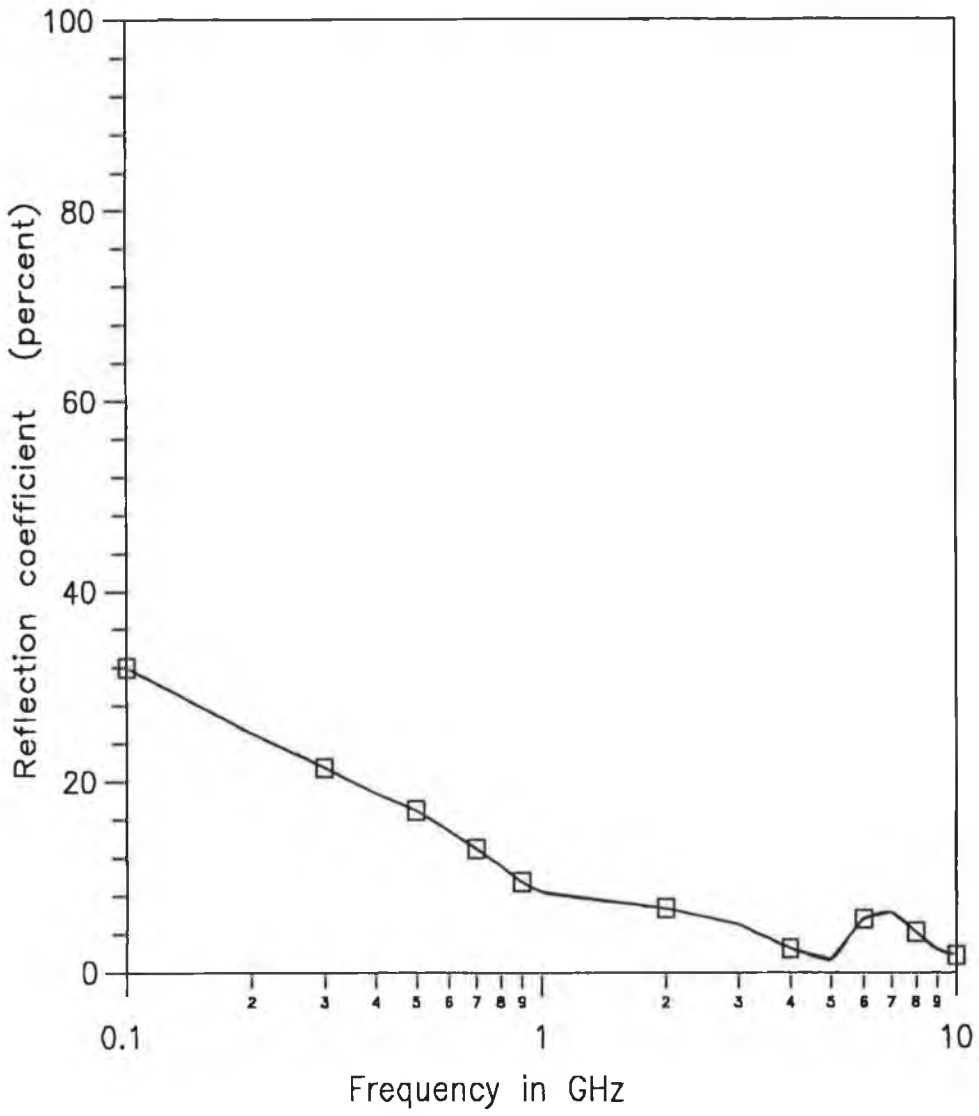

Fig. E4-1 Reflection coefficient in % of the ECCOSRB AN79 good quality flexible foam sheet commercial absorbers. Expressed in % from the reflectivity profile (in dB) suppilied by Emerson and Cuming (UK) (supplier of the absorbing foam).

E5: THEORETICAL CALCULATION OF SE OF THE SAMPLES

SE of the samples, against high impedance field, are calculated on the basis of the idea that this type of field is attenuated due to reflection from the interfaces mainly and similarly SE against low impedance field is calculated assuming that the absorption loss and successive re-reflections inside the material are the constituents of such SE. Sample calculations and the listing of the computer program are given below:

SAMPLE CALCULATIONS

Sample #1
Polyethylene Terephthalate Laminate
ES 301554 (Good Fellow)

Total thickness 0.17 mm,
Polymer thickness 0.075 mm,
Backing material 0.07 mm (70 μm) copper

PET polymer
Dielectric constant @ 1 MHz: 3.0
Surface resistivity ρ_s : 10^{13} Ω/□
Volume resistivity ρ : 10^{14} Ω-cm

Absorption Loss, A

Since the conductivity of the polymer is negligible the absorption loss will occur only in the backing material which is given by

$$A = 8.686t\sqrt{\pi f \mu \sigma_s} \quad \text{dB} \quad \ldots \quad \ldots \quad \text{(E5-1)}$$

Substituting the conductivity of copper and free space permeability in the above eqn. one obtains

$$A = 92.0\sqrt{f} \quad \text{dB} \quad \ldots \quad \ldots \quad \text{(E5-2)}$$

where f is the frequency in 100 MHz.

Reflection Loss, R

R due to the multiple boundaries of the laminate of polymer and backing material is

$$R = 20\log_{10}\frac{|\eta_a + \eta_c||\eta_c + \eta_p||\eta_p + \eta_a|}{8|\eta_a||\eta_c||\eta_p|} \text{ in dB} \quad \ldots \quad \text{(E5-3)}$$

where, η_c is the intrinsic impedance of the metal foil
η_p is the intrinsic impedance of polymer
η_a is the intrinsic impedance of air

Intrinsic impedance of metallic film is given by,

$$\eta_c = \left|(1+j)\sqrt{\frac{\mu\omega}{2\sigma_s}}\right| = 3.68\times10^{-3}\sqrt{f} \quad \Omega \quad \ldots \quad \text{(E5-4)}$$

Intrinsic impedance of polymer can be expressed as ,

$$\eta_p = \frac{\eta_a}{\sqrt{\varepsilon_r}} = 217.6\Omega \quad \text{for } \sigma_p << \omega\varepsilon_p, \text{ where } \varepsilon_p = \varepsilon_0\varepsilon_r \quad \text{(E5-5)}$$

Thus by substituting from (E5-4) and (E5-5) in (E5-3),

$$R = 86.10 - 10\log_{10} f \quad \text{dB} \quad \ldots \quad \ldots \quad \text{(E5-6)}$$

Successive Re-reflection Loss, C

It is assumed that this loss would occur only inside the metallic layer and as its electrical thickness is very small, this loss may not be negligible. This loss is dependent on the absorption loss and is given by,

$$C = 20\log_{10}\left|1-\rho.10^{-\frac{A}{10}}\exp(-j\theta)\right|$$

where $\rho = \left(\frac{\eta_c - \eta_a}{\eta_c + \eta_a}\right)^2 \approx 1$ since $\eta_c << \eta_a$ ... (E5-7)

$$\theta = 3.54t\sqrt{f\mu\sigma_s}$$
$$= 21.1\sqrt{f}$$

Sample #2
Specially made Aluminium -ABS Laminate

Total thickness : 2.2712 mm,
Plastic thickness : 2.095 mm,
Backing material : 0.016 mm (16 μm) aluminium

ABS plastic
Dielectric constant @ 1 MHz: 3.3
Volume resistivity ρ : $>10^{15}$ Ω-cm

Absorption Loss, A

This case is analogous to the previous one, so by putting the conductivity of alluvium in eqn. E5-1,

$$A = 16.33\sqrt{f} \quad \text{dB} \quad ... \quad ... \quad \text{(E5-8)}$$

Reflection Loss, R

Exactly by the similar set of calculations as in case of PET laminate, it is possible to determine the reflection loss of this sample as well. So by substituting the intrinsic impedances of the multiple boundaries in eqn. E5-3 one obtains,

$$R = 83.76 - 10\log_{10} f \quad \text{dB} \quad ... \quad ... \quad \text{(E5-9)}$$

Successive Re-reflection Loss, C

This loss is given by eqn. E5-7 where $\rho \cong 1$ but,

$$\theta = 3.75\sqrt{f} \quad \text{rad} \quad ... \quad ... \quad \text{(E5-10)}$$

Sample #3
Vacuum coated ABS

Total thickness : 2.172 mm,
Plastic thickness : 2.095 mm,
Coating material : 0.008 mm (8 μm) aluminium

ABS plastic
Dielectric constant @ 1 MHz: 3.3
Volume resistivity ρ : $>10^{15}$ Ω-cm

Since , the thickness of the coating is very thin, eqn. 3.2.1 has been used in calculating the SE of this material from which the absorption loss and the successive re-reflection loss have been subtracted to fmd the SE against high impedance field.

Absorption loss can be calculated as above by substituting the thickness of the coating and the conductivity of aluminium in eqn E5-1, which is

$$A = 8.165\sqrt{f} \quad \text{dB} \quad \ldots \quad \ldots \quad \text{(E5-11)}$$

and the successive re-reflection loss will be given by eqn. E5-7, where

$$\theta = 1.875\sqrt{f} \quad \text{rad} \quad \ldots \quad \ldots \quad \text{(E5-12)}$$

COMPUTER PROGRAM LISTING

```
/* This is the computer program to calculate the SE of the samples
theoretically (both against E- and H- fields) and to create the data
files for GRAPHER to plot the theoretical SE along with the measured
SE of the first three samples.
_____ */

#include <math.h>
#include <stdio.h>
#include <complex.h>

#define eta0 376.99 /* Intrinsic impedance of free space */
#define PI 3.141592654
#define speed 3.0e8 /* Speed of light in free space in meter/sec */

main()
{
        int freq,j,npts, sample_no;
        float theta,A,R,Rv,C,SE,qse;
        float lambda0,lambda, beta, eps;
        complex comp1, comp2, comp;

/*      For sample #3, Eqn. no. 3.2.1 has been used, thus the following
        parameters are to be inputted:
        conductivity of aluminium */
        float sigma = 3.58*1.0e7;
/*      Thickness of the aluminium layer in meter coated on to plastic */
        float t = 2.0e-6;
/*      Surface resistance of the aluminium layer in ohms/square */
        float Rs = 1.0/(t*sigma);
/*      Relative permittivity of ABS */
        float epsir = 3.3;

/*      Input files */
        FILE *fld11,*fld12,*fld21,*fld22,*fld31,*fld32;
/*      Output files */
        FILE *sef1r, *sef2r, *sef3r, *sef1a, *sef2a, *sef3a;

    fld11 = fopen("c:\\hafizc\\output\\qcs11.dat","r");
    fld12 = fopen("c:\\hafizc\\output\\qcs12.dat","r");
    fld21 = fopen("c:\\hafizc\\output\\qcs21.dat","r");
    fld22 = fopen("c:\\hafizc\\output\\qcs22.dat","r");
    fld31 = fopen("c:\\hafizc\\output\\qcs31.dat","r");
    fld32 = fopen("c:\\hafizc\\output\\qcs32.dat","r");
    sef1r = fopen("c:\\hafizc\\output\\sethE1.dat","w");
    sef2r = fopen("c:\\hafizc\\output\\sethE2.dat","w");
    sef3r = fopen("c:\\hafizc\\output\\sethE3.dat","w");
    sef1a = fopen("c:\\hafizc\\output\\sethH1.dat","w");
    sef2a = fopen("c:\\hafizc\\output\\sethH2.dat","w");
    sef3a = fopen("c:\\hafizc\\output\\sethH3.dat","w");

/*      freq represents the frequency expressed in 100 MHz */

        for (sample_no =1;sample_no <=3;sample_no++){
        for (freq = 1; freq<= 9; freq++) {
        if (sample_no ==1){
        fscanf (fld11,"%f", &qse);

        A = 92*sqrt(0.1*freq); /* eqn. E5-2 */
        R = 86.1 - 10*log10(0.1*freq);  /* eqn. E5-6 */
        theta = 21.1*sqrt(0.1*freq); /* eqn. E5-7 */
        C = 20*log10(abs(1.0 - complex(cos(theta), -sin(theta))*pow(10.0,-A/10.0)));
        fprintf(sef1r,"%7d  %15.5f\n",freq*10,R);
        fprintf(sef1a,"%7d  %15.5f %15.5f\n",freq*10,A+C,qse);
        }
```

```
        if (sample_no ==2){

        A = 16.33*sqrt(0.1*freq); /* eqn. E5-8 */
        fscanf (fld21,"%f", &qse);

        R = 83.76 - 10*log10(0.1*freq); /* eqn. E5-9 */
        theta = 3.75*sqrt(0.1*freq); /* eqn. E5-10 */
        C = 20*log10(abs(1.0 - complex(cos(theta), -sin(theta))*pow(10.0,-A/10.0)));
        fprintf(sef2r,"%7d  %15.5f\n",freq*10,R);
        fprintf(sef2a,"%7d  %15.5f %15.5f\n",freq*10,A+C,qse);
        }
        if (sample_no ==3){

        A = 8.04075*sqrt(0.1*freq);       /* eqn. E5-11 */
        fscanf (fld31,"%f", &qse);

/*      Wavelength in free space */
        lambda0 = speed*(1.0e-8)/(0.1*freq);
/*      Wavelength in ABS sheet */
        lambda = lambda0/sqrt(epsir);
/*      Phase thickness of the ABS sheet */
        beta = 2*PI*t/lambda;
        comp1 =    complex(1.0, sqrt(epsir)*tan(beta));
        comp2 = complex(1.0, tan(beta)/epsir);
        comp = comp1/comp2;
        Rv = pow((abs(1.0 + eta0/Rs + comp)),2.0);
    eps = (epsir-1)*cos(2.0*beta);

        SE = 10.0*log10((((1+epsir) + eps)/(8.0*epsir))*Rv); /* eqn. 3.2.1 */

        theta = 1.875*sqrt(0.1*freq);       /* eqn. E5-12 */
        C = 20*log10(abs(1.0 - complex(cos(theta), -sin(theta))*pow(10.0,-A/10.0)));
        printf("%7d  %15.5f\n", freq*10,Rv);
        fprintf(sef3r,"%7d  %15.5f\n",freq*10,SE-(A+C));
        fprintf(sef3a,"%7d  %15.5f %15.5f\n",freq*10,A+C,qse);
                }
        }

        for (freq = 1; freq<= 10; freq++) {
        if (sample_no ==1){
        fscanf (fld12,"%f", &qse);

        A = 92*sqrt(freq);
        R = 86.1 - 10*log10(freq);
        theta = 21.1*sqrt(freq);
        C = 20*log10(abs(1.0 - complex(cos(theta), -sin(theta))*pow(10.0,-A/10.0)));
        fprintf(sef1r,"%7d  %15.5f\n",freq*100,R);
        fprintf(sef1a,"%7d  %15.5f %15.5f\n",freq*10,A+C,qse);
        }
        if (sample_no ==2){

        A = 16.33*sqrt(freq);
        fscanf (fld22,"%f", &qse);

        R = 83.76 - 10*log10(freq);
        theta = 21.1*sqrt(freq);
        C = 20*log10(abs(1.0 - complex(cos(theta), -sin(theta))*pow(10.0,-A/10.0)));
        fprintf(sef2r,"%7d  %15.5f\n",freq*100,R);
        fprintf(sef2a,"%7d  %15.5f %15.5f\n",freq*100,A+C,qse);
        }
        if (sample_no ==3){

        A = 8.04075*sqrt(freq);
        fscanf (fld32,"%f", &qse);

        lambda0 = speed*(1.0e-8)/freq;
        lambda = lambda0/sqrt(epsir);
        beta = 2*PI*t/lambda;
        comp1 =    complex(1.0, sqrt(epsir)*tan(beta));
        comp2 = complex(1.0, tan(beta)/epsir);
        comp = comp1/comp2;
        Rv = pow((abs(1.0 + eta0/Rs + comp)),2.0);
        eps = (epsir-1)*cos(2.0*beta);
```

```
            SE = 10.0*log10((((1+epsir) + eps)/(8.0*epsir))*Rv);

            theta = 21.1*sqrt(freq);
            C = 20*log10(abs(1.0 - complex(cos(theta), -sin(theta))*pow(10.0,-A/10.0)));

            printf("%7d  %15.5f\n", freq*10,Rv);
            fprintf(sef3r,"%7d  %15.5f\n",freq*100,SE-(A+C));
            fprintf(sef3a,"%7d  %15.5f %15.5f\n",freq*100,A+C,qse);
                        }
            }
}

            fclose(fld11);
            fclose(fld12);
            fclose(fld21);
            fclose(fld22);
            fclose(fld31);
            fclose(fld32);

            fclose(sef1r);
            fclose(sef2r);
            fclose(sef3r);
            fclose(sef1a);
            fclose(sef2a);
            fclose(sef3a);

            return 0;
}
```

E6: CAPACITANCE BETWEEN THE SEPTUMS OF TEM-T HALVES

Since the septums of the TEM-T cell are very thin, capacitance due to direct field lines would be small. Fringing field lines would contribute to the capacitance between them significantly. Thus it is essential to consider the fringing capacitance as well. Fig. E6-1 shows the fringing flux lines in horizontal plane as well as in vertical planes.

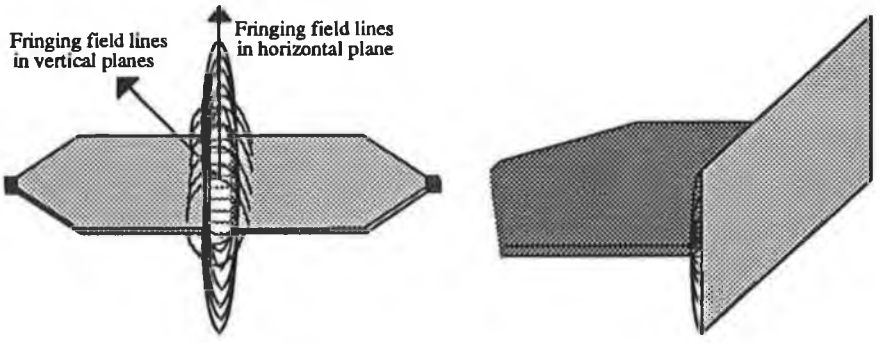

Fig. E6-1 Capacitance between the septums of the TEM-T cell, (a)Fringing field lines between the septums of the TEM-T halves and (b) Fringing field lines between one of the septums and the hypothetical common plate.

Fringing capacitance between the septums may be considered as a pair of capacitors connected in series. Each capacitor of the pair is composed of one septum and a hypothetical common plate placed vertically, half way between the septums. The capacitance of one of the capacitors of the pair is calculated first and then dividing it by 2 one can obtain the total capacitance between the septums. Fig. E6-1(b), one capacitor of the pair is shown. The formulation is developed on the basis of the discussion of Collins[1] for similar type of problem of determining the capacitance between two rectangular plates of unequal dimensions. Sample calculations performed by Mathcad® are presented below:

Approximate analysis of the capacitance between the septum and the sample using Mathcad

---

Half width of the septum,

$w := 0.1$

Distance between the septums in meter,

$d := .002$

Thickness of the septum in meter,

$t := .001$

Calculation of capacitance due to fringing field in the vertical plane

---

$$k := \frac{1}{\cosh\left[\frac{4 \cdot p \cdot t}{4 \cdot d}\right]}$$

$$k1 := \sqrt{1 - k^2}$$

$$Kk := \int_0^1 \frac{1}{\sqrt{\left[1 - x^2\right] \cdot \left[1 - k^2 \cdot x^2\right]}}\, dx$$

$Kk = 1.639$

$$Kk1 := \int_0^1 \frac{1}{\sqrt{\left[1 - x^2\right] \cdot \left[1 - k1^2 \cdot x^2\right]}}\, cx$$

$Kk1 = 2.369$

$$v_0 := \frac{Kk}{Kk1}$$

$v_0 = 0.692$

$C_v := 2 \cdot 8.854 \cdot 10^{-12} \cdot \frac{0.2}{v_0}$

$C_v = 5.117 \cdot 10^{-12}$

Capacitance due to fringing field in the horizontal plane

$Kk := \frac{p}{2}$

$Kk1 := \ln\left[2 + \frac{p \cdot w}{d}\right]$

$v_0 := \frac{Kk}{Kk1}$

$v_0 = 0.01$

$C_h := \frac{2 \cdot 8.852 \cdot t \cdot 10^{-12}}{v_0}$

$C_h = 1.778 \cdot 10^{-12}$

Direct capacitance between the septum and the hypothetical plate

---

$C_d := 8.852 \cdot 10^{-12} \cdot 4 \cdot w \cdot \frac{t}{d}$

$C_d = 1.77 \cdot 10^{-12}$

Total Capacitance between the septum and the hypothetical plate

---

$C := C_v + C_h - C_d$

$C = 5.125 \cdot 10^{-12}$

Total Capacitance between the septums of the two halves

$C_c := \frac{C}{2}$

$C_c = 2.562 \cdot 10^{-12}$

Capacitive Reactance

Frequency in MHz,

$f := 10, 20 .. 100$

Reactance in ohms,

$$\left[2 \cdot p \cdot f \cdot 10^{6} \cdot C_c\right]^{-1}$$

$6.211 \cdot 10^{3}$
$3.106 \cdot 10^{3}$
$2.07 \cdot 10^{3}$
$1.553 \cdot 10^{3}$
$1.242 \cdot 10^{3}$
$1.035 \cdot 10^{3}$
887.346
776.428
690.158
621.142

E7: RADIAL TRANSMISSION LINE MODEL OF THE FLANGES

The annulus between two rectangles as shown in Fig. E7-1(a). (having common centre of gravity) can be considered as a doubly connected region closed by boundaries $\Im_1$ (i.e ABCD) and $\Im_2$ (i.e. EFGH) (such that Z= 0 is interior to $\Im_1$ and Z= $\infty$is exterior to $\Im_2$). It is possible to numerically transform such region approximating as the sum of two polynomials. One of these polynomials maps the exterior of the inner boundary, while the other map the interior of the outer boundary. Together they can be represented by the polynomial transformation equation

$$w \cong \sum_{k=-m}^{n} a_k z^k \qquad \ldots \qquad \ldots \qquad \text{(E7-1)}$$

As the above mentioned doubly connected region is a symmetric region (which has two axes of symmetry), a polynomial of simpler structure can approximate it.

When a simple connected region exhibits p axes of symmetry, its interior (which should include Z=0) can be approximated by a polynomial which contains only terms with Z raised to the power k.p + 1 where k = 0,1,2 .... Furthermore, the coefficients will be real numbers. Eqn. E7-1 then reduces to

$$w \cong \sum_{k=0}^{n} a_{kp+1} z^{kp+1} \qquad \ldots \qquad \ldots \qquad \text{(E7-2)}$$

and for its exterior(which excludes Z=∞) the form is

$$w \equiv \sum_{k=0}^{n} a_{1-kp} z^{1-kp} \quad \ldots \quad \ldots \quad \text{(E7-3)}$$

The two polynomials can be combined to handle a doubly connected region.

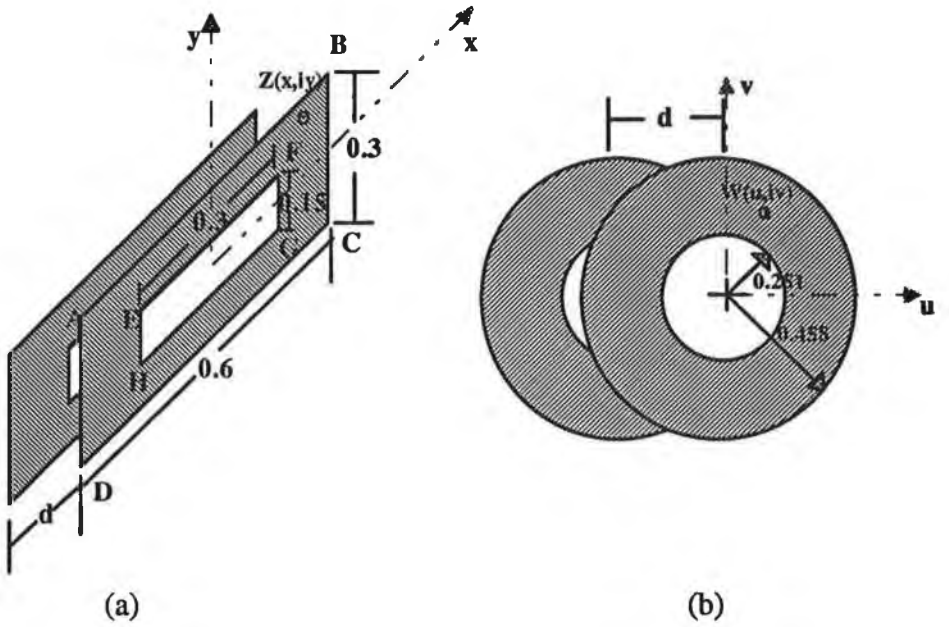

Fig. E7-1 Geometry of the radial transmission line between the flanges of the TEM-T cell. (a) Radial transmission line between Rectangular flanges and (b) Equivalent circular radial transmission lines.

In the present problem, the outer boundary is a rectangle of size 4a×4b with corners at x + iy = ±2a±i2b. The inner boundary is another rectangle of size 2a×2b with corners at x + iy = ±a±ib. Our objective is to map the interior region of the outer boundary in Z-plane as the interior of a circle in the W-plane and the exterior region of the inner rectangle onto the exterior of a circle in the W-plane.

The numerical approach of Kantarovich and Krylov[1] and Gaier[2] has been used to perform the transformation. This is a method of orthogonalization based on setting up and solving simultaneous equations with the assistance of determinants. The analysis presented here follows the discussion of Roland and Patricio[3] where a scalar product is defined in terms of Z-plane variables as follows

---

[1]Kantarovich, L. B. and Krylov, D. I. , *Approximate Methods of Higher Analysis*, First Russian edition 1936; English translation of 1941 ed. by C. D. Benster, Noordhoff, Groningen, 1964. pp. 382.
[2]Gaier, Dieter, *Konstruktive Methoden der konformen Abbildung*, Springer Verlag, 1964.
[3]Schinzinger, R. and Laura, P. A. A.,*Conformal Mapping: Methods and Applications*, Elesevier science publishing company Inc. Amsterdam, 1991, Chapter 4, section 4.3.

$$h_{jk} = \left(Z^j, \overline{Z}^k\right) = \frac{1}{C}\int_{\Im} Z^j Z^k |dZ| \qquad \ldots \qquad \text{(E7-4)}$$

where Z(=x+iy) is a point on the boundary $\Im$ and $\overline{Z}$ is the complex conjugate of that point. C is the perimeter of the boundary $\Im$. Applying the numerical values of the corner points of the rectangular regions one finds for the outer rectangle

$$h_{jk} = \frac{1}{8(a+b)}\left\{\int_{-2a}^{2a}(x-i2b)^j(x+i2b)^k|dx| + \int_{-2a}^{2a}(x+i2b)^j(x-i2b)^k|dx| + \int_{-2b}^{2b}(2a+iy)^j(2a-iy)^k|dy| + \int_{-2b}^{2b}(2a-iy)^j(2a+iy)^k|dy|\right\}$$

$$\ldots \qquad \ldots \qquad \text{(E7-5)}$$

A **Mathematica®** program was written to evaluate and tabulate the elements h_{jk} for j=0,1..5 and k =0,1..5. Then accordingly the Szego polynomials[4] are formed using the equations (4.58) and (4.59) of Roland and Patricio. Next using eqns. (4.68) and (4.72)of the same text , the $K_n(0,Z)$ terms are evaluated and the mapping function W=f(Z) is found as

$$W = f(Z) = 0.424Z + 0.02262Z^5 + 0.000103Z^9 \qquad \ldots \qquad \text{(E7-6)}$$

A larger number of terms would provide greater accuracy. For only three terms the results are quite good. Note, however, that the accuracy decreases as |Z| increases. The radius of the circle appears to be near 0.458 m where a = 0.15 m and b = 0.075 m.

Following similar procedure, the mapping function for the region exterior to the inner rectangle can be derived as a dual of the preceding problem which is

$$W = f(Z) = 0.250Z - 0.041705Z^{-3} + 0.00454Z^{-7} - 0.0016Z^{-11} + 0.0009Z^{-15}$$

$$\ldots \qquad \ldots \qquad \text{(E7-7)}$$

This transform adequately maps the inner rectangle into an inner circle. The radius of the circle is found to be approximately 0.251 m. In this case the accuracy decreases as |Z| decreases. However, in both the cases it is not possible to get a perfect circle using this approximate numerical approach but the accuracy is sufficient.

---

[4]Szego, G., "Conformal mapping related to torsional rigidity principle frequency and electrostatic capacity," in Beckenbach, 1952, pp. 79-83.

F1: COMPUTER PROGRAM FOR PLOTTING RADIATION PATTERN

Polar and Azimuthal pattern of the radiated field of both the AUTs have been recorded by the X-Y plotter and was plotted in rectangular co-ordinates; X-axis represented the angle in degrees and Y-axis represented the received field strength at the test location in dBV. In case of TEM-T cell, the angular positions (θ,ϕ) are expressed in terms of rectangular co-ordinate positions (x,y) and in case of Q-loop antenna the relative field intensities were computed at different angular (θ,ϕ) positions in space. The computational procedures have been elucidated in sections 6.2.3.1 and 6.2.3.2 respectively. The computer programs referred there in the text which generate the data file in the form of m x n matrix or ι x λ matrix are presented here.

GENERATING THE M X N MATRIX DATA FOR PLOTTING THE PATTERN OF TEM-T HALF

```
/* This is a program to compute the field strength in per unit ( and noramlized to
the maximum radiation intensity) at the test site radiated by the TEM-T half acting as an antenna (test results)
_____________________________________________________________ */

#include <math.h>
#include <stdio.h>

main()
{
        int  phi, theta, t, tt, i, j;
        float  angli, angl, dbvx,dbvy, f1,temp, temp1;
        float x[100],y[100],vmt[100],vm[100],vmp[100],vmpt[100];
        float  degrad(float);


        FILE *sef, *sef1, *sef2, *fld,*fld1;
        sef = fopen("c:\\hafizc\\output\\orcsts.dat","w");
        sef1 = fopen("c:\\hafizc\\output\\orcsts1.dat","w");
        sef2 = fopen("c:\\hafizc\\output\\orcsts2.dat","w");
        fld = fopen("c:\\hafizc\\output\\dmvx.dat","r");
        fld1 = fopen("c:\\hafizc\\output\\dmvy.dat","r");

        angli = 85.0;  /*initial angle in degrees */

        /* Distance from the centre of the co-ordinate system i.e. the feed point
        of the TEM-T transmitting half to the point of observation (1.0+0.6=)
        1.6 meters. Since the half length of the cell was 0.6 meters.*/
        x[0] = - 1.6*sin(degrad(angli));
        x[20] = 1.6*sin(degrad(angli));
        y[0] = -1.6*sin(degrad(angli));
        y[20] =     1.6*sin(degrad(angli));

/* Converting the theta, phi positions in terms of rectangular co-ordinate x,y positions */

        for(i=1; i <=19; i++)
        {
        angl = -81.0 + (i-1)*9.0; /* step angles in degrees */
        x[i] = y[i] = 1.6*sin(degrad(angl));
        }
```

```
        float max = 0.0;
        float max1 = 0.0;

/* Computing the maximum radiation intensity in x- direction in order to normalize the field strength */

    for(phi=0; phi <=20; phi++)
    {
        fscanf (fld,"%f", &dbvx);
        temp = (dbvx +120 -36 + 24.3)/20.0;
        vm[phi] = 0.000001*pow(10,temp);
        if(max1<=fabs(vm[phi]))
        max1= fabs(vm[phi]);
        }

/* Normalizing the field strengths recorded along x- direction by the maximum radiation in that direction */

        for(phi=0; phi <=20; phi++)
    {
        vmp[phi] = vm[phi]/max1;
        fprintf(sef,"%5d %15.5f %15.5f\n",phi,vm[phi],vmp[phi]);
        printf("%5d %15.5f %15.5f\n",phi,vm[phi],vmp[phi]);
        }

/* Computing the maximum radiation intensity in y- direction in order to normalize the field strength */

        for(theta=0; theta <=20; theta++)
    {
        fscanf (fld1,"%f", &dbvy);
        temp1 = (dbvy +120 -36 + 24.3)/20;
        vmt[theta] = 0.000001*pow(10,temp1);
        if(max<=fabs(vmt[theta]))
        max= fabs(vmt[theta]);
        }

/* Normalizing the field strengths recorded along y- direction by the maximum radiation in that direction */

        for(theta=0; theta <=20; theta++)
    {
        vmpt[theta] = vmt[theta]/max;
        fprintf(sef1,"%5d %15.5f %15.5f\n",theta,vmt[theta],vmpt[theta]);
        printf("%5d %15.5f %15.5f\n",theta,vmt[theta],vmpt[theta]);
        }

/* Generating the data file in the 3-D surface plot format of GT (GraphTool) */

        float zero = 0.0;
        fprintf(sef2,"%6.4f\t", zero);

        for(tt=0; tt <=20; tt++)
    {
        fprintf(sef2,"%6.4f\t",y[tt]);
        }

        fprintf(sef2,"\n");

        for(t=0; t <=20; t++)
    {
        fprintf(sef2,"%7.4f\t",x[t]);
        for(j=0; j <=20; j++)
    {
        f1 = vmp[j]*vmpt[t];
        fprintf(sef2,"%5.4f\t",f1);
        }
        fprintf(sef2,"\n");
        }

        fclose(sef);
        fclose(sef1);
        fclose(sef2);
```

```
        return 0;
}
float degrad(float angl)
{
float PI = 3.141592654;
        return (angl/180.0)*PI;
}
```

GENERATING THE M X N MATRIX DATA FOR PLOTTING THE PATTERN OF Q-LOOP

```
/* This is a program to compute the field strength in per unit and noramlized to
the maximum radiation intensity at the test site radiated by the Q-loop antenna (test results)
_____ */


#include <math.h>
#include <stdio.h>

main()
{
        int  phi, theta, t, j;
        float  dbuvt,dbuvp,vmt[100],vm[100],vmp[100],vmpt[100], f1,temp, temp1;

        FILE *sef, *sef1, *sef2, *fld,*fld1;
    sef = fopen("fldstc.dat","w");
    sef1 = fopen("fldstc1.dat","w");
    sef2 = fopen("fldstc2.dat","w");
    fld = fopen("d:\\hafizc\\output\\dmuvpc.dat","r");
    fld1 = fopen("d:\\hafizc\\output\\dmuvtc.dat","r");

        float max = 0.0;
        float max1 = 0.0;

/* Computing the maximum radiation intensity in azimuth direction order to normalize the field strength */

    for(phi=0; phi <=26; phi++)
    {
        fscanf (fld,"%f", &dbuvp);
        temp = (dbuvp +120 -36 + 24.3)/20.0;
        vm[phi] = 0.000001*pow(10,temp);
        if(max1<=fabs(vm[phi]))
        max1= fabs(vm[phi]);
        }
/* Normalizing the field strengths recorded in azimuth direction by the maximum radiation in that direction */

        for(phi=0; phi <=26; phi++)
    {
        vmp[phi] = vm[phi]/max1;
        fprintf(sef,"%5d %15.5f %15.5f\n",phi,vm[phi],vmp[phi]);
        printf("%5d %15.5f %15.5f\n",phi,vm[phi],vmp[phi]);
        }

/* Computing the maximum radiation intensity in polar direction order to normalize the field strength */

        for(theta=0; theta <=30; theta++)
    {
        fscanf (fld1,"%f", &dbuvt);
        temp1 = (dbuvt +120 -36 + 24.3)/20;
        vmt[theta] = 0.000001*pow(10,temp1);
        if(max<=fabs(vmt[theta]))
        max= fabs(vmt[theta]);
        }

/* Normalizing the field strengths recorded in polar direction by the maximum radiation in that direction */

        for(theta=0; theta <=30; theta++)
    {
        vmpt[theta] = vmt[theta]/max;
```

```
            fprintf(sef1,"%5d %15.5f %15.5f\n",theta,vmt[theta],vmpt[theta]);
            printf("%5d %15.5f %15.5f\n",theta,vmt[theta],vmpt[theta]);
            }

/* Generating the data file in the 3-D surface plot (in spherical co-ordinate) format of GT (GraphTool) */

            for(t=0; t <=30; t++)
    {
            for(j=0; j <=26; j++)
    {

            f1 = vmp[j]*vmpt[t];
            fprintf(sef2,"%5.4f\t",f1);
            }
            fprintf(sef2,"\n");
            }

            fclose(sef);
            fclose(sef1);
            fclose(sef2);
            return 0;
}
```

F2: FRIIS TRANSMISSION FORMULA

A relation can be established between the received and transmitted powers between two antennas through the Friis[1] Transmission formula. The separation between the antennas, R should be such that $R>2D^2/\lambda$, where D is the largest dimension of either antenna.

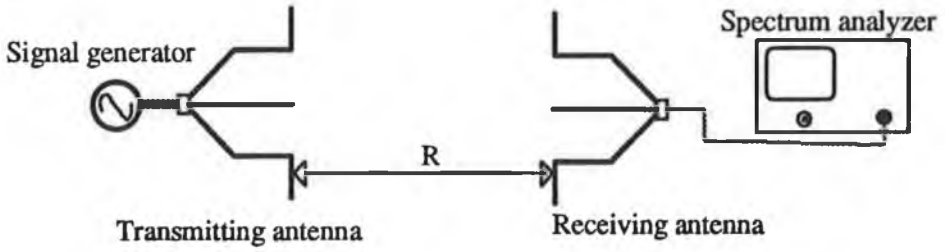

Fig. F2-1 Geometry of the pair of antennas to demonstrate the Friis transmission formula.

Referring to Figure F2-1, let the signal generator feed a power P_t to a transmitting antenna. At a distance R a receiving antenna intercepts some of the power radiated by the transmitting antenna and delivers it to the spectrum analyzer. With the assumption that the

[1]This formula was published by Herald T. Friis of the Bell Telephone Laboratories in 1946 as "A note on a simple transmission formula," in the *Proc. IRE*, 34 pp. 254-256.

transmitting antenna is an isotropic radiator then its power density W_0 at distance R from the antenna is

$$W_0 = e_{tt} \frac{P_t}{4\pi R^2} \quad \ldots \quad \ldots \quad \ldots \quad \text{(F2-1)}$$

where e_{tt} is to total efficiency of the transmitting antenna. For a non isotropic transmitting antenna, this power in the direction θ_t,ϕ_t can be written as

$$W_i = \frac{P_t G_{0t}(\theta_t,\phi_t)}{4\pi R^2} = e_{tt} \frac{P_t D_{gt}(\theta_t,\phi_t)}{4\pi R^2} \quad \ldots \quad \ldots \quad \text{(F2-2)}$$

where $G_{0t}(\theta_t,\phi_t)$ is the gain and $D_{gt}(\theta_t,\phi_t)$ is the directive gain of the antenna in the direction θ_t,ϕ_t. Let the effective aperture of the receiving antenna be A_r which is related to its efficiency e_{tr} and directive gain D_{gr} by

$$A_r = e_{tr} D_{gr}(\theta_r,\phi_r)\left(\frac{\lambda^2}{4\pi}\right) \quad \ldots \quad \ldots \quad \text{(F2-3)}$$

Now, the amount of power P_r collected by the receiving antenna can be written, using (F2-2), (F2-3), and the polarization loss factor[2] as

$$P_r = e_{tr} D_{gr}(\theta_t,\phi_t)\frac{\lambda^2}{4\pi} W_i = e_{tt} e_{tr} \frac{\lambda^2 D_{gt}(\theta_t,\phi_t) D_{gr}(\theta_t,\phi_t) P_t}{(4\pi R)^2} \left|\hat{\rho}_t \cdot \hat{\rho}_r^*\right|^2 \quad \text{(F2-4)}$$

where $\hat{\rho}_t$ and $\hat{\rho}_r$ represent the polarization vectors respectively. Thus the ratio of the received and transmitted power can be expressed as

$$\frac{P_r}{p_t} = e_{cdt} e_{cdr}\left(1-|\Gamma_t|^2\right)\left(1-|\Gamma_r|^2\right)\left(\frac{\lambda}{4\pi R}\right)^2 D_{gt}(\theta_t,\phi_t) D_{gr}(\theta_r,\phi_r)\left|\hat{\rho}_t \cdot \hat{\rho}_r^*\right|^2 \quad \text{(F2-5)}$$

In case of polarization matched antennas, if they are aligned for maximum directional radiation and reception, (F2-5) reduces to

---

[2]Polarization loss factor includes the losses that might occur due to the mismatches in polarization between the two antennas. It is well described in Antenna Theory by C.A. Balanis.

$$\frac{p_r}{p_t} = \left(\frac{\lambda}{4\pi R}\right)^2 G_{ot} G_{or} \quad \ldots \quad \ldots \quad \text{(F2-6)}$$

Equation (F2-5) or (F2-6) is known as the Friis Transmission Equation, and it relates the power P_r (delivered to the receiver load) to the input power of the transmitting antenna P_t. The term $(\lambda / 4\pi R)^2$ is called the free-space loss factor, and it takes into account the losses due to the spherical spreading of the energy by the antenna.

F3: AVERAGE INTENSITY FOR DIRECTIVITY CALCULATION

The X-Y plotter output (refer to Fig. 6.5 and Fig. 6.8) gives the radiation intensity of the AUTs in two different planes as functions of angular positions for a complete revolution (0^o to 360^o or -180^o to 180^o) of the AUTs. It is possible to calculate the normalized radiation intensities in 4π Sr. (Total angle subtended by a sphere) from those two plots as described earlier appendix F1 (through the computer programs listed there).

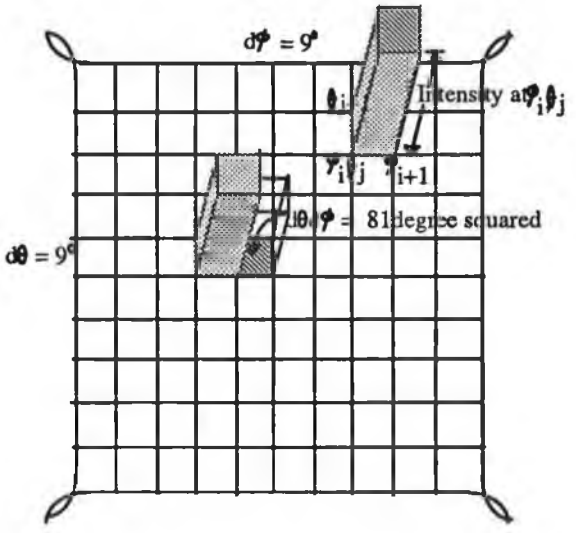

Fig. F3-1 Geometry of the area in angular domain to compute the average radiation intensity.

A radiation intensity profile can be estimated using similar programs over the $360^o \times 360^o$ angular spread as shown in Fig. 6.12 and Fig. 6.13. Now if we assume an average

intensity of E_{ij} corresponding to the location $\phi = \phi_i$ and $\theta = \theta_j$ is spread over the region between ϕ varying from ϕ_i to ϕ_{i+1} and θ varying from θ_j to θ_{j+1} then the product of the area $d\theta d\phi$ with that average intensity would give the intensity content in that differential amount of area, where $d\theta$ and $d\phi$ are the intervals of θ and ϕ. In the present analysis, the interval is 9^o in each direction as shown in Fig. F3-1. The sum of all those area $\times$ amplitude when divided by the over all area of the region i.e. $360^o \times 360^o$, gives the average intensity. The same computer program can be applied to compute the average radiation intensity for both the antennas only by changing the I/O data entry files. The listing of the program which calculate the directivity of the TEM-T half antenna is given bellow:

COMPUTER SUBPROGRAM LISTING

```
/* This is a program to compute the directivity of the TEM-T half
acting as an antenna (test results)
_____ */

#include <math.h>
#include <stdio.h>
#define PI 3.141592654

main()
{
        int anglp, anglt, phi, theta, t, tt, i, j;
        float dbvx,dbvy, f1,temp, temp1;
        float vmt[100],vm[100],vmp[100],vmpt[100];
        float degrad(float);


        FILE *sef, *sef1, *sef2, *sef3,*fld,*fld1;
    sef = fopen("c:\\hafizc\\output\\orfsf.dat","w");
    sef1 = fopen("c:\\hafizc\\output\\orfsf1.dat","w");
    sef2 = fopen("c:\\hafizc\\output\\orfsf2m.dat","w");
    sef3 = fopen("c:\\hafizc\\output\\orfsf3.dat","w");
    fld = fopen("c:\\hafizc\\output\\dmvxx.dat","r");
    fld1 = fopen("c:\\hafizc\\output\\dmvyy.dat","r");

        int angli = -180; /*initial angle in degrees */
        float direc = 0.0;
    float area = 360.0*360.0;


        float max = 0.0;
        float max1 = 0.0;

/*      Computation of the maximum value of the intensity in the
        azimuth direction i.e. in phi direction */

    for(phi=1; phi <=40; phi++)
    {
        fscanf (fld,"%f", &dbvx);
        temp = (dbvx +120 -36 + 24.3)/20.0;
        vm[phi] = 0.000001*pow(10,temp);
        if(max1<=fabs(vm[phi]))
        max1= fabs(vm[phi]);
        }
```

```
/*          Normalizing the intensities in the azimuth direction i.e. in phi direction */

            for(phi=1; phi <=40; phi++)
    {
            vmp[phi] = vm[phi]/max1;
            fprintf(sef,"%5d %15.5f %15.5f\n",phi,vm[phi],vmp[phi]);
            printf("%5d %15.5f %15.5f\n",phi,vm[phi],vmp[phi]);
            }

/*          Computation of the maximum value of the intensity in the
            polar direction i.e. in theta direction */

            for(theta=1; theta <=40; theta++)
    {
            fscanf (fld1,"%f", &dbvy);
            temp1 = (dbvy +120 -36 + 24.3)/20;
            vmt[theta] = 0.000001*pow(10,temp1);
            if(max<=fabs(vmt[theta]))
            max= fabs(vmt[theta]);
            }

/*          Normalizing the intensities in the polar direction i.e. in theta direction */

            for(theta=1; theta <=40; theta++)
    {
            vmpt[theta] = vmt[theta]/max;
            fprintf(sef1,"%5d %15.5f %15.5f\n",theta,vmt[theta],vmpt[theta]);
            printf("%5d %15.5f %15.5f\n",theta,vmt[theta],vmpt[theta]);
            }

            for(tt=0; tt <=40; tt++)
    {
            anglp = angli + tt*9;
            fprintf(sef2,"%6d\t",anglp);
            }

            fprintf(sef2,"\n");

            for(t=1; t <=40; t++)
    {
            fprintf(sef2,"%6d\t",angli+(t-1)*9);
            for(j=1; j <=40; j++)
    {
            f1 = vmp[j]*vmpt[t];
            direc = direc + f1*81;
            fprintf(sef2,"%6.4f\t",f1);
            }
            fprintf(sef2,"\n");
            }
/* Computation of the average intensity */
            float intensity_avg = direc/area;
            float directivity = 1.0/intensity_avg;
            fprintf(sef3,"DIRECTIVITY OF THE TEM-T HALF ANTENNA\n");
            fprintf(sef3,"%6.4f\n", directivity);


            fclose(sef);
            fclose(sef1);
            fclose(sef2);
            return 0;
}

float degrad(float angl)
{
            return (angl/180.0)*PI;
}
```

APPENDIX G

LIST OF PUBLICATIONS OUT OF THIS WORK

[1] H. Rahman, P. K. Saha, Jim Dowling and T. Curran," Shielding effectiveness measurement techniques for various materials used for EMI shielding," *IEE Colloquium Digest on Screening of Connectors, Cables and Enclosures*, no. 1992/012, pp. 9/1-6, London, January 1992.

[2] H. Rahman, P. K. Saha and Jim Dowling," Application of frequency sensitive surface in electromagnetic shielding," *Proceedings of the International Conference on Advances in Materials and Processing Technology*, vol. 2, pp. 1017-1028, Dublin, August 1993.

[3] H. Rahman and Jim Dowling," Calibration of TEM-T cell for on-line SE measurement," *19th ARMMS Conference Digest*, pp. 2/1-9, Leeds, September 1993.

[4] H. Rahman, P. K. Saha and Jim Dowling," Application of frequency sensitive surface in electromagnetic shielding," accepted for publishing in the *Journal of Advanced Material Processing Technology*, August 1994.

REFERENCES

[1] *IEEE Standard Dictionary of Electrical and Electronics Terms*, ANSI/IEEE Std. 100-1977, 2nd ed., F.Jay, Ed., New York: Wiley, 1977.

[2] G. A. Jackson, " Survey of EMC measurement techniques," *Electronics and Communication Engineering Journal*, pp. 61-70, March/April 1989.

[3] Jan-I-225, Joint Army-Navy Specification, " Interference measurements, radio methods of, 150 kilocycles to 20 Megacycles (for components and complete assemblies)," June 14, 1945.

[4] A. N. St. John, "Grounds for signal referencing," *IEEE Spectrum*, pp. 42-45, June 1992.

[5] "Electromagnetic fields and the risk of cancer," *Document of the NRPB (National Radiological Protection Board)*, vol. 3, no. 1, Didcot, 1992.

[6] D. A. Savitz, "Childhood cancer and electromagnetic exposure," *AM Journal of Epidemiology*, vol. 128, pp.21-38, 1988.

[7] K. A. McLauchlan, "A possible mechanism for the effects of electromagnetic fields on biological cells," *Elektor Electronics*, pp. 46-48, Feb. 1993.

[8] K. F. Schoch and H. E. Saunders, "Conducting polymers," *IEEE Spectrum*, pp. 52-54, June 1992.

[9] "Lightning and its interaction with aircraft," *IEEE Transac. on EMC*, Special issue (Part 1), vol. 24, May 1982.

[10a] Fuchs, K., "The conductivity of thin metallic films according to the electron theory of metals," *Proc. Camb. Phil. Soc.*, vol. 30, pp. 100, 1938.

[10b] Sondheimer, E. H., "The mean free path of electrons in metals," *Advances in Physics*, vol.1, pp.1, 1952.

[11] R. B. Schulz and E. L. Bronaugh, " US national voluntary EMC standards," Northcon/82, Seattle, WA, USA, pp. 10/3/1-12, 18-20 May, 1982.

[12] IEEE C95.1-1991 Standard, *IEEE Standards for Safety Levels with Respect to Human Exposure to Radio Frequncy Electromagnetic Fields, 3 kHz to 300 GHz*, IEEE Service Center, 445 Hose Lane, Box 1331, Piscataway, NJ 08855-1331, USA.

[13] Chris Marshman, "How to survive the EMC directive" *IEE Review, EMC Supplement*, S-3, July 1993.

[14] J. Catrysse, M. Delesie and W. Steenbakkers." The influence of the test fixture on shielding effectiveness measurements," *IEEE Transac. on EMC*, vol. 34, no. 3, pp. 348-351, August 1992.

[15] P. A. Chatterton and M. A. Houlden, *EMC Electromagnetic Theory to Practical Design*, John Wiley and Sons Inc., Chichester, 1992.

[16] M. T. Ma, M. Kanda, M. L. Crawford and E. B. Larsen, "A review of the electromagnetic compatibility/interference measurement methodologies," *Proceedings of the IEEE*, vol. 73, no. 3, pp. 388-411, March 1985.

[17] Product Feature, "Preselector enhances EMI measurements," *Electronic Engineering*, pp. 21, January 1993.

[18] M. L. Crawford, "Using a TEM cell for EMC measurements of electronic equipment," NBS Tech. Note 1013, April 1979.

[19] M. L. Crawford, "Evaluation of a reverberating chamber facility for performing EM radiated field susceptibility measurements," NBSIR 81-1638, Feb. 1981.

[20] Tech. Brochure, "GTEM cell," Radio Frequency Interference Technology Ltd., UK, 1992.

[21] "Recommended methods of measurement of radiated and conducted interference from receivers for amplitude-modulation, frequency modulation, and television broadcast transmission, " Int. Electro-Tech. Commission Pub. 106, 1974.

[22] "Calibration of a radiation measurement site-site attenuation," FCC Docket 21371, Appendix A, Bulletin OCE 44, Sept. 1977.

[23] International Special Committee on Radio Interference (ISCRI) Pub. 13, 1975.

[24] W. H. Emerson, "Electromagnetic wave absorbers and anechoic chambers through the years," *IEEE Transac. Antennas and Propagation*, vol. AP-21, pp. 484-490, 1973.

[25] MIL-STD 462, Defense logistic Agency, OASD, VA, USA.

[26] MIL-SPEC 59-41, Ministry of Defense, Directorate of Standardization, Glasgow, UK,1986.

[27] An interview of David Potter, chairman of Psion Computer manufacturer published in *New Electronics on Campus*, pp. 28, Summer 1993.

[28] W. Boxleitner, " How to defeat electrostatic discharge," *IEEE Spectrum*, pp. 36-40, August 1989.

[29] L. W. Rickets, J. E. Bridges and J. Miletta, *EMP Reduction and Protective Techniques*, NY: Wiley, 1976.

[30] *Electromagnetic Interference*, Report on IEE public Affairs Board Study Group, IEE (London), Sept. 1987.

[31] M. Rabinowitz, "Effect of the first Electromagnetic pulse on the electric power grid nation wide: A different view," *IEEE Transac. on Power Delivery*, PWRD-2, pp. 1199-1208, Sept. 1987.

[32] D.V. Giri, Foreword to the special issue on HPM of *IEEE Transac. Electromagn. Compat.*, vol. EMC-34, no. 3, August 1992.

[33] Bob Buxton, "Automated EMC measurements," *Electronic Engineering*, pp. 85-92, Nov. 1990.

[34] S. Benda, "ABB process automation is well prepared for future EC directives," *ABB Review* 2/92, pp. 31-38, ABB Automation AB, Sweden, 1992.

[35] T. Mukaihata and R. D. Johnstone, "Implementation and use of small automated-test systems," *Proceedings of the IEEE*, vol. 66, no. 4, pp. 403-413, April 1978.

[36] P. F. Wilson, M. T. Ma and J. W. Adams, "Techniques for measuring the electromagnetic shielding effectiveness of materials: Part I:- Far-field source simulation," *IEEE Transac. on Electromag. Compat.*, vol. 30, no. 3, pp. 239-250, August 1988.

[37] B. Audone, E. R. Totto and M. D. Barba, "The computer-aided approach to emission testing," *IEEE Transac. on EMC*, vol. 26, no. 1, pp. 43-49, Feb. 1984.

[38] B. Audone and G. Gerbi, "The computer-aided approach to susceptibility testing," *IEEE Transac. on EMC*, vol. 22, no. 2, pp. 130-135, May 1980.

[39] T. Armfield, M. Howard and S. Walter, "Automated component level EMC test facility," *IEEE Conference on EMC*, pp. 364-369, Sandiego, CA, 1988.

[40] S. Yasufuku, " Technical progress of EMI shielding materials in Japan," *IEEE Electrical Insulation Magazine*, vol.6 , no. 6, pp. 21-30, Nov./Dec., 1990.

[41] B. Schulz, C. Plantz and R. Brush, "Shielding Theory and Practice," *IEEE Transac. on EMC*, vol.30, no.3, pp. 187-201, August 1988.

[42] S.A. Schelkunoff, *Electromagnetic Waves*. New York: Van Nostrand. 1943, pp. 303-315.

[43] W. Graf and E. F. Vance, "Shielding effectiveness and electromagnetic protection," *IEEE Transac. EMC*, vol. 30, no.3, pp. 289-293, Aug. 1988.

[44] R. S. Elliot, *Antenna Theory and Design*, Englewood Cliffs, NJ: Printice-Hall, 1981.

[45] C. R. Cockrell, "The input admittance of the rectangular cavity backed slot antenna," *IEEE Transac. on AP*, vol. 24. no. 3, pp. 288-294, May 1976.

[46] K. F. Casey, "Low frequency electromagnetic penetration of loaded apertures," *IEEE Transac. EMC*, vol. 23, no. 4, pp.367-377, Nov. 1981.

[47] E. M. Davenport, "Application of finite element methods to the modelling of field ingress to structures," *Int. Conf. Computation Electromagn.* (London, U.K.), pp. 6-9, Nov. 1991.

[48] L.K. Warne and K.C. Chen, "Electromagnetic penetration of slot apertures with depth and losses," in *Proc. Int. Conf. Electromagn. Aerospace Application*, Turin, Italy, pp.95-98, Sept. 1991.

[49] ----"Apertures having depth and losses described by local transmission line theory," *IEEE Transac. EMC*, vol. 32, no. 3, pp. 185-196, Aug. 1990.

[50] B. Audone and M. Balma, "Shielding effectiveness in apertures in rectangular cavities, *IEEE Transac. EMC*, vol. 31, no. 1, pp. 102-106, Feb. 1989.

[51] G. Cerri, R. D. Leo and V. M. Primiani, "Theoretical and experimental evaluation of the electromagnetic radiation from apertures in shielded enclosure," *IEEE Transac. EMC*, vol. 34, no. 4, Nov. 1992.

[52] *Application Notes on Grounding*, Advanced Energy Industries, Inc., 1600 Prospect Parkway, Fort Collins, CO 80525, 1991.

[53] I. P. MacDiarmid, "Shielded equipment enclosure design," *IEE Colloquium Digest*, no. 1992/012, Jan. 1992.

[54] T. Dikvall and M. Marchner, "EMP leakage through the joints of a shield, development of the methods for the measurement of shielding effectiveness," *IEEE Nat. Symp. on EMC*, San Antonio, TX, October 1984.

[55] P. J. Mooney, " Plastics EMI shielding: the evolving state of the art," *EMC Techn.*, vol. 4, pp.19-28, Oct-Dec. 1985.

[56] P. Hanifan, "Plating on plastics- a solution for RFI shielding," *Design Engineering*, pp.53-59, April 1989.

[57] J. H. Ling, "Conductive coating in EMI/RFI shielding techniques," Journal of New Electronics(GB), vol.16, no.1, pp.29-34, 1983.

[58] B. Ballance, "Conductive engineering plastics for EMC applications," *Fourth International Conference on Plastics in Telecommunications*, London, England, 17-19 Sept., pp.29/1-8, (London, England, Plastic and rubber Inst. -1986).

[59] T. A. Skotheim, Ed., Handbook of conducting polymers. New York: Marcel Dekker, 1986.

[60] R. W. Simpson, Jr., "Flexible laminates for use in EMI shielding applications," *IEEE Electrical Insulation Magazine*, vol. 4, no. 1, pp.11-13, Jan./Feb. 1988.

[61] M. B. Miller, "Materials and techniques used in the EMI/RFI shielding of plastic chasis," *SPE Shielding Plastic Symp. Rec.*, Chicago, IL., pp. 139-149, June, 1984.

[62] K. B. Kaner and A.G. MacDiarmid, "Plastics that conduct electricity," *Scientific American*, vol.258, pp.108-109,1988.

[63] K. H. Mobius, "Filler-containing electrically conductive plastics," *Kunstsoffle*, vol. 78, no. 1, pp. 53-58, 1988.

[64] N. Williams, V. K. Varadan, D. Ghodgaonkar and V. V. varadan, "Measurement of transmission and reflection of conductive lossy polymers at millimeter-wave frequencies," *IEEE Transac. EMC*-32 no. 3, pp. 236-241, August 1990.

[65] N. F. Colaneri and L.W. Shacklette, "EMI shielding measurement of conductive polymer blends," *IEEE Transac. on Instrum. and Meas.*, vol.41, no.2, , pp. 291-297, April 1992.

[66] Product Feature, "New conductive fabrics for EMI shielding," T.W. International, Santa Cruz, CA, USA, *Microwave Journal*, Nov. 1985, pp.222-225.

[67] A. I. Medalia, *Rubber Chemical Technol*, vol. 59, pp. 432, 1986.

[68] P. B. Jana, A. K. Mallick, and S. K. De, *Polym. Compos.*, vol. 22, pp. 1, 1991.

[69] D. M. Bigg, *Polym. Engg. Sci.*, vol. 19, no.16, pp. 1188, 1979.

[70] D. M. Bigg, *Polym. Compos.*, vol. 7, no.2, pp. 69, 1986.

[71] Y. S. Wang et.al., *Polym. Compos.*, vol. 7, no.5, pp. 349, 1986.

[72] J. V. Foy and J. T. Lindt, *Polym. Compos.*, vol. 8, no.6, pp. 419, 1987.

[73] J. Martinsson and J. L. White, *Polym. Compos.*, vol. 7, no.5, pp. 302, 1986.

[74] P. B. Jana, S. K. De, S. Chaudhuri and A. K. Pal, "Electrical conductivity of Barium-ferrite vulcanized polychloroprene filled with short carbon fiber," *Rubber Chemical Technol*, vol. 65, pp. 7-23, 1992.

[75] J. Benford and J. Swegle, *High Power Microwave Sources*, Artech House, 1992.

[76] N. May, " RFI shielding of enclosure," *Electronic Engineering*, vol. 55, pp. 77-78, August 1984.

[77] MIL-STD-285, "Attenuation measurements for enclosures, electromagnetic shielding, for electronic test purposes, method of," August 1956.

[78] M. T. Ma and M. Kanda, " Electromagnetic Compatibility and Interference Methodology," *Nat. Bur.Stand. (U.S.) Tech. Note 1099*, Boulder, CO, pp. 362-363, July 1986.

[79] L.C. Oberholtzer, " A Treatise of the NEW ASTM EMI Shielding Standard," *ITEM*, pp. 174-178, 1984.

[80] D.M. Bigg, W. Mirick and D.E. Stutz, " Measurement of EMI shielding of plastic composites using a dual chamber facility," *Polymer Testing (UK)*, vol.5(3), pp. 169-181, 1985.

[81] E. Hariya and U. Masahiro, "Instruments for Measuring the Shielding Effectiveness," *IEEE international symposium on EMC*, Tokyo, Japan, pp. 800-805, October 1984.

[82] J. Catrysse, "A new test-cell for the characterisation of shielding materials in the far field," *IEE proceedings of the 7th International Conference on EMC*, York, UK, pp. 62-67, August 1990.

[83] J.W. Adams and E.J.Vanzura, "Shielding Effectiveness Measurements of Plastics," *NBSIR 85-3035*, NBS, Boulder, CO., January 1985.

[84] J.R. Andrews, M.G. Arthur, "Spectrum Amplitude -- Definition, Generation and Measurement," *NBS technical note 699*, NBS, Boulder, CO, October 1977.

[85] S. Ramo, J. R. Whinnery and T. Van Duzzor, *Fields and Waves in Communication Electronics*, NY: John Wiley and Sons Inc., 2nd. ed., 1984.

[86] P. F. Wilson and M. T. Ma, "Techniques for measuring the shielding effectiveness of materials," *In Proc. of 7th International Symp. on EMC*, Zurich,pp. 547-552, March,1987.

[87] A.R. Ondrejka and J.W. Adams, "Shielding effectiveness measurement techniques" , *IEEE Nat. Symp. on EMC. San Antanio*, TX, 1984. pp. 249-250.

[88] H. Zheng and C.E. Smith, "Permittivity measurements using a short open-ended coaxial line probe," *IEEE Microwave and Guided Letters*, vol. 1, no. 11, pp. 33-36, November 1991.

[89] P.D. Langhe, K. Blomme, L. Martens, and D. D. Zutter, "Measurement of low-permittivity materials based on spectral-domain analysis for the open-ended coaxial probe," *IEEE Transac. on IM,* vol. 42, no. 5, pp.879-886, Oct. 1993.

[89] K.F. Staebell and D. Misra, "An experimental technique for in vico permittivity measurement of materials at microwave frequencies," *IEEE Transac. on MTT,* vol. 38, no. 3, pp.337-339, March 1990.

[90] N.E.B. Tahar, A.F. Lamer and H. Chanterac, "Broad-band simultaneous measurement of complex permittivity and permeability using a coaxial discontinuity," *IEEE Transac. on MTT*, vol. 38, no. 1, pp. 1-7, January 1990.

[91] A. N. Faught, Jr., J.T. Dowell, R.D. Scheps, "Shielding Material Insertion Loss Measurement using a Dual TEM Cell System," *IEEE Internl. Symp. on EMC*, Washington DC, pp. 286-290, August 1983.

[92] R. D. Scheps, "Shielding Effectiveness Measurements Using a Dual-TEM Cell Fixture," *EMC Tech.*, vol. 2, pp. 61-65, July-September 1983.

[93] P. F. Wilson, D. C. Chang and M. T. Ma, "Excitation of a TEM cell by a vertical electric Hertzian pole," NBS, Boulder, CO. Tech. Note 1037, Mar. 1981.

[94] P. F. Wilson and M. T. Ma, "Shielding effectiveness measurements with a dual TEM cell," *IEEE Transac. on EMC* , vol.EMC-27, no.3, pp. 137-142, August,1985.

[95] M.L. Crawford, G.H. Koepke, "Design, evaluation and use of a reverberation chamber for performing electromagnetic susceptibility/vulnerability measurement," *NBS Tech. Note 1092*, April, 1986.

[96] M.O. Hatfield, "Shielding effectiveness measurements using mode-stirred chambers: a comparison of two approaches," *IEEE Transac. on EMC*, vol. 30,

no.3, pp.229-238, Aug. 1988.

[97] P.F. Wilson, M.T. Ma, and J.W Adams, "Techniques For Measuring The Electromagnetic Shielding Effectiveness of Materials: Part II: Near-Field Source Simulation," *IEEE Transac. on EMC*, vol.30, no.3 pp.547-555, August, 1988.

[98] G. Dike, "Electromagnetic Relationships Between Shielding Effectiveness And Transfer Impedance," *IEEE International Symp. on EMC*, Oct.1979.

[99] T.A. Jerse, "Low Transfer Impedance A Key To Effective Shielding," *R.F Design*, vol.7. pp. 29-32, July/August 1984.

[100] A. Pugh, *Robot Sensors*. Berlin, Germany: Springer-Verlag, 1986.

[101] B. G. Batchelor, D. A. Hill and D. C. Hodgson, *Automated Visual Inspection*. Berlin, Germany: Springer-Verlag, 1985.

[102] R. M. Simon, "Test methods for shielding materials," *EMC Technology*, pp. 39-48, Oct.-Dec.1983.

[103] H. Rahman, *Project Proposal*, submitted to the school of Electronic Engineering, Dublin City University, March 1992.

[104] P.F. Wilson and M. T. Ma, "A study of techniques for measuring the electromagnetic shielding effectiveness of materials," Nat. Bur. Stand., Boulder, CO, *NBS Tech. Note 1095*, May 1986.

[105] H. M. Shen, R. W. P. King and T. T. Wu , "V-conical antenna," *IEEE Transac. on Antennas and Propagation*, vol. 36, no. 11, pp. 1519-1525, Nov. 1988.

[106] S.Y. Liao, "RF Shielding Effectiveness and Light Transmission of Copper or Silver Film Coating on Plastic Substrate," *IEEE Transac. on EMC*, vol. EMC-18, no. 4, pp. 148-153, Nov. 1976.

[107] S.Y. Liao, *Microwave Devices and Circuits*. Printice-Hall Inc., Englewood Cliffs, NJ, 1980.

[108] C. A. Klien, "Microwave shielding effectiveness of EC coated dielectric slabs," *IEEE Transac. on MTT*, vol. 38, no. 3, pp. 321-324, March 1990.

[109] M. -S. Lin and C. H. Chen, "Plane-wave shielding characteristics of anisotropic laminated composites," *IEEE Transac. on EMC*, vol. 65, no. 1, pp. 21-27, Feb. 1993.

[110] C. R. Paul, *Introduction to Electromagnetic Comaptibility*, NY: John Wiley and Sons, Inc., pp. 8, 1991.

[111] W. J. Hendricks, "The totally random versus the bin approach for random arrays," *IEEE Transac. on Antennas and Propagation*, vol. 39, no. 12, pp. 1757-1762, Dec. 1991.

[112] K. Miyasaka, *et al.*, *Journal of Material Science*, vol. 17, pp. 1610, 1982.

[113] W. F. Verhelst, *et al.*, *Rubber Chemical Technology*, vol. 50, pp. 735, 1977.

[114] R.D. Sherman, L. M. Middleman and S. M. Jacobs, *Polym. Engg. Sci.*, vol. 23, pp. 36, 1983.

[115] M. T. Kortschot and R. T. Woodhams, "Electromagnetic interference shielding with nickel coated mica composites," *Polymer composites*, vol. 6, no. 4, pp. 296-303, October 1985.

[116] D. E. Davenport, *Conductive Polymers* (R. B. Seymor, ed.), 1981, pp. 39-47.

[117] R. B. Kieburtz and A. Ishimaru, "Scattering by a periodically apertured conducting screen," *IRE Transac. Antennas and Propagation*, vol. AP-9, pp. 506-514, Nov. 1961.

[118] R. H. Ott, R. G. Kouyoumjian and L. Peters, Jr., " The Scattering by a two-dimensional periodic narrow arrays of plates," *Radio Sci.* vol. 2(new Series), no. 11, Nov. 1967.

[119] B. A. Munk, R. G. Kouyoumjian and L. Peters, Jr., "Reflection properties of periodic surfaces of loaded dipoles," *IEEE Transac. Antennas and Propagation*, vol. AP-19, no. 5 pp. 612-617, Sept. 1971.

[120] R. J. Luebbers and B. A. Munk, "Some effects of dielectric loading on periodic slot arrays," *IEEE Transac. Antennas and Propagation*, vol. AP-26, no. 4 pp. 536-542, July 1978.

[121] Luebbers, "Analyses of various periodic slot array geometries using modal matching," Ph.D dissertation, Dept. of Elec. Engg., Ohio State Univ. Sept. 1975.

[122] C. H. Tsao and R. Mittra, "Spectral domain analysis of frequency selective surfaces comprised of periodic arrays of crossed dipoles and jerusalem crosses," *IEEE Transac. Antennas and Propagation*, vol. AP-32, no. 5 pp. 478-486, May 1984.

[123] R. Mittra, C. H. Chan and T. Cwik, "Techniques for analyzing frequency selective surfaces - a review," *Proceedings of the IEEE*, vol. 76, no. 12, pp. 1593-1615, Dec. 1988.

[124] P. W. Grounds and K. J. Webb, "Numerical Analysis of finite frequency selective surfaces with rectangular patches of various aspect ratio," *IEEE Transac. Antennas and Propagation*, vol. AP-39, no. 5 pp. 478-486, May 1991.

[125] E. C. Jordan and K. G. Balmain, *Electromagnetic Waves and Radiating Systems*, 2nd ed., pp. 496-497, Prentice-Hall, Englewood Cliff, New Jersey, 1968.

[126] J. D. Krauss, *Antennas*, 2nd ed., McGraw-Hill Inc., Singapore, 1988.

[127] W. L. Ko and R. Mittra, "Scattering by a truncated periodic array," *IEEE Transac. Antennas and Propagation*, vol. AP-36, no. 4 pp. 496-503, April 1988.

[128] J. A. Stratton, *Electromagnetic Theory*, NY: McGraw-Hill, 1941.

[129] J. D. Jackson, *Classical Eelectrodynamics*, 2nd. ed., NY: Wiley and Sons, 1975.

[130] J. N. Violette, D. R. J. White, *Electromagnetic Compatibility Handbook*, NY: Van Nostrand-Reinhold, 1987.

[131] R.L. Carrel, "The characteristic impedance of two infinite cones of arbitrary cross-section," *IRE Transac. Antennas and Propagation*, vol. AP-6, pp. 197-201, 1958.

[132] D. K. Ghodgaonkar, V. V. Varadan and V. K. Varadan, "A free-space method for measurement of dielectric constants and loss tangents at microwave frequencies," *IEEE Transac. on Instrum. and Meas.*, vol. IM-38, no. 3, pp. 789-793, June 1989.

[133] J. Musil and F. Zacek, *Microwave Measurements of Complex permittivity by Free space Methods* and *Their Applications*. NY: Elsevier, pp. 44-60, 92-166, 1986.

[134] A. L. Cullen, "A new free-wave method for ferrite measurement of millimeter wavelengths," *Radio Sci.*, vol. 22, pp. 1168-1170, 1987.

[135] E. Collett, " Digital spectrometry measurement of dielectric constant at millimeter frequencies," *Microwave J.*, vol. 29, pp. 307-312, 1986.

[136] D. K. Ghodgaonkar, V. V. Varadan and V. K. Varadan, "Free-space measurement of complex permeability of magnetic materials at microwave frequencies," *IEEE Transac. on Instrum. and Meas.*, vol. IM-39, no. 2, pp. 387-394, April 1990.

[137] V. V. Varadan and V. K. Varadan, D. K. Ghodgaonkar, "Free-space broadband measurement of high temperature complex dielectric properties at microwave frequencies," *IEEE Transac. on Instrum. and Meas.*, vol. IM-40, no. 5, pp. 842-846, October 1991.

[138] R. Ro, V. V. Varadan, V. K. Varadan, "Electroagnetic activity and absorption in microwave chiral composites," *IEE proc. pt. H*,vol. 139, no. 5, pp. 441-447, Oct. 1992.

[139] M. R. Taherian, D. J. Yuen, T. M. Habashy and J. A. Kong, "A coaxial-circular waveguide for dielectric measurement," *IEEE Transac. Geosc. and Remo. Sens.*, vol-29, no. 2, pp. 321-329, March 1991.

[140] D. K. Misra, "A quasi-static analysis of open-ended coxial lines," *IEEE Transac. MTT*, vol. 35, no. 10, pp. 925-928, October 1987.

[141] G. M. Wilkins, J. F. Lee and R. Mittra, "Numerical modeling of axisymmetric coaxial waveguide discontinuities," *IEEE Transac. on MTT*, vol. 29, no. 8, pp. 1323-1328, August 1991.

[142] M. A. Saed, "A method of moment solution of a cylindrical cavity placed

between two coaxial tarnsmission lines," *IEEE Transac. on MTT*, vol. 39, no. 10, Oct. 1991.

[143] W.R. Scott, " A new technique for measuring the constitutive parameters of planar materials," *IEEE Transac. on IM*, vol. 41 no. 5, pp. 639-645, Oct. 1992.

[144] Y. Xu and R. G. Bosisio, "Nondestructive measurements of the resistivity of thin conductive films and the dielectric constant of thin substrates using an open-ended coaxial line," *IEE Proceedings-H*, vol. 139, no. 6, Dec. 1992.

[145] J. C. Tippet and D. C. Chang, "Radiation characteristic of electrically small devices in a TEM cell" *IEEE Transac. on EMC*, vol. 18, no. 4, pp. 134-140, Nov. 1976.

[146] J. C. Tippet and M. L. Crawford, "Analytical determination of the first higher-order mode in a TEM cell" *NBS Technical Note: 76-841*, pp. 11, Nov. 1976.

[147] *MATHCAD*, Mathsoft Inc., 201 Broadway, Cambridge, Massachusetts, 02139, USA.

[148] C. A. Balanis, "Antenna theory: a review," *Proccedings of the IEE*, vol. 80 , no. 1, pp. 7-23, January 1992.

[149] D. I. Wu and M. Kanda, "Comaprison of theoretical and experimental data for the near field of an open-ended waveguide," *IEEE Transac. on EMC*, vol. 31, no. 4, pp. 353-358, Nov. 1989.

[150] Galejs, J., *Antennas in Inhomogeneous Media*, chapter 3, NY: Pergamon, 1969.

[151] W. L. Stutzman and G. A. Thiele, *Antenna Theory and Design*, NY: John Wiley and Sons, Inc., pp. 394, 1981.

[152] R.W. Klopfenstien, "Corner reflector antennas with arbitrary dipole orientation and apex angle," *IRE Transac. Antennas and Propagation*, AP-5, pp. 297-305, July 1957.

[153] W. F. Decker, P. F. Wilson, and M. L. Crawford, "Construction of a large transverse electromagnetic cell," *NBS Tech. Note 1011*, Feb. 1979.

[154] W. D. Burnside *et. al.*, "Curved edge modification of compact range reflectors," *IEEE Transac. Antennas and Propagation*, AP-35, pp. 176-182, Feb. 1987.

[155] J. C. Tippet and D.C. Chang, " Higher order modes in rectangular co-axial line with infinitely thin inner conductor," *NBSIR 78-873*, Mar. 1978.

[156] M. L. Crawford, "Generation of standard EM fields using TEM transmission cells," *IEEE Transac. on EMC*, vol-16, no.4, pp. 189-195, Nov. 1974.

[157] J. C. Tippet, " Modal characteristic of rectangular coaxial transmission line," Ph.D Dissertation, Department of Electrical Engineering, University of Colorado, Bulder, 1978.

[158] J. C. Tippet and D.C. Chang and M. L. Crawford, " An analysis and experimental determination of cut-off frequencies of higher order TE modes in a TEM cell," NBSIR 76-841, June 1976.

[159] J. D. Krauss, *Radio Astronomy* , 2nd ed., Cygnus-Quasar, pp. 642-646, 1986.

[160] H. Rahman et. al."Application of frequency sensitive surfaces in electromagnetic shielding," in *AMPT'93 Conference Proceedings*, vol. 2, pp. 1017-1027, Dublin 1993.

[161] GOODFELLOW CATALOGUE 1993/94, Goodfellow Cambridge Ltd.,Cambridge Science Park, Cambridge CB4 4DJ, England, pp. 428.

[162] Technical brochure , TOP TECH Ireland Ltd., August 1993.

[163] Technical report on conductive plastics for electromagnetic interference shielding, BASF Terblend product, pp. 32-33, August 1993.

[164] Siqi Fan, Katie Staebell and D. K. Misra," Static Analysis of an open-ended coaxial line terminated by layered media," *IEEE Transac. on IM, vol.* 39, no. 2, April 1990, pp. 435-437.

[165] D. G. Ashworth and P.A. Davies, "The Doppler effect in a reflecting system," *Proc. IEEE*, vol. 64, pp.280-281, 1976.

[166] C. Yeh, "Reflection and transmission of electromagnetic waves by a moving dielectric medium," *J. Appl. Phys.*,vol. 36, no. 11, pp. 3513-1517, 1965.

[167] V. P. Payati, "Reflection refraction of electromagnetic waves by a moving dielectric medium," *J. Appl. Phys.*, vol.38, no. 2, pp. 652-655,1967.

[168] P. Daly and H. Gruenberg, "Energy relations for plane waves reflected from moving media," *J. Appl. Phys.*, vol.38, no. 11, pp. 4486-4489,1967.

[169] G. R. Valenzuela, " Scattering of electromagnetic wave from a slightly rough surface moving with uniform velocity," *Radio Sci.*, vol. 3, no. 12, pp. 1154-1157, 1968.

[170] D. P. Chrissoulidis and E. E. Kriezis, " The Scattering behaviour of a slightly rough surface moving parallel to its mean plane with uniform velocity," *IEEE Transac. Antennas and propagation*, vol. AP-33, no. 7, pp. 793-796, July 1985.

[171] H. Rahman, *Project Proposal*, submitted to the school of Electronic Engineering, Dublin City University, January 1993.

[172] Balanis, C. A., Antenna Theory: Analysis and Design, NY: Wiley, 1982.

[173] ANSI/IEEE Std. 149-1979, *IEEE Standard Test Procedures for Antennas*, IEEE Inc., 1979.

[174] GRAFTOOL, Graphical Analysis System, 3-D Vesions Corporation, 412 Pacific Coast Highway, Redondo Beach, CA 90277.

[175] Product Feature: New chase antenna solves a critical problem, *Electronic*

Engineering, pp. 21, May 1993.

[176] The Chase guide to EMC emission measurement, *Poster published by Chase ADVANTEST,* 1992.

[177] Plonsey, R. and Collin, R. E., *Prinicples and Applications of Electromagnetic Fields*, NY: McGraw-Hill, 1961.

[178] Zhou, G. and Smith, G. S., " An accurate theoretical model for thin-wire circular half-loop antenna," *IEEE Transac. Antennas and Propagation* vol 39, no. 8, pp. 1167-1177, Aug. 1991.

[179] D. A. Hill, Bandwidth limitations of TEM cells due to resonnaces," *J. Microwave Power*, vol. 18, no. 2, pp. 181-195, 1983.

[180] P. L. Rustan Jr., " Description of an aircraft lightning and simulated nuclear electromagnetic pulse (NEMP) threat based on experimental data," *IEEE Transac. on EMC,* vol. 29, no. 1, pp. 49-63, Feb. 1987.

[181] E. F. Vance and M. A. Uman, " Differences between lightning and nuclear electromagnetic pulse interaction," *IEEE Transac. on EMC,* vol. 30, no. 1, pp. 49-63, Feb. 1988.

[182] J. C. G. Field, " An introduction to electromagnetic screening theory," *IEE Colloquium on EMC Digest,* pp. 1/1-15, Feb. 1983.